FACULTY OF ENGINEERING
AND ARCHITECTURE

Heterogeneous Silicon Nitride Integrated Photonic Devices Based on Micro-Transfer Printing

Stijn Cuyvers

Doctoral dissertation submitted to obtain the academic degree of
Doctor of Photonics Engineering

Supervisors
Prof. Bart Kuyken, PhD - Kasper Van Gasse, PhD
Department of Information Technology
Faculty of Engineering and Architecture, Ghent University

August 2023

GHENT
UNIVERSITY

ISBN 978-94-6355-738-2
NUR 965, 926
Wettelijk depot: D/2023/10.500/70

Members of the Examination Board

Chair

Prof. Em. Daniël De Zutter, PhD, Ghent University

Other members entitled to vote

Prof. Peter Bienstman, PhD, Ghent University
Jean Decobert, PhD, III-V Lab, France
Marianna Pantouvaki, PhD, Microsoft, United Kingdom
Prof. Geert Van Steenberge, PhD, Ghent University

Supervisors

Prof. Bart Kuyken, PhD, Ghent University
Kasper Van Gasse, PhD, Ghent University

Dankwoord
Acknowledgements

Dit werk gaat over geïntegreerde fotonica: licht genereren, manipuleren en detecteren op een chip. Een chip gelijkaardig aan de chips die we kennen van de meer mature micro-elektronica. De hoofdrol is bij geïntegreerde fotonica niet weggelegd voor elektronen en transistoren, maar voorbehouden voor fotonen, lasers, fotodetectoren en nog veel meer. Als de voorgaande zin u niet te veel afgeschrikt heeft, kan ik u aanbevelen om verder te lezen. Een meer diepgaande technische uiteenzetting komt aan bod in de volgende hoofdstukken.

Als we even terugblikken, dan was het in 2016 dat ik voor het eerst kennis maakte met fotonica. Het was tijdens het 3^e Bachelor jaar ingenieurswetenschappen dat Professor Roel Baets en Professor Gunther Roelkens ons de basisprincipes van het vak bijbrachten. Eerlijk gezegd was ik sinds dat vak al verkocht aan dit onderzoeksdomein wegens het interdisciplinaire karakter en de vele beloftevolle toepassingen. In datzelfde semester ontmoette ik voor het eerst pas gepromoveerd professor Bart Kuyken die samen met toenmalig doctoraatstudent Laurens Bogaert onze Bachelorproef begeleidde. Samen met 3 goede vrienden, waaronder huidig collega Stijn Poelman, bouwden we een (weliswaar eenvoudig) systeem om historische schilderijen automatisch te analyseren met een gespecialiseerde infraroodcamera. Om dit te realiseren gebruikten we afstandssensoren gebaseerd op laserdiodes die we van een niet nader genoemd Chinees e-commerceplatform bestelden. Die waren namelijk veel goedkoper dan wat we op de westerse markt konden vinden. Wellicht waren dit dan ook de enige commercieel verkrijgbare lasers die een nog korter leven waren beschoren dan diegene die ik later zelf zou maken tijdens mijn doctoraat.

Na het afronden van mijn Bachelor brak een periode van grote twijfel aan. Kies ik de master in fotonica? Of ga ik toch verder in elektrotechniek? Er werd mij namelijk verteld dat ik nog steeds aan de slag zou kunnen gaan in fotonica na een opleiding elektrotechniek. Aangezien ik mijn opties open wou houden bleef ik uiteindelijk bij elektrotechniek en koos ik voor een interdisciplinair masterthesis gerelateerd aan fotonica. Op die manier kon ik alvast eens proeven van het onderzoeksleven in de fotonicagroep. Dat was een fantastisch jaar. Opnieuw on-

der toezicht van Bart Kuyken enerzijds en Hendrik Rogier, Sam Lemey and Dries Vande Ginste van IDLab anderzijds. In die periode was Bart ook op zoek naar doctoraatsstudenten voor zijn nieuw ERC project rond optische frequentiekammen. Dat klonk allemaal geweldig, maar toen ik hoorde over het bestaan van een BAEF-beurs zou zo'n doctoraat toch nog even moeten wachten. Die beurs liet mij ten slotte toe om een jaar naar Amerika te gaan! Het was Professor Bart Kuyken zelf die mij op de hoogte had gebracht van deze opportuniteit en ook de nodige hulp heeft aangeboden bij het voorbereiden van de BAEF applicatie. Ik heb dat misschien nooit duidelijk gezegd, maar bedankt daarvoor Bart!

Aan Columbia University merkte ik dat de Photonics Research Group (PRG) in Gent een excellente reputatie genoot. Dat bevestigde mijn keuze om verder te gaan met fotonisch onderzoek in Gent. Eenmaal terug uit Amerika begon ik aan mijn doctoraat in september 2019. Een nieuw avontuur, dat bijna 4 jaar zou duren, was aangebroken.

Zoals gewoonlijk is dit doctoraatsproefschrift niet het resultaat van een enkel individu. Dit werk zou nooit tot stand gekomen zijn zonder de hulp, het advies en de steun van veel mensen. Ik doe graag een poging om de vele betrokkenen te bedanken.

Laat mij beginnen bij de collega's waarmee ik het genoegen had onze bureau te delen. In het begin waren dat Lucas, Kasper, Nina, Camiel, Stijn P., Maximilien, Zuyang, Isaac, en later, in chronologische volgorde, Tom Vdk, Max, Tom R., en Xin. Wat hebben we toch plezier gemaakt op de bureau! Zuyang, my apologies for all the noise and chatter in our office! I suspect Bart's students have gradually inherited his talking skills. In our defense, it is said that communication is key in a team, so this is something we took to heart and continuously practiced. Kasper, mijn co-promotor alsook gereputeerd mode-locked laser expert, zat tegenover mij en was dus steeds ter beschikking (of kon alleszins moeilijk ontsnappen) om mijn vele technische vragen te beantwoorden. Misschien waren mijn vele vragen de druppel om naar California te vluchten? Stijn P., altijd bereid om te helpen met IPKISS-problemen of om mijn ebeam exposure in orde te brengen. Het post-processen van de Ligentec chips ging minder vlot dan gehoopt, maar we hebben er toch veel uit geleerd hé! Camiel, pionier van de heterogene integratie op silicium nitride. Bedankt om mij de kneepjes van het transferprinten te leren! Maximilien, I admire your perseverance throughout the Panasonic project. It was great to work together with you on this project!

Daarnaast vormden we natuurlijk een hechte groep met de collega's op de andere bureau's waaronder Ewoud, Tom V., Dennis, Emiel, Robbe, Emmanuel, Laurens, Jasper, Dongbo, Luis, Korneel, en later Margot, Konstantinos en Tom nummer 4. Tom Vdk en Tom V., ik bewonder jullie doorzettingsvermogen om een (initieel) schijnbaar onmogelijk micro-transfer-printbaar materiaal te micro-transfer printen. Luis, your inappropriate jokes will be missed! Emannuel, altijd bereid om te debatteren over politieke, filosofische, en sociaal-economische thema's zodat ook onze niet wetenschappelijke competenties op peil bleven. Ewoud, jouw uniek ritueel om de middagpauze om 11:59 (stipt!) aan te kondigen zal ik niet vergeten!

Thank you Camiel, Jeroen, Jing, Mattias, en Maximilien for the invaluable tips and tricks in the cleanroom. Your guidance has been essential to quickly manage on my own. Verder bedank ik graag Professor Günther Roelkens en de transfer printing groep (met bijna 30 leden!) voor het delen van ervaringen en ideeën over transfer printen en III-V halfgeleiders. Uiteraard zou de cleanroom niet lang stand houden zonder de continue inzet van Steven, Liesbet en Muhammad. Bedankt voor de metaaldeposities, SEM- en FIB sessies, en het operationeel houden van de vele toestellen die op regelmatige basis en zonder goede reden beslissen het te begeven!

Ik bedank ook graag Michael, Jasper, en Clemens voor alle hulp in de meetlabo's, en Kristien, Bert, en Ilse (2x) voor de IT- en HR-ondersteuning.

Aan alle collega's, en in het bijzonder de collega's van Team Bart, bedankt voor de gezellige Friday drinks, de Cava fridays, de teambuildingactiviteiten, de sportieve aangelegenheden, en de conferenties samen. Thank you Viktor, Brecht, Migle, Sarah, Emiel and later Korneel, Max, Rohan, and Athanasios. It was great to organise events with the Photonics Society Ghent!

Verder bedank ik graag alle professoren van de PRG voor hun toegankelijkheid en gedrevenheid. In het bijzonder bedank ik graag mijn promotoren, Bart en Kasper, die steeds paraat stonden om mij te helpen met allerhande vragen en problemen. Jullie gaven mij alle vrijheid om mijn eigen ding te doen maar waren steeds beschikbaar als er feedback nodig was. Bedankt daarvoor!

Tot slot bedank ik graag het Fonds voor Wetenschappelijk Onderzoek (FWO) - Vlaanderen voor het verkrijgen van een doctoraatsbeurs.

Tot zover mijn "professioneel" dankwoord. Dat brengt mij tot de meer persoonlijke rubriek.

Eerst en vooral wil ik graag mijn ouders bedanken voor jullie steun doorheen al deze jaren. Moeke had gelijk, wij waren echte "prinsenkinderen". Jullie hebben steeds naar mij geluisterd, mij ondersteund, en mij geïnspireerd. Verder hebben jullie mij het doorzettingsvermogen geleerd dat essentieel is om mijn studies en doctoraat tot een goed einde te brengen. Zonder jullie steun was dit alles niet gelukt. Bedankt voor de warme thuis!

Verder bedank ik ook graag mijn broer en zus. Ik kan niet meteen iets concreets bedenken, maar toch merci! Het was plezant in Gentbrugge!

Tot slot wil ik mijn vriendin Lotte uitdrukkelijk bedanken voor haar onvoorwaardelijke steun en eindeloos geduld. Ik weet het, ik ben een echte "sjarel". Niet alleen heb ik regelmatig last van spreekwoordelijke "mieren in mijn gat" zowel op professioneel als op persoonlijk vlak, ik zorg ook op recurrente basis voor uitdagende periodes met mijn avonturen in het buitenland.

Het begon met een jaartje New York en de loze belofte dat ik nadien voor eeuwig en altijd in België zou blijven, het liefst zo dicht mogelijk bij de spreekwoordelijke kerktoren. Na enkele jaren werd die loze belofte toch meesterlijk vervormd om een "korte" stage van 3 maanden in Cambridge mogelijk te maken. Dat was een opportuniteit die ik toch niet kon laten liggen? Eerlijk gezegd, ik denk dat ik dat talent doorheen de jaren een beetje van jou heb geleerd: ge moet overal een

uitleg aan kunnen geven! Ondertussen staan er al terug nieuwe avonturen in het buitenland op de planning, maar gelukkig zijn deze van kortere duur.

Lotte, bedankt om dit alles te doorstaan. Je hebt mij altijd gesteund en ik ben je daar ontzettend dankbaar voor!

Gent, april 2023
Stijn Cuyvers

This work was enabled by a fundamental research grant from Research Foundation - Flanders (grant number 11F8120N and 11F8122N).

Table of Contents

List of Figures

List of Tables

List of Acronyms

A

AFM	Atomic Force Microscopy
ASE	Amplified Spontaneous Emission
APD	Avalanche Photodetector
a-Si:H	Hydrogenated amorphous silicon

B

BCB	Benzocyclobutene

C

CMOS	Complementary Metal-Oxide-Semiconductor
CMP	Chemical Mechanical Polishing
CW	Continuous Wave

D

DBR	Distributed Bragg Reflector
DC	Direct Current
DFB	Distributed Feedback
DI	Deionized water
DKS	Dissipative Kerr Soliton
DUV	Deep Ultraviolet
DVS-BCB	Divinylsiloxane-bis-benzocyclobutene

E

EO	Electro-optic
ESA	Electrical Spectrum Analyzer

F

FCA	Free Carrier Absorption
FDTD	Finite-Difference Time-Domain
FFT	Fast Fourier Transform
FPC	Fiber Polarization Controller
FSR	Free Spectral Range
FWHM	Full Width at Half Maximum

G

GaAs	Gallium Arsenide
GBP	Gain-Bandwidth Product
GVD	Group-Velocity Dispersion

H

HF	Hydrofluoric Acid

I

InP	Indium Phosphide
IPA	Isopropyl alcohol (2-Propanol)
IV	Current-Voltage

L

LI	Light-Current
LIV	Light-Current-Voltage
LN	Lithium Niobate
LNOI	Thin-film Lithium Niobate on Insulator
LPCVD	Low Pressure Chemical Vapor Deposition

M

MLL	Mode-Locked Laser
MOVPE	Metalorganic Vapour-Phase Epitaxy
MSM	Metal-Semiconductor-Metal
MQW	Multiple Quantum Well
MZI	Mach-Zehnder Interferometer

N

NLSE	Nonlinear Schrödinger Equation

O

OSA	Optical Spectrum Analyzer

P

PD	Photodetector
PDMS	Polydimethylsiloxane
PECVD	Plasma-Enhanced Chemical Vapor Deposition
PIC	Photonic Integrated Circuit
PSD	Power Spectral Density

Q

QCL	Quantum Cascade Laser

QW	Quantum Well

R

RBW	Resolution Bandwidth
RF	Radio Frequency
RIE	Reactive Ion Etching
RSOA	Reflective Semiconductor Optical Amplifier
RTA	Rapid Thermal Annealing

S

SA	Saturable Absorber
SCOWL	Slab-Coupled Optical Waveguide Laser
SEM	Scanning Electron Microscope
SESAM	Semiconductor Saturable Absorber Mirror
SNR	Signal-to-Noise Ratio
SOA	Semiconductor Optical Amplifier
SOI	Silicon-on-Insulator
SPM	Self-Phase Modulation
SSB-PN	Single-Sideband Phase Noise

T

TE	Transverse Electric
TFLN	Thin-Film Lithium Niobate
TIA	Transimpedance Amplifier
TLM	Transfer Length Method
TOX	Thermal Oxide
TP	Transfer Printing
TPA	Two-Photon Absorption
TWM	Traveling-Wave Model

U

UTC	Uni-Traveling-Carrier

V

VCSEL Vertical-Cavity Surface-Emitting Laser

Samenvatting

Introductie

Sinds het begrip "geïntegreerde optica" in 1969 door S. Miller en zijn medewerkers werd geïntroduceerd, heeft fotonische integratie enorme technologische vooruitgang geboekt. Wetenschappers en ingenieurs begrepen dat geïntegreerde fotonica beter bestand is tegen thermische, mechanische en akoestische verstoringen uit de omgeving in vergelijking met klassieke optische componenten, en economische schaalbaarheid mogelijk maakt door gebruik te maken van fotolithografische technieken uit de micro-elektronica industrie. Grotendeels gedreven door de opmars van optische communicatie, domineerden III-V halfgeleiders aanvankelijk het domein. III-V-halfgeleiders zoals Indiumfosfide combineren immers van nature lichtopwekking, modulatie en detectie op één enkel platform. Gedurende de laatste twee decennia heeft silicium fotonica zich gevestigd als een onmisbaar concurrerend geïntegreerd fotonisch platform, ondanks de nood aan een externe lichtbron. Het succes van silicium fotonica steunt op een aantal belangrijke kenmerken. Ten eerste kan silicium fotonica bestaande CMOS-infrastructuur hergebruiken om schaalbare en kosteneffectieve productie mogelijk te maken, alsook genieten van een naadloze compatibiliteit met micro-elektronische schakelingen. Ten tweede is silicium transparant bij telecommunicatiegolflengten (1310 nm en 1550 nm), waardoor men deze fotonische geïntegreerde schakelingen (PICs) kan gebruiken voor datacom- en telecommunicatietoepassingen. Bovendien maakt het SOI-platform (silicium-op-isolator), door zijn hoog indexcontrast en laag verlies, compacte integratie van optische componenten mogelijk, alsook de realisatie van passieve componenten die beter presteren dan die op concurrerende III-V-platformen.

In de voorbije jaren is siliciumnitride naar voor gekomen als een belangrijk materiaal ter aanvulling van conventionele silicium fotonische geïntegreerde schakelingen. Siliciumnitride heeft een breed transparantievenster - tot in het zichtbare spectrale bereik - wat het toepassingsgebied van conventionele silicium fotonica sterk uitbreidt. Daarnaast maken de extreem lage golfgeleidingsverliezen en het hoge tolereerbare optische vermogen ongekende prestaties mogelijk. Het siliciumnitride-platform op zichzelf is echter een zuiver passief platform (afgezien van thermo-optische afstemmingsmogelijkheden) en berust derhalve op hybride of heterogene integratiemethoden om actieve componenten te bouwen en het volledige technologische potentieel te benutten.

Dit doctoraatsproefschrift beschrijft onze inspanningen om het huidige toepassingsgebied en de bijbehorende functionaliteiten van siliciumnitride fotonische geïntegreerde schakelingen uit te breiden door middel van heterogene integratie

van materialen en actieve componenten. De gekozen heterogene integratietechniek is micro-transfer printen, een “pick-and-place” methode om (op voorhand gefabriceerde) componenten (of “coupons”) van een bronsubstraat over te brengen naar een doelsubstraat. Aangezien micro-transfer printen enkele belangrijke eigenschappen van wafer bonden en flip-chip integratie combineert, heeft het verschillende voordelen ten opzichte van concurrerende integratiemethoden. Ten eerste is het mogelijk om op voorhand gefabriceerde componenten te testen op het bronsubstraat, voorafgaand aan de integratie op het doelsubstraat, net zoals bij flip-chip integratie. Bovendien kunnen coupons met een hoge integratiedichtheid geïntegreerd worden op het bronsubstraat, waardoor het vaak dure bronmateriaal kostenefficiënt gebruikt kan worden. Daarnaast kunnen vele componenten gelijktijdig worden opgepakt en geprint, wat parallelle integratie en volumefabricage mogelijk maakt. Een ander voordeel is dat verschillende materialen kunnen worden geïntegreerd op hetzelfde doelsubstraat voor de implementatie van verschillende functionaliteiten. Belangrijk is dat componenten en materialen kunnen worden geïntegreerd op het einde van de fabricatiecyclus, wat essentieel is om de CMOS-incompatibiliteit van materialen zoals III-V-halfgeleiders of lithiumniobaat te omzeilen, of vroeg in de fabricatiecyclus om gebruik te maken van fabricage op waferschaal.

De eerste heterogeen geïntegreerde lasers op siliciumnitride werden minder dan vier jaar geleden gedemonstreerd. Actieve componenten op siliciumnitride vormen aldus een erg recente ontwikkeling. Het eerste deel van dit proefschrift bouwt verder op deze ontwikkelingen door het demonstreren van een heterogene passief mode-vergrendelde kamlaser op siliciumnitride. Dergelijke kamlasers zijn uitermate geschikt voor opkomende toepassingen zoals draagbare spectroscopische sensoren. Daarnaast wordt een nieuwe modelleerstrategie gepresenteerd om efficiënte simulatie van dergelijke lasers mogelijk te maken. In het tweede deel van dit proefschrift wordt een nieuwe integratiemethode ontwikkeld om heterogene laserintegratie mogelijk te maken op generieke, commerciële siliciumnitride platformen. Door gebruik te maken van twee micro-transfer printstappen, één om een kristallijne Si koppellaag te integreren, en één om de III-V halfgeleider optische versterker te integreren, kunnen heterogene lasers worden gebouwd op vrijwel elk geïntegreerd fotonisch platform met lage brekingsindex. In het derde deel van dit proefschrift worden micro-transfer printbare silicium fotodetectoren en GaAs optische halfgeleiderversterkers bestudeerd om de mogelijkheden van het siliciumnitride uit te breiden in het (bijna) zichtbare spectrale bereik, ten dienste van een breed scala aan opkomende toepassingsgebieden.

Resultaten

Passief mode-vergrendelde lasers op siliciumnitride

Het eerste apparaat dat in dit proefschrift wordt gepresenteerd is een heterogeen geïntegreerde III-V-op-silicium-nitride passief mode-vergrendelde laser (MLL), schematisch weergegeven in Fig. 1(a). Er wordt een lange ringvormige cavi-

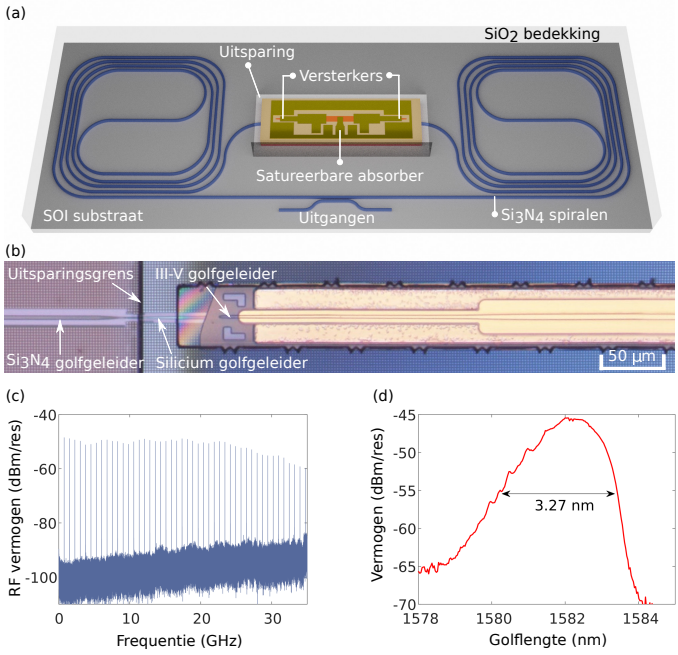

Figuur 1: (a) Illustratie van de heterogene mode-vergrendelde laser met een Si_3N_4 ringcaviteit en op InP/InAlGaAs gebaseerde versterkers met satureerbare absorbeerder. De uitsparing in de oxidebedekking voor het micro-transfer printen van de III-V coupon is aangeduid. (b) Microscoopbeeld van de geïntegreerde coupon bovenop de koppelingstructuur. (c) RF-spectrum van de gegenereerde pulstrein op het gekozen werkpunt. (d) Optisch spectrum gemeten met een resolutie van 30 pm. Een 10-dB optische bandbreedte van 3.27 nm is gemeten.

teit, bestaande uit twee 10 cm Si_3N_4 spiralen, gebruikt. Het Si_3N_4 werd gedeponeerd door middel van lagedruk chemische dampdepositie (LPCVD) op een SOI-substraat. De Si_3N_4-golfgeleiders zijn gedefinieerd met behulp van diepe-UV-lithografie en hebben een breedte van 2 µm en een hoogte van 330 nm. Om heterogene integratie mogelijk te maken is lokaal een uitsparing geëtst in de 4.2 µm dikke siliciumoxide (SiO2) topbedekking. Om het grote indexverschil te overbruggen en een efficiënte evanescente koppeling van licht van de Si_3N_4 naar de III-V-golfgeleider te verzekeren, wordt een tweetraps taper structuur gebruikt: eerst van de Si_3N_4-golfgeleider naar een siliciumgolfgeleider eronder, en vervolgens naar de III-V-golfgeleider. Een microscoopbeeld van de tweetraps taper structuur met geïntegreerde III-V coupon wordt getoond in figuur 1(b). De MLL werd gekarakteriseerd bij 15°C en de versterkers en satureerbare absorber werden van een elektrische spanning voorzien door middel van een PGSGP contactprobe. Passieve mode-vergrendeling bij de fundamentele frequentie bleek op te treden bij een SA spanning van -2.9 V met een SA-stroom van -0.5 mA, en een versterker spanning

van 1.88 V met een injectiestroom van 75 mA. Het optische vermogen in de vezel was ongeveer -24 dBm, wat overeenkomt met een op-chip vermogen van ongeveer 125 μW wanneer rekening wordt gehouden met de verliezen van de grating coupler. Dit optische vermogen is voldoende als de laser bijvoorbeeld gebruikt wordt in een op-chip dubbele-kam spectrometer. Figuur 1(c) toont het elektrische spectrum van de MLL bij het bovengenoemde werkpunt, verkregen met een elektrische spectrumanalysator (ESA) met een bandbreedte van 300 kHz resolutie. Een lage herhalingssnelheid van 755 MHz wordt gemeten met een vlak en dens kamspectrum. Het afrollen van de radiofrequentie (RF) kam bij hoge frequenties is een gevolg van de bandbreedtebeperking van 30 GHz van de transimpedantieversterker van de fotodetector. Een dergelijk dicht kamspectrum is bijzonder nuttig voor opchips gebaseerde spectroscopische detectietoepassingen met hoge resolutie. Het optische spectrum van de MLL werd gemeten met een optische spectrumanalysator (OSA) met een resolutie van 30 pm en is afgebeeld in figuur 1(d). Een 10-dB optische bandbreedte van 3.27 nm wordt bereikt, wat overeenkomt met meer dan 500 dicht en gelijkmatig gespreide kamlijnen. De optische lijnbreedte werd gekarakteriseerd door de MLL-uitgang te mengen met een afzonderlijke afstembare laser (60 kHz lijnbreedte). Dit resulteerde in een mixsignaal met een optische lijnbreedte van minder dan 200 kHz. Bovendien werden metingen van de fase-ruis op één zijband uitgevoerd. Hieruit bleek een record-lage 1 Hz versterkte spontane emissie beperkte RF-lijnbreedte.

Als aanvulling op het hierboven beschreven experimentele werk, wordt een nieuwe hybride simulatiestrategie voorgesteld om dergelijke apparaten te modelleren. De hybride aanpak combineert een zogenemaand traveling-wave model voor de halfgeleidersecties met een split-step Fourier-implementatie van de uitgebreide niet-lineaire Schrödingervergelijking voor de passieve caviteit, zoals geïllustreerd in Fig. 2. Een dergelijke benadering maakt het mogelijk om een brede waaier aan fysische verschijnselen te beschouwen, zoals de halfgeleiderfysica van de optische versterker en de SA, alsook de dispersieve en niet-lineaire eigenschappen van de passieve lasercaviteit, terwijl tegelijkertijd de computationele vereisten van het model worden beperkt. Het model werd geïllustreerd aan de hand van een simulatie van een 2.6 GHz III-V-op-silicium MLL. Een dergelijk hybride model kan waardevol zijn om MLL's met lage herhalingssnelheid te bestuderen, aangezien voor deze apparaten dispersieve en niet-lineaire effecten van de lange passieve caviteit belangrijk kunnen zijn. Er is echter nog extra werk nodig om praktisch gebruik van het model mogelijk te maken. Bovendien is een verdere validatie essentieel om de betrouwbaarheid en fysische nauwkeurigheid van het model aan te tonen.

Micro-transfer printen van dunne silicium lagen

Het tweede deel van dit proefschrift gaat over een nieuwe integratiemethode om lasers heterogeen te integreren op generieke, commerciële Si_3N_4-platformen, of andere geïntegreerde fotonische platformen met lage index, zoals dunne-film lithiumniobaat (TFLN). Hoewel een aangepast meerlaags Si_3N_4/SOI-platform, zoals

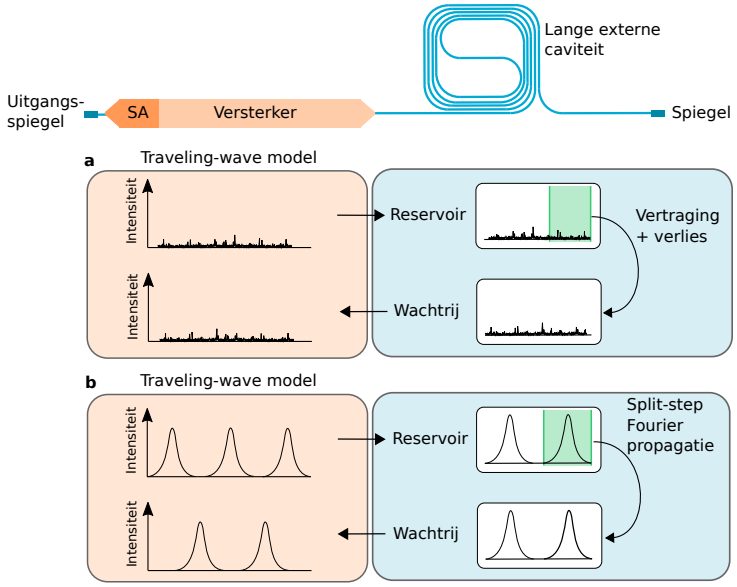

Figuur 2: Mode-vergrendelde laser simulatie methode, bestaande uit een traveling-wave model voor het actieve gebied en een split-step Fourier propagatie-algoritme voor de externe passieve golfgeleidercaviteit. (a) Indien er geen pulsen worden waargenomen, bijvoorbeeld bij het opstarten van de laser, wordt het split-step Fourier-algoritme niet gebruikt en wordt de externe caviteit eenvoudigweg voorgesteld door een vertraging met verlies. (b) Wanneer pulsen worden waargenomen, wordt de split-step Fourier-methode gebruikt en wordt rekening gehouden met dispersieve en niet-lineaire effecten.

gebruikt voor de bovengenoemde heterogene Si_3N_4 mode-vergrendelde laser, uitstekende prestaties levert, is het duur en momenteel (nog) niet verkrijgbaar bij de meeste commerciële gieterijen. Bovendien omzeilt de voorgestelde aanpak enkele van de nadelen van een gehydrogeneerde amorfe silicium tussenkoppelingslaag. De integratiemethode bestaat uit twee micro-transfer printstappen. In een eerste stap wordt een 400 nm dikke coupon van kristallijn silicium micro-transfer geprint op de siliciumnitride golfgeleider om te dienen als tussenliggende koppelingslaag. De golfgeleiders in de kristallijne Si coupon kunnen voor of na het micro-transfer printen worden gedefinieerd. Afbeeldingen van micro-transfer geprinte Si coupons voor en na het definiëren van patronen worden getoond in figuren 3(a) en (b). Zodra de Si golfgeleider gedefinieerd is, wordt de III-V versterker geïntegreerd met een tweede micro-transfer printstap. Twee verschillende methodes werden ontwikkeld om kristallijne silicium coupons te maken voor micro-transfer printen, enerzijds door onderetsen met waterstoffluoride in dampfase, anderzijds door inkapsulatie van de Si coupon met fotoresist en onderetsen met waterstoffluoride in vloeibare toestand. Hoewel deze laatste methode meer fabricagestappen vereist, hebben

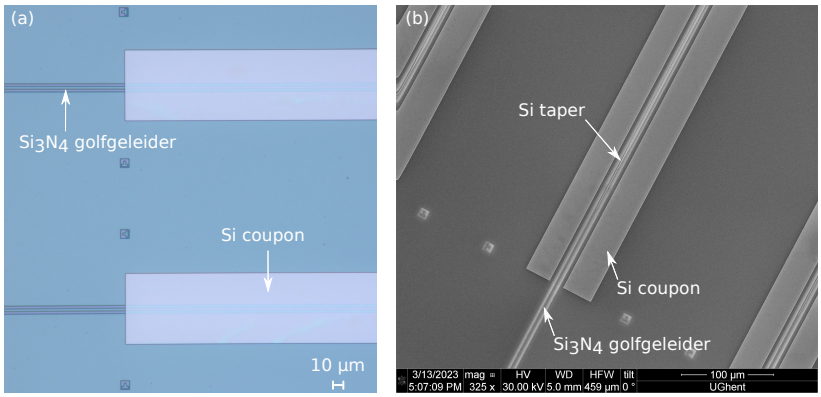

Figuur 3: (a) Microscoopfoto van een siliciumnitride PIC met micro-transfer geprinte kristallijne Si coupons. (b) Foto van de chip, genomen met een rasterelektronenmicroscoop, na het definiëren van de Si golfgeleiders.

de coupons een consistent lage oppervlakteruwheid en geen last van restdeeltjes, in tegenstelling tot experimenten met etsen in de dampfase. Transmissiemetingen van Si coupons op 300 nm dikke Si_3N_4 golfgeleiders, wijzen op taperverliezen rond 0.8 dB/taper en overtollige golfgeleidingsverliezen van 7.5 dB/cm (voor een 2 µm brede, 400 nm dikke volledig geëtste Si golfgeleider), wat bevestigt dat de micro-tranfser geprinte silicium golfgeleiders verliezen vertonen die vergelijkbaar zijn met standaard SOI-golfgeleiders (voor dezelfde lithografie- en etsprocessen). Aangezien aanzienlijke ruwheid aan de zijkant van de Si golfgeleider wordt waargenomen, wordt verwacht dat een verdere reductie van de golfgeleiderverliezen mogelijk is door optimalisering van de e-beam-lithografie en de etsprocessen. De relevantie en het potentieel van de integratiemethode worden geïllustreerd aan de hand van een aantal gedemonstreerde apparaten, waaronder multimode en modevergrendelde lasers op Si_3N_4, en een elektro-optische afstembare laser en elektro-optische frequentiekamgenerator op TFLN.

Detectoren en versterkers voor bijna-zichtbare golflengten

Het derde deel van dit proefschrift beschrijft onze inspanningen om het portfolio van siliciumnitride in het (bijna) zichtbare spectrum uit te breiden met Si fotodetectoren en GaAs optische halfgeleiderversterkers.

Allereerst worden micro-transfer geprinte Si p-i-n fotodiodes op imec's commerciële BioPIX Si_3N_4 platform voorgesteld voor golflengten onder 850 nm. De fotodiodes zijn gerealiseerd op imec's iSiPP25G geïntegreerd silicium fotonica platform via een multi-project wafer (MPW) run. Ribgolfgeleiders zijn gedefinieerd in een 220 nm Si laag bovenop een 2 µm thermisch gegroeide siliciumoxide (SiO2) laag. De 300 nm dikke Si_3N_4-laag werd gedeponeerd met behulp van plasmaversterkte chemische dampdepositie (PECVD) bovenop een 3.3 µm SiO2-op-Si wafer. Bovendien werd een 2 µm diepe uitsparing lokaal geëtst in

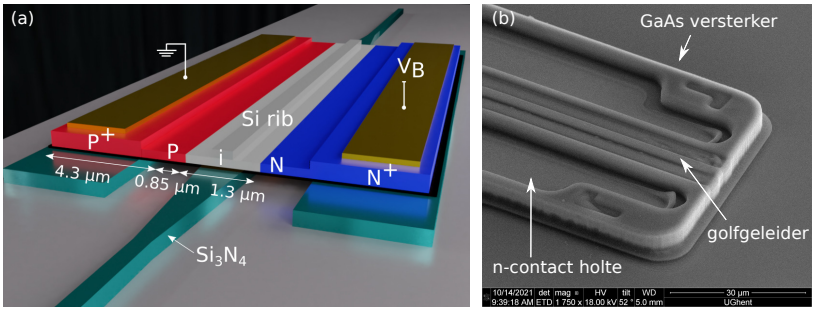

Figuur 4: (a) Illustratie van de Si p-i-n fotodiode bovenop een Si_3N_4 golfgeleider. Een elektrische spanning wordt aangelegd op de metaalcontacten bovenop de gedopeerde gebieden. (b) Foto, genomen met een elektronenmicroscoop, van een micro-transfer geprinte GaAs-halfgeleider optische versterker.

de SiO2 topbekleding met behulp van droge etstechnieken om een deel van de Si_3N_4-golfgeleider bloot te leggen. Hierdoor wordt evanescente koppeling met de Si ribgolfgeleider erboven mogelijk gemaakt. Een schematische voorstelling van de 200 µm lange fotodiode wordt getoond in Fig. 4(a). De fotodiodes leveren degelijke prestaties met een lage donkerstroom van 107 pA bij -3 V spanning, externe quantum efficiënties rond 30% bij 775 nm en 800 nm, en een geschatte 3-dB bandbreedte van 6 GHz. Bovendien wordt lawineversterking met een waargenomen versterking-bandbreedteproduct van 68 GHz bij -45 V spanning aangetoond, wat bijzonder relevant is voor toepassingen waar een hogere ontvangstgevoeligheid nodig is.

Ten tweede worden micro-transfer printbare horizontaal-gekoppelde GaAs halfgeleider optische versterkers ontwikkeld als eerste stap in de ontwikkeling van heterogene lasers op siliciumnitride die rond 780 nm werken. De versterkers zijn gebaseerd op een (Al)GaAs epitaxiale lagenstructuur, gegroeid met behulp van metaalorganische dampfase-epitaxie (MOVPE), met 4 AlGaAs quantum wells met een fotoluminescentiegolflengte van 780 nm. Verder is een 500 nm dikke InGaP opofferingslaag opgenomen in de lagenstructuur om de apparaten op het bronsubstraat te kunnen onderetsen en vervolgens te kunnen micro-transfer printen. Een rasterelektronenmicroscoopbeeld van een micro-transfer geprinte optische versterker (SOA) is afgebeeld in Fig. 4(b). Een eenvoudig doelsubbstraat werd vervaardigd om de SOA's te testen, en een versterkte spontane emissie rond 770 nm werd waargenomen met een optische spectrumanalysator. De hoge differentiële weerstand ($>$14 Ω bij 60 mA biasstroom) en de ruwe chiprand, als gevolg van het snijden van de chip, beperkten naar alle waarschijnlijkheid het optische vermogen dat met een lensvormige optische vezel kon worden opgevangen. Voortbouwend op deze resultaten zijn onlangs GaAs Fabry-Pérot lasers met 3 mW vezelgekoppeld uitgangsvermogen gedemonstreerd op basis van een geoptimaliseerde (Al)GaAs epitaxie en enkele besproken procesverbeteringen.

Conclusie

In dit proefschrift werd de heterogene integratie met behulp van micro-transfer printen onderzocht om het huidige toepassingsgebied en de bijbehorende functionaliteiten van siliciumnitride fotonische geïntegreerde schakelingen uit te breiden. In het bijzonder demonstreerden we een passief mode-vergrendelde laser op siliciumnitride, een nieuwe methodologie voor heterogene laserintegratie op generieke en commerciële siliciumnitride platformen, alsmede Si fotodetectoren en GaAs halfgeleider optische versterkers voor bijna-zichtbare golflengten. Verwacht wordt dat deze ontwikkelingen een belangrijke rol zullen spelen voor geavanceerde fotonische geïntegreerde schakelingen op siliciumnitride, en een breed scala aan gevestigde en toekomstige toepassingsgebieden (waaronder spectroscopische sensoren, optische beeldvorming met onder meer optische coherentie tomografie, en quantum fotonische toepassingen) in het nabij-infrarood en het zichtbare spectrum zullen dienen.

Summary

Introduction

Since the introduction of "integrated optics" in 1969 by S. Miller and coworkers, photonic integration has undergone tremendous progress. From early on, scientists and engineers realized that photonic integration benefits from improved resilience to thermal, mechanical and acoustic perturbations from the environment compared to bulk optical components, and, importantly, enables economic scalability by leveraging photolithographic techniques from the microelectronics industry. Largely fueled by the demands of optical communications, III-V semiconductors initially dominated the stage. After all, III-V semiconductors such as Indium Phosphide naturally combine light generation, modulation and detection on a single platform. However, during the last two decades, silicon photonics has established itself as an invaluable competing integrated photonics platform, despite its need for an external light source. Its success is underpinned by a number of features. First of all, the ability to leverage existing CMOS infrastructure enables scalable and cost-effective manufacturing, and provides seamless compatibility with microelectronic circuits. Secondly, silicon is transparent at telecom wavelengths (1310 nm and 1550 nm), allowing one to use these photonic integrated circuits (PICs) for datacom and telecom applications. In addition, the silicon-on-insulator (SOI) platform's high index contrast and low loss enable dense integration of optical components and the realization of passive devices that outperform those on competing III-V platforms.

Recently, silicon nitride has emerged as an important material to complement conventional silicon photonic integrated circuits. Not only does silicon nitride's wide transparency window - down to the visible spectral range - greatly expand the application scope of conventional silicon photonics, its attainable ultra-low waveguide losses and high power-handling capabilities allow reaching unprecedented device performance. Still, the silicon nitride platform by itself is a purely passive platform (apart from thermo-optic tuning capabilities) and therefore relies critically on hybrid- or heterogeneous integration methods to build active devices and unlock its full technological potential.

This dissertation describes our efforts to extend the current application scope and corresponding functionalities of silicon nitride photonic integrated circuits by heterogeneously integrating materials and active devices. The selected heterogeneous integration technique is micro-transfer printing, which is a pick-and-place

method to transfer (pre-processed) devices (or more general: "coupons") from a source wafer to a target wafer. As micro-transfer printing combines some key properties of wafer bonding and flip-chip integration, it benefits from several advantages over competing integration methods. Firstly, it is possible to pre-test pre-processed devices on the source wafer, prior to integration on the target wafer, similar to flip-chip integration. Furthermore, the source wafer can be densely populated with devices, ensuring efficient usage of the often expensive source material. In addition, many coupons can be picked up and printed simultaneously, enabling massively parallel integration and volume manufacturing. Yet another advantage is that different materials can be co-integrated on the same target wafer to implement diverse functionalities. Importantly, devices and materials can be integrated at the back-end-of-line, which is essential to overcome the CMOS incompatibility of materials such as III-V semiconductors or lithium niobate, or early on in the process flow to benefit from wafer-scale manufacturing.

With the first heterogeneously integrated lasers on silicon nitride demonstrated less than four years ago, active devices on silicon nitride signify a fairly recent development. The first part of this dissertation builds further on these developments by demonstrating a heterogeneous passively mode-locked comb laser on silicon nitride, hereby supporting emerging applications such as portable spectroscopic sensors. In addition, a novel modeling strategy is presented to enable efficient simulation of such devices. In the second part of this dissertation, a novel integration methodology is developed to enable heterogeneous laser integration on generic, commercial silicon nitride platforms. By using two micro-transfer printing steps, one to integrate a crystalline Si coupling layer, and one to integrate the III-V semiconductor optical amplifier, heterogeneous lasers can be build on virtually any low-index integrated photonic platform. In the third part of this dissertation, micro-transfer printable silicon photodetectors and GaAs semiconductor optical amplifiers are investigated to expand the toolbox of silicon nitride in the (near-)visible spectral range, serving a wide range of upcoming application domains.

Results

Passively mode-locked laser on silicon nitride

The first device that is presented in this dissertation is a heterogeneously integrated III-V-on-silicon-nitride passively mode-locked laser (MLL), schematically depicted in Fig. 1(a). An extended ring cavity geometry is employed, consisting of two 10 cm Si_3N_4 spirals, deposited by means of low-pressure chemical vapor deposition on top of an SOI wafer. The Si_3N_4 waveguides are defined using deep-UV lithography and have a width of 2 μm and a height of 330 nm. To enable heterogeneous integration, a recess is locally etched in the 4.2 μm silicon oxide (SiO_2) top cladding. A two-stage taper structure is employed to bridge the large index difference and ensure efficient evanescent coupling of light from the Si_3N_4 to the III-V stack: first from the Si_3N_4 waveguide to a silicon waveguide underneath, and

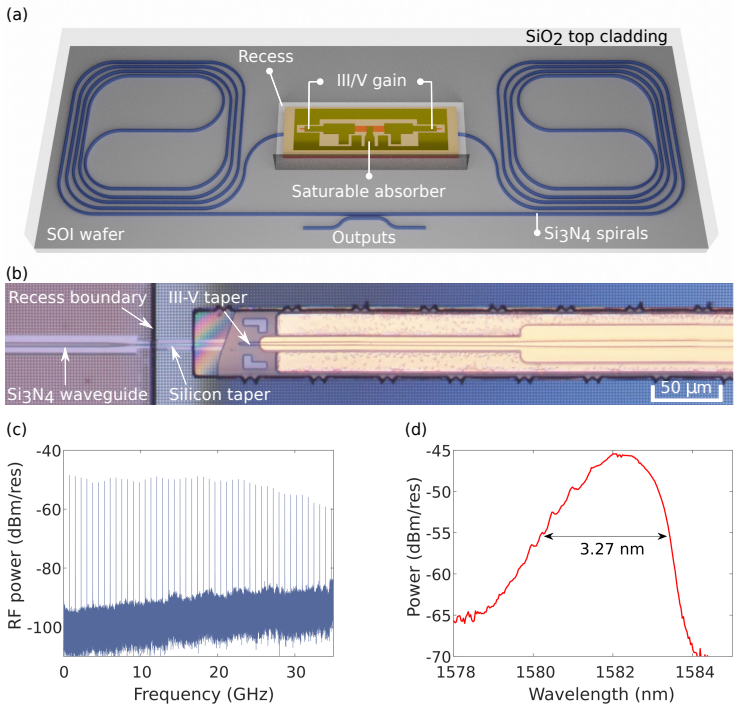

Figure 1: (a) Schematic of the heterogeneous mode-locked laser with a Si_3N_4 ring cavity and InP/InAlGaAs-based amplifiers with saturable absorber. The recess for microtransfer printing the III-V coupon is indicated. (b) Microscope image of the transfer printed coupon on top of the taper structure. (c) RF spectrum of the generated pulse train at the chosen operating point. (d) Optical spectrum measured with a 30 pm resolution. A 10-dB optical bandwidth of 3.27 nm is measured.

subsequently to the III-V waveguide. A microscope image of the two-stage taper with transfer printed coupon is shown in Fig. 1(b).

The MLL was characterized at 15°C and the amplifiers and saturable absorber (SA) were biased using a PGSGP contact probe. Passive mode-locking at the fundamental frequency was found to occur at an SA reverse bias voltage of -2.9 V with a -0.5 mA SA current, and an amplifier bias of 1.88 V with a 75 mA injection current. The optical power in the fiber was measured to be around -24 dBm, corresponding with an on-chip power of approximately 125 µW when the grating coupler losses are taken into account. This optical power is sufficient if the laser is to be used, for example, in an on-chip dual-comb spectrometer. Figure 1(c) shows the electrical spectrum of the MLL at the aforementioned bias point, obtained with an Electrical Spectrum Analyzer (ESA) with a 300 kHz resolution bandwidth. A flat, densely-spaced comb spectrum is achieved with a low repetition rate of 755 MHz. The roll-of of the radiofrequency (RF) comb at high frequen-

cies is a consequence of the 30 GHz bandwidth limitation of the transimpedance amplifier of the photodetector. Such a dense comb spectrum is particularly useful for high-resolution chip-based spectroscopic sensing applications. The optical spectrum of the MLL was measured with an Optical Spectrum Analyzer (OSA) with a 30 pm resolution and is depicted in Figure 1(d). A 10-dB optical bandwidth of 3.27 nm is achieved, corresponding with over 500 densely and evenly spaced comb lines. The optical linewidth was characterized by beating the MLL output with a tunable laser (60 kHz linewidth), resulting in a heterodyne beatnote with a sub-200 kHz optical linewidth. In addition, single-sideband phase-noise measurements were carried out, showing a record-low 1 Hz amplified spontaneous emission limited RF linewidth.

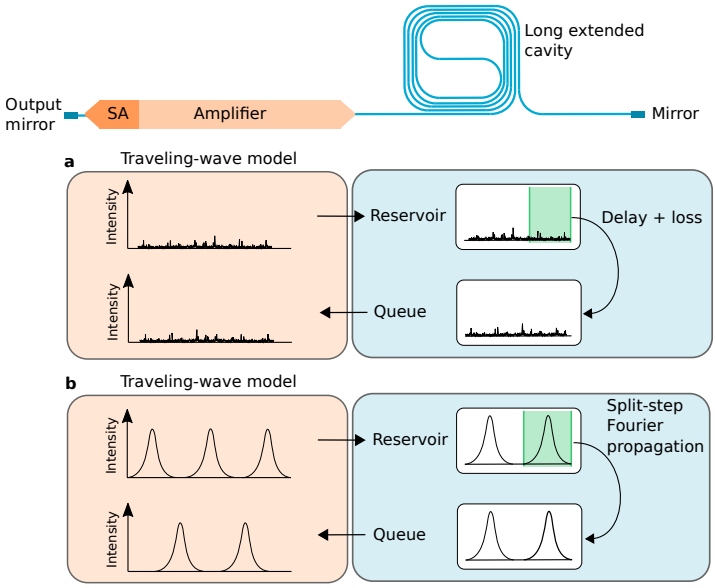

Figure 2: Mode-locked laser simulation flow, consisting of a traveling-wave model for the active region and a split-step Fourier propagation algorithm for the extended passive waveguide cavity. (a) In case no pulses are observed, e.g. at laser start-up, the split-step Fourier algorithm is not employed and the extended cavity is simply represented by a delay with some loss. (b) When pulses are observed, the split-step Fourier method is used and dispersive and nonlinear effects are accounted for.

In addition to the experimental work on heterogeneous extended cavity mode-locked laser diodes, a novel hybrid simulation strategy is proposed to model such devices. The hybrid approach combines a traveling-wave model for the semiconductor sections with a split-step Fourier implementation of the extended nonlinear Schrödinger equation for the extended passive cavity, as illustrated in Fig. 3.2. Such an approach paves the way to include a wide range of physical phe-

nomena, such as the semiconductors physics of the semiconductor optical amplifier (SOA) and SA, as well as the dispersive and nonlinear properties of the extended passive laser cavity, while simultaneously limiting the model's computational workload. The model was exemplified by simulating a 2.6 GHz III–V-on-silicon MLL. Such a hybrid modeling strategy can be of value to study low-repetition-rate MLLs, as for these devices dispersive and nonlinear effects of the long extended cavity can become important. However, some additional work is still needed to further enable practical usage of the model. Furthermore, extensive validation remains essential to proof the model's reliability and physical accuracy.

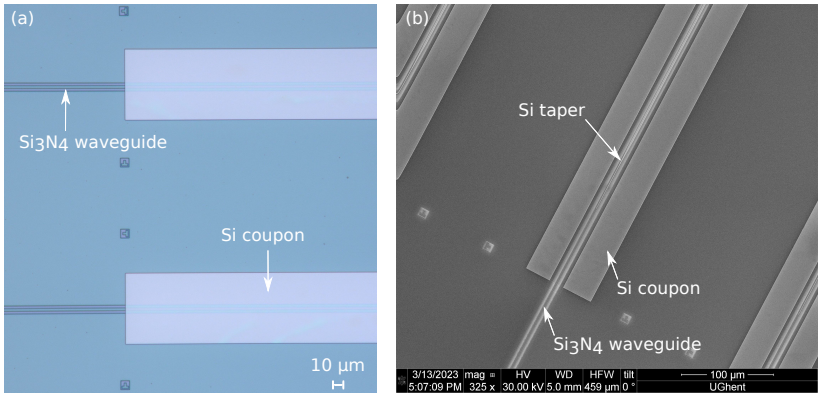

Figure 3: (a) Microscope picture of a silicon nitride PIC with micro-transfer printed crystalline Si coupons. (b) Scanning electron microscope image of the sample after patterning the Si waveguides.

Micro-transfer printing silicon thin films

The second part of this dissertation elaborates on a novel integration methodology to heterogeneously integrate lasers on generic, commercial Si_3N_4 platforms, or other low-index integrated photonic platforms such as thin-film lithium niobate (TFLN). Although a custom multi-layer Si_3N_4/SOI platform, as used for the aforementioned heterogeneous Si_3N_4 mode-locked laser, provides excellent performance, it is expensive and currently not (yet) readily available from most commercial foundries. Furthermore, the presented approach overcomes some of the drawbacks of a hydrogenated amorphous silicon intermediate coupling layer. The integration methodology consists of two micro-transfer printing steps. In a first step, a 400 nm thick crystalline silicon coupon is micro-transfer printed on the silicon nitride waveguide to serve as an intermediate coupling layer. The crystalline Si coupon can be patterned before or after micro-transfer printing. Images of micro-transfer printed Si coupons before and after patterning are shown in Figs. 3(a) and (b). Once the Si layer is patterned, the III-V amplifier is integrated with a second micro-transfer printing step. Two different approaches were developed to create crystalline silicon coupons for micro-transfer printing, either through vapor-phase

release etching or through a liquid release etch with a photoresist encapsulation. Although the latter requires more processing steps, the coupons benefit from a consistently low surface roughness and do not suffer from residual particles, in contrast to vapor-phase etching experiments. Transmission measurements of patterned Si coupons on a patterned 300 nm Si_3N_4 layer, indicate taper losses on the order of 0.8 dB/taper and excess waveguide losses of 7.5 dB/cm (for a 2 μm wide, 400 nm thick fully etched Si waveguide), confirming that the micro-tranfser printed silicon waveguides exhibit losses comparable to standard SOI waveguides (assuming the same lithography and etching processes). As significant sidewall roughness is observed, a further reduction of the losses is expected to be possible by optimizing the e-beam lithography and etching processes. The relevance and potential of the integration methodology is exemplified by a number of demonstrated devices, including multimode and mode-locked lasers on Si_3N_4, and an electro-optic tunable laser and electro-optic frequency comb generator on TFLN.

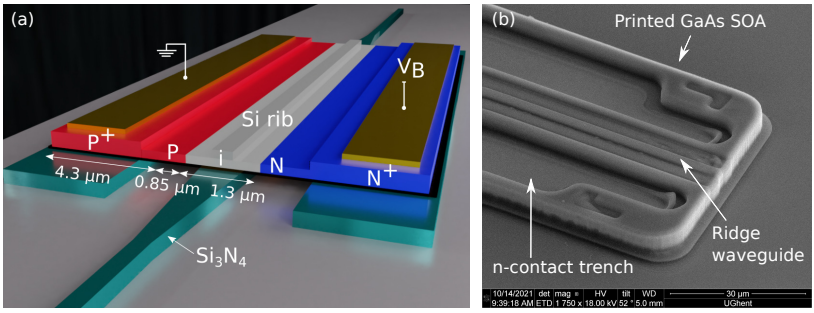

Figure 4: (a) Schematic of the Si p-i-n photodiode on top of a Si_3N_4 waveguide. The device is reverse biased by applying a voltage via the metal contacts on top of the doped regions. (b) Scanning electron microscope image of a micro-transfer printed GaAs semiconductor optical amplifier.

Detectors and amplifiers for near-visible wavelengths

The third part of this dissertation describes our efforts to extend the toolbox of silicon nitride in the (near-)visible spectrum with Si photodetectors and GaAs semiconductor optical amplifiers.

Firstly, micro-transfer printed Si p–i–n photodiodes on imec's commercial BioPIX Si_3N_4 platform are presented to target wavelengths below 850 nm. The photodiodes are realized on imec's iSiPP25G integrated silicon photonics platform through a multi-project wafer (MPW) run. Rib waveguides are defined in a 220 nm Si layer on top of a 2 μm thermally grown silicon oxide (SiO_2) layer. The 300 nm thick Si_3N_4 layer is deposited using plasma-enhanced chemical vapor deposition (PECVD) on top of a 3.3 μm SiO_2-on-Si wafer. Furthermore, a 2 μm deep recess is locally etched in the SiO_2 top cladding using dry etching techniques to expose part of the Si_3N_4 waveguide, enabling evanescent coupling to the Si rib waveguide

above it. A schematic of the 200 μm long photodiode is shown in Fig. 4(a). The photodiodes feature competitive performance with a low dark current of 107 pA at 3 V reverse bias, external quantum efficiencies around 30% at 775 nm and 800 nm, and an estimated 3-dB bandwidth of 6 GHz. In addition, avalanche gain with an observed gain–bandwidth product of 68 GHz at 45 V reverse bias, is demonstrated to serve applications where higher receiver sensitivities are needed.

Secondly, micro-transfer printable edge-coupled GaAs semiconductor optical amplifiers are developed as a first step towards heterogeneous lasers on silicon nitride that emit around 780 nm. The amplifiers are based on an (Al)GaAs epitaxial layer stack, grown using metalorganic vapor-phase epitaxy (MOVPE), with 4 AlGaAs quantum wells with a photoluminescence wavelength of 780 nm. Furthermore, a 500 nm thick InGaP sacrificial layer is included to enable suspension of the devices on the source wafer, and subsequent micro-transfer printing. A scanning electron microscope image of a printed SOA is depicted in Fig. 4(b). A dummy target sample was fabricated to test the SOA's, and amplified spontaneous emission around 770 nm was observed with an optical spectrum analyzer. However, the high differential resistance ($>$14 Ω at 60 mA bias current) and the rough sample edge, resulting from dicing the sample, likely limited the optical power that could be captured with a lensed fiber. Building further on these results, GaAs Fabry-Pérot lasers with 3 mW fiber-coupled output powers have recently been demonstrated based on an optimized (Al)GaAs epitaxy and some discussed process flow refinements.

Conclusion

In this dissertation, heterogeneous integration using micro-transfer printing was explored to extend the current application scope and corresponding functionalities of silicon nitride photonic integrated circuits. Specifically, we demonstrated a passively mode-locked laser on silicon nitride, a novel process flow for heterogeneous laser integration on commercial silicon nitride platforms, as well as Si photodetectors and GaAs semiconductor optical amplifiers for near-visible wavelengths. These developments are expected to play an important role for advanced silicon nitride PICs in the future, serving a wide range of established and upcoming application domains (including spectroscopic sensing devices, optical imaging systems such as optical coherence tomography, and quantum photonics applications) across the near-infrared and visible spectrum.

1 Introduction

During the 20^{th} century, the electronics industry has radically transformed the way we live. The invention of the vacuum tube, and more importantly, the invention of the first transistor in 1948, marked the beginning of a new digital era. At first by using transistors as discrete components, essentially replacing vacuum tubes, and later by building complex integrated circuits in which, today, several billion transistors are incorporated into a single semiconductor chip. This unprecedented miniaturization has revolutionized the way in which we process and communicate information, and has given rise to numerous conveniences that we have become accustomed to.

Today, 75 years after the invention of the first transistor, a similar revolution is unfolding. This time, the stage is not reserved for electrons of the mature electronics industry, but rather for photons of the nascent field of photonics. The word "photonics" is sometimes interchangeably used with the term "optics", which likely sounds more familiar. The latter term dates back to ancient Mesopotamia and Greece where the first lenses as well as theories about light and vision originate from. Anno 2023, "optics" likely still invokes thoughts about lenses, prisms, astronomy, etc. Yet, it encompasses much more than these well-known examples, and is broadly defined as the branch of physics that deals with light. The term "photonics" on the other hand was coined more recently in 1967 by Pierre Aigrain, and is generally defined as the branch of optics that deals with the generation, detection and manipulation of light. One application lies at the heart of photonics and remains especially important today: optical communication.

1.1 A historical perspective

For millennia, light has been harnessed for communication purposes if we interpret optical communication in a broad sense. Early civilizations used mirrors, fire beacons and smoke signals to convey simple messages, and similar concepts where employed until the late 18^{th} century [1]. On the other hand, telecommunication as we know it today can be traced back to the notable inventions of the telegraph in 1837 by Samuel Morse, and the telephone by Alexander Graham Bell in 1876. In 1880, Bell invented another device, termed the photophone, which transmitted information through air using a modulated beam of sunlight. It worked by converting sound into modulated light and transmitting the light to a receiver where it was converted back into sound. Although the photophone can be considered as the precursor of modern optical communication systems, it was less practical than the telephone and was not further developed [2]. Around the same time, the Scottisch mathematician James C. Maxwell formulated his famous "Maxwell's equations", which can arguably be considered as one of the greatest scientific achievements of the 19^{th} century [3]. These equations describe the propagation of electromagnetic waves and have laid the theoretical groundwork that was invaluable for later discoveries. Indeed, shortly thereafter, Heinrich Hertz and Guglielmo Marconi demonstrated radio waves and radio communication based on the electromagnetic theory elucidated by Maxwell. Ever since these seminal achievements, scientists and engineers have made steady progress towards better and faster communication systems to support the growing demands which are largely fueled by the increases in computational power. It was soon realized that an enormous increase in the bit rate - distance product, a commonly used figure of merit for communication systems, would be possible by using optical waves instead of microwave carriers. After all, higher carrier frequency waves naturally benefit from enhanced modulation bandwidths to carry information. However, at the time, neither a coherent optical source nor a suitable transmission medium were existent, and the interests in optical communication systems remained dormant.

In the 1960s, two parallel developments triggered a renewed interest in optical communications. A first breakthrough was the demonstration of the laser by Theodore Maiman in 1960 [4]. Building on the fundamental principle of "stimulated emission" predicted by Einstein in 1917, and following the Nobel prize winning work of C. H. Townes, N. Basov, and A. Prokhorov on the maser (Microwave Amplification by Stimulated Emission of Radiation) amongst others, Maiman operated the first functional laser using a flashlamp-pumped synthetic ruby crystal to produce red laser light. Numerous demonstrations quickly followed suit, and in that same year, the first gas laser was developed which generated continuous infrared light from a a helium-neon mixture [5]. The first semiconductor laser, which could be pumped electrically in contrast to optical pumping mechanisms of

earlier demonstrations, was developed in 1962 by R. N. Hall and coworkers [6]. Although lasers quickly caught the public imagination, likely for their similarity to "death rays" of science fiction novels, the relevance of Maiman's accomplishment was initially unclear. Maiman himself observed that "a laser is a solution seeking a problem". However, this statement did not linger for very long as lasers where commercialized by several companies in the 1960s and practical applications became apparent. Still, for communication purposes, the laser by itself offered limited opportunities. Despite being able to generate a powerful and directional beam, sending a laser beam through air has obvious limitations for communication over longer distances [2]. A way to guide light efficiently remained an essential missing building block. In 1966, Charles K. Kao proposed that optical glass fibers could be used to transmit light over long distances [7], a discovery which later granted him the Nobel prize in physics. At first, the losses of optical fibers were too high for practical fiber communication links. However, in 1970, a major breakthrough was made in reducing fiber losses to below 20 dB/km by depositing a highly purified SiO_2 vapor on the inside of a glass tube, and subsequently heating and drawing the tube into a fiber [8]. This process is referred to as inside vapor deposition (IVD) and is still commonly used today. Around the same time, gallium arsenide (GaAs) semiconductor lasers that could operate continuously at room temperature became commercially available. With the simultaneous availability of these compact optical sources and low-loss optical fibers, a worldwide effort was initiated to develop fiber-optic communication networks [1].

Since the 1970s, fiber-optic communication systems have progressed at a rapid pace, as is evident from the increase in bit rate by more than a factor of 10^5 as well as the increase in transmission distance from 10 km to more than 10 000 km over a period of a few decades [1]. Several technological advances have contributed to this evolution, including the shift towards longer operating wavelengths to benefit from low chromatic dispersion in fibers (near 1.3 μm) and achieve low propagation losses (near 1.55 μm), as well as the development of single-mode fibers, dispersion-shifted fibers, and single-mode lasers to overcome the limitations imposed by fiber dispersion. Furthermore, erbium-doped fiber amplifiers, developed in 1987 [9] and commercialized in 1990, replaced electronic repeaters, making long-distance transatlantic and transpacific submarine communication channels viable. In addition, the advent of wavelength-division multiplexing (WDM) where several optical carriers are simultaneously send through a single fiber using different wavelengths, resulted in a tremendous improvement in system capacity.
With all these developments in place, fiber-optic communication technology has reached a certain stage of maturity and now connects the entire globe to form the backbone of the internet today. Further improvements were to largely come from the transmitter and receiver sides of the fiber links, a trend that fueled the development of a new field: integrated photonics.

1.2 Integrated photonics

The concept of integrated photonics - or integrated optics as it was called in the early days - was first proposed by S. Miller in 1969 [10]. The proposal entailed "a miniature form of laser beam circuitry", allowing to guide and manipulate light on an integrated circuit. As Miller elaborated, such an approach would not only benefit from improved resilience to thermal, mechanical and acoustic perturbations from the environment (compared to bulk optical components), but also enables economic scalability by leveraging established photolithographic techniques from the microelectronics industry. Historically, a single integrated optical circuit was envisioned to contain many different optical devices (lasers, switches, modulators, detectors, etc.) and hence incorporate a wide range of distinct materials [11]. However, at the time it was quickly realized that fabricating such versatile circuits was difficult. As a result, the development of circuits with a limited number of different components became conventional.

From early on, several material platforms were investigated to realize photonic integrated circuits (PICs). One important requirement when selecting a material system is that the involved materials are transparent for the chosen wavelength range. Furthermore, the refractive indices of the materials influence the integration density that can be achieved. On a PIC, light is guided by a dielectric waveguide core with a refractive index higher than the surrounding material, similar to how light is guided in optical fibers. When the refractive index contrast becomes larger, the optical mode is more closely confined to the core waveguide and small bend radii can be tolerated without excessive losses. The improved integration density comes at the expense of a higher sensitivity to fabrication tolerances and a higher susceptibility to surface roughness.

The principal material platforms used to build the first PICs were silica, lithium niobate, and GaAs and indium phosphide (InP) semiconductors [12, 13]. Silica and lithium niobate platforms have a low refractive index contrast and benefited from low propagation losses, making them suitable for passive functionalities such as filters and multiplexers in optical networks [10, 13]. Moreover, lithium niobate exhibits a high electro-optic coefficient, making it a valuable platform to realize high-speed modulators [14]. Still, both platforms are unsuitable to fabricate lasers and detectors. Driven by the demands of telecommunication, III-V semiconductor platforms quickly dominated the stage. By epitaxially growing lattice-matched group III and V layers on GaAs and InP substrates, direct bandgaps in a wide wavelength range could readily be engineered. As a result, this material system was - and still is today - the material system of choice to fabricate high quality semiconductor lasers. In the 1980s, the first PICs capable of fulfilling multiple functions were demonstrated based on GaAs and InP platforms [15–17]. These circuits incorporated a single-mode laser and a modulator on a single monolithic

PIC, serving high-capacity optical fiber links.

1.3 The advent of silicon photonics

Crystalline silicon (Si) has been the workhorse of the microelectronics industry. However, in the early days of integrated photonics, the research community was betting on III-V semiconductors for the development of optoelectronic devices, and silicon solely served as a substrate material to explore other waveguiding materials such as Ta_2O_5, ZnO, etc. [18]. Still, the relevance of using silicon for optical waveguiding was quickly recognized, and some pioneering work was performed by Soref and coworkers during the 1980s [18, 19]. The drivers to explore silicon for integrated photonics were multifold. Firstly, the high transparency at fiber-optical communication wavelengths (1.3 μm and 1.55 μm) and the low transmission losses in high-quality crystalline silicon showed great promise for telecommunications. Moreover, there was reason to believe that silicon could serve as a medium for a variety of optical functionalities, similar to the capabilities of III-V semiconductor compounds, while at the same time avoiding the complexities and costs of III-V alloys [18, 20]. In addition, two important considerations stimulated the early development of silicon photonics [18]: 1) the processing technologies developed for the microelectronics industry could also be applied to silicon optical devices, enabling scalable and cost-effective manufacturing, and 2) silicon electronic circuits could be merged with silicon optical components on a single monolithic chip.

Around the turn of the century, the field of silicon photonics really started booming. Epitaxial growth of germanium on silicon was mastered, enabling the fabrication of CMOS-compatible high-speed detectors [21, 22]. High-speed modulators on silicon with bandwidths exceeding 1 GHz were demonstrated shortly thereafter [23]. Around the same time, the silicon-on-insulator (Si-on-SiO_2 or SOI) platform was further developed to replace the earlier silicon photonic platforms which were based on doping gradients in silicon [20, 24]. This transition resulted in an enhanced refractive-index contrast (and hence a higher integration density) and enabled lower losses. Furthermore, the problem of efficient optical coupling between optical fibers and integrated silicon waveguides was tackled using tapers [25–27] and grating couplers [28], and numerous other noteworthy advances followed suit [20, 29].

During the last two decades, the emphasis gradually shifted from research and development to commercialization. Not only established players such as Intel and IBM have invested heavily in silicon photonics technology, but also several new companies have been incorporated to obtain some market share in the silicon photonics landscape, for example Luxtera (acquired by Cisco in 2019), Kotura (acquired by Mellanox in 2013 and later Nvidia), and Aurrion (acquired by Juniper

Networks in 2016). According to a report published in 2021 by MarketsandMarkets, the global silicon photonics market is expected to grow from USD 1.1 billion in 2021 to USD 4.6 billion in 2027, corresponding with an expected compound annual growth rate (CAGR) of 26.8 % [30]. A similar forecast has been predicted in the 2022 report by Yole development [31], as illustrated in Fig. 1.1. The silicon photonics market value at the die-level was valued at USD 152 million in 2021 and is expected to reach USD 1 billion by 2027 at a compound annual growth rate of 36 %. Importantly, this growth will likely be fueled by many novel applications beyond established telecom and datacom markets. For example, medical and consumer health applications, photonic computing for AI, as well as the development of LiDAR for the automotive industry amongst others could significantly contribute to the further growth of silicon photonics technology. Some promising applications are discussed in greater detail in section 1.6.

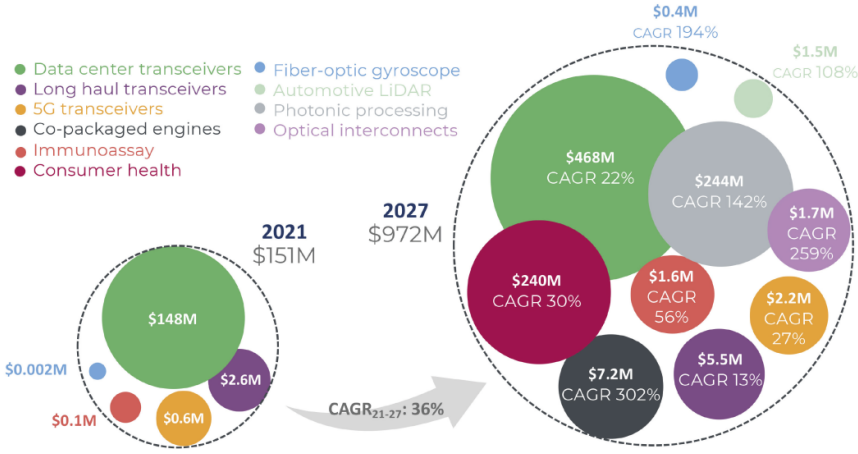

Figure 1.1: Silicon photonic die market forecast by application by Yole Intelligence [31].

1.4 Expanding silicon photonics with silicon nitride

Silicon nitride (Si_3N_4) photonic circuits have been of interest from early on due to their wide transparency range, which extends to visible wavelengths where silicon becomes absorbing, as well as their compatibility with silicon processing technologies [32]. Already in the late 1970s, low propagation losses down to 0.1 dB/cm at visible wavelengths were achieved with Si_3N_4 slab waveguides. For this, thin silicon nitride films were deposited through chemical vapor deposition on thermally oxidized silicon substrates [33]. The low losses and transparency at visible

wavelengths proved instrumental for biosensing applications as long interaction lengths with the analyte were made possible. Indeed, in the 1990s, the first Si_3N_4 PICs for highly sensitive immunosensing emerged based on Si_3N_4 interferometers [34, 35]. Waveguide losses at telecommunication wavelengths were initially significantly higher due to hydrogen-based absorption around 1.52 μm (absorption in Si_3N_4) and 1.4 μm (absorption in the SiO_2 cladding). To this end, low-pressure chemical vapor deposition (LPCVD) with a high temperature annealing step has proven effective to remove the hydrogen and reduce the losses [36]. As the name suggests, LPCVD Si_3N_4 is deposited at a low pressure but at a high temperature ($>$700°C), whereas plasma-enhanced chemical vapor deposition (PECVD) Si_3N_4 is deposited at lower temperatures ($<$400°C), making the latter compatible with CMOS back-end processing. LPCVD Si_3N_4 is typically close to stoichiometric Si_3N_4, exhibits higher internal strain, and provides excellent control over the material refractive index and film thickness [37]. The properties of PECVD Si_3N_4 depend more strongly on the deposition conditions and can be Si-rich (resulting in a higher refractive index) or nitrogen-rich (resulting in a lower refractive index). Regardless of the chosen deposition technique, the fact that silicon nitride is added through a deposition process comes with a lot of flexibility. It implies, for example, that silicon nitride waveguides can be combined with SOI waveguides to merge the merits of both platforms on a single chip [37].

Further improvements of the deposition and etching processes have led to ultra-low propagation losses necessary for realizing long optical delay lines for optical packet routing and antenna beam steering [38, 39]. Waveguide losses on the order of 1 dB/m have recently been attained at infrared wavelengths, two orders of magnitude lower than what has been achieved using SOI waveguides [32, 40]. Such ultra-low losses have enabled microring resonators with Q-factors exceeding 10^7 [41]. In addition, the lower refractive index contrast compared to SOI, results in reduced sensitivity to fabrication tolerances. These properties have made Si_3N_4 a suitable platform to develop high-performance optical filters [32, 42].

Recently, thick Si_3N_4 waveguides have been developed to increase the mode confinement and enable efficient nonlinear optical interactions [32]. Although the third-order nonlinearity of silicon is more than an order of magnitude higher than that of silicon nitride, it is virtually useless at telecommunications wavelengths because of two-photon absorption (TPA) resulting from its small bandgap of 1.1 eV [43]. Silicon nitride does not suffer from this TPA and has therefore been used extensively for frequency comb- and supercontinuum generation [44].

Today, silicon nitride has become an established wafer-scale platform to complement the features and strengths of SOI and III-V waveguide technologies. Several commercial foundry platforms have emerged and are now offering Si_3N_4 PICs, including imec, LioniX, Ligentec, CNM-IMB, AMF, and CEA-Leti amongst others. With the aforementioned advantages, the field of silicon nitride photonics

Properties & building blocks	InP	Si	Si_3N_4
Transparency range (μm)	1 - 1.7 [47]	1.1 - 4	0.4 - 4
Index contrast (%)	10 [48, 49]	140	38/28
Waveguide loss at 1550 nm (dB/cm)	2 - 4 [50]	1	0.01 [40]
Thermo-optic coefficient (K^{-1})	$2{\cdot}10^{-4}$ [51]	$1.86{\cdot}10^{-4}$	$2.45{\cdot}10^{-5}$
TPA coefficient (m/W)	$3{\cdot}10^{-10}$ [52]	$9{\cdot}10^{-12}$	0
Nonlinear Kerr coefficient (m^2/W)	$27{\cdot}10^{-18}$ [53]	$4.5{\cdot}10^{-18}$	$0.26{\cdot}10^{-18}$
Passives	+	++	+++
Modulators	+++	++	+
Detectors	+++	+++	-*
Lasers	+++	-*	-*
CMOS compatibility	-	++	+/++

Table 1.1: Some key properties and available building blocks of common integrated photonic platforms. Adapted from [43, 45, 46].
* Such devices can be fabricated using hybrid or heterogeneous integration techniques.

is expected to grow significantly in the coming years, and many of the novel applications envisioned in the silicon photonics roadmap will likely rely critically on silicon nitride's unique features.

1.5 III-V semiconductor integration techniques

A comparison of some widely used and commercially available integrated photonic platforms is laid out in Table 1.1. As evident from the previous sections and Table 1.1, the InP, SOI and Si_3N_4 platforms each have their own strengths and limitations. The InP platform is used extensively for commercial transceiver products as it can naturally incorporate high-quality semiconductor lasers, modulators and detectors [54]. Still, its relatively high propagation losses impede the performance of passive components such as filters, optical delay lines and extended laser cavities [55–57]. On the other hand, SOI and Si_3N_4 platforms benefit from waveguides with lower losses, but there is no straight forward solution to realize electrically pumped light sources (owing to silicon's indirect bandgap). Combining different materials is therefore desirable to overcome the shortcomings of the individual platforms. For this reason, various III-V integration methods have been developed in recent years to bring III-V opto-electronic components to the silicon (nitride) photonic platforms. Some common III-V integration techniques are discussed in the following sections.

1.5.1 Hetero-epitaxial growth

Direct growth of III-V materials on silicon is challenging due to the large lattice mismatch between both materials, the difference in thermal expansion coefficient, and the difference in polarity. These dissimilarities typically lead to threading dislocations, misfit defect formation, stacking faults and point defects, greatly deteriorating the optical properties of the grown layers [58]. Several approaches have been investigated to alleviate these problems such as the growth of a strain relaxed buffer layer [59] or selective area growth [60]. However, with the first approach, very thick buffer layers (>3 μm) are currently needed to reach sufficiently low threading dislocations, while the attainable III-V volume is limited for the latter approach [61]. Recently, an alternative technique called nano-ridge engineering was developed at imec [62]. This technique is based on selective area growth using metalorganic vapor-phase epitaxy and aspect ratio trapping inside a narrow trench. As the III-V growth can be continued out of the trench, the possible III-V volume is significantly increased while the defects remain efficiently trapped inside the trenches. Based on this process, monolithic lasers [61] and detectors [63] have recently been demonstrated. Despite the impressive progress that has been made, this integration approach is still far from reaching technological maturity. Moreover, contamination issues have to be addressed when hetero-epitaxial growth on silicon is to be combined with the fabrication of CMOS electronics.

1.5.2 Butt-coupling

The concept of butt-coupling or edge-coupling is - in principle - straight forward: two different PICs, each terminated with an appropriate facet, are brought in close proximity to each other to enable efficient optical coupling. This way, a hybrid III-V/Si or III-V/Si_3N_4 device can readily be assembled. An example of an InP-Si_3N_4 hybrid laser is shown in Fig. 1.2(a). The optical modes at the interfaces are closely matched in shape and size to minimize the optical coupling loss. Furthermore, to avoid parasitic reflections at the interface, the waveguide is typically terminated under an angle and/or an anti-reflection coating is added [64, 65].

Butt-coupling benefits from two key advantages. Firstly, the passive and active PICs are processed separately on their native substrate, resulting in excellent epitaxial quality and hence optimal device performance. Secondly, superior thermal performance can be achieved compared to most heterogeneously integrated devices because the active III-V PIC can be mounted directly on a heatsink [64]. As a result, hybrid lasers with high powers (exceeding 100 mW [66]) and ultra-narrow linewidths ($<$320 Hz [67]) have been demonstrated. Although butt-coupling can deliver excellent performance, heterogeneously integrated counterparts surpass it in terms of device footprint and integration density. Moreover, the necessary sequential assembly of devices with highly accurate alignment tools significantly

increases the overall cost of the device. Still, butt-coupling remains an excellent approach for lower volume applications where a limited number of lasers and/or detectors are required for each PIC, but it is unsuitable to serve high-volume markets.

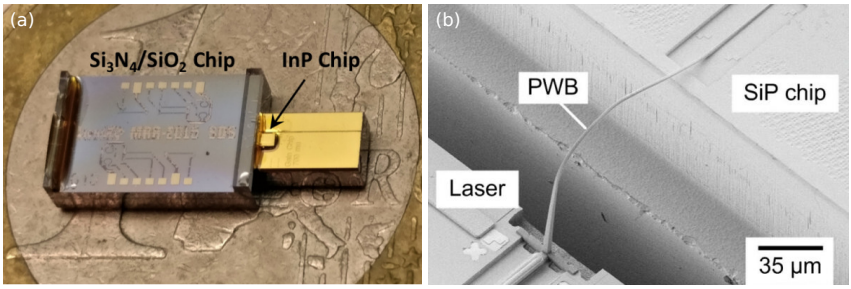

Figure 1.2: (a) Photograph of a butt-coupled Si_3N_4-InP PIC, adapted from [65]. (b) Image of a photonic wirebond between an InP-based laser and a passive silicon photonic circuit, adapted from [68].

1.5.3 Photonic wire bonding

Analogous to electronics, where metal wire bonds are used to connect integrated circuits with external circuitry, photonic wire bonds are three-dimensional freeform polymer waveguides that connect PICs to each other or to optical fibers. The fabrication process goes as follows: the different PICs are first mounted on a common substrate, and the interconnection regions are embedded in a negative-tone photoresist. Using a pulsed laser, the wirebonds are subsequently defined based on a two-photon polymerization process. As the exact shapes of the photonic wire bonds are adapted to the positions of the integrated waveguide facets, high-precision alignment of the individual PICs becomes obsolete. After laser writing, the unexposed photoresist is removed and the remaining structures are embedded in a low-index cladding material [69]. An image of a photonic wirebond is shown in Fig. 1.2(b). Insertion losses of 1.6 dB [69] and 0.7 dB [70] between two SOI PICs have been demonstrated, as well as coupling losses of 4.3 dB between InP edge-emitting lasers and SOI PICs [71]. Furthermore, the reliability was recently assessed, indicating that photonic wirebonds can withstand optical powers in excess of $\sim$100 mW [70]. In addition, it has been shown that photoic wire bonds can be densely integrated with a pitch below 5 μm [70]. Overall, this interconnect technology has proven to be versatile, enabling high interconnect densities as well as mass manufacturability. Owing to its potential to complement existing interconnect and integration methods, the concept of photonic wirebonding was recently commercialized by the start-up company Vanguard Automation GmbH and Freedom Photonics LLC.

1.5.4 Flip chip bonding

In microelectronics, flip-chip integration is a widely used pick-and-place method to mount electronic dies on a printed circuit board. Typically, solder bumps are used to mechanically bond the die to the substrate while at the same time provide an electrical and thermal connection. A similar process can be used for integrated photonics to integrate III-V devices on SOI or Si_3N_4 PICs. In this case, not only electrical contacts need to be realized, but also accurate alignment between the optical facets of the III-V die and the passive waveguide on the host PIC needs to be ensured. Accurate vertical alignment can be achieved passively by using mechanical alignment stops or pedestals in the recess of the host PIC, enabling a precision on the order of $\pm$10 nm [72, 73]. Horizontal alignment can be carried out actively, for example by utilizing optical backscatter reflectometry [73], by monitoring the device output while operating the active device [74], or based on visual cues using alignment markers [74]. With the latter approach, a horizontal alignment precision as low as 300 nm has been reported using an advanced assembly tool with a visual fiducial recognition system [75]. Alternatively, passive alignment can be utilized based on V-grooves in the target PIC combined with a self-aligning solder bump technique [76]. However, such an approach is rarely used owing to the significantly higher coupling losses. To relax the required alignment precision, the optical modes of the III-V and passive PICs can be expanded using integrated tapers allowing for an improved alignment tolerance, typically on the order of ± 1 μm [74]. Recent demonstrations have reported coupling losses of 2.1 dB between a flip-chipped InP DFB laser and a Si_3N_4 waveguide using optical backscatter reflectometry [73], and 1.5 dB between an InP DFB laser and an SOI waveguide using a visual recognition system [75].

Besides excellent process maturity, flip-chip integration benefits from several advantages. Firstly, III-V devices can be pre-tested on the source wafer before flip-chip integration. Additionally, compared to butt-coupling, flip-chip integration results in a reduced footprint and lower packaging cost as III-V devices are integrated on the same substrate, while still maintaining good thermal contact between the III-V device and the silicon substrate. Despite these advantages, flip-chip integration remains a sequential process with a relatively low throughput ($\sim$100 units/hour using an advanced ASM Amicra Nano System [75]), making it less suitable to serve high-volume applications.

1.5.5 Wafer bonding

Apart from heteroepitaxy which forms a category on its own, the previously discussed integration techniques (butt-coupling, photonic wire bonding and flip-chip integration) are typically categorized as hybrid integration techniques. With hybrid integration, two or more fully-processed PICs or dies, usually from different

material technologies, are assembled to construct a single device. In contrast, heterogeneous integration refers to an integration process where two or more material technologies or devices are combined on a single PIC chip, often at an early stage of the fabrication process. One of the key benefits of heterogeneous integration is that wafer-scale manufacturing can be leveraged to fabricate devices in large volumes at a low cost. Moreover, one can obtain a high alignment accuracy and low coupling losses when transitioning between different waveguide material technologies, leading to similar functionalities as monolithically integrated devices [77].

Currently, the most widespread heterogeneous integration method is wafer bonding, where unprocessed wafers (in the case of wafer-to-wafer bonding) or dies (referred to as die-to-wafer bonding) are transferred onto a patterned and planarized host wafer. After wafer bonding, the substrate material of the transferred stack is selectively removed and devices are processed on the host wafer using conventional lithography and etching tools. A typical example is the bonding of III-V wafers onto silicon photonics wafers [78, 79], as illustrated in Fig. 1.3(a). Depending on the application, (multiple) die-to-wafer bonding is often more economical as the expensive III-V material can be used more efficiently [80].

Wafer bonding is generally subdivided in direct bonding, which was pioneered at the University of California Santa-Barbara (UCSB), and adhesive bonding, which was developed at Ghent University. As the name suggests, no intermediate adhesive layer is used for direct bonding, leading to excellent thermal conductivity between the bonded film and the host wafer. However, direct bonding poses stringent requirements on the involved surfaces: extremely clean surfaces with low surface roughness are essential. These restrictions are significantly relaxed by utilizing an intermediate adhesive layer, typically a polymer such as divinylsiloxane-bis-benzocyclobutene (DVS-BCB or BCB) or SU-8. Although the resulting thermal contact is inferior to that of direct wafer bonding, the overall thermal performance of the PIC is generally dominated by the much thicker burried oxide layer and not by the adhesive layer [77].

Although wafer bonding enables wafer-scale manufacturing with a high level of integration, low coupling losses and minimal packaging complexity compared to hybrid integration approaches, it suffers from several drawbacks. First of all, separate processing tools are necessary to process the III-V materials on the silicon (nitride) host wafers due to incompatibility with CMOS processes. As such, wafer bonding only becomes economically viable at high volumes because only then, the high initial investment needed to finance the manufacturing infrastructure becomes acceptable. Secondly, compared to hybrid integration approaches, pre-testing of III-V devices is not possible. Excellent process control is therefore paramount to achieve a high device yield. In addition, as III-V devices are realized on top of the host PIC, thermal performance is degraded compared to hybridly integrated devices where the III-V device can be mounted directly on a thermoelectric cooler

or submount. Still, wafer bonded lasers on SOI with relatively high optical output powers in excess of 50 mW have been reported [81].

Direct wafer bonding has been adopted by several companies, for example by Nexus photonics to develop heterogeneous devices for the visible and near-infrared spectrum [82], by Rockley Photonics to develop wearable biosensors, and by Intel to fabricate transceivers for data centers. According to a recent market analysis by Yole, Intel shipped over 3 million units of its 100G pluggable transceivers by 2020, hence meeting the high volumes necessary to make wafer bonding economically excel.

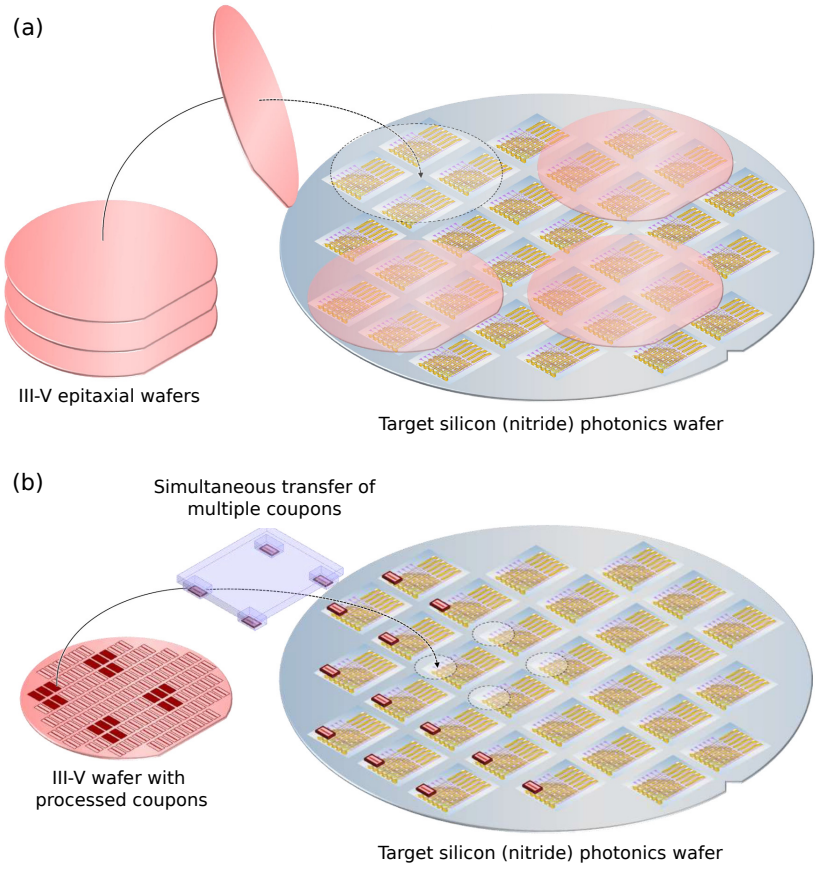

Figure 1.3: Schematic representation of (a) wafer-to-wafer bonding and (b) micro-transfer printing. With wafer bonding, the III-V device is processed only after its integration. With micro-transfer printing, the device is pre-processed on the III-V source wafer and typically few processing steps are carried out after the integration.

1.5.6 Micro-transfer printing

Micro-transfer printing (μTP) is a versatile heterogeneous integration technique that uses a high-precision motion controlled elastomer stamp to selectively pick-up and print microscale devices (or pieces of material) on a target substrate or PIC. The concept was originally invented by John Rogers at the University of Illinois-Urbana Champaign and later developed by Semprius Inc. In 2013, X-Celeprint was incorporated to further develop and license the technology.

The micro-transfer printing concept is illustrated in Fig. 1.3(b), and a detailed process flow is depicted in Fig. 1.4. In a first step, pre-processed functional devices are defined on the native source substrate. For example, InP semiconductor optical amplifiers can be fabricated at a dedicated III-V foundry. A sacrificial layer is included in the layer stack to enable suspension of the devices on the source wafer by encapsulating the devices (for example using photoresist) and selectively removing the sacrificial layer with wet or vapor-phase under-etching. The suspended structures or devices are often referred to as "coupons". Once the coupons are suspended, a polydimethylsiloxane (PDMS) stamp is laminated against the coupons and the stamp is rapidly retracted from the source wafer. Due to the fast movement and the stamp's viscoelasticity, the adhesion strength between the coupon and the stamp exceeds that of the coupon-source interface, making the anchor points (tethers) of the encapsulation break at well-designed locations. After pick-up, the coupon is transferred to the target wafer by laminating the coupon-loaded stamp to the target wafer and subsequently retracting the stamp slowly (often complemented with some shear force applied to the stamp). Again, based on the principle of kinetically controlled adhesion, the slow movement during the printing phase ensures that the adhesion between the target wafer and the coupon exceeds the adhesion of the coupon-stamp interface. Similar to adhesive wafer bonding, an adhesive bonding agent can be utilized (typically DVS-BCB) to ease the printing process, although molecular bonding without an adhesive is also possible if the involved surfaces have a sufficiently low surface roughness, ideally subnanometer. Furthermore, similar to wafer bonding, the transfer printed devices can be integrated directly on the optical waveguides, allowing for adiabatic evanescent coupling with minimal coupling losses. However, also other coupling schemes are compatible with micro-transfer printing, for example grating-assisted coupling [83] or edge-coupling [84] which resembles flip-chip integration. Although the coupling loss of the latter is typically significantly higher than an evanescent coupling approach, edge-coupling can be valuable for broadband and high-power applications.

Micro-transfer printing has matured considerably over recent years, and coupons can now routinely be integrated with a near-perfect yield (>99% printing yield [77, 86]) and with high precision, typically ± 1.5 μm (3σ) with entry-level tools and below ± 500 nm (3σ) with state-of-the-art tools from ASMPT AMICRA [87]. In addition, micro-transfer printing benefits from several advantages over com-

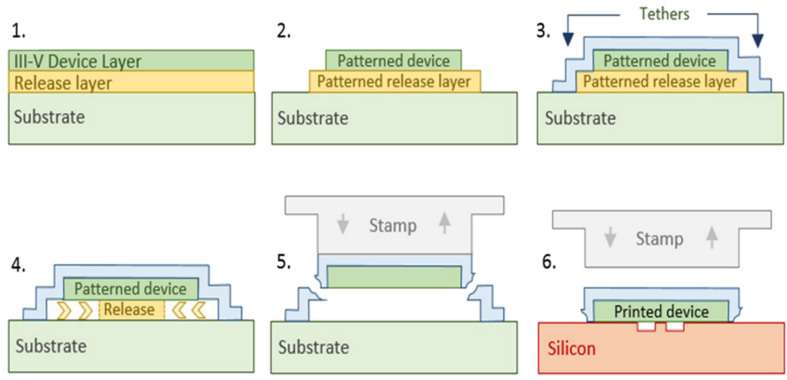

Figure 1.4: Pre-fabrication of III-V devices on their native substrate and the micro-transfer printing process. Reproduced from [85].

peting integration techniques. Firstly, it is possible to pre-test the pre-processed devices on the source wafer prior to integration on the target wafer, similar to flip-chip integration. Furthermore, the source wafer can be densely populated with pre-processed devices, ensuring efficient usage of the often expensive source material. In addition, many coupons can be picked up and printed simultaneously by using array stamps, enabling massively parallel integration and volume manufacturing [87]. Yet another advantage is that different materials can be co-integrated on the same target wafer to implement diverse functionalities. For example, besides III-V optical amplifiers and detectors, also lithium niobate coupons for high-speed electro-optic modulation [88] as well as nonlinear materials such as GaP [89] can be integrated using micro-transfer printing. This unparalleled versatility is achieved by combining the advantages of flip-chip integration and wafer-bonding. Devices and materials can be integrated at the back-end-of-line, which is essential to overcome the strict CMOS incompatibility of materials such as lithium niobate, or early on in the process flow to benefit from wafer-scale manufacturing.

Recently, micro-transfer printed III-V-on-Si DFB lasers with more than 25 mW output power [87], as well as C-band narrow-linewidth III-V-on-Si double laser structures with 110 nm wavelength tuning range [90] have been demonstrated. Furthermore, a wide range of micro-transfer printed devices on silicon nitride have been reported, including but not limited to continuous-wave lasers [91] and mode-locked lasers [92], high-speed InP photodetectors with a 3-dB bandwidth of 155 GHz [93], GaAs VCSELs at 850 nm with $>$0.1 mW output power and 5 nm tuning range [94], and GaAs-based single-photon sources for integrated quantum photonics [95].

Table 1.2 summarizes the strengths and limitations of the various aforementioned integration techniques both in terms of device performance (optical cou-

Properties	Hetero-epitaxy	Hybrid Integration			Heterogeneous integration	
		Butt-coupling	Photonic wire bond	Flip-chip	Wafer bonding	Transfer printing
Coupling efficiency	+++	+	+	+	+++	++
Thermal performance	+	+++	++	++	+	+
Integration density	+++	-	+	+	++	+++
Maturity	-	+++	++	+++	+++	++
Device cost at volume	$	$$$$	$$$	$$$	$$	$
Attainable device yield	-	+++	++	+++	++	+++
CMOS compatibility	++	+++	+++	+++	++	+++
Scalability (throughput)	+++	+	++	++	+++	+++
Versatility*	+	++	++	++	+	+++

Table 1.2: Comparison of III-V integration techniques on silicon (nitride) integrated photonic platforms.
* Integration technology can be leveraged to simultaneously integrate other materials or devices besides lasers and detectors, for example electro-optic modulators or nonlinear optical materials.

pling efficiency, thermal management, integration density) as in economical terms (cost, yield, CMOS compatibility, throughput, etc.).

1.6 Applications

Some applications of silicon (nitride) photonics have been briefly introduced throughout the previous sections. In the following sections, a selected number of relevant and promising applications are discussed in greater detail.

1.6.1 Telecom and datacom

Silicon photonics was originally developed to serve optical tele- and datacom networks. At both sides of the fiber link, high-speed optical transceivers are needed to modulate and detect optical signals and convert them from or into electrical signals. In the early days, III-V photonics dominated the transceiver market, serving long-haul fiber links. However, with the explosive growth of Internet Protocol (IP) traffic, there has been a fast-paced uptake of optical communication technology for ever shorter distances, hereby replacing purely electrical technologies. This trend of short reach optical communication has been accompanied by a steep increase in required transceiver volumes, making hybrid and heterogeneous III-V-silicon photonics both technologically and economically surpass pure III-V alternatives.

To this day, tele- and datacom remain of utmost importance to fuel the demand for silicon photonic PICs. With the rise of AR/VR, ultra-HD video, machine learning, and the Internet of Things amongst others, demands both in terms of transceiver performance as well as in volume, will likely increase further. According to Cisco's recent reports [96, 97], global internet traffic exceeded 7.7 Exabytes per day in 2021 compared to 2.4 Exabytes per day in 2016, a 3.2-fold increase over 5 years. Moreover, Cisco predicts that over 29.3 billion devices will be connected to the internet in 2023. To accommodate this astonishing growth, datacenters will continue to evolve rapidly, with optical links not only facilitating inter- and intra-rack communication, but also penetrating deeper into the network down to the chip-level. Indeed, it is expected that chip-to-chip intra-package optical interconnects will be deployed commercially by 2025 [98].

During the past decade, silicon photonics also started to play a major role to facilitate state-of-the-art wireless networks. One example is Radio over Fiber (RoF) technology, where the RF signal is encoded on an optical carrier and transmitted over a fiber towards the wireless base station. As such, all the signal processing and base station functionalities can be carried out at central points, greatly reducing the complexity of remote radio heads. This makes RoF much cheaper to build, operate and maintain compared to traditional wireless distribution networks. These features are deemed essential to enable 5G and beyond 5G wireless networks, where small cell sizes and a large number of antenna units are indispensable to meet the envisioned low latency and high bandwidth specifications [99].

1.6.2 LiDAR

While silicon along with InP and GaAs currently dominate the tele- and datacom markets, many other applications can benefit greatly from the superior passive performance of silicon nitride. One example is LiDAR, an acronym for Light Detection and Ranging, which has become increasingly relevant for autonomous vehicles and machine perception sensors in general.

In most cases, LiDAR or laser ranging is based on one of two different principles: time-of-flight or coherent ranging [100]. With time-of-flight ranging, the distance to an object is inferred from the delay of laser pulses that reflect on the object. At present, all commercially mature LiDAR solutions are based on a time-of-flight detection method. On the other hand, coherent ranging, also known as frequency-modulated continuous-wave (FMCW) ranging, relies on the homodyne detection of a reflected linearly chirped CW laser beam. The latter method can simultaneously reveal the object's distance as well as its velocity, greatly simplifying image classification. Moreover, due to eye-safe power limits, a higher sensitivity and hence a longer ranging distance can be achieved with coherent LiDAR. Despite these advantages, coherent LiDAR exhibits a higher complexity compared to

time-of-flight ranging as it requires a laser with a narrow linewidth as well as the capability for fast and linear frequency chirping [101].

Recently, on-chip solid-state LiDARs based on optical phased arrays have been developed, enabling accurate 3D imaging of the surrounding environment without requiring mechanical scanning with moving or rotating components. Numerous companies have been developing solid-state coherent and time-of-flight LiDAR technology, some of which based on silicon nitride such as Voyant Photonics, Deeplight, Tower Photonics (acquired by Intel in 2022), and Aeva Technologies[1] amongst others. Using silicon nitride for LiDAR offers several advantages: 1) sufficiently high output powers, necessary for laser ranging, are attainable without suffering from nonlinear absorption and 2) the low waveguide losses are instrumental to realize narrow-linewidth lasers for high temporal coherence. Furthermore, optical comb sources (sources which generate coherent, equally spaced discrete laser lines) on silicon nitride have been used for massively parallel laser ranging, providing a promising technological basis for compact and ultra-fast coherent LiDAR systems [101].

1.6.3 Sensing and spectroscopy

Besides LiDAR, silicon photonics has enormous potential in a plethora of other sensing applications. In recent years, silicon photonics has for example found its way into structural health monitoring solutions. Based on fiber Bragg gratings combined with a silicon photonics interrogator, the mechanical integrity of critical infrastructure such as bridges and windturbines can be continuously monitored in a cost-effective manner [102].

Furthermore, silicon photonics holds particular promise in medical applications. A first promising, upcoming medical market for silicon photonics is optical coherence tomography (OCT), which is a label-free three-dimensional non-invasive imaging modality. OCT has become a standard tool in diverse medical disciplines, notably in ophthalmology, to obtain high-resolution images of the retina [104], and dermatology [105]. In addition, OCT is an emerging imaging tool in various other medical areas such as gastroenterology [106] and oncology [107]. Typically, a broadband light source or a widely tunable laser are employed to illuminate the specimen. The emitted light is first split into a reference arm and a sensing arm, and reflected light from the specimen is superimposed with light from the reference arm to retrieve a depth profile. Currently, OCT tools are expensive, limiting their use to few medical specialists who can afford it. Significant cost savings could be achieved by leveraging silicon photonics technology to integrate the light source, the interferometer and the spectrometer into a single mass-manufacturable

[1] While most LiDAR companies do not reveal details of their photonics platform, their recent patent applications can be insightful to make an educated guess.

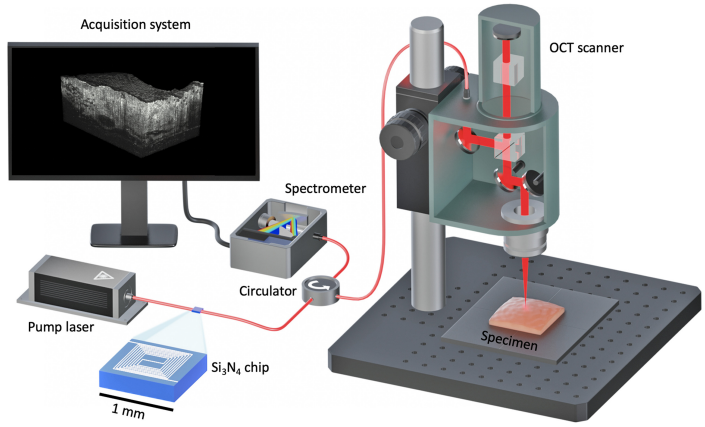

Figure 1.5: Schematic of an optical coherence tomography (OCT) setup with a broadband supercontinuum source generated with a silicon nitride PIC. Reproduced from [103].

PIC [103, 108, 109]. The availability of compact, high-performance OCT tools at a fraction of the cost of traditional systems could enable general practitioners to adopt this imaging modality, greatly expanding their diagnostic capabilities. A notable first step to serve this vision was recently reported in [103], where a silicon nitride PIC was employed to generate a broad supercontinuum light source for OCT-based breast tissue imaging. A schematic of the corresponding OCT setup is shown in Fig. 1.5.

Another widely anticipated application realm for silicon photonics is related to molecular analysis, typically either spectroscopic sensing in an industrial or environmental setting, or the analysis of gasses or liquids in biomedical applications. Generally, three common sensing modalities can be distinguished in this context: refractive index sensing, absorption spectroscopy, and Raman spectroscopy.

With refractive index sensing, minuscule changes in the refractive index are detected to reveal the presence of a to-be-detected analyte. Such label-free biosensors are most often based on a Mach-Zehnder Interferometer (MZI), where one of the two arms is exposed to the analyte and the other arm acts as a reference arm, a microring resonator, or a photonic crystal cavity [110]. Some photonic biosensors are schematically illustrated in Fig. 1.6. The light source is typically either a broadband emitter or a tunable laser. Furthermore, as several biosensing applications operate in the visible wavelength range, material platforms such as silicon nitride have been widely used. A silicon nitride lab-on-a-chip optofluidic sensor at visible wavelengths for human blood analysis was demonstrated in [111], while a silicon nitride MZI-based biosensor for biomarker detection in urine was reported in [112]. Similar devices could be employed to target countless other biosensing applications, including COVID-19 serology testing [113] or the detection of food

pathogens [114].

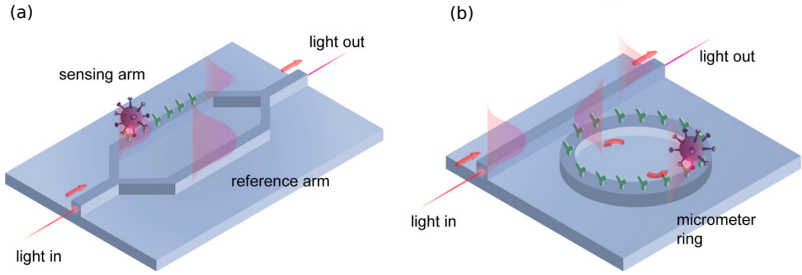

Figure 1.6: Schematic illustrations of some label-free integrated photonic biosensors. (a) Mach–Zehnder interferometric (MZI) biosensor. (b) Ring resonator biosensor. Reproduced from [115].

Absorption spectroscopy, as the name suggests, quantifies the amount of light absorbed by a sample as a function of wavelength. As the absorption spectrum is primarily determined by the atomic and molecular composition of the sample, one can detect the presence of a particular chemical substance and, in most cases, quantify the amount of the substance present. Similar to many other photonic sensing devices, a broadband emitter or a tunable laser can be employed to scan the wavelength range of interest for spectral analysis. With a global diabetes prevalence over 8%, affecting over 400 million people worldwide [116], one exciting application of absorption spectroscopy is continuous glucose monitoring. As the glucose absorption spectrum has clear features in the 1530-1820 nm range originating from the C-H stretching vibrations, infrared light is used for this purpose [117]. Several companies have been developing wearable continuous glucose monitoring solutions, including Rockley Photonis and Ghent University spin-off Indigo Diabetes. Such wearable spectrometers could also unlock various other sensing functions, for example to monitor lactate, alcohol, blood pressure etc. [118]. Another promising, upcoming implementation of absorption spectroscopy is dual-comb spectroscopy, which holds wide promise for many applications, including environmental sensing to monitor sources and sinks of greenhouse gases or industrial pollution [119]. With dual-comb spectroscopy, two optical comb sources are used to enable highly multiplexed interrogation of broadband absorption spectra using a single photodetector. The concept of dual-comb spectroscopy will be discussed in greater detail in Chapter 2, after a thorough introduction of mode-locked lasers and on-chip optical comb sources.

Finally, another promising spectroscopic sensing modality is Raman spectroscopy, named after the discoverer of Raman scattering. It relies on the inelastic scattering of light by a material or molecule, which results in a change in the energy and hence frequency of the scattered photons. This shift in frequency, known as the Raman shift, is used to obtain information about the chemical structure and

composition of the sample under study. Unlike absorption spectroscopy, the probe photon energy is typically much higher than the energy related to the studied excitations, and it is usually not tuned to an electronic transition of the medium, avoiding substantial absorption of light. As a consequence, one can typically use a laser source with a fixed optical frequency rather than a tunable laser source. Several Raman spectroscopy experiments have been demonstrated on-chip, including a silicon nitride trace gas Raman sensor [120]. Although lab-on-a-chip Raman sensors now reportedly outperform conventional confocal Raman microscopes [121], acquiring sufficient detection sensitivity remains challenging. For this reason, other material platforms than silicon nitride are being explored to enhance the Raman signal intensity (e.g. Ta_2O_5 [122]), as well as nanoplasmonic waveguide structures to suppress the Raman background contribution [123].

1.6.4 Integrated quantum photonics

Another emerging yet widely publicized application realm of silicon photonics lays in quantum technology. This emerging field aims to develop devices and system to control the superposition and entanglement of quantum states of light and matter, offering fundamental performance advantages over classical systems [124]. With the first integrated photonic quantum logic gate demonstrated only a decade ago [125], integrated quantum photonics is relatively immature compared to platforms such as trapped-ion- and superconducting systems. Still, it offers important advantages, including seamless compatibility with optical communication technology, integratability using CMOS-compatible manufacturing, and scalability to realize large-scale quantum systems. A silicon nitride optical waveguide platform - likely complemented with other materials through micro-transfer printing or wafer bonding - is particularly promising in this context owing to its ultra-low propagation losses and the access to nonlinear optical processes to implement frequency conversion [126] or entangled photon-pair generation through spontaneous parametric down-conversion [127]. Moreover, essential building blocks can readily be integrated on silicon nitride, including single-photon detectors [128] and single-photon sources [95, 129] amongst others. In addition, silicon nitride could play a key role to scale trapped trapped-ion- and cold-atom quantum computers. This prospect is supported by the recent demonstration of an ion qubit controlled by a silicon nitride PIC [130], hereby setting the stage for portable, high-fidelity quantum information processors.

1.7 Research objectives and thesis outline

The goal of this PhD project has been to extend the current application scope and corresponding functionalities of silicon nitride photonic integrated circuits by het-

erogeneously integrating active devices and materials using micro-transfer printing. Although silicon nitride has been studied as an integrated photonic platform for several decades, its use has long been limited to implement simple passive functions such as filters and optical delay lines. With the first fully integrated lasers on silicon nitride demonstrated less than four years ago [131, 132], active devices on silicon nitride signify a much more recent evolution. Building further on these recent developments, our objectives have been to build more advanced heterogeneous devices on silicon nitride, namely mode-locked comb lasers to support emerging applications such as portable spectroscopic sensors, as well as micro-transfer printable detectors and semiconductor optical amplifiers to unlock the full potential of silicon nitride in the (near-)visible spectral range. Furthermore, a novel integration process based on two micro-transfer printing steps was developed to enable heterogeneous laser integration on generic commercial silicon nitride platforms. Based on these research objectives, this work is divided into 7 chapters.

Chapter 1 has provided a historical perspective to integrated optics, introduced the field of silicon photonics, and emphasized the relevance of silicon nitride to extend the capabilities of traditional silicon photonic platforms. Furthermore, several III-V semiconductor integration techniques were discussed to build lasers, and active devices in general, on silicon (nitride) photonic platforms. It was shown that micro-transfer printing is particularly promising in this context, as it combines the advantages of two widely used integration methods: wafer bonding and flip-chip integration. Finally, the economical relevance of silicon (nitride) photonics was highlighted by illustrating the vast application realm that drives the development of this field.

Chapter 2 elaborates on integrated optical comb sources and on-chip mode-locked lasers. The concept of dual-comb spectroscopy is introduced as one of several promising applications of on-chip mode-locked lasers. Furthermore, the layout, fabrication, and characterization of the first heterogeneous passively mode-locked laser on silicon nitride are discussed in great detail.

Chapter 3 continues on the topic of heterogeneous on-chip mode-locked lasers by introducing a novel modeling strategy to simulate such devices. This hybrid model unifies the traveling-wave modeling technique, which has been widely used to simulate semiconductor lasers, with a nonlinear Schrödinger equation, which describes optical pulse propgation in a nonlinear, dispersive, passive waveguide. By combining these two distinct simulation methods, a wide range of physical phenomena can - in principle - be included, while limiting the model's computational workload. Such a hybrid model could therefore serve useful as a mode-locked

laser design tool in the future.

Chapter 4 presents a novel integration methodology to build heterogeneous lasers on silicon nitride photonic integrated circuits. By using two micro-transfer printing steps, one to integrate a crystalline Si coupling layer, and one to integrate III-V semiconductor optical amplifiers, heterogeneous lasers can be build on virtually any generic commercial low-refractive-index photonic integrated platform such as silicon nitride or thin-film lithium niobate. After a detailed description of the process flow and characterization of the losses imposed by the Si coupons, several recent device demonstrations are discussed to exemplify the potential of this integration strategy.

Chapter 5, unlike chapters 2 and 4 where demonstrated devices operate at telecom wavelenghts, focuses on extending the capabilities of silicon nitride in the near-visible spectral region. For this purpose, micro-transfer printed Si p-i-n photodiodes on silicon nitride are demonstrated for operation below 850 nm, serving applications such as biosensing, imaging and quantum photonics amongst others. The photodiode layout, fabrication process, and experimental performance are discussed in detail.

Chapter 6 complements chapter 5 by further extending the silicon nitride toolbox in the near-visible spectrum with micro-transfer printable GaAs semiconductor optical amplifiers (SOA's). These amplifiers constitute a first step to build narrow-linewidth, tunable, and mode-locked- heterogeneous lasers on silicon nitride which operate around 780 nm. The SOA design and process flow, as well as some preliminary measurement results are presented.

Chapter 7 formulates a number of conclusions to this dissertation and provides an outlook on future developments.

Contributions from colleagues: parts of this dissertation are the results of work from colleagues at the Photonics Research Group of Ghent University - imec. These contributions are specified in the introductions of the corresponding chapters.

1.8 Publications and awards

This dissertation has led to the following patent applications, awards, and publications in international conferences and peer-reviewed journals.

1.8.1 Patent applications

1. **S. Cuyvers**, G. Roelkens, K. Van Gasse, and B. Kuyken, "A source wafer and methods related thereto for micro-transfer printing", Patent Cooperative Treaty application, publication number: WO2023094232, published on June 1, 2023.

1.8.2 Publications in international journals

1. T. Vanackere, T. Vandekerckhove, L. Bogaert, M. Billet, S. Poelman, **S. Cuyvers**, J. Van Kerrebrouck, A. Moerman, O. Caytan, N. Singh, S. Lemey, G. Torfs, P. Ossieur, G. Roelkens, S. Clemmen, B. Kuyken, "Heterogeneous integration of a High-Speed Lithium Niobate Modulator on Silicon Nitride using Micro-Transfer Printing", APL Photonics, 8 (8): 086102 (2023).

2. T. Vandekerckhove, T. Vanackere, J. De Witte, **S. Cuyvers**, L. Reis, M. Billet, G. Roelkens, S. Clemmen, B. Kuyken, "Reliable micro-transfer printing method for heterogeneous integration of lithium niobate and semiconductor thin films", Optical Materials Express 13, 1984-1993 (2023).

3. G. Roelkens, J. Zhang, L. Bogaert, M. Billet, D. Wang, B. Pan, C.J. Krückel, E. Soltanian, D. Maes, T. Vanackere, T. Vandekerckhove, **S. Cuyvers**, J. De Witte, I. Luntadila Lufungula, X. Guo, H. Li, S. Qin, G. Muliuk, S. Uvin, B. Haq, C. Op de Beeck, J. Goyvaerts, G. Lepage, P. Verheyen, J. Van Campenhout, G. Morthier, B. Kuyken, D. Van Thourhout, R. Baets, "Micro-transfer printing for heterogeneous Si photonic integrated circuits", IEEE Journal on Selected Topics in Quantum Electronics (**invited**), vol. 29, no. 3: Photon. Elec. Co-Inte. and Adv. Trans. Print., pp. 1-14, Art no. 8200414 (2022).

4. **S. Cuyvers**, A. Hermans, M. Kiewiet, J. Goyvaerts, G. Roelkens, K. Van Gasse, D. Van Thourhout, B. Kuyken, "Heterogeneous integration of Si photodiodes on silicon nitride for near-visible light detection", Optics Letters 47, 937-940 (2022).

5. **S. Cuyvers**, B. Haq, G. Roelkens, K. Van Gasse, B. Kuyken, "Mode-locked comb lasers for chip-scale spectroscopy", Compound Semiconductor (**invited**), 27 (7), 60-64 (2021).

6. C. Op De Beeck, F. M. Mayor, **S. Cuyvers**, S. Poelman, J. F. Herrmann, O. Atalar, T. P. McKenna, B. Haq, W. Jiang, J. D. Witmer, G. Roelkens, A. H. Safavi-Naeini, R. Van Laer, B. Kuyken, "III/V-on-lithium niobate amplifiers and lasers", Optica, 8 (10), 1288-1289 (2021).

7. **S. Cuyvers**, B. Haq, C. Op de Beeck, S. Poelman, A. Hermans, Z. Wang, A. Gocalinska, E. Pelucchi, B. Corbett, G. Roelkens, K. Van Gasse, B. Kuyken, "Low Noise Heterogeneous III-V-on-Silicon-Nitride Mode-Locked Comb Laser", Laser & Photonics Reviews, p.2000485 (2021).

8. A. Hermans, K. Van Gasse, J. O. Kjellman, C. Caer, T. Nakamura, Y. Inada, K. Hisada, T. Hirasawa, **S. Cuyvers**, S. Kumari, A. Marinins, R. Jansen, G. Roelkens, P. Soussan, X. Rottenberg, B. Kuyken, "2-pJ-pulse-energy mode-locked III-V-on-silicon-nitride comb laser", APL Photonics, 6, p.096102 (2021).

9. **S. Cuyvers**, S. Poelman, K. Van Gasse, B. Kuyken, "Hybrid model for mode-locked laser diodes with cavity dispersion and nonlinearity", Scientific Reports, 11, 10027 (2021).

10. Q. Van den Brande, S. Lemey, **S. Cuyvers**, S. Poelman, L. De Brabander, O. Caytan, L. Bogaert, I. Lima De Paula, S. Verstuyft, A. C. F. Reniers, B. Smolders, B. Kuyken, D. Vande Ginste, H. Rogier, "A Novel Hybrid Integration Strategy for Compact, Broadband and Highly Efficient Millimeter-Wave On-Chip Antennas", IEEE Antennas and Wireless Propagation Letters, 18(11), p.2424-2428 (2019).

1.8.3 Publications in international conferences

1. M. Billet, T. Vanackere, T. Vandekerckhove, M. Niels, L.N Reis, D. Maes, M. Kiewiet, K. Akritidis, **S. Cuyvers**, S. Poelman, T. Reep, V. Bonito Oliva, F. Leo, G. Roelkens, B. Kuyken, "Recent progress in heterogeneous integration on the silicon nitride platform using micro-transfer printing", (invited) publication in SPIE Photonics West 2024, United States, (submitted).

2. M. Billet, **S. Cuyvers**, A. Hermans, G. Roelkens, S. Seema Saseendra, T. Nakamura, S. Okamoto, Y. Inada, K. Hisada, T. Hirasawa, J. Kjellman, B. Kuyken, "Tunable heterogeneous III-V-on-silicon-nitride mode-locked laser", submitted for publication in SPIE Photonics West 2024, United States, (submitted).

3. M. Billet, T. Vanackere, T. Vandekerckhove, M. Niels, L.N Reis, D. Maes, M. Kiewiet, K. Akritidis, **S. Cuyvers**, S. Poelman, T. Reep, V. Bonito Oliva, F. Leo, G. Roelkens, B. Kuyken, "Filling the gap of silicon nitride photonic platform functionalities using micro-transfer printing", (invited) publication in Advanced Photonics Congress, South Korea, to be published (2023).

4. J. Zhang, L. Bogaert, M. Billet, D. Wang, B. Pan, S. Qin, E. Soltanian, **S. Cuyvers**, D. Maes, T. Vanackere, T. Vandekerckhove, S. Poelman, M.

Kiewiet, I. Luntadila Lufungula, X. Guo, H. Li, J. De Witte, G. Lepage, P. Verheyen, J. Van Campenhout, B. Kuyken, G. Morthier, D. Van Thourhout, R. Baets, G. Roelkens, "Photonic integrated circuits realized using micro-transfer printing", (invited) publication in PIERS, to be published (2023).

5. J. Zhang, L. Bogaert , S. Qin, **S. Cuyvers** , I. Krestnikov, M. Konstantin , A. Farrell, R. Loi, D. Gomez, J. Rimbock, P. Ossieur, G. Lepage, P. Verheyen, J. Van Campenhout , G. Morthier, G. Roelkens, "O-band GaAs QD-on-Si integrated optical amplifier realized using micro-transfer printing", submitted to Opto-Electronics and Communications Conference (OECC), (China, 2023).

6. S. Poelman, **S. Cuyvers**, E. Vissers, J. De Witte, B. Haq, A. Hermans, N. Picque, G. Roelkens, B. Kuyken, "Low Repetition Rate Mode-Locked Laser on a Commercial Foundry Low-Index Photonic Platform", accepted for publication in Conference on Lasers and Electro-Optics (CLEO), (USA, 2023).

7. M. Kiewiet, **S. Cuyvers**, A. Hermans, M. Billet, J. Zhang, G. Roelkens, K. Van Gasse, B. Kuyken, "Scalable Heterogeneous Integration of a Pre-Processed Facet-Emitting Visible-Wavelength GaAs Laser", accepted for publication in Conference on Lasers and Electro-Optics (CLEO), (USA, 2023).

8. T. Vandekerckhove, T. Vanackere, J. De Witte, **S. Cuyvers**, L.N Reis, M. Billet, G. Roelkens, S. Clemmen, B. Kuyken, "Pillar-Based High-Yield Heterogeneous Integration of Lithium Niobate and Gallium Phosphide Thin Films", accepted for publication in Conference on Lasers and Electro-Optics (CLEO), (USA, 2023).

9. T. Vanackere, T. Vandekerckhove, L. Bogaert, M. Billet, S. Poelman, **S. Cuyvers**, J. Van Kerrebrouck, A. Moerman, O. Caytan, S. Lemey, G. Torfs, G. Roelkens, S. Clemmen, B. Kuyken, "High-Speed Lithium Niobate Modulator on Silicon Nitride using Micro-Transfer Printing", accepted for publication in Conference on Lasers and Electro-Optics (CLEO), (USA, 2023).

10. J. Zhang, L. Bogaert, M. Billet, D. Wang, B. Pan, S. Qin, E. Soltanian, **S. Cuyvers**, D. Maes, T. Vanackere, T. Vandekerckhove, S. Poelman, M. Kiewiet, I. Luntadila Lufungula, X. Guo, H. Li, J. De Witte, G. Lepage, P. Verheyen, J. Van Campenhout, B. Kuyken, G. Morthier, D. Van Thourhout, R. Baets, G. Roelkens, "Photonic integrated circuits realized using micro-transfer printing", PIERS (invited), Prague (2023).

11. G. Roelkens, J. Zhang, L. Bogaert, M. Billet, D. Wang, B. Pan, C. Kruckel, E. Soltanian, D. Maes, T. Vanackere, T. Vandekerckhove, **S. Cuyvers**, S.

Poelman, M. Kiewiet, J. De Witte, I. Luntadila Lufungula, X. Guo, H. Li, S. Qin, G. Lepage, P. Verheyen, J. Van Campenhout, G. Morthier, B. Kuyken, D. Van Thourhout, R. Baets, "Micro-transfer printing for silicon photonics", Optical Fiber Communication Conference (OFC), USA (2023).

12. M. Kiewiet, **S. Cuyvers**, G. Roelkens, K. Van Gasse, B. Kuyken, " " "Facet-coupled heterogeneous integration of GaAs SOAs on silicon nitride through micro-transfer printing for near-visible applications", Annual Symposium of the IEEE Photonics Benelux, Netherlands (2022).

13. M. Torreele, **S. Cuyvers**, T. Reep, K. Van Gasse, E. B. Kuyken, " Hybrid modeling technique for on-chip extended cavity semiconductor mode-locked lasers", 2022 28th International Semiconductor Laser Conference (ISLC), (Japan, 2022), pp. 1-2.

14. **S. Cuyvers**, A. Hermans, S. Poelman, C. Op de Beeck, B. Haq, G. Roelkens, K. Van Gasse, B. Kuyken, "III-V-on-Silicon-Nitride mode-locked comb lasers", Conference on Lasers and Electro-Optics/Pacific Rim (**invited**), (Japan, 2022).

15. **S. Cuyvers**, T. Vanackere, T. Vandekerckhove, S. Poelman, C. Op de Beeck, J. De Witte, A. Hermans, K. Van Gasse, N. Picque, D. Van Thourhout, G. Roelkens, S. Clemmen, B. Kuyken, "High-Yield Heterogeneous Integration of Silicon and Lithium Niobate Thin Films", Conference on Lasers and Electro-Optics", in Conference on Lasers and Electro-Optics (CLEO), (USA, 2022), paper STu4G.2.

16. I. Luntadila Lufungula, A. Shams-Ansari, D. Renaud, C. Op de Beeck, **S. Cuyvers**, S. Poelman, G. Roelkens, M. Loncar, B. Kuyken, "Post-deadline: On-chip electro-optic frequency comb generation using a heterogeneously integrated laser, Conference on Lasers and Electro-Optics", in Conference on Lasers and Electro-Optics (CLEO), (USA, 2022), paper JTh6B.7.

17. I. Luntadila Lufungula, A. Shams-Ansari, C. Op de Beeck, **S. Cuyvers**, S. Poelman, G. Roelkens, M. Loncar, B. Kuyken, "Universally printable single-mode laser on low-index platforms", Conference on Lasers and Electro-Optics (CLEO), (USA, 2022), paper SM2P.4.

18. B. Kuyken, **S. Cuyvers**, A. Hermans, S. Poelman, C. Op de Beeck, B. Haq, K. Van Gasse, J. O. Kjellman, C. Caër, G. Roelkens, P. Soussan, X. Rottenberg, "III-V-on-Silicon-Nitride Mode-Locked Lasers", in Optical Fiber Communication Conference (OFC) (USA, 2022), paper Tu2E.1.

19. I. Luntadila Lufungula, A. Shams-Ansari, C. Op de Beeck, **S. Cuyvers**, S. Poelman, B. Haq, M. Loncar, B. Kuyken, "Two-step transfer printed sin-

gle mode DFB laser on LN", Annual Symposium of the IEEE Photonics Benelux, Belgium (2021).

20. **S. Cuyvers**, G. Morthier, F. Leo, K. Van Gasse, B. Kuyken, "Generalized hybrid model for extended cavity mode-locked laser diodes", Annual Symposium of the IEEE Photonics Benelux, Belgium (2021).

21. S. Poelman, **S. Cuyvers**, J. De Witte, A. Hermans, K. Van Gasse, N. Picqué, G. Roelkens, D. Van Thourhout, B. Kuyken, "Generic Heterogeneous Integration Process Flow for Commercial Foundry Low-Index Photonic Platforms", in Frontiers in Optics + Laser Science (USA, 2021), paper FM1B.6.

22. J. De Witte, **S. Cuyvers**, S. Poelman, B. Kuyken, D. Van Thourhout, "Realization of Fabrication-tolerant Si3N4-Si Mode Transformers", 2021 IEEE Photonics Conference (IPC), (Canada, 2021), pp. 1-2.

23. J. Zhang, C. Op de Beeck, B. Haq, B. Kuyken, D. Van Thourhout, J. Van Campenhout, G. Lepage, P. Verheyen, G. Agnieszka, **S. Cuyvers**, E. Pelucchi, B. Corbett, A. Hermans, A. J. Trindade, C. Bower, R. Baets, G. Roelkens, G. Morthier, "III-V-on-Si/SiN lasers realized using microtransfer-printing", Proc. SPIE 11705, Novel In-Plane Semiconductor Lasers XX, 117050J (online, 2021).

24. **S. Cuyvers**, B. Haq, C. Op de Beeck, S. Poelman, A. Hermans, Z. Wang, G. Roelkens, K. Van Gasse, B. Kuyken, "Chip-scale electrically-pumped III-V-on-Silicon-Nitride frequency comb", Photonics Online Meetup (2020).

25. **S. Cuyvers**, B. Haq, C. Op de Beeck, S. Poelman, A. Hermans, Z. Wang, G. Roelkens, K. Van Gasse, B. Kuyken, "Ultra-Dense III-V-on-Silicon Nitride Frequency Comb Laser" , 2020 European Conference on Optical Communications (ECOC), (Belgium, 2020), pp. 1-3.

26. J. Zhang, C. Op de Beeck, B. Haq, J. Goyvaerts, **S. Cuyvers**, S. Kumari, G. Muliuk, A. Hermans, G. Agnieszka, E. Pelucchi, C. Brian, A. Jose Trindade, C. Bower, J. Van Campenhout, G. Lepage, P. Verheyen, B. Kuyken, D. Van Thourhout, G. Morthier, G. Roelkens, "Micro-Transfer-Printing for III-V/Si PICs", in Asia Communications and Photonics Conference/International Conference on Information Photonics and Optical Communications 2020 (ACP/IPOC), (China, 2020), paper T4G.3.

27. **S. Cuyvers**, S. Poelman, K. Van Gasse, B. Kuyken, "Novel Hybrid Modeling Strategy for Semiconductor Mode-Locked Lasers", in Laser Congress 2020 (ASSL, LAC), (USA, 2020), paper JTh2A.39.

1.8.4 Awards

1. Huawei PhD student contest - Bronze medal, September 2021
   For the paper: *S. Cuyvers, B. Haq, C. Op de Beeck, S. Poelman, A. Hermans, Z. Wang, A. Gocalinska, E. Pelucchi, B. Corbett, G. Roelkens, K. Van Gasse, B. Kuyken, "Low Noise Heterogeneous III-V-on-Silicon-Nitride Mode-Locked Comb Laser", Laser & Photonics Reviews, p.2000485 (2021).*

2. Best student paper award (1^{st} place), December 2020
   For the paper: *S. Cuyvers, B. Haq, C. Op de Beeck, S. Poelman, A. Hermans, Z. Wang, G. Roelkens, K. Van Gasse, B. Kuyken, "Ultra-Dense III-V-on-Silicon Nitride Frequency Comb Laser" , 2020 European Conference on Optical Communications (ECOC), (Belgium, 2020), pp. 1-3.*

References

[1] G. P. Agrawal. *Fiber-optic communication systems*. John Wiley & Sons, 2012.

[2] R. S. Quimby. *Photonics and lasers: an introduction*. John Wiley & Sons, 2006.

[3] J. C. Maxwell. *A treatise on electricity and magnetism*, volume 1. Oxford: Clarendon Press, 1873.

[4] A. H. Rawicz. *Theodore Harold Maiman and the invention of laser*. In P. Tománek, D. Senderáková, and M. Hrabovský, editors, Photonics, Devices, and Systems IV, volume 7138, page 713802. International Society for Optics and Photonics, SPIE, 2008.

[5] A. Javan, W. R. Bennett, and D. R. Herriott. *Population Inversion and Continuous Optical Maser Oscillation in a Gas Discharge Containing a He-Ne Mixture*. Phys. Rev. Lett., 6:106–110, Feb 1961.

[6] R. N. Hall, G. E. Fenner, J. D. Kingsley, T. J. Soltys, and R. O. Carlson. *Coherent Light Emission From GaAs Junctions*. Phys. Rev. Lett., 9:366–368, Nov 1962.

[7] K. C. Kao and G. A. Hockham. *Dielectric-fibre surface waveguides for optical frequencies*. In Proceedings of the Institution of Electrical Engineers, volume 113, pages 1151–1158. IET, 1966.

[8] J. Hecht. *The Breakthrough Birth of Low-Loss Fiber Optics*. Opt. Photon. News, 31(3):26–33, Mar 2020.

[9] R. J. Mears, L. Reekie, I. Jauncey, and D. N. Payne. *Low-noise erbium-doped fibre amplifier operating at 1.54 μm*. Electronics Letters, 19(23):1026–1028, 1987.

[10] S. E. Miller. *Integrated optics: An introduction*. The Bell System Technical Journal, 48(7):2059–2069, 1969.

[11] P. Tien. *Integrated optics and new wave phenomena in optical waveguides*. Reviews of Modern Physics, 49(2):361, 1977.

[12] R. Schmidt and I. Kaminow. *Metal-diffused optical waveguides in LiNbO3*. Applied Physics Letters, 25(8):458–460, 1974.

[13] T. Tamir. *Integrated optics*. Topics in applied physics, 1979.

[14] F. Chen and W. Benson. *A lithium niobate light modulator for fiber optical communications*. Proceedings of the IEEE, 62(1):133–134, 1974.

[15] Y. Kawamura, K. Wakita, Y. Itaya, Y. Yoshikuni, and H. Asahi. *Monolithic integration of InGaAs/InP DFB lasers and InGaAs/InAlAs MQW optical modulators*. Electronics Letters, 5(22):242–243, 1986.

[16] M. Suzuki, Y. Noda, H. Tanaka, S. Akiba, Y. Kushiro, and H. Isshiki. *Monolithic integration of InGaAsP/InP distributed feedback laser and electroabsorption modulator by vapor phase epitaxy*. Journal of lightwave technology, 5(9):1277–1285, 1987.

[17] Y. Kawamura, K. Wakita, Y. Yoshikuni, Y. Itaya, and H. Asahi. *Monolithic integration of a DFB laser and an MQW optical modulator in the 1.5 μm wavelength range*. IEEE Journal of Quantum Electronics, 23(6):915–918, 1987.

[18] R. Soref and J. Larenzo. *All-silicon active and passive guided-wave components for λ= 1.3 and 1.6 μm*. IEEE Journal of Quantum Electronics, 22(6):873–879, 1986.

[19] R. Soref and J. Lorenzo. *Single-crystal silicon: a new material for 1.3 and 1.6 μm integrated-optical components*. Electronics Letters, 21(21):953–954, 1985.

[20] N. Daldosso and L. Pavesi. *Nanosilicon photonics*. Laser & Photonics Reviews, 3(6):508–534, 2009.

[21] P. Huang, K. Sakamoto, K. Wang, P. Trinh, and B. Jalali. *Epitaxial SiGeC waveguide photodetector grown on Si substrate with response in the 1.3-1.55-μm wavelength range*. IEEE Photonics Technology Letters, 9(2):229–231, 1997.

[22] L. Colace, G. Masini, and G. Assanto. *Ge-on-Si approaches to the detection of near-infrared light*. IEEE Journal of Quantum Electronics, 35(12):1843–1852, 1999.

[23] A. Liu, R. Jones, L. Liao, D. Samara-Rubio, D. Rubin, O. Cohen, R. Nicolaescu, and M. Paniccia. *A high-speed silicon optical modulator based on a metal–oxide–semiconductor capacitor*. Nature, 427(6975):615–618, Feb 2004.

[24] M. Bruel and B. A. Auberton-Hervé. *Smart-Cut: A New Silicon On Insulator Material Technology Based on Hydrogen Implantation and Wafer Bonding*. Japanese Journal of Applied Physics, 36(3S):1636, mar 1997.

[25] V. R. Almeida, R. R. Panepucci, and M. Lipson. *Nanotaper for compact mode conversion*. Opt. Lett., 28(15):1302–1304, Aug 2003.

[26] T. Shoji, T. Tsuchizawa, T. Watanabe, K. Yamada, and H. Morita. *Low loss mode size converter from 0.3 μm square Si wire waveguides to singlemode fibres*. Electronics Letters, 38(25):1669–1670, 2002.

[27] M. Lipson. *Guiding, modulating, and emitting light on Silicon-challenges and opportunities*. Journal of Lightwave Technology, 23(12):4222–4238, 2005.

[28] D. Taillaert, W. Bogaerts, P. Bienstman, T. Krauss, P. Van Daele, I. Moerman, S. Verstuyft, K. De Mesel, and R. Baets. *An out-of-plane grating coupler for efficient butt-coupling between compact planar waveguides and single-mode fibers*. IEEE Journal of Quantum Electronics, 38(7):949–955, 2002.

[29] J. E. Bowers, T. Komljenovic, M. Davenport, J. Hulme, A. Y. Liu, C. T. Santis, A. Spott, S. Srinivasan, E. J. Stanton, and C. Zhang. *Recent advances in silicon photonic integrated circuits*. In G. Li and X. Zhou, editors, Next-Generation Optical Communication: Components, Sub-Systems, and Systems V, volume 9774, page 977402. International Society for Optics and Photonics, SPIE, 2016.

[30] MarketsandMarkets. *Silicon Photonics Market Report*, 2021.

[31] Yole Development. *Silicon Photonics 2022 Report*, 2022.

[32] D. J. Blumenthal, R. Heideman, D. Geuzebroek, A. Leinse, and C. Roeloffzen. *Silicon Nitride in Silicon Photonics*. Proceedings of the IEEE, 106(12):2209–2231, 2018.

[33] W. Stutius and W. Streifer. *Silicon nitride films on silicon for optical waveguides*. Appl. Opt., 16(12):3218–3222, Dec 1977.

[34] R. Heideman, R. Kooyman, and J. Greve. *Performance of a highly sensitive optical waveguide Mach-Zehnder interferometer immunosensor*. Sensors and Actuators B: Chemical, 10(3):209–217, 1993.

[35] E. Schipper, A. Brugman, C. Dominguez, L. Lechuga, R. Kooyman, and J. Greve. *The realization of an integrated Mach-Zehnder waveguide immunosensor in silicon technology*. Sensors and Actuators B: Chemical, 40(2):147–153, 1997.

[36] R. de Ridder, K. Warhoff, A. Driessen, P. Lambeck, and H. Albers. *Silicon oxynitride planar waveguiding structures for application in optical*

communication. IEEE Journal of Selected Topics in Quantum Electronics, 4(6):930–937, 1998.

[37] R. Baets, A. Z. Subramanian, S. Clemmen, B. Kuyken, P. Bienstman, N. Le Thomas, G. Roelkens, D. Van Thourhout, P. Helin, and S. Severi. *Silicon photonics: Silicon nitride versus silicon-on-insulator*. In 2016 Optical Fiber Communications Conference and Exhibition (OFC), pages 1–3, 2016.

[38] J. F. Bauters, M. J. R. Heck, D. D. John, J. S. Barton, C. M. Bruinink, A. Leinse, R. G. Heideman, D. J. Blumenthal, and J. E. Bowers. *Planar waveguides with less than 0.1 dB/m propagation loss fabricated with wafer bonding*. Opt. Express, 19(24):24090–24101, Nov 2011.

[39] M. Burla, D. A. I. Marpaung, L. Zhuang, M. R. Khan, A. Leinse, W. Beeker, M. Hoekman, R. G. Heideman, and C. G. H. Roeloffzen. *Multiwavelength-Integrated Optical Beamformer Based on Wavelength Division Multiplexing for 2-D Phased Array Antennas*. Journal of Lightwave Technology, 32(20):3509–3520, 2014.

[40] X. Ji, F. A. S. Barbosa, S. P. Roberts, A. Dutt, J. Cardenas, Y. Okawachi, A. Bryant, A. L. Gaeta, and M. Lipson. *Ultra-low-loss on-chip resonators with sub-milliwatt parametric oscillation threshold*. Optica, 4(6):619–624, Jun 2017.

[41] X. Ji, S. Roberts, M. Corato-Zanarella, and M. Lipson. *Methods to achieve ultra-high quality factor silicon nitride resonators*. APL Photonics, 6(7):071101, 2021.

[42] C. G. H. Roeloffzen, L. Zhuang, C. Taddei, A. Leinse, R. G. Heideman, P. W. L. van Dijk, R. M. Oldenbeuving, D. A. I. Marpaung, M. Burla, and K. J. Boller. *Silicon nitride microwave photonic circuits.* Optics express, 21 19:22937–61, 2013.

[43] A. Rahim, E. Ryckeboer, A. Z. Subramanian, S. Clemmen, B. Kuyken, A. Dhakal, A. Raza, A. Hermans, M. Muneeb, S. Dhoore, Y. Li, U. Dave, P. Bienstman, N. Le Thomas, G. Roelkens, D. Van Thourhout, P. Helin, S. Severi, X. Rottenberg, and R. Baets. *Expanding the Silicon Photonics Portfolio With Silicon Nitride Photonic Integrated Circuits*. Journal of Lightwave Technology, 35(4):639–649, 2017.

[44] A. L. Gaeta, M. Lipson, and T. J. Kippenberg. *Photonic-chip-based frequency combs*. Nature Photonics, 13(3):158–169, Mar 2019.

[45] K. Wörhoff, R. G. Heideman, A. Leinse, and M. Hoekman. *TriPleX: a versatile dielectric photonic platform*. Advanced Optical Technologies, 4(2):189–207, 2015.

[46] K. Alexander. *Integrated Silicon Nitride Photonics with Highly Nonlinear Thin Films and 2D Materials: Properties and Devices*. PhD thesis, Ghent University, 2018.

[47] *Why Can Silicon Nitride Be an Ideal Platform for Photonic Integrated Circuits? https://www.photondelta.com/news/why-can-silicon-nitride-sin-be-ideal-platform-for-photonic-integrated-circuits/.* Accessed: 2023-02-20.

[48] C. R. DOERR. *Integrated Photonic Platforms for Telecommunications: InP and Si*. IEICE Transactions on Electronics, E96.C(7):950–957, 2013.

[49] S. Adachi. *Refractive indices of III–V compounds: Key properties of InGaAsP relevant to device design*. Journal of Applied Physics, 53(8):5863–5869, 1982.

[50] M. Smit, X. Leijtens, H. Ambrosius, E. Bente, J. van der Tol, B. Smalbrugge, T. de Vries, E.-J. Geluk, J. Bolk, R. van Veldhoven, L. Augustin, P. Thijs, D. D'Agostino, H. Rabbani, K. Lawniczuk, S. Stopinski, S. Tahvili, A. Corradi, E. Kleijn, D. Dzibrou, M. Felicetti, E. Bitincka, V. Moskalenko, J. Zhao, R. Santos, G. Gilardi, W. Yao, K. Williams, P. Stabile, P. Kuindersma, J. Pello, S. Bhat, Y. Jiao, D. Heiss, G. Roelkens, M. Wale, P. Firth, F. Soares, N. Grote, M. Schell, H. Debregeas, M. Achouche, J.-L. Gentner, A. Bakker, T. Korthorst, D. Gallagher, A. Dabbs, A. Melloni, F. Morichetti, D. Melati, A. Wonfor, R. Penty, R. Broeke, B. Musk, and D. Robbins. *An introduction to InP-based generic integration technology*. Semiconductor Science and Technology, 29(8):083001, jun 2014.

[51] F. G. Della Corte, G. Cocorullo, M. Iodice, and I. Rendina. *Temperature dependence of the thermo-optic coefficient of InP, GaAs, and SiC from room temperature to 600 K at the wavelength of 1.5μm*. Applied Physics Letters, 77(11):1614–1616, 2000.

[52] D. Vignaud, J. F. Lampin, and F. Mollot. *Two-photon absorption in InP substrates in the 1.55μm range*. Applied Physics Letters, 85(2):239–241, 2004.

[53] Y. Jiao, J. van der Tol, V. Pogoretskii, J. van Engelen, A. A. Kashi, S. Reniers, Y. Wang, X. Zhao, W. Yao, T. Liu, F. Pagliano, A. Fiore, X. Zhang, Z. Cao, R. R. Kumar, H. K. Tsang, R. van Veldhoven, T. de Vries, E.-J. Geluk, J. Bolk, H. Ambrosius, M. Smit, and K. Williams. *Indium Phosphide Membrane Nanophotonic Integrated Circuits on Silicon*. physica status solidi (a), 217(3):1900606, 2020.

[54] J. Klamkin, H. Zhao, B. Song, Y. Liu, B. Isaac, S. Pinna, F. Sang, and L. Coldren. *Indium Phosphide Photonic Integrated Circuits: Technology and*

Applications. In 2018 IEEE BiCMOS and Compound Semiconductor Integrated Circuits and Technology Symposium (BCICTS), pages 8–13, 2018.

[55] B. Stern, X. Ji, A. Dutt, and M. Lipson. *Compact narrow-linewidth integrated laser based on a low-loss silicon nitride ring resonator*. Opt. Lett., 42(21):4541–4544, Nov 2017.

[56] H. Lee, T. Chen, J. Li, O. Painter, and K. J. Vahala. *Ultra-low-loss optical delay line on a silicon chip*. Nature Communications, 3(1):867, May 2012.

[57] M. A. Tran, D. Huang, and J. E. Bowers. *Tutorial on narrow linewidth tunable semiconductor lasers using Si/III-V heterogeneous integration*. APL Photonics, 4(11):111101, 2019.

[58] B. Kunert, Y. Mols, M. Baryshniskova, N. Waldron, A. Schulze, and R. Langer. *How to control defect formation in monolithic III/V hetero-epitaxy on (100) Si? A critical review on current approaches*. Semiconductor Science and Technology, 33(9):093002, aug 2018.

[59] G. Wang, R. Loo, E. Simoen, L. Souriau, M. Caymax, M. M. Heyns, and B. Blanpain. *A model of threading dislocation density in strain-relaxed Ge and GaAs epitaxial films on Si (100)*. Applied Physics Letters, 94(10):102115, 2009.

[60] Y. Han, Y. Xue, Z. Yan, and K. M. Lau. *Selectively Grown III-V Lasers for Integrated Si-Photonics*. Journal of Lightwave Technology, 39(4):940–948, 2021.

[61] D. Colucci, M. Baryshnikova, Y. Shi, Y. Mols, M. Muneeb, Y. D. Koninck, D. Yudistira, M. Pantouvaki, J. V. Campenhout, R. Langer, D. V. Thourhout, and B. Kunert. *Unique design approach to realize an O-band laser monolithically integrated on 300 mm Si substrate by nano-ridge engineering*. Opt. Express, 30(8):13510–13521, Apr 2022.

[62] D. Van Thourhout, Y. Shi, M. Baryshnikova, Y. Mols, N. Kuznetsova, Y. De Koninck, M. Pantouvaki, J. Van Campenhout, R. Langer, and B. Kunert. *Chapter Eight - Nano-ridge laser monolithically grown on (001) Si*. In S. Lourdudoss, J. E. Bowers, and C. Jagadish, editors, Future Directions in Silicon Photonics, volume 101 of *Semiconductors and Semimetals*, pages 283–304. Elsevier, 2019.

[63] C. I. Ozdemir, Y. De Koninck, D. Yudistira, N. Kuznetsova, M. Baryshnikova, D. Van Thourhout, B. Kunert, M. Pantouvaki, and J. Van Campenhout. *Low Dark Current and High Responsivity 1020nm InGaAs/GaAs Nano-Ridge Waveguide Photodetector Monolithically Integrated on a 300-mm Si Wafer*. Journal of Lightwave Technology, 39(16):5263–5269, 2021.

[64] E. Vissers, S. Poelman, C. Op de Beeck, K. V. Gasse, and B. Kuyken. *Hybrid integrated mode-locked laser diodes with a silicon nitride extended cavity*. Opt. Express, 29(10):15013–15022, May 2021.

[65] K.-J. Boller, A. van Rees, Y. Fan, J. Mak, R. Lammerink, C. Franken, P. van der Slot, D. Marpaung, C. Fallnich, J. Epping, R. Oldenbeuving, D. Geskus, R. Dekker, I. Visscher, R. Grootjans, C. Roeloffzen, M. Hoekman, E. Klein, A. Leinse, and R. Heideman. *Hybrid Integrated Semiconductor Lasers with Silicon Nitride Feedback Circuits*. Photonics, 7(1):4, Dec 2019.

[66] D. Kharas, J. J. Plant, W. Loh, R. B. Swint, S. Bramhavar, C. Heidelberger, S. Yegnanarayanan, and P. W. Juodawlkis. *High-Power (>300 mW) On-Chip Laser With Passively Aligned Silicon-Nitride Waveguide DBR Cavity*. IEEE Photonics Journal, 12(6):1–12, 2020.

[67] C. Xiang, P. A. Morton, and J. E. Bowers. *Ultra-narrow linewidth laser based on a semiconductor gain chip and extended Si3N4 Bragg grating*. Opt. Lett., 44(15):3825–3828, Aug 2019.

[68] M. R. Billah, M. Blaicher, T. Hoose, P.-I. Dietrich, P. Marin-Palomo, N. Lindenmann, A. Nesic, A. Hofmann, U. Troppenz, M. Moehrle, S. Randel, W. Freude, and C. Koos. *Hybrid integration of silicon photonics circuits and InP lasers by photonic wire bonding*. Optica, 5(7):876–883, Jul 2018.

[69] N. Lindenmann, G. Balthasar, D. Hillerkuss, R. Schmogrow, M. Jordan, J. Leuthold, W. Freude, and C. Koos. *Photonic wire bonding: a novel concept for chip-scale interconnects*. Opt. Express, 20(16):17667–17677, Jul 2012.

[70] M. Blaicher, M. R. Billah, J. Kemal, T. Hoose, P. Marin-Palomo, A. Hofmann, Y. Kutuvantavida, C. Kieninger, P.-I. Dietrich, M. Lauermann, S. Wolf, U. Troppenz, M. Moehrle, F. Merget, S. Skacel, J. Witzens, S. Randel, W. Freude, and C. Koos. *Hybrid multi-chip assembly of optical communication engines by in situ 3D nano-lithography*. Light: Science & Applications, 9(1):71, Apr 2020.

[71] T. Hoose, M. Billah, M. Blaicher, P. Marin, P.-I. Dietrich, A. Hofmann, U. Troppenz, M. Moehrle, N. Lindenmann, M. Thiel, P. Simon, J. Hoffmann, M. L. Goedecke, W. Freude, and C. Koos. *Multi-chip integration by photonic wire bonding: Connecting surface and edge emitting lasers to silicon chips*. In 2016 Optical Fiber Communications Conference and Exhibition (OFC), pages 1–3, 2016.

[72] A. Moscoso-Mártir, F. Merget, J. Mueller, J. Hauck, S. Romero-García, B. Shen, F. Lelarge, R. Brenot, A. Garreau, E. Mentovich, A. Sandomirsky, A.

Badihi, D. E. Rasmussen, R. Setter, and J. Witzens. *Hybrid Silicon Photonics Flip-Chip Laser Integration with Vertical Self-Alignment*. In 2017 Conference on Lasers and Electro-Optics Pacific Rim, page s2069. Optica Publishing Group, 2017.

[73] M. Theurer, M. Moehrle, A. Sigmund, K.-O. Velthaus, R. M. Oldenbeuving, L. Wevers, F. M. Postma, R. Mateman, F. Schreuder, D. Geskus, K. Wörhoff, R. Dekker, R. G. Heideman, and M. Schell. *Flip-Chip Integration of InP to SiN Photonic Integrated Circuits*. J. Lightwave Technol., 38(9):2630–2636, May 2020.

[74] M. Theurer, M. Moehrle, A. Sigmund, K.-O. Velthaus, R. M. Oldenbeuving, L. Wevers, F. M. Postma, R. Mateman, F. Schreuder, D. Geskus, K. Wörhoff, R. Dekker, R. G. Heideman, and M. Schell. *Flip-Chip Integration of InP and SiN*. IEEE Photonics Technology Letters, 31(3):273–276, 2019.

[75] A. Marinins, S. Hänsch, H. Sar, F. Chancerel, N. Golshani, H.-L. Wang, A. Tsiara, D. Coenen, P. Verheyen, G. Capuz, Y. De Koninck, O. Yilmaz, G. Morthier, F. Schleicher, G. Jamieson, S. Smyth, A. McKee, Y. Ban, M. Pantouvaki, D. C. La Tulipe, and J. Van Campenhout. *Wafer-Scale Hybrid Integration of InP DFB Lasers on Si Photonics by Flip-Chip Bonding With sub-300 nm Alignment Precision.* IEEE Journal of Selected Topics in Quantum Electronics, 29(3: Photon. Elec. Co-Inte. and Adv. Trans. Print.):1–11, 2023.

[76] S. Lindgren, H. Ahlfeldt, L. Backlin, L. Forssen, C. Vieider, H. Elderstig, M. Svensson, L. Granlund, L. Andersson, B. Kerzar, B. Broberg, O. Kjebon, R. Schatz, E. Forzelius, and S. Nilsson. *24-GHz modulation bandwidth and passive alignment of flip-chip mounted DFB laser diodes*. IEEE Photonics Technology Letters, 9(3):306–308, 1997.

[77] P. Kaur, A. Boes, G. Ren, T. G. Nguyen, G. Roelkens, and A. Mitchell. *Hybrid and heterogeneous photonic integration.* APL Photonics, 6(6):061102, 2021.

[78] H. Park, A. W. Fang, S. Kodama, and J. E. Bowers. *Hybrid silicon evanescent laser fabricated with a silicon waveguide and III-V offset quantum wells*. Opt. Express, 13(23):9460–9464, Nov 2005.

[79] G. Roelkens, J. Van Campenhout, J. Brouckaert, D. Van Thourhout, R. Baets, P. R. Romeo, P. Regreny, A. Kazmierczak, C. Seassal, X. Letartre, G. Hollinger, J. Fedeli, L. Di Cioccio, and C. Lagahe-Blanchard. *III-V/Si photonics by die-to-wafer bonding*. Materials Today, 10(7):36–43, 2007.

[80] X. Luo, Y. Cao, J. Song, X. Hu, Y. Cheng, C. Li, C. Liu, T.-Y. Liow, M. Yu, H. Wang, Q. J. Wang, and P. G.-Q. Lo. *High-Throughput Multiple Dies-to-Wafer Bonding Technology and III/V-on-Si Hybrid Lasers for Heterogeneous Integration of Optoelectronic Integrated Circuits*. Frontiers in Materials, 2, 2015.

[81] K. Van Gasse, R. Wang, and G. Roelkens. *27 dB gain III-V-on-silicon semiconductor optical amplifier with $>$ 17 dBm output power*. Optics Express, 27(1):293–302, 2019.

[82] H. Park, C. Zhang, M. A. Tran, and T. Komljenovic. *Heterogeneous silicon nitride photonics*. Optica, 7(4):336–337, Apr 2020.

[83] J. Goyvaerts, S. Kumari, S. Uvin, J. Zhang, R. Baets, A. Gocalinska, E. Pelucchi, B. Corbett, and G. Roelkens. *Transfer-print integration of GaAs p-i-n photodiodes onto silicon nitride waveguides for near-infrared applications*. Opt. Express, 28(14):21275–21285, Jul 2020.

[84] J. Juvert, T. Cassese, S. Uvin, A. de Groote, B. Snyder, L. Bogaerts, G. Jamieson, J. V. Campenhout, G. Roelkens, and D. V. Thourhout. *Integration of etched facet, electrically pumped, C-band Fabry-Pérot lasers on a silicon photonic integrated circuit by transfer printing*. Opt. Express, 26(17):21443–21454, Aug 2018.

[85] G. Roelkens, J. Zhang, A. De Groote, J. Juvert, N. Ye, S. Kumari, J. Goyvaerts, G. Muliuk, S. Uvin, G. Chen, B. Haq, B. Snyder, J. Van Campenhout, D. Van Thourhout, A. J. Trindade, C. Bower, J. O'Callaghan, R. Loi, B. Roycroft, and B. Corbett. *Transfer Printing for Silicon Photonics Transceivers and Interposers*. In 2018 IEEE Optical Interconnects Conference (OI), pages 13–14, 2018.

[86] J. Zhang, G. Muliuk, J. Juvert, S. Kumari, J. Goyvaerts, B. Haq, C. Op de Beeck, B. Kuyken, G. Morthier, D. Van Thourhout, R. Baets, G. Lepage, P. Verheyen, J. Van Campenhout, A. Gocalinska, J. O'Callaghan, E. Pelucchi, K. Thomas, B. Corbett, A. J. Trindade, and G. Roelkens. *III-V-on-Si photonic integrated circuits realized using micro-transfer-printing*. APL Photonics, 4(11):110803, 2019.

[87] G. Roelkens, J. Zhang, L. Bogaert, M. Billet, D. Wang, B. Pan, C. J. Kruckel, E. Soltanian, D. Maes, T. Vanackere, et al. *Micro-transfer printing for heterogeneous Si photonic integrated circuits*. IEEE Journal of Selected Topics in Quantum Electronics, 29(3: Photon. Elec. Co-Inte. and Adv. Trans. Print.):1–14, 2022.

[88] T. Vanackere, M. Billet, C. Op de Beeck, S. Poelman, G. Roelkens, S. Clemmen, and B. Kuyken. *Micro-Transfer Printing of Lithium Niobate on Silicon Nitride*. In 2020 European Conference on Optical Communications (ECOC), pages 1–4, 2020.

[89] M. Billet, L. Reis, Y. Léger, C. Cornet, F. Raineri, I. Sagnes, K. Pantzas, G. Beaudoin, G. Roelkens, F. Leo, et al. *Gallium phosphide-on-insulator integrated photonic structures fabricated using micro-transfer printing*. Optical Materials Express, 12(9):3731–3737, 2022.

[90] E. Soltanian, G. Muliuk, S. Uvin, D. Wang, G. Lepage, P. Verheyen, J. Van Campenhout, S. Ertl, J. Rimböck, N. Vaissiere, et al. *Micro-transfer-printed narrow-linewidth III-V-on-Si double laser structure with a combined 110 nm tuning range*. Optics Express, 30(22):39329–39339, 2022.

[91] C. Op de Beeck, B. Haq, L. Elsinger, A. Gocalinska, E. Pelucchi, B. Corbett, G. Roelkens, and B. Kuyken. *Heterogeneous III-V on silicon nitride amplifiers and lasers via microtransfer printing*. Optica, 7(5):386–393, May 2020.

[92] A. Hermans, K. Van Gasse, J. O. Kjellman, C. Caër, T. Nakamura, Y. Inada, K. Hisada, T. Hirasawa, S. Cuyvers, S. Kumari, A. Marinins, R. Jansen, G. Roelkens, P. Soussan, X. Rottenberg, and B. Kuyken. *High-pulse-energy III-V-on-silicon-nitride mode-locked laser*. APL Photonics, 6(9):096102, 2021.

[93] D. Maes, S. Lemey, G. Roelkens, M. Zaknoune, V. Avramovic, E. Okada, P. Szriftgiser, E. Peytavit, G. Ducournau, and B. Kuyken. *High-speed uni-traveling-carrier photodiodes on silicon nitride*. APL Photonics, 8(1):016104, 2023.

[94] J. Goyvaerts, A. Grabowski, J. Gustavsson, S. Kumari, A. Stassen, R. Baets, A. Larsson, and G. Roelkens. *Enabling VCSEL-on-silicon nitride photonic integrated circuits with micro-transfer-printing*. Optica, 8(12):1573–1580, Dec 2021.

[95] J. De Witte, A. Shadmani, T. Vanackere, T. Vandekerckhove, P. Lodahl, G. Roelkens, L. Midolo, B. Kuyken, and D. Van Thourhout. *Towards single-photon sources heterogeneously integrated on SiN*. In International Conference on Integrated Quantum Photonics, 2022.

[96] Cisco. *Cisco Annual Internet Report (2018–2023) White Paper*, 2020.

[97] Cisco. *Cisco Global - 2021 Forecast Highlights*, 2016.

[98] Q. Cheng, M. Bahadori, M. Glick, S. Rumley, and K. Bergman. *Recent advances in optical technologies for data centers: a review*. Optica, 5(11):1354–1370, Nov 2018.

[99] K. Van Gasse, L. Bogaert, L. Breyne, J. Van Kerrebrouck, S. Dhoore, C. Op de Beeck, A. Katumba, C.-Y. Wu, H. Li, J. Verbist, et al. *Analog radio-over-fiber transceivers based on III–V-on-silicon photonics*. IEEE Photonics Technology Letters, 30(21):1818–1821, 2018.

[100] M.-C. Amann, T. M. Bosch, M. Lescure, R. A. Myllylae, and M. Rioux. *Laser ranging: a critical review of unusual techniques for distance measurement*. Optical Engineering, 40(1):10 – 19, 2001.

[101] J. Riemensberger, A. Lukashchuk, M. Karpov, W. Weng, E. Lucas, J. Liu, and T. J. Kippenberg. *Massively parallel coherent laser ranging using a soliton microcomb*. Nature, 581(7807):164–170, May 2020.

[102] *Sentea*. *https://www.senteatech.com/*. Accessed: 2023-03-01.

[103] X. Ji, D. Mojahed, Y. Okawachi, A. L. Gaeta, C. P. Hendon, and M. Lipson. *Millimeter-scale chip–based supercontinuum generation for optical coherence tomography*. Science Advances, 7(38):eabg8869, 2021.

[104] W. Drexler, U. Morgner, R. K. Ghanta, F. X. Kärtner, J. S. Schuman, and J. G. Fujimoto. *Ultrahigh-resolution ophthalmic optical coherence tomography*. Nature medicine, 7(4):502–507, 2001.

[105] J. Welzel. *Optical coherence tomography in dermatology: a review*. Skin Research and Technology: Review article, 7(1):1–9, 2001.

[106] K. Li, W. Liang, J. Mavadia-Shukla, H.-C. Park, D. Li, W. Yuan, S. Wan, and X. Li. *Super-achromatic optical coherence tomography capsule for ultrahigh-resolution imaging of esophagus*. Journal of biophotonics, 12(3):e201800205, 2019.

[107] F. T. Nguyen, A. M. Zysk, E. J. Chaney, J. G. Kotynek, U. J. Oliphant, F. J. Bellafiore, K. M. Rowland, P. A. Johnson, and S. A. Boppart. *Intraoperative evaluation of breast tumor margins with optical coherence tomography*. Cancer research, 69(22):8790–8796, 2009.

[108] G. Yurtsever, N. Weiss, J. Kalkman, T. G. Van Leeuwen, and R. Baets. *Ultra-compact silicon photonic integrated interferometer for swept-source optical coherence tomography*. Optics Letters, 39(17):5228–5231, 2014.

[109] V. D. Nguyen, B. I. Akca, K. Wörhoff, R. M. De Ridder, M. Pollnau, T. G. van Leeuwen, and J. Kalkman. *Spectral domain optical coherence*

tomography imaging with an integrated optics spectrometer. Optics letters, 36(7):1293–1295, 2011.

[110] J. Wang, M. M. Sanchez, Y. Yin, R. Herzer, L. Ma, and O. G. Schmidt. *Silicon-Based Integrated Label-Free Optofluidic Biosensors: Latest Advances and Roadmap*. Advanced Materials Technologies, 5(6):1901138, 2020.

[111] M. Kumar, V. Muniswamy, K. Guha, J. Iannacci, and N. Krishnaswamy. *Analysis of integrated silicon nitride lab-on-a-chip optofluidic sensor at visible wavelength for absorbance based biosensing applications*. Microsystem Technologies, 27(9):3499–3506, Sep 2021.

[112] D. Martens, P. Ramirez-Priego, M. S. Murib, A. A. Elamin, A. B. González-Guerrero, M. Stehr, F. Jonas, B. Anton, N. Hlawatsch, P. Soetaert, et al. *A low-cost integrated biosensing platform based on SiN nanophotonics for biomarker detection in urine*. Analytical methods, 10(25):3066–3073, 2018.

[113] S. Ikegami, R. C. Benirschke, H. Fakhrai-Rad, M. H. Motamedi, R. Hockett, S. David, H. K. Lee, J. Kang, and T. J. Gniadek. *Target specific serologic analysis of COVID-19 convalescent plasma*. PLoS One, 16(4):e0249938, 2021.

[114] K. Seo, R. Brackett, N. Hartman, and D. Campbell. *Development of a Rapid Response Biosensor for Detection of Salmonella Typhimurium*. Journal of Food Protection, 62(5):431–437, 1999.

[115] M. Soler, M. C. Estevez, M. Cardenosa-Rubio, A. Astua, and L. M. Lechuga. *How Nanophotonic Label-Free Biosensors Can Contribute to Rapid and Massive Diagnostics of Respiratory Virus Infections: COVID-19 Case*. ACS Sensors, 5(9):2663–2678, 2020. PMID: 32786383.

[116] *World Health Organization - Diabetes*. *https://www.who.int/news-room/fact-sheets/detail/diabetes*. Accessed: 2023-03-02.

[117] E. Ryckeboer, R. Bockstaele, and R. Baets. *Absorption spectroscopy of glucose based on a silicon photonics evanescent sensor*. In 2013 IEEE Photonics Conference, pages 163–164. IEEE, 2013.

[118] M. Kim. *The Quest for Noninvasive Glucose Monitoring*. Optics and Photonics News, 33(10):30–37, 2022.

[119] K. Van Gasse, Z. Chen, E. Vicentini, J. Huh, S. Poelman, Z. Wang, G. Roelkens, T. W. Hänsch, B. Kuyken, and N. Picqué. *An on-chip III-V-semiconductor-on-silicon laser frequency comb for gas-phase molecular spectroscopy in real-time*. Preprint at `https://arxiv.org/abs/2006.15113`, 2020.

[120] S. A. Holmstrom, T. H. Stievater, D. A. Kozak, M. W. Pruessner, N. Tyndall, W. S. Rabinovich, R. A. McGill, and J. B. Khurgin. *Trace gas Raman spectroscopy using functionalized waveguides*. Optica, 3(8):891–896, Aug 2016.

[121] A. Dhakal, A. Raza, P. Wuytens, F. Peyskens, A. Skirtach, N. Le Thomas, and R. Baets. *Lab-on-a-chip Raman sensors outperforming Raman microscopes*. In 2016 Conference on Lasers and Electro-Optics (CLEO), pages 1–2, 2016.

[122] Z. Liu, Q. Zhao, P. Shi, B. Mitchell, H. Zhao, N. Le Thomas, D. J. Blumenthal, and R. Baets. *Tantalum Pentoxide Slot Waveguides for Waveguide Enhanced Raman Spectroscopy*. In The European Conference on Lasers and Electro-Optics, page ch_6_2. Optica Publishing Group, 2021.

[123] A. Raza, S. Clemmen, P. Wuytens, M. Muneeb, M. Van Daele, J. Dendooven, C. Detavernier, A. Skirtach, and R. Baets. *ALD assisted nanoplasmonic slot waveguide for on-chip enhanced Raman spectroscopy*. APL Photonics, 3(11):116105, 2018.

[124] J. Wang, F. Sciarrino, A. Laing, and M. G. Thompson. *Integrated photonic quantum technologies*. Nature Photonics, 14(5):273–284, May 2020.

[125] A. Politi, M. J. Cryan, J. G. Rarity, S. Yu, and J. L. O'brien. *Silica-on-silicon waveguide quantum circuits*. Science, 320(5876):646–649, 2008.

[126] M. Churaev, A. Riedhauser, R. N. Wang, C. Möhl, V. Snigirev, S. Hönl, T. Blésin, D. Caimi, J. Liu, Y. Popoff, P. Seidler, and T. J. Kippenberg. *Nonlinear Frequency Conversion in the Hybrid Silicon Nitride - Lithium Niobate Integrated Platform*. In Conference on Lasers and Electro-Optics, page SM4B.1. Optica Publishing Group, 2021.

[127] X. Cheng, M. C. Sarihan, K.-C. Chang, Y. S. Lee, F. Laudenbach, H. Ye, Z. Yu, and C. W. Wong. *Design of spontaneous parametric down-conversion in integrated hybrid SixNy-PPLN waveguides*. Opt. Express, 27(21):30773–30787, Oct 2019.

[128] C. Schuck, X. Guo, L. Fan, X. Ma, M. Poot, and H. X. Tang. *Quantum interference in heterogeneous superconducting-photonic circuits on a silicon chip*. Nature Communications, 7(1):10352, Jan 2016.

[129] X. Lu, Q. Li, D. A. Westly, G. Moille, A. Singh, V. Anant, and K. Srinivasan. *Chip-integrated visible–telecom entangled photon pair source for quantum communication*. Nature Physics, 15(4):373–381, Apr 2019.

[130] R. J. Niffenegger, J. Stuart, C. Sorace-Agaskar, D. Kharas, S. Bramhavar, C. D. Bruzewicz, W. Loh, R. T. Maxson, R. McConnell, D. Reens, G. N. West, J. M. Sage, and J. Chiaverini. *Integrated multi-wavelength control of an ion qubit*. Nature, 586(7830):538–542, Oct 2020.

[131] C. Op de Beeck, L. Elsinger, B. Haq, G. Roelkens, and B. Kuyken. *Heterogeneously Integrated Laser on a Silicon Nitride Platform via Micro-Transfer Printing*. In Frontiers in Optics + Laser Science APS/DLS, page FTu6B.1. Optica Publishing Group, 2019.

[132] C. Xiang, W. Jin, J. Guo, J. D. Peters, M. J. Kennedy, J. Selvidge, P. A. Morton, and J. E. Bowers. *Narrow-linewidth III-V/Si/Si3N4 laser using multilayer heterogeneous integration*. Optica, 7(1):20–21, Jan 2020.

2

III-V-on-silicon-nitride mode-locked laser

This chapter describes the layout, fabrication and characterization of a low-noise heterogeneous III-V-on-silicon-nitride mode-locked laser and compares it to state-of-the-art devices. The content presented in this chapter has been published in part in [1, 2].

2.1 Introduction

Mode-locked lasers are a special class of lasers that can generate ultra-short optical pulses by phase-locking a large number of longitudinal lasing modes inside their cavity. As dictated by the Fourier theorem, such an optical pulse train in the time domain corresponds with an optical comb, i.e. a set of coherent equally spaced discrete laser lines, in the spectral domain. The frequency spacing between adjacent comb lines is equal to the pulse repetition rate of the mode-locked laser. These devices have played an essential role in several scientific breakthroughs such as the development of fully stabilized optical frequency combs and optical clocks [3]. As a result, their impact has been widely recognized, most notably in 2005 when John Hall and Theodor Hänsch were awarded the Nobel prize in physics "for their contributions to the development of laser-based precision spectroscopy, including the optical frequency comb technique" [4].

Mode-locked lasers exist in various types and formats. Solid-state bulk lasers

are based on doped-insulator crystals or glasses such as Ti:Sapphire or Nd:YAG as an optical gain material [5]. These systems offer unparalleled performance reaching extremely short pulsewidths (pulses down to 5 fs have been generated using Ti:sapphire mode-locked lasers [6]) and high pulse energies. With the advent of mode-locked fiber lasers in the past decade, mode-locked laser systems capable of generating fully stabilized optical frequency combs have become commercially available [7]. These mode-locked fiber lasers typically rely on Erbium- or Ytterbium doped glass fibers as an optical gain material [8]. Finally, semiconductor mode-locked lasers, often denoted as mode-locked laser diodes, form a third category. These devices can be easily miniaturized and can be electrically pumped, unlike solid-state and fiber lasers which rely on optical pumping. This greatly reduces the complexity and cost of the laser.

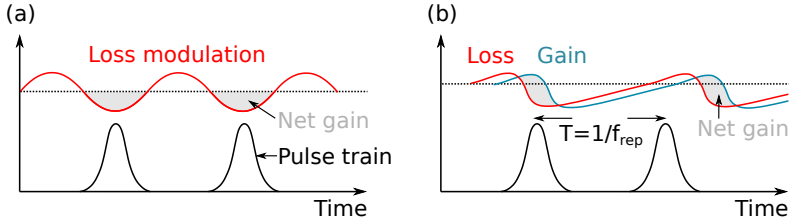

Figure 2.1: Schematic of active mode-locking (a) and passive mode-locking (b) with the time dependence of the pulse train and gain and loss dynamics.

Alongside different gain materials, various mode locking techniques exist, and they can mostly be categorized in two main classes: active and passive mode locking [5]. With active mode locking, an intracavity loss modulator is incorporated in the laser cavity which is actively driven at a frequency equal to the pulse repetition rate, as illustrated in Fig. 2.1(a). In the time domain, this approach can be visualized as a periodic shutter which opens once every pulse roundtrip time. With passive mode locking, a nonlinear optical element is employed whose loss decreases with optical intensity, hence discriminating low-intensity continuous wave light with respect to intense optical pulses. The gain and loss dynamics as well as the optical pulse train as a function of time are schematically illustrated in Fig. 2.1(b). Passive mode locking has the advantage that no externally driven modulator is required. Moreover, much shorter pulses can be achieved compared to active mode locking as the cavity loss modulation is automatically synchronized with the optical pulse train and the pulse-shortening mechanism can remain effective even for ultrashort optical pulses [5]. The possible implementations of passive mode locking greatly depend on the platform used. Solid-state mode-locked lasers often employ ultrafast nonlinear phenomena, for example by using Kerr lens mode locking as with Ti:Sapphire mode-locked lasers [9]. Here, the nonlinear refractive index change of the material is exploited to realize self-amplitude modula-

tion through self-focusing [5]. Similarly, mode-locked fiber lasers often rely on nonlinear polarization rotation [10] or a nonlinear amplifying loop mirror [11] to realize ultrafast artificial saturable absorption. On the other hand, mode-locked laser diodes mainly utilize semiconductor saturable absorbers [5]. In this case, the saturable absorption is related to an interband transition. For low optical intensities the number of excited electrons remains low and unsaturated. However, when the optical intensity increases, many electrons accumulate in the conduction band and Pauli blocking limits further absorption [5]. Although integrated mode-locked lasers with ultrafast artificial saturable absorbers have been demonstrated [12], the optical pulse intensities and material nonlinearities of established integrated photonic platforms currently seem too restrictive to realize practical devices. So far, semiconductor saturable absorbers have therefore been the dominant technology for integrated devices [13]. A third class of mode locking, widely used for quantum cascade lasers (QCLs), is so-called self mode locking. In this case, there is no active or passive modulation element and the self mode locking is achieved through four-wave mixing in the active medium combined with spatial hole burning [14]. This approach has the advantage that a higher efficiency can be achieved as no lossy intracavity element needs to be included to establish mode locking. However, self mode locking does not necessarily yield single optical pulses: although the longitudinal modes of the laser maintain a stable phase relationship, they might not share a uniform phase over the comb spectrum [15].

2.2 Optical comb sources on a photonic chip

Although traditionally optical comb spectra have mostly been generated using Ti:Sapphire solid-state lasers and Erbium- or Ytterbium-doped fiber mode-locked lasers, these laser sources are bulky and hence merely suitable for experiments in a lab environment. To unlock the full potential of optical frequency combs, miniaturization to a compact mass-manufacturable device is indispensable. In recent years, considerable effort has therefore gone into realizing more compact and cost-efficient optical comb generators, extending their application range well beyond fundamental frequency metrology [13, 15, 16]. For example, considerable progress has been made on the development of quantum cascade laser frequency combs for operation in the mid- and far-infrared and terahertz spectral regions [17–20]. Furthermore, resonant electro-optic comb generators, which employ phase modulation in a resonator with a strong second-order nonlinearity, have gained attention, owing to the excellent stability and unique complement of frequency reconfigurability [21]. Phase modulation leads to the growth of sidebands at the modulation frequency, which are subsequently modulated as well, resulting in a cascading effect and hence the formation of an optical comb. Electro-optic comb generators have recently been demonstrated on-chip, for example by the

group of Marko Lončar et al. on a thin-film lithium niobate platform [21].

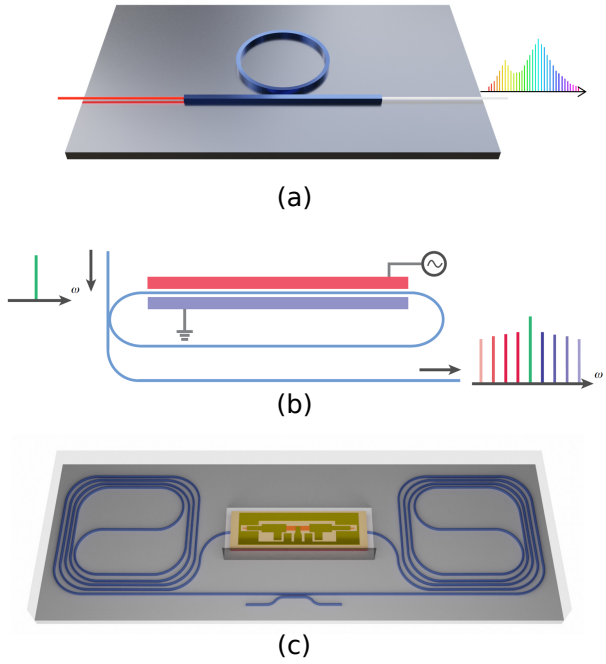

Figure 2.2: Schematic of different optical frequency comb technologies. (a) Kerr microcomb. (b) Resonant electro-optic comb. Reproduced from [22]. (c) On-chip heterogeneously integrated mode-locked laser diode [1].

Thirdly, a large number of Kerr-effect-based frequency comb generators have been demonstrated using different material platforms in various spectral windows [23–30]. In these devices, a comb is generated based on nonlinear four-wave mixing in an optically pumped dispersion-engineered microresonator [16]. The comb spacing is in this case determined by the free spectral range (FSR) of the resonator. A fourth class contains the so-called quadratic microcombs where the optical comb is generated by exploiting the quadratic nonlinearity through sum- and difference frequency generation. Although quadratic combs naturally exhibit higher efficiencies than Kerr combs, they require a non-centrosymmetric crystal to operate [31]. Finally, a fifth class entails the traditional optical frequency comb technique translated to a chip-scale device: the integrated mode-locked laser. Although integrated mode-locked lasers can rely on various gain materials, semiconductor mode-locked lasers have so far been the dominant approach for realizing mode-locked lasers on a photonic chip [15]. These integrated solutions can offer a small footprint and can be manufactured in large volumes using established semi-

conductor processing technology [32]. Figure 2.2 depicts some common on-chip comb generation techniques, including the Kerr comb (2.2(a)), the electro-optic comb (2.2(b)), and the on-chip mode-locked laser (2.2(c)).

The miniaturization of optical comb sources has allowed for the identification of many new applications, beyond fundamental metrology, such as ultra-low-noise microwave signal generation [33, 34], optical communication [35], LIDAR [36], astronomical spectrograph calibration [37], and on-chip spectroscopy [38]. In particular the concept of dual-comb spectroscopy has received substantial interest, as it allows for a highly multiplexed interrogation of broadband absorption spectra using a single photodetector, enabling accurate characterization of rotational-vibrational transitions of numerous gasses, liquids and solids [38–45]. With this spectroscopic tool, one of the combs is sent through the sample under study, while another comb with a slightly different repetition rate acts as a 'local oscillator', as depicted in Fig. 2.3. By interfering the two combs on a photodetector, a frequency comb in the radiofrequency (RF) domain is generated, composed of distinguishable beats between pairs of optical comb lines. The sample's spectral information is hence readily available in the RF domain and accessible for electronic processing. As all spectral components are simultaneously measured, systematic errors such as temporal variations in the sample are effectively equalized. Moreover, the frequency combs can be calibrated with an atomic clock, providing unrivalled precision. A key requirement for this spectroscopic technique is the ability to generate a dense low-noise optical comb on-chip. As the resolution of the spectral measurement is directly related to the spacing between adjacent comb lines, a denser comb allows for the identification of otherwise undetectable features in the sample's spectral response [46].

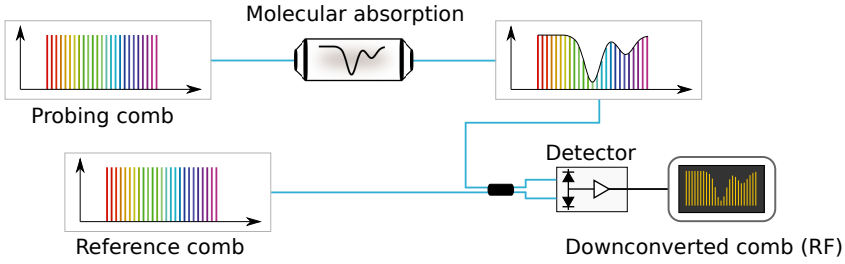

Figure 2.3: Simplified schematic of a setup for dual-comb spectroscopy.

Although the aforementioned integrated nonlinear comb generation techniques such as Kerr combs, quadratic combs and electro-optic combs have shown impressive results, their integration challenges (optical pump source is required), low conversion efficiency (particularly for the well-known bright dissipative Kerr soliton (DKS) combs [47]) and most importantly, their large comb line spacing ($>$ 10 GHz), inhibit their use in certain applications. In particular molecular dual-

comb spectroscopy in the gas-phase has proven difficult because gasses typically have narrow absorption features with a full width at half maximum (FWHM) on the order of a few GHz. Optical combs with a narrow line spacing are therefore critical to accurately sample these spectra without the need for interleaving multiple spectra measured at different times. Recent attempts were aimed at densifying the comb spectrum of Kerr- and electro-optic-comb generators [48, 49]. However, their implementations are rather complex and their comb-line spacing exceeded 2 GHz, even after densification.

Mode-locked laser diodes on the other hand can provide low repetition rates, high conversion efficiencies, turnkey operation and are electrically powered. Therefore, this class of comb generators nicely complements the application scope of other comb generation techniques and is well fit for the demands of on-chip gas-phase dual-comb spectroscopy.

2.3 Low repetition rate III-V-on-silicon-nitride mode-locked laser

Semiconductor mode-locked lasers can be fabricated on a chip using the same manufacturing techniques as used for continuous-wave laser diodes. The primary difference is the addition of a Saturable Absorber (SA) which favors the formation of pulses over continuous wave lasing. The SA is typically realized by electrically isolating a part of the gain waveguide and reverse biasing it [32]. Furthermore, numerous material platforms have been used for developing integrated mode-locked laser diodes, ranging from InP/InGaAsP or InP/InAlGaAs quantum wells to InAs/InP, InAs/GaAs and InP/InAlGaAs quantum dots [13, 50–55]. However, as the noise performance and comb line spacing are proportional to the cavity length, there has been a large incentive to extend the size of the laser cavity to broaden their application scope. This has lead to the development of extended-cavity InP lasers [56], and more recently, heterogeneous III/V-on-silicon lasers [44, 53, 55] with a long passive waveguide cavity. To push performance further, the silicon nitride platform has been widely recognized as a promising passive photonic platform for integrated laser sources [57, 58]. While typical silicon waveguides exhibit losses around 0.7 dB/cm, silicon nitride waveguides can routinely achieve ultra-low losses close to 1 dB/m [59]. Moreover, owing to the smaller bandgap, silicon waveguides suffer from nonlinear two-photon and free-carrier absorption, fundamentally limiting the attainable cavity size and lasing power. Switching from a III/V-on-silicon to a III/V-on-silicon-nitride platform can therefore eliminate these pitfalls and enable a new generation of improved on-chip mode-locked lasers [1, 60].

In the remainder of this chapter, we provide a detailed description of the layout,

fabrication and characterization of the first heterogeneously integrated III-V-on-silicon-nitride mode-locked laser [1, 2]. This MLL features a low repetition rate of 755 MHz and record noise performance, making it well suited for high-resolution on-chip dual-comb spectroscopy applications. The author took the lead in the fabrication of the devices, while the device characterization was led by Prof. Dr. Kasper Van Gasse. The semiconductor optical amplifiers used for micro-transfer printing were fabricated by Dr. Bahawal Haq.

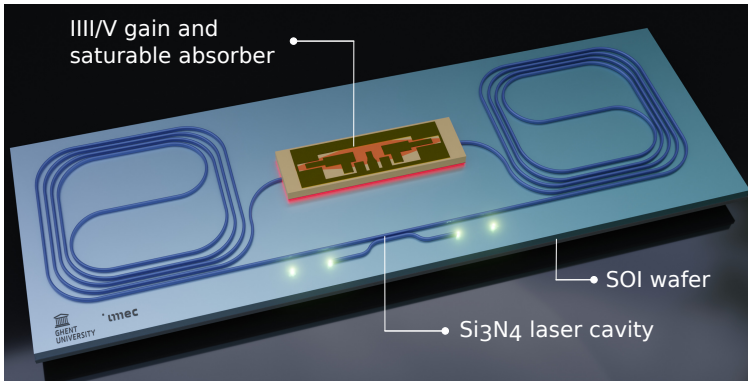

Figure 2.4: Rendering of the extended ring cavity MLL with two 10 cm long silicon nitride spirals and InP/InAlGaAs-based amplifiers with saturable absorber.

2.4 Design and fabrication

The laser is designed based on a ring-type extended cavity topology where a waveguide-based directional coupler is used to couple light out of the laser cavity [13]. This is a colliding-pulse mode-locked laser topology where two counter propagating pulses collide in the saturable absorber [56, 61]. A rendering of the ring-cavity MLL is shown in Figure 2.4. Compared to other semiconductor MLL topologies such as Fabry-Pérot-cavity MLLs, the ring-cavity MLL has the advantage that no gratings are needed, avoiding any unwanted spectral shaping. This comes at the expense of a larger surface area that is required compared to a Fabry-Pérot-cavity MLL. Moreover, Fabry-Pérot-cavities with e.g. Distributed Bragg Reflector (DBR) mirrors are typically preferred when some tunability is desired [62].

It has been shown theoretically [63] and experimentally [64] that compared to colliding-pulse topologies, an anti-colliding mode-locked laser design, where the SA is placed next to the low-reflectivity output coupler of a Fabry-Pérot cavity, can lead to an increase in output power, a reduction in amplitude and timing jitter, a reduction of pulse duration, and an enlargement of the range of currents where stable passive mode-locking can be achieved. However, such an anti-colliding

design is more complicated to fabricate on a Si_3N_4 platform compared to a ring-cavity geometry because the distance between the SA and the output mirror needs to be sufficiently small. This ensures that the optical pulse can interact with itself within the SA. It was shown in [65] that when the distance between the SA and output mirror increases, the pulse energy decreases and the stability of the pulse train degrades. Typically, stable passive mode-locking can be achieved when the distance between the SA and the output mirror does not exceed the width of the pulse and is less than 4 times the optical path length of the SA [62]. To meet these requirements, one possible approach to build an anti-colliding MLL on a Si_3N_4 platform could be to use a broadband multimode interference reflector in a Si layer as an output mirror, right next to the III-V SA [66].

The extended ring-cavity MLL is realized using two 10 cm long and 2 μm wide waveguide spirals that are patterned with deep ultraviolet (DUV) lithography in a Si_3N_4 layer. The loss of the spirals is estimated to be 0.05 dB/cm at a wavelength of 1550 nm. The 330 nm thick nitride layer is deposited by means of low-pressure chemical vapor deposition (LPCVD) on top of a Silicon-on-Insulator (SOI) wafer, which consists of a 400 nm thick silicon layer on top of a 3 μm thermally grown silicon oxide (TOX) layer [67]. A Chemical-Mechanical Polishing (CMP) step was employed to planarize the SOI surface prior to the silicon nitride deposition. LPCVD-based Si_3N_4 can provide superior thickness uniformity and lower optical losses compared to a PECVD-based deposition [57]. A drawback is that a higher deposition temperature is needed as the breakdown of precursor gases into radicals for film growth is a purely thermal process [68]. Moreover, LPCVD-based Si_3N_4 can suffer from high internal stress, complicating the growth of thick Si_3N_4 films which may be required to obtain anomalously dispersive waveguides. Fortunately, several remedies have been demonstrated to overcome crack formation, for example by using crack barriers and thermal cycling [69]. Here, the silicon nitride thickness is only 330 nm, and the waveguides exhibit -444 ps/nm/km normal dispersion.

Using a silicon-nitride-on-silicon-on-insulator platform has some advantages compared to the hydrogenated-amorphous-silicon-on-silicon-nitride platform [70]. The first advantage are the reduced waveguide losses: typically 20 dB/cm versus 0.7 dB/cm for hydrogenated amorphous silicon (a-Si:H) waveguides and crystalline silicon waveguides respectively. Furthermore, it was observed that the properties of deposited a-Si:H layer tend to exhibit some variability, inhibiting precise reproducibility. A more detailed comparison of different heterogeneous III-V-Si_3N_4 platforms is provided in Chapter 4.

A two-stage taper is employed to couple the light from the Si_3N_4 waveguide to the III-V amplifier waveguide [70, 71]. The light is first coupled from the nitride layer to the 400 nm thick silicon layer underneath and subsequently to the III-V layer, allowing for a better match in refractive index and consequently a higher

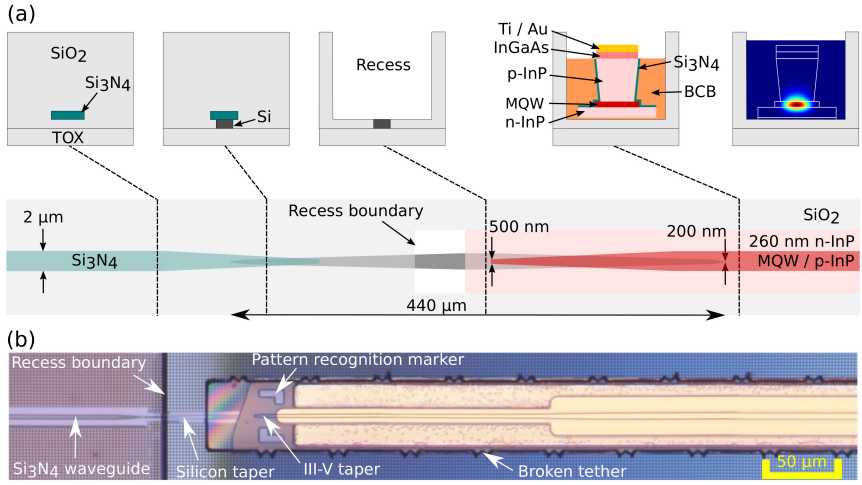

Figure 2.5: Silicon nitride to InP/InAlGaAs waveguide taper. (a) Schematic of the two-stage taper from the Si_3N_4 to the InP/InAlGaAs amplifier through an intermediate silicon coupling layer. A cross-section is visualized for different stages of the taper and the mode profile is visualized in the III-V SOA. (b) An optical microscope image of the micro-transfer printed amplifier coupon on top of the taper structure.

coupling efficiency. A schematic of the two-stage taper is depicted in Fig. 2.5(a) and an optical microscope image is shown in Fig. 2.5(b). To enable the heterogeneous integration of a III-V semiconductor optical amplifier (SOA) and coupling to the silicon layer, a recess of 1450 µm × 300 µm is locally etched in the top oxide cladding using dry etching techniques, resulting in a local exposure of the silicon waveguides. The Si_3N_4 waveguide is tapered over a length of 155 µm and is terminated at a distance of 10 µm from the recess boundary. The silicon waveguide has a total length of 440 µm at each side of the recess, and consists of a 160 µm and a 180 µm taper, respectively at the Si_3N_4 and the III-V side. In between the two silicon tapers is a 2 µm wide silicon waveguide with a length of 100 µm. The recess in the top cladding starts and ends at a distance of 110 µm from the Si taper tips. This ensures the mode is well confined to the silicon waveguide at the recess interfaces, minimizing parasitic reflections. The reflection induced by the discontinuity of the SiO_2 cladding is investigated using a 3D finite-difference time-domain (FDTD) simulation. Fig. 2.6(a) shows the reflection coefficient $|S_{11}|^2$ as a function of the silicon waveguide width. A low reflection around -60 dB is achieved when the waveguide width exceeds 500 nm. The Si waveguide width which was used in the presented MLL is highlighted with a black star in Fig. 2.6(a). For completeness, the reflection for a silicon nitride waveguide of the same dimensions is included in the figure as well, demonstrating that the reflection is more than two orders of

magnitude higher due to a reduced mode confinement.

The III-V SOA layer stack consists of a 200 nm n-doped InP cathode on top of a 60 nm intrinsic InP layer, six InAlGaAs quantum wells and barriers, a 25 nm etch stop InGaAsP layer underneath a 1.5 μm p-doped InP cladding and a 200 nm highly p-doped InGaAs contact layer. The quantum wells and barriers are surrounded by a pair of 75 nm thick InAlGaAs separate confinement heterostructure (SCH) layers and a pair of 40 nm thick InAlGaAs transition layers. More details on the III-V SOA can be found in Ref. [72], where an identical layer stack was employed. The multiple-quantum-well (MQW) layers and p-InP are tapered to a tip width of 500 nm at a distance of 51 μm from the recess interfaces to couple the light from the silicon to the III-V and vice versa. The III-V tapers are based on the alignment tolerant design, proposed in Ref. [72]. Fig. 2.6(b) depicts the simulated optical transmission of the fundamental TE mode from the Si waveguide to the III-V waveguide for different lateral alignment errors of the III-V amplifier. The coupling efficiency is nearly 100 % for alignment errors up to 750 nm, and still exceeds 70 % for an alignment error of 1 μm. Only for alignment errors beyond 1 μm, the coupling efficiency rapidly drops.

For the heterogeneous integration of the III-V amplifier in the recess on the Si_3N_4 target chip, the micro-transfer printing technique is used. Unlike wafer bonding techniques, this approach allows for the integration of III/V devices in a cavity. This first demonstration of micro-transfer printing in a recess is therefore an important technical milestone to demonstrate the compatibility with ultra-low-loss top-cladded waveguide platforms.

The micro-transfer printing process starts by the definition of the III-V SOA's, which are here denoted as "coupons", on a III-V source substrate. The III-V processing is illustrated in Figure 2.7(a)-(d). Next, the active devices are transferred to a target sample, which in this case is the Si_3N_4 passive cavity chip (Figures 2.7(e)-(i)). Finally, the active devices are post-processed to isolate the saturable absorber, open the N- and P-contacts and add electrical contacts (Figures 2.7(j)-(l)).

The III-V layer stack is epitaxially grown on 50 nm InGaAs on top of a 500 nm thick AlInAs release layer, which can be selectively etched with respect to the InP substrate. The layer stack is depicted in Fig. 2.7(a). In a first step, the III-V SOA mesa and active regions are patterned using contact lithography and dry and wet etching processes. Next, PECVD Si_3N_4 is deposited to cover the sidewalls of the MQW and p-InP. A lift-off step is used to deposit Ni/Ge/Au on the n-InP cathode. The wafer is subsequently planarized with divinylsiloxane-bis-benzocyclobutene (DVS-BCB or BCB) and the InGaAs contact layer is opened to deposit Ti/Au contacts on the anode. A dry etching step is employed to pattern the DVS-BCB and n-InP, hereby exposing the release layer. Next, the release layer is patterned and openings are created down to the InP substrate by means of dry etching (Fig. 2.7(b)). Thereafter, a photoresist (TI 35E) encapsulation layer is deposited on top

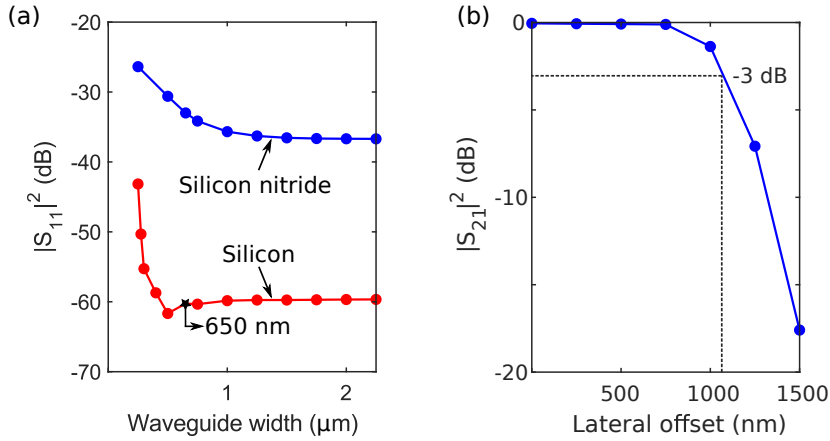

Figure 2.6: (a) Reflection induced by the SiO_2 recess boundary for a Si waveguide and a Si_3N_4 waveguide, simulated using Lumerical's 3D FDTD solver. The used Si waveguide width of 650 nm is highlighted with a star. (b) Optical transmission from the silicon waveguide to the III-V waveguide as a function of the lateral alignment offset, simulated using Lumerical's EigenMode Expansion solver.

of the SOA coupon and afterwards patterned (Fig. 2.7(c)). This encapsulation resist is highly resilient to the release etchant and attaches the coupon to the III-V substrate through thin tethers. A $FeCl_3$:H_2O solution at 7°C is then used to selectively etch the AlInAs release layer (Fig. 2.7(d)). After the release etch, the coupons are solely supported by the encapsulation resist and are ready to be printed. The total coupon size after patterning is 1411 µm × 47.5 µm.

Next, the transfer printing target is prepared, which is the Si_3N_4 passive ring cavity. A thin adhesive layer of DVS-BCB (Cyclotene 3022-35 from Dow Chemicals), diluted with mesitylene to a 1:4 volumetric ratio, is spincoated at 3000 rpm for 40 s and baked at 150°C for 10 min, during which the mesitylene solvent evaporates (Fig. 2.7(g)). This adhesive layer is approximately 50 nm thin, and enhances the yield of the micro-transfer printing process. Moreover it effectively planarizes surface roughness in the recess.

The source with the SOA coupons and target sample are loaded into the X-Celeprint µTP-100 micro-transfer printing tool and are carefully aligned. The printing procedure is illustrated in Figures 2.7(h) and (i). A PDMS stamp with a length of 1400 µm and a width of 50 µm was used to pick a single coupon by laminating the stamp against the coupon and then rapidly moving upwards. During this movement, the adhesion between the coupon and stamp increases and the tethers break at predetermined locations. To print the coupon on the target sample, the coupon is laminated against the target and then retracts very slowly, leaving the coupon behind on the target. Some shear force can be applied to ease the printing

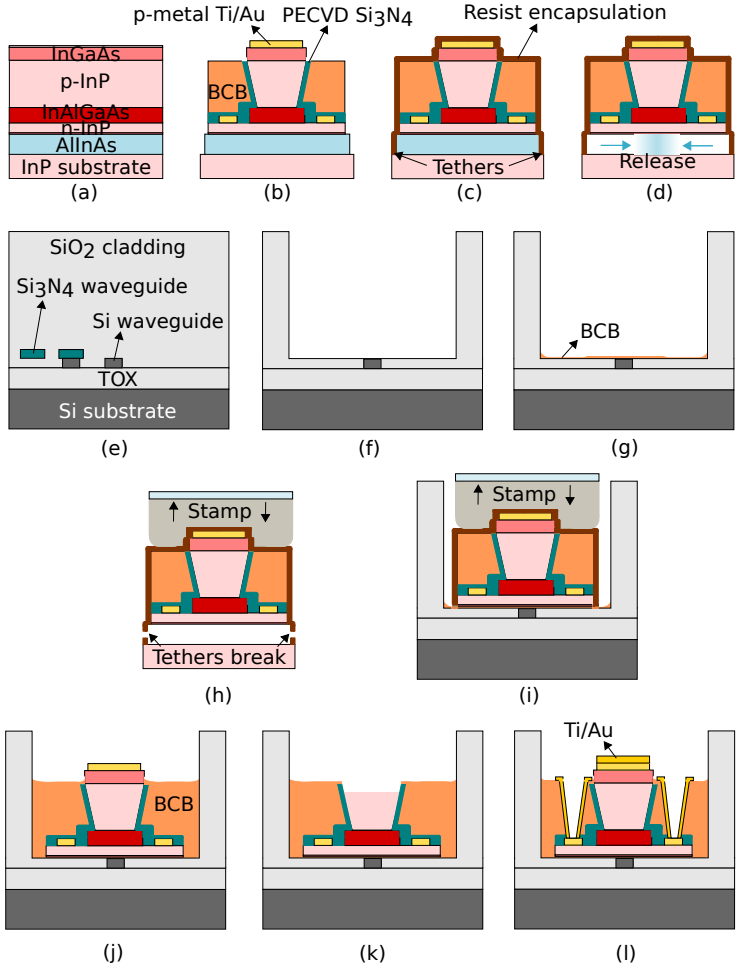

Figure 2.7: Illustration of the device process flow. (a)-(d) III-V SOA fabrica- tion, (e)-(g) preparation of the target, (h)-(i) micro-transfer printing, (j)-(l) post-processing. (a) III-V layer stack, (b) III-V SOA definition on source substrate, (c) coupon encapsulation with photoresist, (d) release layer etch, (e) target layer stack, (f) recess etch in SiO_2 top cladding, (g) BCB adhesive layer deposition, (h) pick-up coupon from source, (i) print coupon on target, (j) encapsulation removal and BCB cladding, (k) SA isolation, (l) via opening and final metallization.

process. To warrant efficient coupling between the silicon taper on the target sample and the III-V SOA, accurate alignment is indispensable. Pattern recognition software has been developed to auto-align a coupon to a desired location on the target sample. For printing single coupons, an alignment accuracy of 1 μm (3σ) is achieved [70]. However, for this particular device, the alignment for micro-transfer

printing was performed manually and no image recognition was utilized.

After transfer printing, the encapsulation is removed with an oxygen plasma and the adhesive DVS-BCB layer is cured at 180°C. Thereafter, a DVS-BCB cladding (Cyclotene 3022-57) is spincoated for 40 s at 2000 rpm and cured at 280°C, yielding a film thickness of approximately 8 µm. The DVS-BCB is subsequently etched back by means of RIE dry etching using O_2 and SF_6 to expose the top of the mesa. As the printed coupon is a conventional SOA, a saturable absorber still needs to be defined to enable mode-locking. For this purpose, two isolation trenches are defined with a width of 30 µm and separated by 34 µm. The Au and Ti metal of the anode are locally removed by means of a KI/I_2 (20 s) and a 10 s 1 % buffered hydrofluoric acid (buffered HF) wet etch, respectively. Afterwards, an inductively coupled plasma (ICP) etch at 60°C with CH_4 and H_2 gasses is used to locally remove the InGaAs. A photoresist mask with 45° inclined trenches was used for the ICP etch to suppress parasitic reflections from the discontinuity of the layer stack. Next, vias are etched to access the n-InP cathode using a thick AZ10XT photoresist. By reflowing a thick resist (1 min bake at 120° after photoresist development), vias with a slightly inclined slope are achieved, ensuring better metal coverage. Finally, 1 µm Au with a 40 nm Ti adhesion layer is deposited for electrical contacting. An optical microscope image of the post-processed III-V coupon is shown in Figure 2.8 and the vias and probing pads are indicated. The SA is approximately 34 µm long and isolated by two isolation trenches of approximately 30 µm each. The amplifiers are 600 µm long at both sides. The footprint of the realized device is 4.7 mm^2. A microscope image of the entire mode-locked laser cavity is shown in 2.9.

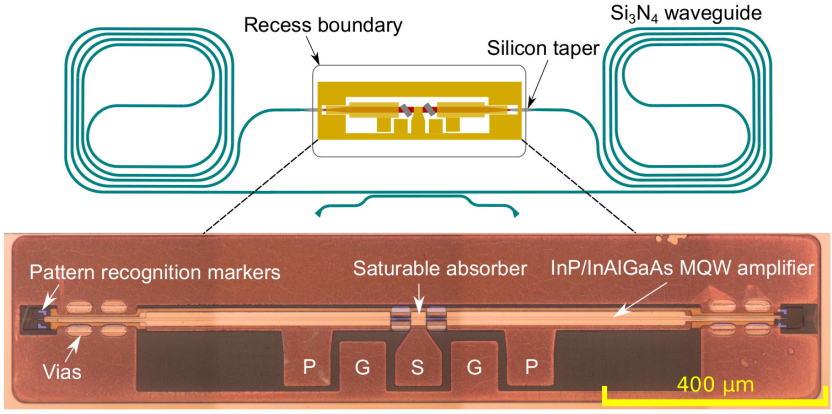

Figure 2.8: Optical microscope image of the post-processed coupon with a saturable absorber and 600 µm long III-V amplifiers at each side. P-G-S-G-P denotes the power-signal-ground-signal-power probing pads for biasing.

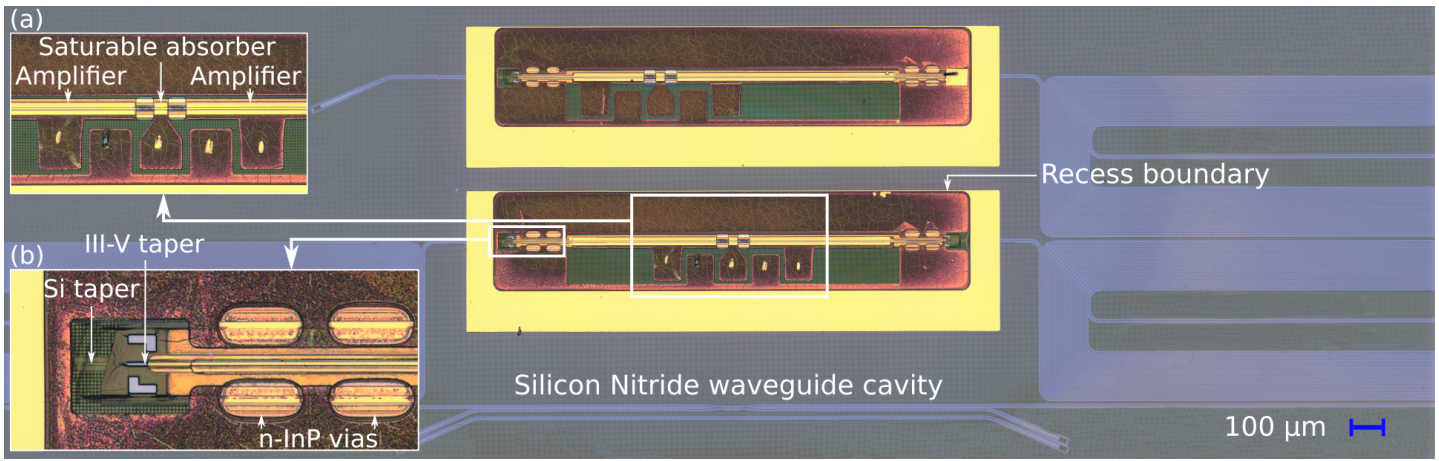

Figure 2.9: Microscope image of the III-V-semiconductor-on-Si_3N_4 mode-locked laser chip, consisting of two 10 cm Si_3N_4 spirals and InP/InAlGaAs amplifiers and saturable absorber, as depicted in inset (a). Light couples from the Si_3N_4 waveguide to the InP waveguide through an intermediate silicon waveguide, depicted in inset (b).

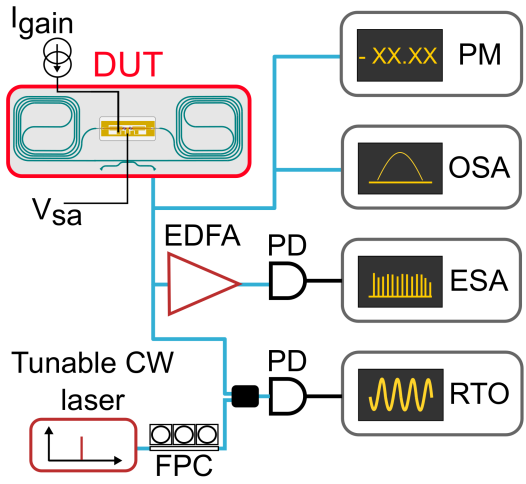

Figure 2.10: Measurement setup. DTU: Device under Test; EDFA: Erbium Doped Fiber Amplifier; FPC: Fiber Polarization Controller; PD: Photodetector; CW: Continuous Wave laser; OSA: Optical Spectrum Analyzer; PM: Power Meter; ESA: Electrical Spectrum Analyzer; RTO: Real-Time Oscilloscope.

2.5 Characterization

To characterize the MLL, the chip containing the MLL was placed on a temperature-controlled chuck, consisting of an aluminium block on top of a Peltier element, which was controlled using a Thorlabs TH10K thermistor and a TED200C temperature controller. This setup allows to keep the device substrate at a temperature of $15\,^{\circ}\mathrm{C}$. The laser was electrically contacted using a custom-designed RF-probe and two Keithley 2400 current sources. The optical output was collected using a chip-to-fiber grating coupler and a cleaved SMF-28 fiber. The Si_3N_4 grating couplers exhibit a coupling loss of approximately 9 dB per coupler at 1580 nm. A schematic overview of the measurement set-up is shown in Figure 2.10.

As shown in Fig. 2.9, the MLL has a symmetric ring-cavity design resulting in two outputs. All presented measurement results were obtained from the same output. Furthermore, the measurement results were checked with the other output and were found to show no discernible difference, confirming stable operation of the symmetric ring-cavity MLL. In Figure 2.11(a) a 2-dimensional map is shown of the optical output power of the MLL, as a function of the SA bias voltage and SOA injection current. To determine which combinations of SA bias and SOA current

lead to mode-locking, the electrical signal at the repetition frequency was analyzed for a wide range of settings. This was achieved by sending the optical pulse train to a photo-receiver and analyzing the output signal with an electrical spectrum analyzer (ESA) in a band of 200 MHz centered around the designed repetition frequency of 750 MHz. In Figure 2.11(b) a map of the power of the repetition frequency signal is shown for different SA bias and SOA current settings. From this map, one can deduce that mode-locking occurs for a wide range of settings when the SOA current exceeds 70 mA and the SA bias is more negative than -2.0 V. For an SOA current of 75 mA (corresponding with a current density of approximately 2.3 kA/cm^2) and a bias of -2.9 V applied to the SA, optimal low-noise operation was identified. At this bias point, the SA current is approximately -0.50 mA and the total consumed electrical power is approximately 143 mW. For these settings both the optical linewidth of the comb lines and the RF linewidth of the repetition rate were minimized.

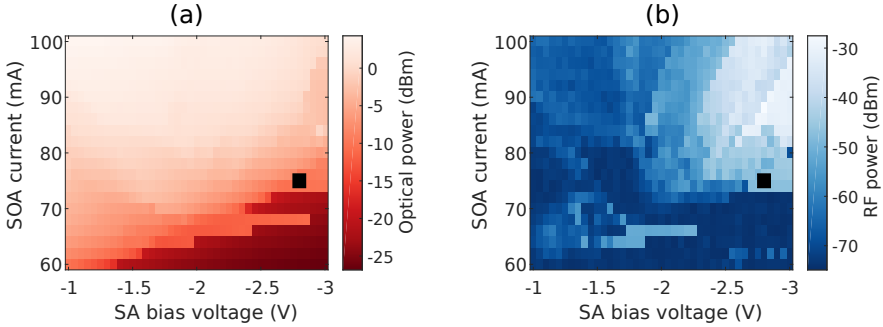

Figure 2.11: Map of the optical output power (b) and RF power (c) as a function of SA reverse bias voltage and SOA injection current. The operating point used to obtain the measurement results is indicated with a black square.

For optimal low-noise operation the output power in the silicon-nitride waveguide is approximately 125 µW for a single optical output. This optical power is sufficient if the laser is to be used, for example, in an on-chip dual-comb spectrometer. It has been demonstrated that gas-phase molecular dual-comb spectroscopy can be performed with an on-chip mode-locked laser with 10 µW of optical output power [46]. If for other applications higher optical output power is desired, either the amplifier inside the laser cavity can be redesigned to exhibit a lower mode confinement in the quantum wells, or an on-chip amplifier can be integrated at the output of the MLL. For example, integrated InP/InGaAsP-on-silicon optical amplifiers with an on-chip optical-output power exceeding 50 mW have been demonstrated [73, 74]. Furthermore, passively mode-locked SCOWLs (slab-coupled optical waveguide lasers) have been demonstrated with pulse energies beyond 50 pJ [75]. Such high-power SCOW amplifiers could in principle also be integrated

through micro-transfer printing. Moreover, connecting a heatsink to the amplifier or utilizing thermal shunts could improve the thermal impedance, enabling higher injection currents and enhanced gain. Finally, the n-contact layer area can be enlarged to serve as a heat spreader, an approach previously demonstrated with die-to-wafer bonded devices [44].

2.5.1 Optical pulse train

Figure 2.12(a) shows the pulse train of the MLL recorded using the aforementioned Discovery (DSC-R409) photo-receiver and a Teledyne Lecroy real-time oscilloscope (RTO). A pulse train without satellite pulses was found, confirming stable mode-locked operation. The ripple in the tail of the pulses is due to the overshoot of the photo-receiver and is an artefact not related to the optical pulse. As the analog bandwidth of both the photo-receiver and the RTO are insufficient to estimate the pulse duration, an intensity auto-correlation measurement was performed using an APE pulseCheck intensity autocorrelator. The resulting auto-correlation trace together with a sech^2 fit and the calculated deconvoluted pulse width, are shown in Figure 2.12(b). For sech^2-shaped pulses, the pulse duration is approximately 0.65 times the width of the autocorrelation signal [76]. Using this relation, the calculated deconvoluted pulse has a full width at half maximum (FWHM) of approximately 7.5 ps, indicating that the generated pulses are not transform-limited. As the transform-limited sech^2 pulse has a time-bandwidth product of 0.315, the estimated minimal pulse duration is 1.53 ps for the observed 3-dB optical bandwidth of 1.72 nm [5].

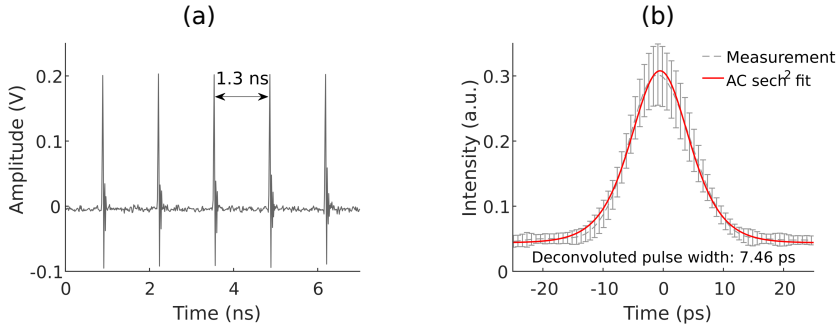

Figure 2.12: (a) Recorded pulse train by a real-time oscilloscope. (b) Measured autocorrelation (AC) trace with a sech^2 fit.

2.5.2 Electrical spectrum

Figure 2.13 shows a large bandwidth (10 MHz to 35 GHz) electrical spectrum of the MLL at the chosen bias point, recorded using an Agilent electrical spectrum an-

alyzer (N9010A) with a frequency operation range of 10 Hz to 44 GHz. The resulting spectrum shows a flat densely-spaced RF comb spectrum with a 755 MHz linespacing. Moreover, a high signal-to-noise ratio, exceeding 40 dB, of the repetition frequency signal and harmonics is obtained with a resolution bandwidth (RBW) of 300 kHz. This confirms stable mode-locking and strong phase coherence between the different optical modes [77]. The roll-off of the RF comb at higher frequencies is caused by the limited (30 GHz) analog bandwidth of the transimpedance amplifier (TIA) inside the photo-receiver. The measured repetition rate of 755.2 MHz is one of the lowest reported repetition rates to date for any integrated passively mode-locked laser and enables an unparalleled resolution for spectroscopy applications when compared to other on-chip approaches [30, 48, 49].

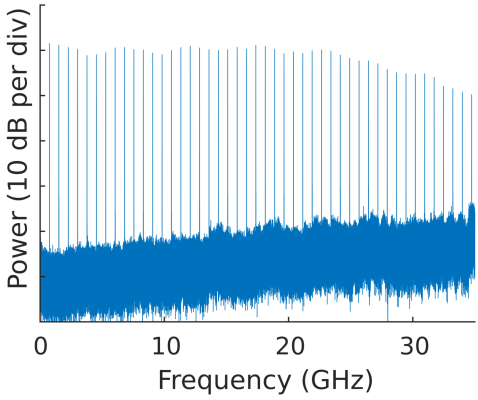

Figure 2.13: RF spectrum of the generated pulse train at the chosen operating point for a RBW of 300 kHz.

2.5.3 Optical linewidth

For most applications, the optical linewidth of the individual lasing modes is an important quality for an optical frequency comb. As the presented device primarily targets heterodyne dual-comb spectroscopy, a heterodyne measurement is most appropriate to characterize the optical linewidth. Therefore, the optical linewidth of the central lasing mode was measured by heterodyning the output of the MLL with a Santec-770 external-cavity tunable laser (60 kHz), using a fiber coupler, on a Discovery photo-receiver (DSC-R409). The optical linewidth of the other modes can then be extrapolated based on the knowledge of the optical linewidth of the central lasing mode and RF linewidth of the repetition frequency [78]. The beating signal of the MLL and the tunable laser was recorded using an ESA, set to a 400 MHz span with a 100 kHz RBW. The resulting spectrum is shown in

Figure 2.14. The heterodyne signal was fitted using a Voigt profile with a FWHM of 146 kHz, based on the datapoints above the -142 dBm/Hz noise floor of the ESA. This sub-200 kHz optical linewidth confirms the exceptional low-noise performance of the MLL. Furthermore, the optical linewidth of the MLL approaches that of a diode-laser-pumped Kerr-comb [79].

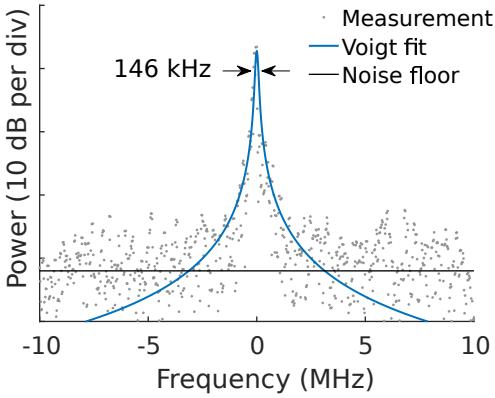

Figure 2.14: Optical linewidth measurement by heterodyning the MLL with a Santec-770 tunable laser (RBW is 100 kHz). The black horizontal line indicates the -142 dBm/Hz noise floor of the ESA.

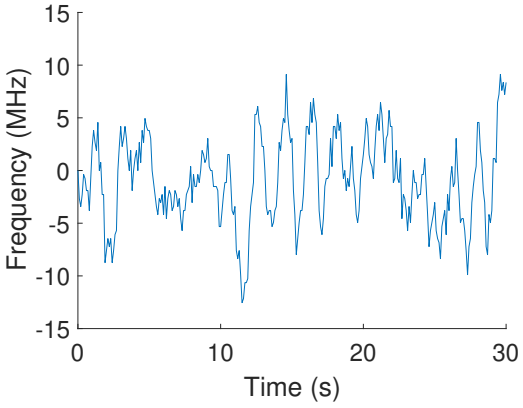

Figure 2.15: Drift of the frequency of the optical beatnote between the mode-locked laser and the Santec-770 tunable laser as a function of time.

Because of the relatively small thermo-optic coefficient of silicon nitride [80], the temperature sensitivity of the MLL is limited compared to devices with silicon waveguide cavities. Figure 2.15 shows the frequency drift of the beatnote between

the mode-locked laser output and the Santec-770 tunable laser over a time interval of 30 seconds. As presented in the plot, the central lasing mode drifts approximately 20 MHz during this time interval. As the MLL was not placed in a temperature controlled container, ambient conditions limited the temperature stability of the sample. During the measurement, the temperature stability of the sample was estimated to be approximately 20 mK. This corresponds to a frequency drift of the central lasing mode of approximately 1 MHz/mK, which is similar to the stability (1.3 MHz/mK) of a state-of-the-art narrow linewidth III-V-on-silicon-nitride CW laser [71]. This result demonstrates the excellent stability of the individual lasing modes, complementing the overall low-noise performance of the MLL.

2.5.4 Optical spectrum

To determine the spectral shape of the comb, the optical spectrum of the MLL was measured with an Anritsu MS9740A OSA with a resolution of 30 pm. The resulting spectrum is shown in Fig. 2.16. The spectral shape results from the complex interplay of the gain spectrum, absorption spectrum and the waveguide cavity properties. Asymmetric spectra are not unusual for semiconductor mode-locked lasers [81, 82]. For example, the work in [81] demonstrated that the mode-locked laser spectrum can be slightly skewed because the gain and absorption do not have flat spectra. The comb has a 10 dB bandwidth of 3.27 nm, corresponding with 519 narrowly spaced comb lines. The ability to generate several hundreds of lines with a sub-GHz linespacing and a flat-top shape is unrivaled by other comb generators such as QCLs, soliton microcombs or nanophotonic resonant EO-combs. Moreover, it allows for a flat spectrum without an intense central optical pump signal.

Several approaches can be investigated to further broaden the comb spectrum. Firstly, due to chromatic dispersion, the longitudinal modes of the mode-locked laser are typically not exactly equidistant, and the mode-locking mechanism enforces - to some extent - the laser to operate at frequencies which can slightly deviate from the natural resonant frequencies. Moreover, depending on the used material platform and envisioned pulse intensity, it might be necessary to take optical nonlinearities into account to determine the exact resonance frequencies of the resonator modes. Hence, proper engineering of the cavity, including dispersion engineering and spectral shaping of the gain, would allow for a broader comb spectrum. In [83], a tunable gain-flattening filter for integrated mode-locked laser diodes was presented. This filter was an asymmetrical Mach-Zehnder interferometer (MZI) and provides the inverse of the semiconductor spectral gain profile to achieve a broad flattened net gain, enhancing the performance of the MLL by enabling more longitudinal modes to lase simultaneously. A 10 dB comb bandwidth of 17 nm was reported. More recently, quantum-well mode-locked lasers

generating combs with a spectral bandwidth as wide as 40 nm have been demonstrated [51, 84]. Furthermore, several of these MLLs can be integrated and multiplexed on a single chip allowing to span any wavelength interval of interest. Such a superposition approach can consist of various sub-combs that are mutually incoherent as e.g. dual-comb spectroscopy can be carried out for each spectral region separately [42]. Finally, one could use on-chip amplification of the output pulse and on-chip nonlinear broadening to achieve a wider comb, enabling for example the measurement of the carrier-envelope offset frequency.

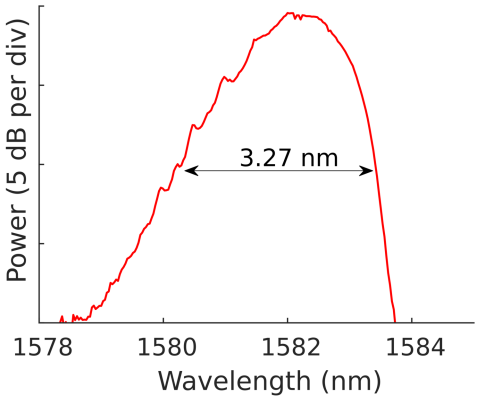

Figure 2.16: Optical spectrum, with a 10-dB span of 3.27 nm, measured with a 30 pm resolution. The individual comb lines cannot be distinguished due to their dense spacing.

2.5.5 Repetition frequency linewidth

The repetition frequency RF linewidth is a commonly used figure of merit for the noise properties of a semiconductor mode-locked laser [13, 55]. Furthermore, the RF linewidth is related to both the timing-jitter of the pulse train, the comb-line spacing noise and the optical linewidth of the comb lines [77, 78]. A 60 kHz wide ESA spectrum, centered at the repetition frequency, measured with a 100 Hz resolution bandwidth (RBW) and a 25 Hz frequency spacing is depicted in Figure 2.17. From the graph it is clear that the repetition rate has a high Signal-to-Noise Ratio (SNR) and a very small FWHM. Due to the narrow RF linewidth, a quantitative analysis can only reliably be achieved using a single-sideband phase-noise (SSB-PN) measurement, as discussed in section 2.5.6. From Figure 2.17, a qualitative -10 dB RF linewidth of 300 Hz can be deduced from the raw data. The narrow RF linewidth indicates that all optical modes are tightly phase-locked and that the optical linewidth of all comb lines is similar to the linewidth of the central lasing mode [78]. However, the RF linewidth deviates from the expected Lorentzian

profile and is therefore broadened by noise not related to laser dynamics. To gain additional insight in the noise sources affecting the laser, a single-sideband phase-noise (SSB-PN) measurement of the repetition frequency is needed.

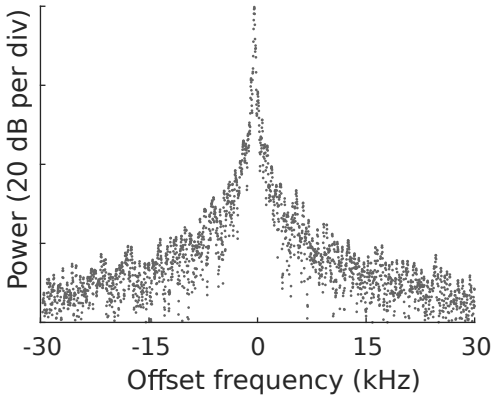

Figure 2.17: Zoom-in of the repetition frequency signal with a center frequency of 755.2 MHz (RBW is 100 Hz).

2.5.6 Single-sideband phase noise

As described by von der Linde [77], measuring the electrical spectrum of the photo-current pulse train, generated by the output of the mode-locked laser, allows to identify different perturbations of the optical pulse train. For example, if one assumes that the pulse train only exhibits timing-fluctuations and no amplitude fluctuations, then it can be shown that the phase noise of the harmonics signal is directly related to the phase noise of repetition frequency. Namely, the phase noise increases quadratically with the harmonic number. In the other case, if only amplitude noise is present in an otherwise ideal pulse train, all harmonics will show a noise pedestal identical to the repetition frequency. For passively mode-locked semiconductor lasers, the RF linewidth of the repetition frequency signal is in most cases dominated by the ASE-induced timing jitter of the pulse train [77, 85–89]. In this case the repetition frequency signal has a Lorentzian profile. However, if the Lorentzian linewidth becomes sufficiently narrow, the RF linewidth can be dominated by environmental and technical noise resulting in a non-Lorentzian profile [55]. To determine the RF linewidth achievable when eliminating technical and environmental noise, a SSB-PN measurement can be performed [86].

Figure 2.18(a) shows the SSB-PN of the repetition frequency signal (755 MHz) at sufficiently large offset frequencies from the carrier to avoid influence of technical noise. Together with the measured SSB-PN, a Lorentzian profile with a 1 Hz

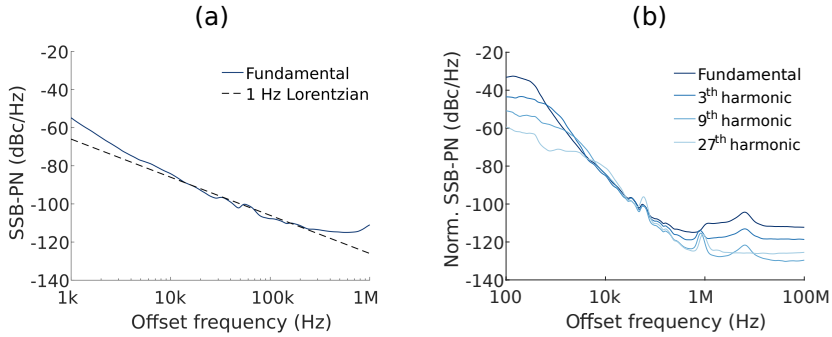

Figure 2.18: (a) Single-sideband phase noise (SSB-PN) of the repetition-frequency beat signal. A fundamental RF linewidth of 1 Hz FWHM is achieved. (b) Normalized SSB-PN of the repetition-frequency beat signal and its 3^{rd}, 9^{th} and 27^{th} harmonic.

FWHM is plotted. At offset frequencies exceeding 200 kHz the white noise floor of the photo-receiver is reached. Furthermore, between 10 kHz and 200 kHz the SSB-PN follows the Lorentzian profile, while at lower frequencies the influence of technical noise becomes apparent. This can be attributed to noise from the current sources and acoustic noise sources, which result from both air circulation as well as vibrations from the lab environment. As the presented device has not been packaged and is hence not shielded in any way from acoustic perturbations, the technical noise is significant. Moreover, the device was characterized using contact probes, cleaved fibers (not glued) for coupling, as well as long optical fiber cables, making the experimental setup susceptible to acoustic disturbances. For commercial deployment, the device could be packaged using a butterfly package, glued fibers and wire bonded contacts to limit the device's susceptibility to acoustic perturbations. However, environmental temperature changes could still affect the stability of the mode-locked laser. If a fully stabilized optical comb is envisioned, it will be necessary to include feedback circuitry with thermoelectric actuators, enabling continuous stabilization of the laser cavity [90, 91].

As the the direct spectrum SSB-PN measurement method was used to obtain the SSB-PN, one cannot distinguish between phase noise and amplitude noise. This method is applied assuming that phase noise dominates all amplitude noise in the measurement range of interest. To verify that this assumption is correct, the SSB-PN of the harmonics of the repetition frequency signal was measured. If the SSB-PN is phase-noise-dominated than it should scale quadratically with harmonic number [77]. In Fig. 2.18(b) the SSB-PN for the repetition frequency and its third, ninth and twenty-seventh harmonic divided by the square of the harmonic number is shown. One can see that in the offset frequency range between 10 kHz and 500 kHz the normalized SSB-PN spectra overlap. This confirms that in this frequency offset interval the SSB-PN is generated by timing fluctuation of the

pulse train. At frequencies exceeding 500 kHz the spectrum does not overlap as it is dominated by amplitude noise of the photo-receiver. Therefore, the SSB-PN at offset frequencies exceeding 500 kHz is not related to properties of the optical pulse train. Similarly, at offset frequencies smaller than 10 kHz the phase noise does not scale and is related to technical noise.

The resulting ASE-limited 1 Hz RF linewidth is the lowest reported so far for an on-chip passively mode-locked laser and is determined in the same way as was done for the previously reported narrowest linewidths [86]. This 1 Hz linewidth corresponds to a pulse-to-pulse root-mean-square timing jitter of 19 fs for a repetition period of 1.3 ns [87].

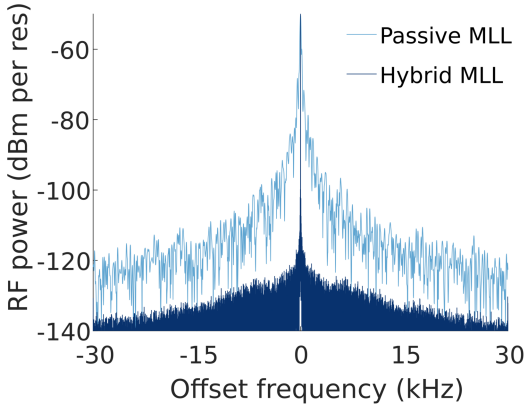

Figure 2.19: Impact of hybrid mode-locking on the RF linewidth of the fundamental 755.2 MHz tone.

2.5.7 Hybrid mode-locking

Although the laser shows excellent stability and noise performance, for a number of applications it is useful if the line-spacing can be locked to an external RF synthesizer, as this allows for relating the comb-line spacing to a frequency standard such as a hydrogen maser. To lock the comb-line spacing one can modulate the saturable absorber with the output of a reference frequency synthesizer, effectively gating the optical pulse train [87]. To experimentally lock the MLL to a synthesizer hybrid mode-locking is employed, where the SA is modulated with the low-power (10 μW) output of a low-noise synthesizer at the repetition frequency of the passively MLL. The spectrum centered on the repetition frequency for both passive and hybrid mode-locking is shown in Fig. 2.19. Under hybrid mode-locking, a clear single frequency signal with high SNR exactly matching the driving signal frequency is found. This confirms that the repetition rate is locked to the synthe-

sizer. For low RF powers a locking range of approximately 10 kHz is found.

The SSB-PN measured under both passive and hybrid mode-locking is shown in Figure 2.20(a). It is clear that for frequencies below 10 kHz the phase noise is strongly suppressed by locking the laser to the reference synthesizer. For higher frequencies the phase-noise remains unchanged and is dominated by the ASE-induced pulse train timing jitter. At the same time the noise floor at higher offset frequencies is still dominated by the amplitude noise coming from the TIA. These results show that the line-spacing can be locked to a synthesizer with a low-power RF signal of 10 µW (22 mV), hereby offering a straightforward solution to eliminate any residual line-spacing noise.

Figure 2.20(b) depicts the same spectra as 2.20(a) with the addition of the SSB-PN spectrum of the twenty-seventh harmonic (normalized by dividing by the square of the harmonic number) under hybrid mode-locked operation. As is clear from the plot, the SSB-PN spectrum of the repetition frequency and the normalized twenty-seventh harmonic overlap perfectly up to offset frequencies of 500 kHz. This indicates that the hybrid mode-locking operation strongly suppresses the low-frequency noise not only for the repetition frequency but for all harmonics.

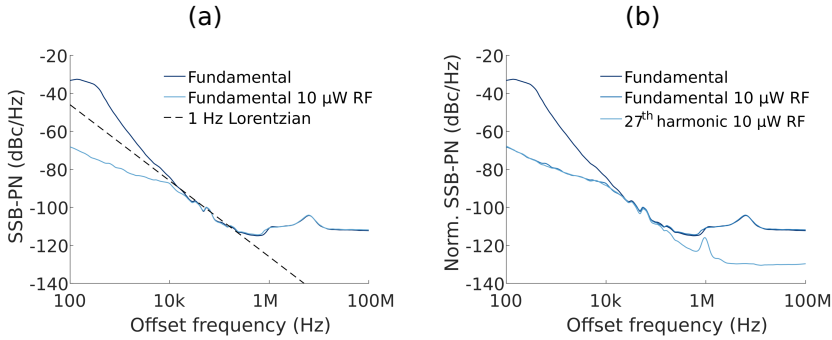

Figure 2.20: (a) SSB-PN for hybrid mode-locking. Hybrid operation suppresses the low frequency noise but leaves the Lorentzian noise undisturbed. (b) Normalized SSB-PN of the repetition frequency under both passive and hybrid mode-locking and its twenty-seventh harmonic under hybrid mode-locking.

2.6 Comparison with state-of-the-art

Table 2.1 compares our III-V-on-Si_3N_4 MLL with other state-of-the-art integrated passively mode-locked lasers in the literature. For each device, the platform used to realize the laser is mentioned as well as the repetition rate, pulse duration (τ_p), the RF linewidth (Δf_{RF}), the optical bandwidth ($\Delta\lambda$), the optical linewidth (Δf_{opt}) and the number of optical modes in the comb are specified.

Table 2.1: Comparison of the presented III-V-on-silicon-nitride MLL with state-of-the-art integrated passively mode-locked lasers. τ_p: pulse duration, Δf_{RF}: RF linewidth, $\Delta\lambda$: optical bandwidth, Δf_{opt}: optical linewidth.

Ref.; year	Type	Repetition rate	τ_p	Δf_{RF}	$\Delta\lambda$	Δf_{opt}	Nr. of comb lines
[92]; 2010	Monolithic InP	1 GHz	36 ps	500 kHz	1 nm	70 MHz	110
[50]; 2008	Monolithic InP	92 GHz	312 fs	20 kHz	11.62 nm	n/a	16
[51]; 2014	Monolithic InP	20 GHz	0.9 ps	1 MHz	11.5 nm	1 GHz	67
[56]; 2015	Monolithic InP	2.5 GHz	9.8 ps	18.9 kHz	3 nm	n/a	144
[52]; 2016	Monolithic InP	10 GHz	21.2 ps	15 kHz	8.7 nm	n/a	107
[93]; 2017	Monolithic InP	1 GHz	272 ps	398 kHz	n/a	n/a	n/a
[55]; 2018	III-V-on-Si	20 GHz	0.9 ps	1.1 kHz	3 nm	n/a	18
[94]; 2010	III-V-on-Si	0.93 GHz	200 ps	n/a	0.08 nm	<7 MHz	10
[44]; 2017	III-V-on-Si	1 GHz	7 ps	0.9 kHz	12 nm	400 kHz	1400
[95]; 2019	III-V-on-Si	9.4 GHz	3.2 ps	400 Hz	4.5 nm	n/a	84
[95]; 2019	III-V-on-Si	9.4 GHz	1.7 ps	4 kHz	2.6 nm	n/a	48
[53]; 2019	III-V-on-Si (epitaxial)	20 GHz	5 ps	1.8 kHz	8.6 nm	10.6 MHz	80
[96]; 2021	Hybrid RSOA/Si_3N_4	2 GHz	n/a	110 kHz	25 nm	n/a	1600
[97]; 2021	Hybrid RSOA/Si_3N_4	0.255 GHz	34 ps	40 Hz	0.11 nm	5.4 kHz	<60
[98]; 2021	Hybrid RSOA/Si_3N_4	2.18 GHz	6.31 ps	31 Hz	8.3 nm	N/A	465
[60]; 2021	III-V-on-Si_3N_4	3 GHz	8 ps	400 Hz	4 nm	1 MHz	154
This work; 2021	III-V-on-Si_3N_4	755 MHz	7.46 ps	1 Hz	3.27 nm	146 kHz	519

In [60], a heterogeneous III-V-on-Si_3N_4 MLL is reported where a high pulse energy of 2 pJ was achieved to target applications such as laser ranging and remote sensing. Furthermore, a 400 Hz fundamental RF linewidth, a repetition rate of 3 GHz and a comparable optical comb span of 4 nm are obtained, resulting in 154 comb lines compared to the 519 comb lines demonstrated in this chapter. Although the 0.16 pJ pulse energy of our III-V-on-Si_3N_4 MLL is considerably lower, it suffices to perform on-chip gas-phase molecular dual-comb spectroscopy [46]. While the micro-transfer printing technique was also used in [60], a different integration strategy was followed. An amorphous silicon layer was deposited and patterned on top of the silicon nitride waveguide to enable efficient evanescent coupling, in contrast to the silicon-nitride-on-silicon-on-insulator platform employed in this chapter.

Hybrid integrated mode-locked lasers with a reflective SOA (RSOA) and an external silicon nitride cavity are reported in [98], [97] and [96]. With a hybrid integration approach, a passive cavity chip and a gain chip are fabricated separately with waveguides extending to the edge of the chip. The waveguides are then butt-coupled to minimize the coupling loss between the two chips. Although this approach can offer improved thermal performance and superior flexibility with regard to the gain section design [98], the coupling section induces significant excess loss and the cost associated with assembly and packaging is higher. In [98], 6.3 ps pulses and a repetition rate of 2.18 GHz with 465 comb lines are obtained. Furthermore, the reported RF linewidth of the fundamental RF tone is 31 Hz, higher than the 1 Hz presented in this chapter. In [96], 1600 comb lines are generated within a 25 nm bandwidth. However, the noise performance is rather poor as the measured RF linewidth exceeds 100 kHz. The lowest repetition rate for an integrated mode-locked laser is reported in [97], where a repetition rate of 255 MHz is achieved. However, the optical bandwidth is only 0.11 nm resulting in few comb lines and a large pulse duration of 34 ps.

Furthermore, several III-V-on-Si mode-locked lasers have been reported in recent years [44, 53, 55, 94, 95]. In [44], a III-V-on-Si MLL is presented with a low repetition rate of 1 GHz. Here, an InP/InGaAsP gain material, epitaxially grown on its native substrate, was transferred on top of an SOI passive photonic circuit through a die-to-wafer bonding technique. In this way, a long low-loss silicon waveguide cavity could be combined with a high-quality quantum well gain waveguide to enable a narrow linewidth and a small comb line spacing. The device emits over a wide optical bandwidth of 12 nm, generating a dense optical comb consisting of over 1400 equally spaced optical lines with narrow linewidth of $<$400 kHz. Although the III-V-on-Si_3N_4 MLL presented in this chapter exhibits a narrower optical linewidth $<$200 kHz, the III-V-on-Si MLL achieves a broader optical comb spectrum and a higher pulse energy of 0.5 pJ compared to the 0.16 pJ pulses of the III-V-on-Si_3N_4 MLL. This discrepancy can be attributed

to several factors. Firstly, for the III-V-on-Si_3N_4 MLL in this chapter, the mode is strongly confined to the III-V waveguide as the silicon waveguide is not continued underneath the amplifier and saturable absorber. Hence, reducing the confinement in the quantum wells, as with the III-V-on-Si MLL, could improve the saturation power and increase the pulse energy and comb span. For example, the III-V-on-Si_3N_4 presented in [60] demonstrates 2 pJ pulses by limiting the confinement in the quantum wells and utilizing a Si_3N_4 waveguide cavity to eliminate the detrimental effects of two-photon- and free carrier absorption. Secondly, the thermal impedance with micro-transfer printing typically tends to be inferior compared to a bonding approach. The primary cause for this disparity can likely be attributed to the n-contact layer (as well as the metal on top) which typically spans a larger area in the case of a bonding approach. While the micro-transfer printed III-V coupon is about 1.3 mm long and 40 μm wide, a typical die used for die-to-wafer bonding has a size on the order of 1 cm^2. In the case of die-to-wafer bonding, the n-contact layer is usually etched in such a way that a large area remains, which can subsequently be covered with metal to serve as a heat spreader, hence improving the thermal performance of the device. In principle, a similar approach could be pursued with micro-transfer printing by using wider coupons, or by using a metal heatspreader or thermal shunts [99]. The thermal performance of micro-transfer printed SOA's, as well as the effect of thermal shunts, is discussed in more detail in Appendix A. Finally, although the exact mechanism behind the generation of the wide optical spectrum in [44] is not well understood, it is expected that dispersion engineering of the laser cavity and spectral shaping of the gain, would allow for a significantly broader optical comb spectrum, as was discussed in section 2.5.4.

Finally, numerous monolithic InP MLLs have been demonstrated in the past decade [50–52, 56, 92, 93]. Although pulse widths down to a few hundred femtoseconds have been demonstrated [50], the high waveguide losses of monolithic InP waveguides result in linewidths typically more than two orders of magnitude higher compared to the III-V-on-Si_3N_4 MLL presented in this chapter. Nevertheless, low repetition rates of 1 GHz were reported in [92] and [93], but the optical spectra were very narrow ($<$1 nm), resulting in a limited number of optical comb lines. Moreover, the MLL presented in [92] only displays mode-locking when an external RF source is applied and no passive mode-locking could be demonstrated.

To compare the noise performance of the presented III-V-on-Si_3N_4 on-chip mode-locked laser with low-noise solid-state and fiber mode-locked lasers, the timing jitter power spectral density (PSD) is calculated from the SSB-PN measurement results using the relation [100]:

$$S_x(f) = \left[\frac{1}{2\pi f_{rep}}\right]^2 \cdot 10^{\frac{S_\phi(f)}{10}}, \tag{2.1}$$

where S_x(f) is the timing jitter SD (s^2/Hz), S_ϕ(f) is the phase noise (dBc/Hz), and f_{rep} is the repetition frequency of the MLL. The on-chip mode-locked laser exhibits a timing jitter PSD of 111 fs^2/Hz at a 10 kHz offset frequency, as shown in Fig. 2.21(a). Low-noise passively mode-locked fiber lasers on the other hand exhibit timing jitter PSDs around 10^{-3} fs^2/Hz [8, 90, 91, 101–104]. Furthermore, the integrated timing jitter of the chip-scale mode-locked laser, obtained for a frequency range between 10 kHz and 1 MHz as indicated in Fig. 2.21(b), is 1 ps. As most state-of-the-art low-noise fiber and solid-sate mode-locked lasers routinely achieve an integrated timing jitter below 20 fs, fiber- and solid-state-based systems outperform our chip-scale mode-locked laser by 2 orders of magnitude or more [8, 90, 91, 101–104]. This performance gap can be attributed to several factors.

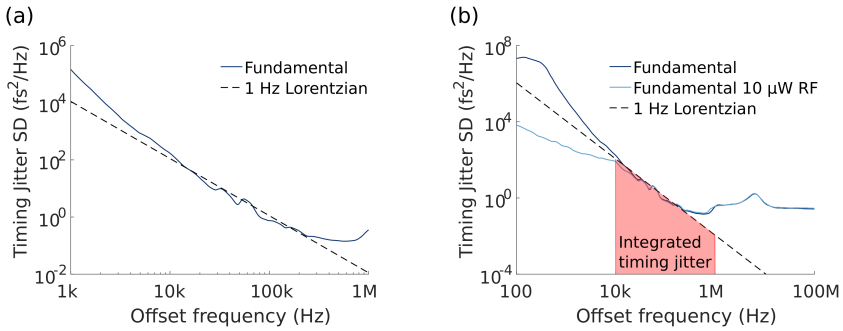

Figure 2.21: Timing jitter Spectral Density (SD). (a) Timing jitter spectral density of the repetition frequency beat signal. (b) Timing jitter spectral density for hybrid mode-locking between 100 Hz and 100 MHz. The interval used to calculate the integrated timing jitter is indicated.

First, fiber- and solid-state lasers often rely on nonlinear artificial saturable absorption. Such saturable absorbers are inherently less noisy compared to a semiconductor saturable absorber which exhibits carrier dynamics. Moreover for the on-chip III-V-on-silicon-nitride MLL the saturable absorber is incorporated in the same epilayer stack as the amplifier. By using a separate optimized epi stack for the saturable absorber (such as with saturable absorber mirrors (SESAM) which are used in some fiber mode-locked lasers [8]) a performance enhancement is likely possible. Alternatively, one could employ a chip-scale Kerr-based artificial saturable absorber similar to what has been demonstrated in [12]. However, to have sufficient modulation depth with an on-chip artificial saturable absorber, a material with a high nonlinear coefficient n_2 is preferred. Heterogeneously integrating a highly nonlinear optical material, for example GaP or AlGaAs, on a silicon nitride photonic chip could therefore be an interesting route to develop improved on-chip

mode-locked lasers [105–107].

Secondly, several experimental methods have been demonstrated to reduce the timing jitter of fiber lasers, for example by introducing an active intracavity phase modulator [108] or by utilizing an intracavity spectral filter [104, 109]. A similar technique could be employed for a chip-scale mode-locked laser, e.g. by introducing a high finesse filter in the silicon nitride laser cavity [110].

Thirdly, the noise performance can be improved by optimizing the semiconductor amplifier in order to acquire lower internal losses, reduced mode confinement and correspondingly, increased saturation energy [75, 111].

Fourthly, a further reduction of the cavity losses would allow to narrow the gap between ultra-low fiber losses and the current 5 dB/m losses of the silicon nitride waveguides. In recent years, silicon nitride waveguides with losses below 1 dB/m have been demonstrated [112].

Finally, the noise performance of mode-locked lasers is not solely determined by spontaneous emission, but also by environmental technical noise [113]. For this reason, low-noise fiber mode-locked lasers are carefully packaged and provided with built-in feedback loops and piezoelectric actuators to accurately control any cavity length fluctuations [90, 91]. The presented chip-scale mode-locked laser on the other hand has not been packaged and is hence not shielded from its environment.

2.7 Conclusion

In this chapter, a III-V-on-silicon-nitride passively mode-locked laser with a low repetition rate of 755 MHz was demonstrated. By using a long low-loss extended Si_3N_4 ring cavity, unparalleled noise performance is achieved with a narrow optical linewidth below 200 kHz and an ASE-limited RF linewidth of 1 Hz. At the time of writing, these record values indicate that this MLL is the lowest noise on-chip passively MLL presented in literature to date, and illustrates the superior noise performance a III-V-on-silicon-nitride-on-silicon-on-insulator platform can offer compared to conventional monolithic III-V, InP, and heterogeneous III-V-on-Si platforms. The device was fabricated by means of micro-transfer printing an InP/InAlGaAs-based multiple quantum-well coupon in a recess, enabling wafer scale manufacturing. State-of-the-art micro-transfer printers can support high throughput integration by utilizing array stamps, enabling multiple coupons to be picked up and printed simultaneously. Furthermore, two mode-locked laser devices were fabricated and both devices displayed similar performance, proving the reproducibility of our methodology.

Such an integrated and electrically pumped dense optical comb generator provides several advantages in terms of cost, device foot-print, robustness and power consumption, enabling its use in high-resolution spectroscopic applications. In the

future, other material platforms, such as GaSb, could be combined with the Si_3N_4 cavity to target the spectral region beyond 2 μm, uncovering the full capabilities of on-chip spectroscopic sensing. Furthermore, the presented work can be extended to target various other applications such as datacom, telecom, and low-noise microwave signal generation by changing the comb line spacing while at the same time keeping the excellent noise properties. This can for example be achieved by introducing a high-finesse resonator filter inside the laser cavity [114, 115] or by co-integrating a pulse interleaver [116].

References

[1] S. Cuyvers, B. Haq, C. Op de Beeck, S. Poelman, A. Hermans, Z. Wang, A. Gocalinska, E. Pelucchi, B. Corbett, G. Roelkens, K. Van Gasse, and B. Kuyken. *Low Noise Heterogeneous III-V-on-Silicon-Nitride Mode-Locked Comb Laser*. Laser & Photonics Reviews, 15(8):2000485, 2021.

[2] S. Cuyvers, B. Haq, G. Roelkens, K. Van Gasse, and B. Kuyken. *Mode-locked comb lasers for chip-scale spectroscopy*. Compound Semiconductor, 27(7):60–64, 2021.

[3] S. A. Diddams, K. Vahala, and T. Udem. *Optical frequency combs: Coherently uniting the electromagnetic spectrum*. Science, 369(6501), 2020.

[4] T. W. Hänsch. *Nobel Lecture: Passion for precision*. Rev. Mod. Phys., 78:1297–1309, Nov 2006.

[5] A. Weiner. *Principles of Mode-Locking*, chapter 2, pages 32–84. John Wiley & Sons, Ltd, 2009.

[6] S. Sartania, Z. Cheng, M. Lenzner, G. Tempea, C. Spielmann, F. Krausz, and K. Ferencz. *Generation of 0.1-TW 5-fs optical pulses at a 1-kHz repetition rate*. Opt. Lett., 22(20):1562–1564, Oct 1997.

[7] P. Del'Haye, O. Arcizet, M. L. Gorodetsky, R. Holzwarth, and T. J. Kippenberg. *Frequency comb assisted diode laser spectroscopy for measurement of microcavity dispersion*. Nat. Photonics, 3(9):529–533, Sep 2009.

[8] J. Kim and Y. Song. *Ultralow-noise mode-locked fiber lasers and frequency combs: principles, status, and applications*. Adv. Opt. Photon., 8(3):465–540, Sep 2016.

[9] T. Brabec, C. Spielmann, P. F. Curley, and F. Krausz. *Kerr lens mode locking*. Opt. Lett., 17(18):1292–1294, Sep 1992.

[10] V. Matsas, T. Newson, D. Richardson, and D. Payne. *Self starting passively mode-locked fibre ring soliton laser exploiting nonlinear polarisation rotation*. Electronics Letters, 28:1391–1393(2), July 1992.

[11] M. E. Fermann, F. Haberl, M. Hofer, and H. Hochreiter. *Nonlinear amplifying loop mirror*. Opt. Lett., 15(13):752–754, Jul 1990.

[12] K. Shtyrkova, P. T. Callahan, N. Li, E. S. Magden, A. Ruocco, D. Vermeulen, F. X. Kärtner, M. R. Watts, and E. P. Ippen. *Integrated CMOS-compatible Q-switched mode-locked lasers at 1900nm with an on-chip artificial saturable absorber*. Opt. Express, 27(3):3542–3556, Feb 2019.

[13] K. Van Gasse, S. Uvin, V. Moskalenko, S. Latkowski, G. Roelkens, E. Bente, and B. kuyken. *Recent Advances in the Photonic Integration of Mode-Locked Laser Diodes*. IEEE Photon. Technol., 31(23):1870–1873, 2019.

[14] J. B. Khurgin, Y. Dikmelik, A. Hugi, and J. Faist. *Coherent frequency combs produced by self frequency modulation in quantum cascade lasers*. Applied Physics Letters, 104(8):081118, 2014.

[15] L. Chang, S. Liu, and J. E. Bowers. *Integrated optical frequency comb technologies*. Nature Photonics, 16(2):95–108, Feb 2022.

[16] A. L. Gaeta, M. Lipson, and T. J. Kippenberg. *Photonic-chip-based frequency combs*. Nat. Photonics, 13(3):158–169, Mar 2019.

[17] L. Consolino, M. Nafa, F. Cappelli, K. Garrasi, F. P. Mezzapesa, L. Li, A. G. Davies, E. H. Linfield, M. S. Vitiello, P. De Natale, and S. Bartalini. *Fully phase-stabilized quantum cascade laser frequency comb*. Nat. Commun., 10(1):2938, Jul 2019.

[18] B. Meng, M. Singleton, M. Shahmohammadi, F. Kapsalidis, R. Wang, M. Beck, and J. Faist. *Mid-infrared frequency comb from a ring quantum cascade laser*. Optica, 7(2):162–167, Feb 2020.

[19] M. Piccardo, P. Chevalier, S. Anand, Y. Wang, D. Kazakov, E. A. Mejia, F. Xie, K. Lascola, A. Belyanin, and F. Capasso. *Widely tunable harmonic frequency comb in a quantum cascade laser*. Appl. Phys. Lett, 113(3):031104, 2018.

[20] Y. Yang, D. Burghoff, D. J. Hayton, J.-R. Gao, J. L. Reno, and Q. Hu. *Terahertz multiheterodyne spectroscopy using laser frequency combs*. Optica, 3(5):499–502, May 2016.

[21] M. Zhang, B. Buscaino, C. Wang, A. Shams-Ansari, C. Reimer, R. Zhu, J. M. Kahn, and M. Lončar. *Broadband electro-optic frequency comb generation in a lithium niobate microring resonator*. Nature, 568(7752):373–377, Apr 2019.

[22] M. Zhang, B. Buscaino, C. Wang, A. Shams-Ansari, C. Reimer, R. Zhu, J. M. Kahn, and M. Lončar. *Broadband electro-optic frequency comb generation in a lithium niobate microring resonator*. Nature, 568(7752):373–377, Apr 2019.

[23] P. Del'Haye, A. Schliesser, O. Arcizet, T. Wilken, R. Holzwarth, and T. J. Kippenberg. *Optical frequency comb generation from a monolithic microresonator*. Nature, 450(7173):1214–1217, Dec 2007.

[24] A. G. Griffith, R. K. Lau, J. Cardenas, Y. Okawachi, A. Mohanty, R. Fain, Y. H. D. Lee, M. Yu, C. T. Phare, C. B. Poitras, A. L. Gaeta, and M. Lipson. *Silicon-chip mid-infrared frequency comb generation*. Nat. Commun., 6(1):6299, Feb 2015.

[25] B. Stern, X. Ji, Y. Okawachi, A. L. Gaeta, and M. Lipson. *Battery-operated integrated frequency comb generator*. Nature, 562(7727):401–405, Oct 2018.

[26] H. Jung, C. Xiong, K. Y. Fong, X. Zhang, and H. X. Tang. *Optical frequency comb generation from aluminum nitride microring resonator*. Opt. Lett., 38(15):2810–2813, Aug 2013.

[27] B. J. M. Hausmann, I. Bulu, V. Venkataraman, P. Deotare, and M. Lončar. *Diamond nonlinear photonics*. Nat. Photonics, 8(5):369–374, May 2014.

[28] L. Razzari, D. Duchesne, M. Ferrera, R. Morandotti, S. Chu, B. E. Little, and D. J. Moss. *CMOS-compatible integrated optical hyper-parametric oscillator*. Nat. Photonics, 4(1):41–45, Jan 2010.

[29] L. Chang, W. Xie, H. Shu, Q.-F. Yang, B. Shen, A. Boes, J. D. Peters, W. Jin, C. Xiang, S. Liu, G. Moille, S.-P. Yu, X. Wang, K. Srinivasan, S. B. Papp, K. Vahala, and J. E. Bowers. *Ultra-efficient frequency comb generation in AlGaAs-on-insulator microresonators*. Nat. Commun., 11(1):1331, Mar 2020.

[30] M.-G. Suh and K. Vahala. *Gigahertz-repetition-rate soliton microcombs*. Optica, 5(1):65–66, 2018.

[31] A. W. Bruch, X. Liu, Z. Gong, J. B. Surya, M. Li, C.-L. Zou, and H. X. Tang. *Pockels soliton microcomb*. Nature Photonics, 15(1):21–27, Jan 2021.

[32] K. Van Gasse, S. Uvin, V. Moskalenko, S. Latkowski, G. Roelkens, E. Bente, and B. kuyken. *Recent Advances in the Photonic Integration of Mode-Locked Laser Diodes*. IEEE Photonics Technology Letters, 31(23):1870–1873, 2019.

[33] J. Liu, E. Lucas, A. S. Raja, J. He, J. Riemensberger, R. N. Wang, M. Karpov, H. Guo, R. Bouchand, and T. J. Kippenberg. *Photonic microwave generation in the X- and K-band using integrated soliton microcombs*. Nat. Photonics, 14(8):486–491, Aug 2020.

[34] X. Xie, R. Bouchand, D. Nicolodi, M. Giunta, W. Hänsel, M. Lezius, A. Joshi, S. Datta, C. Alexandre, M. Lours, P.-A. Tremblin, G. Santarelli, R. Holzwarth, and Y. Le Coq. *Photonic microwave signals with zeptosecond-level absolute timing noise*. Nature Photonics, 11(1):44–47, Jan 2017.

[35] P. Marin-Palomo, J. N. Kemal, M. Karpov, A. Kordts, J. Pfeifle, M. H. P. Pfeiffer, P. Trocha, S. Wolf, V. Brasch, M. H. Anderson, R. Rosenberger, K. Vijayan, W. Freude, T. J. Kippenberg, and C. Koos. *Microresonator-based solitons for massively parallel coherent optical communications*. Nature, 546(7657):274–279, Jun 2017.

[36] P. Trocha, M. Karpov, D. Ganin, M. H. P. Pfeiffer, A. Kordts, S. Wolf, J. Krockenberger, P. Marin-Palomo, C. Weimann, S. Randel, W. Freude, T. J. Kippenberg, and C. Koos. *Ultrafast optical ranging using microresonator soliton frequency combs*. Science, 359(6378):887–891, 2018.

[37] M.-G. Suh, X. Yi, Y.-H. Lai, S. Leifer, I. S. Grudinin, G. Vasisht, E. C. Martin, M. P. Fitzgerald, G. Doppmann, J. Wang, D. Mawet, S. B. Papp, S. A. Diddams, C. Beichman, and K. Vahala. *Searching for exoplanets using a microresonator astrocomb*. Nature Photonics, 13(1):25–30, Jan 2019.

[38] A. Dutt, C. Joshi, X. Ji, J. Cardenas, Y. Okawachi, K. Luke, A. L. Gaeta, and M. Lipson. *On-chip dual-comb source for spectroscopy*. Sci. Adv., 4(3), 2018.

[39] N. Picqué and T. W. Hänsch. *Frequency comb spectroscopy*. Nat. Photonics, 13(3):146–157, Mar 2019.

[40] I. Coddington, N. Newbury, and W. Swann. *Dual-comb spectroscopy*. Optica, 3(4):414–426, Apr 2016.

[41] M. A. Abbas, Q. Pan, J. Mandon, S. M. Cristescu, F. J. M. Harren, and A. Khodabakhsh. *Time-resolved mid-infrared dual-comb spectroscopy*. Sci. Rep., 9(1):17247, Nov 2019.

[42] A. Shams-Ansari, M. Yu, Z. Chen, C. Reimer, M. Zhang, N. Picqué, and M. Lončar. *An integrated lithium-niobate electro-optic platform for spectrally tailored dual-comb spectroscopy*. Preprint at `https://arxiv.org/abs/2003.04533`, 2020.

[43] G. Millot, S. Pitois, M. Yan, T. Hovhannisyan, A. Bendahmane, T. W. Hänsch, and N. Picqué. *Frequency-agile dual-comb spectroscopy*. Nat. Photonics, 10(1):27–30, Jan 2016.

[44] Z. Wang, K. Van Gasse, V. Moskalenko, S. Latkowski, E. Bente, B. Kuyken, and G. Roelkens. *A III-V-on-Si ultra-dense comb laser*. Light Sci. Appl., 6(5):e16260–e16260, May 2017.

[45] D. Grassani, E. Tagkoudi, H. Guo, C. Herkommer, F. Yang, T. J. Kippenberg, and C.-S. Brès. *Mid infrared gas spectroscopy using efficient*

fiber laser driven photonic chip-based supercontinuum. Nat. Commun., 10(1):1553, Apr 2019.

[46] K. Van Gasse, Z. Chen, E. Vicentini, J. Huh, S. Poelman, Z. Wang, G. Roelkens, T. W. Hänsch, B. Kuyken, and N. Picqué. *An on-chip III-V-semiconductor-on-silicon laser frequency comb for gas-phase molecular spectroscopy in real-time*. Preprint at `https://arxiv.org/abs/2006.15113`, 2020.

[47] J. Li, C. Bao, Q.-X. Ji, H. Wang, L. Wu, S. Leifer, C. Beichman, and K. Vahala. *Efficiency of pulse pumped soliton microcombs*. Optica, 9(2):231–239, Feb 2022.

[48] C. Bao, Z. Yuan, H. Wang, L. Wu, B. Shen, K. Sung, S. Leifer, Q. Lin, and K. Vahala. *Interleaved difference-frequency generation for microcomb spectral densification in the mid-infrared*. Optica, 7(4):309–315, Apr 2020.

[49] A. Shams-Ansari, C. Reimer, N. Sinclair, M. Zhang, N. Picqué, and M. Loncar. *Low-repetition-rate Integrated Electro-optic Frequency Comb Sources*. In Conference on Lasers and Electro-Optics (CLEO), San Jose, USA, 5 2020. CLEO.

[50] Z. Lu, J. Liu, S. Raymond, P. Poole, P. Barrios, and D. Poitras. *312-fs pulse generation from a passive C-band InAs/InP quantum dot mode-locked laser*. Opt. Express, 16(14):10835–10840, Jul 2008.

[51] V. Moskalenko, S. Latkowski, S. Tahvili, T. de Vries, M. Smit, and E. Bente. *Record bandwidth and sub-picosecond pulses from a monolithically integrated mode-locked quantum well ring laser*. Opt. Express, 22(23):28865–28874, Nov 2014.

[52] V. Corral, R. Guzmán, C. Gordón, X. J. M. Leijtens, and G. Carpintero. *Optical frequency comb generator based on a monolithically integrated passive mode-locked ring laser with a Mach–Zehnder interferometer*. Opt. Lett., 41(9):1937–1940, May 2016.

[53] S. Liu, X. Wu, D. Jung, J. C. Norman, M. J. Kennedy, H. K. Tsang, A. C. Gossard, and J. E. Bowers. *High-channel-count 20 GHz passively mode-locked quantum dot laser directly grown on Si with 4.1 Tbit/s transmission capacity*. Optica, 6(2):128–134, Feb 2019.

[54] M.-C. Lo, R. Guzmán, and G. Carpintero. *InP femtosecond mode-locked laser in a compound feedback cavity with a switchable repetition rate*. Opt. Lett., 43(3):507–510, Feb 2018.

[55] M. L. Davenport, S. Liu, and J. E. Bowers. *Integrated heterogeneous silicon/III-V mode-locked lasers*. Photon. Res., 6(5):468–478, May 2018.

[56] S. Latkowski, V. Moskalenko, S. Tahvili, L. Augustin, M. Smit, K. Williams, and E. Bente. *Monolithically integrated 2.5 GHz extended cavity mode-locked ring laser with intracavity phase modulators*. Opt. Lett., 40(1):77–80, Jan 2015.

[57] A. Rahim, E. Ryckeboer, A. Z. Subramanian, S. Clemmen, B. Kuyken, A. Dhakal, A. Raza, A. Hermans, M. Muneeb, S. Dhoore, Y. Li, U. Dave, P. Bienstman, N. Le Thomas, G. Roelkens, D. Van Thourhout, P. Helin, S. Severi, X. Rottenberg, and R. Baets. *Expanding the Silicon Photonics Portfolio With Silicon Nitride Photonic Integrated Circuits*. Journal of Lightwave Technology, 35(4):639–649, 2017.

[58] C. Op de Beeck, B. Haq, L. Elsinger, A. Gocalinska, E. Pelucchi, B. Corbett, G. Roelkens, and B. Kuyken. *Heterogeneous III-V on silicon nitride amplifiers and lasers via microtransfer printing*. Optica, 7(5):386–393, May 2020.

[59] X. Ji, F. A. S. Barbosa, S. P. Roberts, A. Dutt, J. Cardenas, Y. Okawachi, A. Bryant, A. L. Gaeta, and M. Lipson. *Ultra-low-loss on-chip resonators with sub-milliwatt parametric oscillation threshold*. Optica, 4(6):619–624, Jun 2017.

[60] A. Hermans, K. Van Gasse, J. O. Kjellman, C. Caër, T. Nakamura, Y. Inada, K. Hisada, T. Hirasawa, S. Cuyvers, S. Kumari, A. Marinins, R. Jansen, G. Roelkens, P. Soussan, X. Rottenberg, and B. Kuyken. *High-pulse-energy III-V-on-silicon-nitride mode-locked laser*. APL Photonics, 6(9):096102, 2021.

[61] S. Keyvaninia, S. Uvin, M. Tassaert, X. Fu, S. Latkowski, J. Mariën, L. Thomassen, F. Lelarge, G. Duan, P. Verheyen, G. Lepage, J. V. Campenhout, E. Bente, and G. Roelkens. *Narrow-linewidth short-pulse III-V-on-silicon mode-locked lasers based on a linear and ring cavity geometry*. Opt. Express, 23(3):3221–3229, Feb 2015.

[62] V. Moskalenko. *Extended cavity passively mode-locked lasers in indium phosphide generic integration technology*. PhD thesis, Eindhoven University of Technology, 2016.

[63] J. Javaloyes and S. Balle. *Anticolliding design for monolithic passively mode-locked semiconductor lasers*. Opt. Lett., 36(22):4407–4409, Nov 2011.

[64] J.-P. Zhuang, V. Pusino, Y. Ding, S.-C. Chan, and M. Sorel. *Experimental investigation of anti-colliding pulse mode-locked semiconductor lasers*. Opt. Lett., 40(4):617–620, Feb 2015.

[65] V. Moskalenko, A. Pellacani, J. Javaloyes, S. Meint, and E. Bente. *Design of monolithically integrated InGaAsP/InP passively-modelocked linear quantum well lasers in an active-passive integration scheme*. In Annual Symposium of the IEEE Photonics Society Benelux Chapter, pages 283–286, 2012.

[66] S. Poelman, K. Van Gasse, and B. Kuyken. *Multimode interference reflector for anti-colliding III-V-on-silicon-nitride mode-locked lasers*. In European Semiconductor Laser Workshop 2020 (ESLW), 2020.

[67] W. D. Sacher, Y. Huang, G. Lo, and J. K. S. Poon. *Multilayer Silicon Nitride-on-Silicon Integrated Photonic Platforms and Devices*. J. Light. Technol., 33(4):901–910, 2015.

[68] C. Yang and J. Pham. *Characteristic Study of Silicon Nitride Films Deposited by LPCVD and PECVD*. Silicon, 10(6):2561–2567, Nov 2018.

[69] Z. Ye, K. Twayana, P. A. Andrekson, and V. Torres-Company. *High-Q Si3N4 microresonators based on a subtractive processing for Kerr nonlinear optics*. Opt. Express, 27(24):35719–35727, Nov 2019.

[70] C. Op de Beeck, B. Haq, L. Elsinger, A. Gocalinska, E. Pelucchi, B. Corbett, G. Roelkens, and B. Kuyken. *Heterogeneous III-V on silicon nitride amplifiers and lasers via microtransfer printing*. Optica, 7(5):386–393, May 2020.

[71] C. Xiang, W. Jin, J. Guo, J. D. Peters, M. J. Kennedy, J. Selvidge, P. A. Morton, and J. E. Bowers. *Narrow-linewidth III-V/Si/Si3N4 laser using multilayer heterogeneous integration*. Optica, 7(1):20–21, Jan 2020.

[72] B. Haq, S. Kumari, K. Van Gasse, J. Zhang, A. Gocalinska, E. Pelucchi, B. Corbett, and G. Roelkens. *Micro-Transfer-Printed III-V-on-Silicon C-Band Semiconductor Optical Amplifiers*. Laser Photonics Rev., 14(7):1900364, 2020.

[73] K. Van Gasse, R. Wang, and G. Roelkens. *27 dB gain III-V-on-silicon semiconductor optical amplifier with $>$ 17 dBm output power*. Optics Express, 27(1):293–302, 2019.

[74] M. L. Davenport, S. Skendžić, N. Volet, J. C. Hulme, M. J. R. Heck, and J. E. Bowers. *Heterogeneous Silicon/III–V Semiconductor Optical Amplifiers*. IEEE J. Sel. Top. Quantum Electron., 22(6):78–88, 2016.

[75] P. W. Juodawlkis, J. J. Plant, W. Loh, L. J. Missaggia, F. J. O'Donnell, D. C. Oakley, A. Napoleone, J. Klamkin, J. T. Gopinath, D. J. Ripin, S. Gee, P. J. Delfyett, and J. P. Donnelly. *High-Power, Low-Noise 1.5-μm Slab-Coupled Optical Waveguide (SCOW) Emitters: Physics, Devices, and Applications*. IEEE Journal of Selected Topics in Quantum Electronics, 17(6):1698–1714, 2011.

[76] E. Zeek, S. Backus, R. Bartels, H. Kapteyn, and M. Murnane. *Measurement of the autocorrelation factor for common pulses*. In Technical Digest. Summaries of papers presented at the Conference on Lasers and Electro-Optics. Postconference Edition. CLEO '99. Conference on Lasers and Electro-Optics (IEEE Cat. No.99CH37013), pages 116–, 1999.

[77] D. von der Linde. *Characterization of the noise in continuously operating mode-locked lasers*. Appl. Phys. B, 39(4):201–217, Apr 1986.

[78] T. Habruseva, S. O'Donoghue, N. Rebrova, F. Kéfélian, S. Hegarty, and G. Huyet. *Optical linewidth of a passively mode-locked semiconductor laser*. Optics letters, 34(21):3307–3309, 2009.

[79] A. S. Raja, A. S. Voloshin, H. Guo, S. E. Agafonova, J. Liu, A. S. Gorodnitskiy, M. Karpov, N. G. Pavlov, E. Lucas, R. R. Galiev, et al. *Electrically pumped photonic integrated soliton microcomb*. Nature communications, 10(1):1–8, 2019.

[80] A. Arbabi and L. L. Goddard. *Measurements of the refractive indices and thermo-optic coefficients of Si3N4 and SiOx using microring resonances*. Opt. Lett., 38(19):3878–3881, Oct 2013.

[81] V. Moskalenko, K. A. Williams, and E. A. J. M. Bente. *Pulse Narrowing and RF Linewidth Reduction of Integrated Passively Mode-Locked Laser in Anticolliding Design by Means of Spectral Tuning*. IEEE Photonics Journal, 8(4):1–10, 2016.

[82] S. Uvin, S. Keyvaninia, F. Lelarge, G.-H. Duan, B. Kuyken, and G. Roelkens. *Narrow line width frequency comb source based on an injection-locked III-V-on-silicon mode-locked laser*. Opt. Express, 24(5):5277–5286, Mar 2016.

[83] J. S. Parker, R. S. Guzzon, E. J. Norberg, A. Bhardwaj, P. R. A. Binetti, and L. A. Coldren. *Theory and Design of THz Intracavity Gain-Flattened Filters for Monolithically Integrated Mode-Locked Lasers*. IEEE Journal of Quantum Electronics, 48(2):114–122, 2012.

[84] V. Moskalenko, K. Williams, J. Koelemeij, and E. Bente. *42 nm wide coherent frequency comb generated by a QW based integrated passively mode-locked laser*. In International Semiconductor Laser Conference (ISLC), pp. 1-2, Kobe, Japan, 2016. IEEE.

[85] F. Kefelian, S. O'Donoghue, M. T. Todaro, J. G. McInerney, and G. Huyet. *RF Linewidth in Monolithic Passively Mode-Locked Semiconductor Laser*. IEEE Photon. Technol., 20(16):1405–1407, 2008.

[86] D. Auth, S. Liu, J. Norman, J. E. Bowers, and S. Breuer. *Passively mode-locked semiconductor quantum dot on silicon laser with 400 Hz RF line width*. Opt. Express, 27(19):27256–27266, Sep 2019.

[87] L. Drzewietzki, S. Breuer, and W. Elsäßer. *Timing jitter reduction of passively mode-locked semiconductor lasers by self-and external-injection: Numerical description and experiments*. Opt. Express, 21(13):16142–16161, 2013.

[88] R. Paschotta. *Noise of mode-locked lasers (Part I): numerical model*. Applied Physics B, 79(2):153–162, Jul 2004.

[89] R. Paschotta. *Noise of mode-locked lasers (Part II): timing jitter and other fluctuations*. Applied Physics B, 79(2):163–173, Jul 2004.

[90] J. Chen, J. W. Sickler, E. P. Ippen, and F. X. Kärtner. *High repetition rate, low jitter, low intensity noise, fundamentally mode-locked 167 fs soliton Er-fiber laser*. Opt. Lett., 32(11):1566–1568, Jun 2007.

[91] C. Ouyang, P. Shum, H. Wang, J. H. Wong, K. Wu, S. Fu, R. Li, E. J. R. Kelleher, A. I. Chernov, and E. D. Obraztsova. *Observation of timing jitter reduction induced by spectral filtering in a fiber laser mode locked with a carbon nanotube-based saturable absorber*. Opt. Lett., 35(14):2320–2322, Jul 2010.

[92] S. Cheung, J.-H. Baek, R. P. Scott, N. K. Fontaine, F. M. Soares, X. Zhou, D. M. Baney, and S. J. B. Yoo. *1-GHz Monolithically Integrated Hybrid Mode-Locked InP Laser*. IEEE Photonics Technology Letters, 22(24):1793–1795, 2010.

[93] R. Guzmán, C. Gordon, L. Orbe, and G. Carpintero. *1 GHz InP on-chip monolithic extended cavity colliding-pulse mode-locked laser*. Opt. Lett., 42(12):2318–2321, Jun 2017.

[94] M. J. R. Heck, M. L. Davenport, H. Park, D. J. Blumenthal, and J. E. Bowers. *Ultra-Long Cavity Hybrid Silicon Mode-locked Laser Diode Operating*

at 930 MHz. In Optical Fiber Communication Conference, page OMI5. Optica Publishing Group, 2010.

[95] D. Auth, S. Liu, J. Norman, J. E. Bowers, and S. Breuer. *Passively mode-locked semiconductor quantum dot on silicon laser with 400 Hz RF line width*. Opt. Express, 27(19):27256–27266, Sep 2019.

[96] H. M. J. Bastiaens, G. Neijts, A. Memon, Y. Fan, J. Mak, D. Geskus, M. Hoekman, V. Moskalenko, E. A. J. M. Bente, and K.-J. Boller. *First demonstration of a hybrid integrated InP-Si3N4 diode laser for broadband optical frequency comb generation*. In A. A. Belyanin and P. M. Smowton, editors, Novel In-Plane Semiconductor Lasers XX, volume 11705, page 1170508. International Society for Optics and Photonics, SPIE, 2021.

[97] M. Yuan, W. Wang, X. Wang, Y. Wang, Q. Yang, D. Cheng, Y. Liu, L. Huang, M. Zhang, B. Liang, W. Zhao, and W. Zhang. *Demonstration of an external cavity semiconductor mode-locked laser*. Opt. Lett., 46(19):4855–4858, Oct 2021.

[98] E. Vissers, S. Poelman, C. Op de Beeck, K. V. Gasse, and B. Kuyken. *Hybrid integrated mode-locked laser diodes with a silicon nitride extended cavity*. Opt. Express, 29(10):15013–15022, May 2021.

[99] M. N. Sysak, D. Liang, R. Jones, G. Kurczveil, M. Piels, M. Fiorentino, R. G. Beausoleil, and J. E. Bowers. *Hybrid Silicon Laser Technology: A Thermal Perspective*. IEEE Journal of Selected Topics in Quantum Electronics, 17(6):1490–1498, 2011.

[100] R. Paschotta. *Noise of mode-locked lasers (Part II): timing jitter and other fluctuations*. Applied Physics B, 79(2):163–173, Jul 2004.

[101] Çağri Şenel, F. Ömer Ilday, O. Kara, C. Birlikseven, C. Erdoğan, and R. Hamid. *All-normal-dispersion fiber lasers for frequency metrology*. In CLEO:2011 - Laser Applications to Photonic Applications, page CFM2. Optical Society of America, 2011.

[102] H. Byun, D. Pudo, J. Chen, E. P. Ippen, and F. X. Kärtner. *High-repetition-rate, 491 MHz, femtosecond fiber laser with low timing jitter*. Opt. Lett., 33(19):2221–2223, Oct 2008.

[103] K. Wu, X. Zhang, J. Wang, and J. Chen. *463-MHz fundamental mode-locked fiber laser based on few-layer MoS2 saturable absorber*. Opt. Lett., 40(7):1374–1377, Apr 2015.

[104] X. Li, W. Zou, K. Wu, and J. Chen. *Timing-Jitter Reduction by Use of a Spectral Filter in a Broadband Femtosecond Fiber Laser*. IEEE Photonics Technology Letters, 27(8):911–914, 2015.

[105] M. Billet, N. Poulvellarie, C. Op de Beeck, L. Reis, Y. Léger, C. Cornet, F. Raineri, I. Sagnes, K. Pantzas, G. Beaudoin, G. Roelkens, F. Leo, and B. Kuyken. *Gallium phosphide transfer printing for integrated nonlinear photonics*. In 2021 Conference on Lasers and Electro-Optics Europe European Quantum Electronics Conference (CLEO/Europe-EQEC), pages 1–1, 2021.

[106] D. J. Wilson, K. Schneider, S. Hönl, M. Anderson, Y. Baumgartner, L. Czornomaz, T. J. Kippenberg, and P. Seidler. *Integrated gallium phosphide nonlinear photonics*. Nature Photonics, 14(1):57–62, Jan 2020.

[107] M. Billet, L. Reis, Y. Léger, C. Cornet, F. Raineri, I. Sagnes, K. Pantzas, G. Beaudoin, G. Roelkens, F. Leo, et al. *Gallium phosphide-on-insulator integrated photonic structures fabricated using micro-transfer printing*. Optical Materials Express, 12(9):3731–3737, 2022.

[108] S. Ozharar, I. Ozdur, F. Quinlan, and P. J. Delfyett. *Jitter reduction by intracavity active phase modulation in a mode-locked semiconductor laser*. Opt. Lett., 34(5):677–679, Mar 2009.

[109] L. A. Jiang, M. E. Grein, E. P. Ippen, C. McNeilage, J. Searls, and H. Yokoyama. *Quantum-limited noise performance of a mode-locked laser diode*. Opt. Lett., 27(1):49–51, Jan 2002.

[110] J. Davila-Rodriguez, K. Bagnell, and P. J. Delfyett. *Frequency stability of a 10 GHz optical frequency comb from a semiconductor-based mode-locked laser with an intracavity 10000 finesse etalon*. Opt. Lett., 38(18):3665–3668, Sep 2013.

[111] S. Gee, S. Ozharar, J. J. Plant, P. W. Juodawlkis, and P. J. Delfyett. *Intracavity dispersion effect on timing jitter of ultralow noise mode-locked semiconductor based external-cavity laser*. Opt. Lett., 34(3):238–240, Feb 2009.

[112] X. Ji, F. A. S. Barbosa, S. P. Roberts, A. Dutt, J. Cardenas, Y. Okawachi, A. Bryant, A. L. Gaeta, and M. Lipson. *Ultra-low-loss on-chip resonators with sub-milliwatt parametric oscillation threshold*. Optica, 4(6):619–624, Jun 2017.

[113] A. J. Benedick, J. G. Fujimoto, and F. X. Kärtner. *Optical flywheels with attosecond jitter*. Nature Photonics, 6(2):97–100, Feb 2012.

[114] E. Chae, E. Kambe, K. Motohara, H. Izumiura, M. Doi, and K. Yoshioka. *A compact green Ti:Sapphire astro-comb with 43-GHz repetition frequency*. Preprint at `https://arxiv.org/abs/2101.05926`, 2021.

[115] K. Bagnell, A. Klee, P. J. Delfyett, J. J. Plant, and P. W. Juodawlkis. *Demonstration of a highly stable 10 GHz optical frequency comb with low timing jitter from a SCOWA-based harmonically mode-locked nested cavity laser*. Opt. Lett., 43(10):2396–2399, May 2018.

[116] M.-C. Lo, R. Guzmán, C. Gordón, and G. Carpintero. *Mode-locked laser with pulse interleavers in a monolithic photonic integrated circuit for millimeter wave and terahertz carrier generation*. Opt. Lett., 42(8):1532–1535, Apr 2017.

3

Modeling extended cavity mode-locked laser diodes

In the previous chapter, experimental work with regard to on-chip mode-locked lasers was presented. However, the performance of such devices remains largely unpredictable due to a lack of design tools and a limited understanding of the mode-locking dynamics. In this chapter we provide a brief overview of existing mode-locked laser modeling techniques and introduce the hybrid modeling concept. This hybrid model unifies the traveling-wave modeling technique for the active semiconductor sections with a nonlinear Schrödinger equation for the passive laser cavity. It is therefore particularly well-suited to model heterogeneous- or hybrid on-chip mode-locked laser diodes with a long extended passive cavity. The operation of the model is illustrated using a heterogeneous III–V-on-silicon mode-locked laser example. Furthermore, the significance of the third order optical nonlinearity and the group-velocity dispersion of the passive waveguide is demonstrated. Finally, some generalizations and suggestions for future work are proposed to further extend the scope and physical accuracy of the model.
The material presented in this chapter has in part been published in [1, 2].

3.1 Introduction

Mode-locked laser diodes, emitting coherent ultrashort optical pulses, are an important class of chip-scale comb generators with numerous applications in fundamental science and technology [3–6]. As illustrated in the previous chapter, a number of such devices have already been demonstrated in the past decades [7–16]. Yet, their design remains challenging as it is often based on simple rules of thumb and hence lacks predictability [17]. It is evident that appropriate modeling techniques are therefore desirable to facilitate the development process and advance the understanding of the complex mode-locking dynamics [18–22]. Ideally, such a model can provide some design guidelines to (approximately) acquire some targeted device parameters such as pulse duration, output power and comb shape. Furthermore, it is preferable that the MLL model not only incorporates the necessary physical details, but also minimizes the computational workload in order to conveniently serve as a design aid and enable parametric studies.

In the past decades, a wide variety of modeling techniques for MLLs have been presented, which, as proposed in [23], can be categorized in two distinct classes: distributed models and discrete models. Distributed models average the effects on the circulating pulses so that a single partial differential equation can be employed to describe the MLL. It is often based on the so-called Haus's master equation [24], which has proven successful for modeling solid-state- and fiber mode-locked lasers [25, 26]. Although distributed models allow for analytical solutions and enable the study of pulse dynamics, they assume that the pulse is near equilibrium and only undergoes mild changes when traveling inside the laser cavity [27, 28]. MLLs with strong gain and high losses in each roundtrip can therefore not be appropriately represented. Moreover, these equations employ generic formalisms to describe gain and absorption and are hence unable to grasp complex semiconductor physics that can greatly affect the gain and saturable absorber characteristics [22, 23].

In contrast, discrete models can be seen as an approach where each component of the laser cavity is modeled separately. This does not necessarily mean a different set of equations is utilized for the various laser components, rather it often implies the parameters in the equations are distinct for different components. In other words, the gain, saturable absorption, etc. happen in different sections of the device and the assumption that the pulse is near equilibrium is therefore eliminated [23]. Such discrete models are typically based on delay differential equations [27–29], a finite difference time domain description of the electromagnetic field [30], the full Maxwell-Bloch equations [18, 31–33], or traveling-wave models [21, 22, 34–36].

In recent years, Traveling-Wave Models (TWMs) have often been favored for semiconductor-based MLL modeling because they can incorporate the rich physics of semiconductors while limiting the computational workload under to the slowly-

varying envelope approximation [19, 21, 34]. However, existing TWMs are mostly geared towards monolithic mode-locked laser diodes with a high repetition rate and are currently unable to incorporate nonlinear and dispersive effects of a long extended passive laser cavity [20, 21, 34]. Although recent work successfully included Kerr-nonlinearity and chromatic dispersion in a TWM [22], these computationally intensive models target single-section diode mode-locked lasers and are consequently not suitable to aid the design of extended cavity semiconductor MLLs or to perform parametric studies. This is particularly troublesome when simulating low-repetition-rate MLLs, which have a long extended passive cavity as compared to the length of the active semiconductor section. For these devices, dispersive and nonlinear effects of the passive waveguides can become important. Moreover, low-repetition-rate heterogeneous- or hybrid mode-locked laser diodes are becoming increasingly relevant in the pursuit of lower repetition rates and low noise performance [8, 17, 37]. Yet, the ability to efficiently model such devices while including relevant nonlinear and dispersive effects of the long extended passive cavity has not been demonstrated by existing traveling-wave models. An exception are commercial tools, such as those currently offered by Photon Design. Their proprietary time-domain traveling-wave model (PICWave [38]) can be combined with a hetero-structure model (Harold [39]) to accurately simulate heterogeneous mode-locked laser diodes [40]. Although such a commercial tool offers excellent performance, it is not open source and requires a license.

Unlike a TWM, the nonlinear Schrödinger equation, implemented using the well-established split-step Fourier method, is well-suited to rapidly simulate pulse evolution in passive waveguides with arbitrary dispersion and nonlinearity [41–43]. It could therefore be advantageous to combine a TWM for the semiconductor laser sections with a split-step Fourier approach for the extended passive laser cavity.

In this chapter, we demonstrate a first implementation of such a hybrid simulation strategy and include nonlinear and dispersive effects of the extended passive laser cavity with low computational penalty. Furthermore, the method is used to simulate a heterogeneous III-V-on-silicon mode-locked laser. In particular the impact of the Kerr nonlinearity, dispersion, two-photon and free-carrier absorption of the extended passive laser cavity on the laser performance is discussed.

This chapter is organized as follows. Section 3.2 introduces the extended nonlinear Schrödinger equation and the split-step Fourier method to simulate optical pulse propagation in a nonlinear waveguide. In section 3.3, the traveling-wave method is introduced to model the active semiconductor sections of the mode-locked laser. A detailed description of the hybrid modeling approach along with a simulation example is provided in section 3.4. Finally, some generalizations and suggestions for future improvements are outlined in section 3.5. The hybrid model was conceived by the author in close collaboration with Dr. Kasper Van

Gasse. Furthermore, the author implemented the model in MATLAB and Python. Ir. Maxim Torreele further extended the model by interfacing it with the PHIsim traveling-wave package, developed by Prof. Erwin Bente et al. at the Technical University of Eindhoven.

3.2 Simulating pulse propagation in passive photonic waveguides

3.2.1 Extended nonlinear Schrödinger equation

The extended nonlinear Schrödinger equation (NLSE) serves as a basic equation to describe optical pulse propagation in a dispersive and nonlinear single-mode waveguide. It can be derived from Maxwell's equations, and a detailed derivation is provided in appendix B. When considering optical pulsewidths exceeding 100 fs, one can write the following extended NLSE

$$\frac{\partial A}{\partial z} - j\frac{\beta_2}{2}\frac{\partial^2 A}{\partial T^2} - \frac{\beta_3}{6}\frac{\partial^3 A}{\partial T^3} + \frac{\alpha}{2}A + \frac{\beta_{TPA}}{2A_{eff}}|A|^2 A - \frac{\sigma N_c}{2}A = \\ - j\gamma(|A|^2 A - \frac{j}{\omega_0}\frac{\partial}{\partial T}(|A|^2 A) - T_R A\frac{\partial |A|^2}{\partial T}) + jk_c k_0 N_c A \quad (3.1)$$

where A(z,T) is the slowly varying pulse envelope (units of $\sqrt{W}$), and z is the spatial variable and has the dimension of distance. A reference frame moving with the pulse at the group velocity v_g was defined using the transformation

$$T = t - z/v_g = t - \beta_1 z \quad (3.2)$$

β_2 and β_3 respectively represent the group-velocity dispersion and third-order dispersion, and α denotes the linear losses. Furthermore, the nonlinear parameter is defined as $\gamma = \frac{n_2\omega_0}{A_{eff}c}$, where n_2 is the material nonlinear coefficient, A_{eff} is the effective mode area, c is the speed of light in vacuum, and ω_0 represents the center frequency. The parameter T_R accounts for intrapulse Raman scattering and is defined as $T_R = \int_0^\infty tR(t)dt$, where the nonlinear response function $R(t) = (1 - f_R)\delta(t) + f_R h_R(t)$ with f_R the fractional contribution of the delayed Raman response to the nonlinear polarization and $h_R(t)$ the Raman response function, which can be approximated by an analytical function [41, 44, 45]

$$h_R(t) = \frac{\tau_1^2 + \tau_2^2}{\tau_1 \tau_2^2} e^{-t/\tau_2} sin(t/\tau_1) \quad (3.3)$$

where $\tau_2 = 1/\Gamma_R$, $\tau_1 = 1/(\omega_R^2 - \Gamma_R^2)^{1/2}$, and for a silicon waveguide, $\Gamma_R/\pi \approx$105 GHz and $\omega_R/2\pi$=15.6 THz respectively determine the Raman-gain

bandwidth and Raman shift [45]. As optical pulses with high intensities can suffer considerably from two (or multi)-photon absorption as well as from absorption due to optically generated free carriers [46], it can be desirable to include these absorption terms. The two-photon absorption is here incorporated through the two-photon absorption parameter β_{TPA}. The free-carrier absorption and dispersion are included through the free-carrier absorption coefficient σ, the free-carrier dispersion k_c, and an auxiliary equation that governs the time dependence of the free-carrier density N_c [47, 48]

$$\frac{dN_c}{dt} = \frac{\beta_{TPA}}{2\hbar\omega_0 A_{eff}^2}|A|^4 - \frac{N_c}{\tau_{FCA}}, \tag{3.4}$$

where τ_{FCA} is the free-carrier lifetime in the waveguide and $\hbar\omega_0$ is the photon energy.

3.2.2 Split-step Fourier method

In most cases, the NLSE does not support analytic solutions and a numerical approach is therefore needed. One method that has been used extensively to simulate optical pulse propagation, for example to simulate supercontinuum generation in a nonlinear fiber or waveguide [49–51], is the split-step Fourier method. As this numerical method relies on the Fast Fourier Transform (FFT) algorithm, this approach is relatively fast compared to competing finite difference schemes [43]. To understand how the split-step Fourier method operates, it is useful to rewrite equation 3.1 as

$$\frac{\partial A}{\partial z} = (\hat{D} + \hat{N})A, \tag{3.5}$$

where the differential operator $\hat{D}$ and the nonlinear operator $\hat{N}$ are given by

$$\hat{D} = j\frac{\beta_2}{2}\frac{\partial^2}{\partial T^2} + \frac{\beta_3}{6}\frac{\partial^3}{\partial T^3} - \frac{\alpha}{2} + \frac{\sigma N_c}{2} + jk_c k_0 N_c \tag{3.6}$$

$$\hat{N} = -j\gamma(|A|^2 - \frac{j}{\omega_0 A}\frac{\partial}{\partial T}(|A|^2 A) - T_R\frac{\partial |A|^2}{\partial T}) - \frac{\beta_{TPA}}{2A_{eff}}|A|^2 \tag{3.7}$$

The split-step Fourier method utilizes the nonlinear- and dispersion operator to act alternately upon the propagating field [42, 43, 52]. Although in reality, the dispersion and nonlinearity act simultaneously on the propagating pulse, the split-step Fourier method approximates the exact solution by assuming the dispersion and nonlinearity to act independently over a short distance δz, an approach that is accurate to second order in the step size [43]. The waveguide length is divided into a large number of segments with length δz so that the pulse can be propagated from segment to segment. For the propagation from z to z+δz, one can write the

propagation step in the symmetric form

$$A(z+\delta z,T) \approx exp(\frac{\delta z}{2}\hat{D})exp(\delta z\hat{N})exp(\frac{\delta z}{2}\hat{D})A(z,T) \tag{3.8}$$

Over the first distance $\delta z/2$, the dispersion operator acts alone. Next, the nonlinear operator is applied over the entire step size δz. Finally, the dispersion operator is applied once again for half a step size, $\delta z/2$. The optimal step size δz depends on the specific problem (for example the considered pulse power and duration), and a typical value is $100\,\mu\mathrm{m}$ [44]. The dispersion operator can be computed efficiently in the Fourier domain:

$$exp(\frac{\delta z}{2}\hat{D})A(z,T) = \mathcal{F}_T^{-1}exp(\frac{\delta z}{2}\hat{D}(\omega))\mathcal{F}_T A(z,T), \tag{3.9}$$

where $\mathcal{F}$ and $\mathcal{F}_T^{-1}$ denote the Fourier transform and the inverse Fourier transform respectively. It is important to note that the use of the FFT imposes periodic boundary conditions. For a standalone optical pulse propagation simulation, this typically does not pose a problem as the temporal window can be taken much larger than the pulse duration. This prevents pulse energy from reaching the window boundaries, avoiding potential numerical instabilities [43]. However, when simulating pulse propagation in resonators and assuming that the actual pulse repetition rate should be preserved (for example to ensure accurate modeling of gain recovery in a mode-locked laser cavity), either the temporal window size should exactly match the natural periodicity of the optical pulse train, or artificial approaches are required to prevent the spectrally spreading or shifting pulse from reaching the temporal window boundaries. This particular issue will be addressed in more detail in section 3.4.

3.3 Traveling-wave model for laser diodes

Traveling-wave models have been widely used to model monolithic laser diodes and mode-locked lasers [21, 22, 34, 53, 54]. With this time-domain simulation method, the photonic circuit is divided into small segments with equal optical pathlengths. For each segment, an average carrier density as well as an average optical intensity (or photon density) is defined, and a set of partial differential equations are used to describe the evolution of the two counterpropagating waves and the carrier densities. Unlike monolithic mode-locked laser models based on delay differential equations (DDEs), no assumption of unidirectional propagation is made [34], and faithful reproduction of experimental observations is therefore possible [55]. The TWM used in this chapter is applied to model the active sections (i.e. semiconductor optical amplifier and saturable absorber) of a previously demonstrated III-V-on-silicon anti-colliding MLL with a 2.6 GHz repeti-

tion rate [8, 56]. The considered laser consists of a 14 mm long silicon waveguide cavity, an $850\,\mu\mathrm{m}$ Semiconductor Optical Amplifier (SOA) gain section and a $60\,\mu\mathrm{m}$ Saturable Absorber (SA) separated with an unbiased $30\,\mu\mathrm{m}$ ISOlation section (ISO) from the gain region. Although several elaborate TWMs have been proposed in the literature for semiconductor quantum well and quantum dot lasers, such as [22] and the open source model FreeTWM [21], a simple TWM is adopted here to demonstrate the hybrid modeling concept. It is nevertheless straight forward to extend the presented approach to any other TWM in order to include more physical details. Assuming the MLL pulse width is significantly larger than the intraband relaxation time of the semiconductor medium, one can describe the temporal and spatial evolution of two counterpropagating waves with amplitudes $|A^{\pm}|$ (units of $\sqrt{W/m^2}$) in the semiconductor laser sections as [34, 57]

$$\frac{1}{v_g}\frac{\partial A^{\pm}}{\partial t} \pm \frac{\partial A^{\pm}}{\partial z'} = \frac{j\omega_0\Gamma}{2n_{eff}c}\chi A^{\pm} - \frac{\beta}{2v_g}A^{\pm}, \tag{3.10}$$

where v_g represents the group velocity of light, Γ the Multiple Quantum Well (MQW) optical confinement factor, n_{eff} the effective modal index, c the speed of light, ω_0 the angular frequency of operation, χ the electrical susceptibility. and z' is the spatial variable with units of meters. The term containing β models the internal losses in the semiconductor material. The above equation can be rewritten as follows

$$\frac{\partial A^{\pm}}{\partial t} \pm \frac{\partial A^{\pm}}{\partial z} = \frac{j\omega_0 v_g\Gamma}{2n_{eff}c}\chi A^{\pm} - \frac{\beta}{2}A^{\pm}, \tag{3.11}$$

where the spatial variable z was divided by the group velocity to yield a dimension of time. Furthermore, the carrier density N can be approximated as [34, 57]

$$\frac{\partial N}{\partial t} = \frac{I}{qV} - \frac{N}{\tau} + \frac{\Gamma\,\mathrm{Im}(\chi(N))}{\hbar n_{eff}c}|A|^2 \tag{3.12}$$

where I is the injected current, q is the electron charge, V is the active volume and τ represents the carrier lifetime. Assuming a parabolic band structure, low temperature, charge neutrality within the quantum well, and k-vector independent intraband relaxation rates, one can express the electrical susceptibility as [19, 20, 58]

$$\chi(N) = -\chi_0[2ln(1 - \frac{\gamma\frac{N}{N_t}}{\omega - \omega_0 - \Omega_g + j\gamma}) - ln(1 - \frac{\Omega_T}{\omega - \omega_0 - \Omega_g + j\gamma})], \tag{3.13}$$

where N_t is the transparency carrier density, Ω_g is the bandgap offset, γ is the intraband relaxation rate, Ω_T is the angular frequency of the top of the energy band and χ_0 is a material gain parameter. To eliminate the frequency-dependency of the susceptibility, one can approximate the susceptibility as a frequency-independent quantity $\chi(\omega = \omega_0, N(z,t))$ by adding a separate spectral filter to the model. This approximation can be motivated by noting that Bragg gratings are utilized as cavity mirrors in the MLL under consideration, causing strong spectral shaping. Here, a Lorentzian filter is incorporated at the output facet of the laser, in correspondence to what was proposed in previous work [34]. In case a more accurate model for gain dispersion is desired, the lumped filter could be replaced by a distributed implementation, similar to what has been demonstrated in [53, 59]. This is particularly important for laser topologies without narrowband reflectors where the gain dispersion of the semiconductor medium plays a salient role [59]. The traveling-wave equations are than given by

$$\frac{1}{v_g}\frac{\partial A^{\pm}}{\partial t} \pm \frac{\partial A^{\pm}}{\partial z'} = \frac{j\omega_0\Gamma}{2n_{eff}c}\chi A^{\pm} - \frac{\beta}{2v_g}A^{\pm} - \hat{\mathcal{D}}A^{\pm}, \tag{3.14}$$

where $\hat{\mathcal{D}}A^{\pm} = \frac{\bar{g}}{2}(A^{\pm} - p^{\pm})$ is a linear operator used to model gain dispersion using a distributed Lorentzian filter. The polarization terms obey

$$\frac{\partial p^{\pm}}{\partial t} = \bar{\gamma}(A^{\pm} - p^{\pm}) + j\bar{\omega}p^{\pm} \tag{3.15}$$

where $\bar{\gamma}$, $\bar{\omega}$ and $\bar{g}$ are the half width at half maximum of the Lorentzian (units rad/ps), the peak position of the Lorentzian with respect to ω_0 and the amplitude of the gain dispersion (units m^{-1}). The Lorentzian FWHM=$2\bar{\gamma}$ and the Lorentzian peak is $\bar{g}^2/4$. The carrier rate equation is than given by

$$\frac{\partial N}{\partial t} = \frac{I}{qV} - R(N) + \frac{\Gamma\,\mathrm{Im}(\chi(N))}{\hbar n_{eff}c}|A|^2 - \frac{v_g}{\hbar\omega_0 v_g}Re\left[A^*(2\hat{\mathcal{D}})A\right] \tag{3.16}$$

In the remainder of this chapter, the localized Lorentzian filter is used for simplicity unless specified otherwise. In order to solve the aforementioned set of equations 3.11 and 3.12, a numerical scheme is used where the semiconductor section is discretized into K segments of normalized length $\Delta z = \Delta t$, where Δt is the time required for light to travel over one segment and Δz is the physical length of the segment normalized with the group velocity of light. A schematic of the TWM numerical scheme is depicted in Fig. 3.1. Combining equations (3.10) and (3.13), the wave solutions in each segment $z_k \leq z \leq z_{k+1}$ are given by [34]

$$A^+(t+\Delta t, z_{k+1}) \approx A^+(t, z_k) exp\left[-\frac{\beta \Delta z}{2} + \frac{j\omega_0 \Gamma v_g}{2 n_{eff} c} \cdot \int_{z_k}^{z_{k+1}} \chi(N(z,t)) dz\right] \quad (3.17)$$

$$A^-(t+\Delta t, z_k) \approx A^-(t, z_{k+1}) exp\left[-\frac{\beta \Delta z}{2} + \frac{j\omega_0 \Gamma v_g}{2 n_{eff} c} \cdot \int_{z_k}^{z_{k+1}} \chi(N(z,t)) dz\right] \quad (3.18)$$

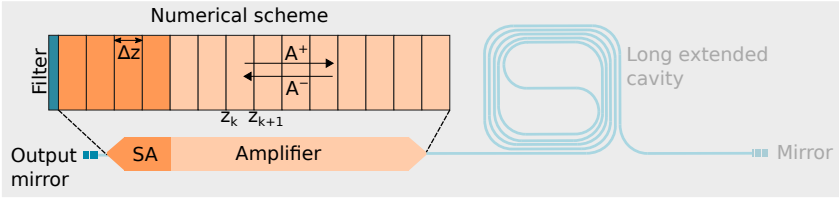

Figure 3.1: Traveling-wave model numerical scheme for the mode-locked laser's active semiconductor sections. The sections are discretized in segments of optical length $\Delta z = \Delta t$. A Lorentzian filter is used at the output facet to model the gain bandwidth and spectral shaping of the gratings. SA: saturable absorber, $A^{\pm}$: amplitudes of the counterpropagating waves in the cavity.

The integrals can be evaluated numerically by using a simple trapezoidal approximation. Furthermore, an expression for the carrier density can be formulated based on equation (3.12) and a first order Euler scheme

$$N(z_k, t) \approx N(z_k, t-\Delta t) + \Delta t \cdot \left(\frac{I}{qV} - \frac{N(z_k, t-\Delta t)}{\tau} + \frac{\Gamma}{\hbar n_{eff} c} \Im\{\chi(N(z_k, t-\Delta t))\} \cdot (|A^+(t, z_k)|^2 + |A^-(t, z_k)|^2)\right) \quad (3.19)$$

Note that in [1] and for the simulation results in the following section 3.4, the stimulated recombination term was chosen to scale with the local field intensity $|A^+ + A^-|^2$ rather than $|A^+|^2 + |A^-|^2$ (i.e. proportional to the photon density). Although experiments with gain-coupled distributed feedback (DFB) lasers show that this recombination term in reality scales with the local field intensity [60, 61], such an approach generally requires the use of coupled wave equations where coupling effects induced by the carrier oscillations resulting from the spatially varying intensity, are incorporated. Although no coupled-wave equations nor carrier diffusion are included in the simple model presented here, the validity of $|A^+ + A^-|^2$

can be motivated by noting that the used discretization scheme employs a step size which is comparable or larger than the wavelength. This leads to an averaging effect which eliminates strong interference effects and allows one to neglect carrier gratings and coupled wave equations. Nevertheless, care should be taken to ensure that the TWM step size is not an exact multiple of the wavelength in the material as this could yield an approximation error. To eliminate this potential pitfall, it is often preferred to work with $|A^+|^2 + |A^-|^2$ [34, 53, 62]. It was confirmed that for the presented simulations this modification does not yield a significant difference.

Finally, a boundary condition can be defined for the left laser facet by convolving the backward propagating wave with the Lorentzian spectral filter f(t) using a first-order infinite impulse response (IIR) filter [34]

$$A^+(t + \Delta t, 0) = \sqrt{r_1} \left[a \cdot A^+(t, 0) + b \cdot A^-(t + \Delta t, 0) \right], \tag{3.20}$$

where r_1 describes the left facet reflectivity, and filter coefficients $a = \frac{exp(-\delta \Delta t)}{\sqrt{r_1}}$ and $b = \delta \Delta t$. Alternatively, one can implement the filter using an FIR filter

$$A^+(t + \Delta t, 0) = \sqrt{r_1} \Delta t \sum_{m=0}^{M} f(m) A^-(t - (m-1)\Delta t, 0) \tag{3.21}$$

When a sufficiently large number of samples is considered for the truncated convolution sum, the output of the model shows no discernible differences compared to the IIR filter implementation.

The right boundary condition (corresponding with the right mirror of Fig. 3.1) is simply defined as $A^-(t + \Delta t, L) = \sqrt{r_2} \cdot A^+(t, L)$.

3.4 Hybrid modeling concept

The hybrid model employs the aforementioned TWM for the active sections of the mode-locked laser diode, i.e. the SOA and SA. The extended passive laser cavity is modeled either with the extended nonlinear Schrödinger equation (using the split-step Fourier method), or by using a simple delay with loss. This approach is schematically illustrated in Fig. 3.2. In the following paragraphs, the interface between the two distinct models is described in detail, and several simulation examples are discussed. The current model is implemented in MATLAB, and the code is available on GitHub [63].

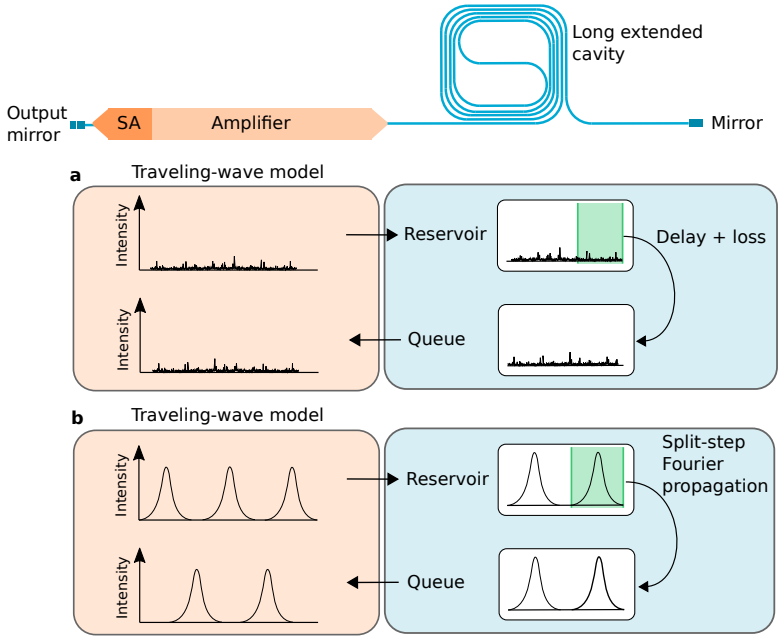

Figure 3.2: Mode-locked laser simulation flow, consisting of a traveling-wave model for the active region and a split-step Fourier propagation algorithm for the extended passive waveguide cavity. (a) In case no pulses are observed, e.g. at laser start-up, the split-step Fourier algorithm is not employed and the extended cavity is simply represented by a delay with some loss. (b) When pulses are observed, the split-step Fourier method is used and dispersive and nonlinear effects are accounted for.

3.4.1 Unifying the traveling-wave model and the split-step Fourier method

To effectively propagate the output of the TWM in the passive waveguide model, a custom algorithm was developed. For the passive waveguide, a so-called *reservoir* and a *queue* data array are defined with a size equal to twice the propagation delay of the passive waveguide cavity divided by the TWM time stepsize, resembling respectively the forward and backward traveling waves in the passive cavity. In other words, the length of these arrays is in correspondance with the delay ΔT (in this case 359 ps) between light leaving the amplifier at the right side (see Fig. 3.2), and reaching the amplifier again at the right side after a roundtrip propagation through the silicon spiral waveguide cavity.

The forward propagating envelope of the TWM gradually fills the reservoir of the cavity, i.e. every iteration the last sample of the forward propagating envelope

A^+ at the interface with the passive cavity (see Fig. 3.2) is send to the reservoir. Simultaneously, a sample from the queue is concatenated to the backwards traveling envelope A^- at the same interface. The forward propagating envelope A^+ hence continuously feeds the reservoir whereas the queue feeds the backward propagating envelope A^-. When the reservoir is full, the split-step Fourier method is activated to propagate (a number of) the reservoir samples. The split-step Fourier method is hence not called with every TWM iteration. The propagated samples are subsequently stored in the queue for continuation in the TWM.

To propagate the pulse, an appropriate time window has to be chosen to center the pulse, ensuring that energy is centralized in the window to comply with the periodic boundary conditions of the split-step Fourier method [43, 64]. This avoids unphysical results and numerical instabilities [43]. A peak search algorithm is employed to detect any pulse-like patterns in the reservoir of the extended passive cavity. In case no peaks are detected, one can conclude that the laser either operates in continuous wave or is in a noisy (start-up) state. In these cases where no pulses are detected, the cavity is simply modeled with loss and a delay, as is shown in Fig. 3.2 (a). In case a single pulse is detected, a time slice is taken from the reservoir data and subsequently used as an input for the passive waveguide model. The slice is taken in such a way that the pulse is centered and can be readily propagated using the split-step Fourier method. Once the pulse is propagated, the resulting output is added to the queue. Finally, in case multiple pulses are detected in the reservoir, a time slice with one or more pulses is selected from the reservoir in a way that centralizes the signal energy in the slice as much as possible. This certifies that the intensity vanishes near the boundaries and warrants valid usage of the FFT in the split-step Fourier method. The resulting output is then again added to the queue that feeds the backward propagating wave of the TWM. As such, when pulsed behavior is observed, nonlinear and dispersive effects of the laser cavity are accounted for.

As expected, simulations confirm that after start-up, the time slice used for split-step Fourier propagation is nearly equal to the entire reservoir size, i.e. the delay ΔT=359 ps. Furthermore, the number of samples employed for the split-step Fourier propagation are equal to the number of samples selected from the reservoir as this avoids the need for interpolation. As such, the propagated signal samples in the queue can simply be concatenated to the backward propagating wave A^- after applying a scaling factor to convert the field envelope in units of $[\sqrt{W}]$ to units of $[\sqrt{W/m^2}]$.

It is observed that once steady-state mode-locking is reached, the split-step Fourier method is consistently employed for all pulses, as is conceptually shown in Fig. 3.2 (b). Moreover, simulations confirm that in case dispersion and nonlinearity of the passive waveguide are omitted, the hybrid model yields results identical to the TWM without the split-step Fourier approach. In case the cavity

dispersion is anomalous, it can be worthwhile to consistently use the full reservoir for split-step Fourier propagation instead of a simple delay with loss. This allows one to account for the breakup of (quasi)-CW light or the amplification of noise through modulation instability. However, the current model is not optimized for continuous-wave-like operating points. Moreover, modeling pulsed regimes with nonvanishing backgrounds is currently outside the scope of the hybrid model owing to the periodic boundary conditions of the FFT. This issue is addressed in section 3.5.

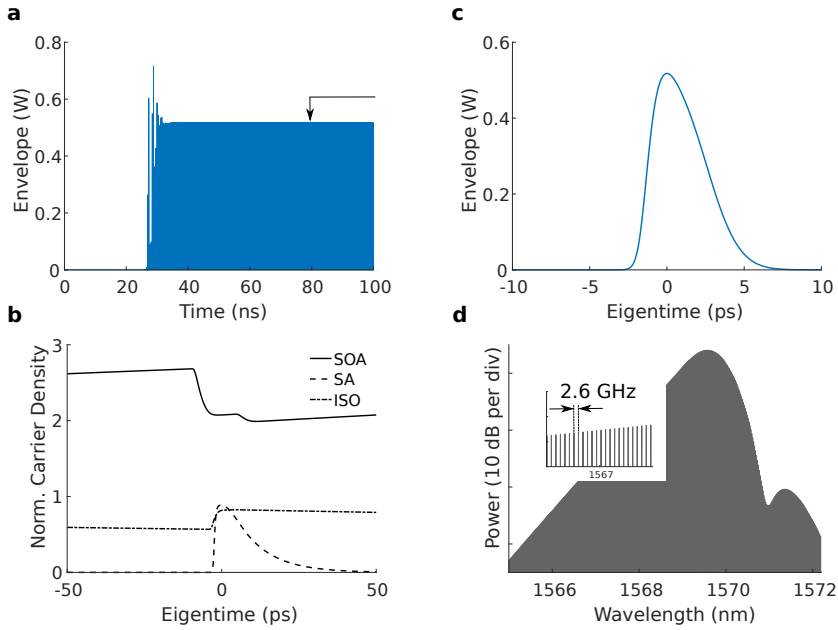

Figure 3.3: Mode-locked laser simulation example. (a)-(d) Hybrid model output with a 20 fs stepsize and a 100 ns (260 roundtrips) duration. (a) Signal build-up at the output facet of the mode-locked laser. The arrow indicates the time instant of the corresponding normalized carrier densities (b) and pulse profile (c). (d) The optical comb spectrum corresponding with the generated pulse train.

3.4.2 Simulation example

Figures 3.3 (a)-(d) show the hybrid model results for the 2.6 GHz anti-colliding III-V-on-silicon MLL. A simulation time of 100 ns (260 roundtrips) was used with a 20 fs stepsize. The model parameters are based on earlier work [48, 65, 66] and are listed in Table 3.1. The real part of the nonlinear coefficient $\gamma_{NL} = \frac{n_2 \omega}{A_{effc}} \approx 69\ m^{-1}W^{-1}$, with n_2 the material nonlinear coefficient and A_{eff} the effective mode area. The dispersion parameters $\beta_2 = 1.3\ ps^2/m$ and $\beta_3 = 0.0042\ ps^3/m$

were acquired using Lumerical [67] based on the silicon waveguide dimensions specified in [56].

Meaning	Symbol	Value	Units
Wavelength	λ	1.57	µm
Group index	n_g	3.85	-
Effective index	n_{eff}	3	-
Transparency carrier density	N_t	$8.7{\cdot}10^{17}$	cm^{-3}
MQW confinement factor	Γ	0.075	-
MQW mode area	A_{MQW}	$0.54 \cdot 10^{-12}$	m^2
Carrier lifetime	$\tau_{SOA}; \tau_{SA}; \tau_{ISO}$	$1; 10^{-2}; 1$	ns
Gain constant	$\chi_{0,SOA}; \chi_{0,SA}; \chi_{0,ISO}$	0.07; 0.48; 0.07	-
Intraband relaxation rate	$\gamma_{SOA}; \gamma_{SA}; \gamma_{ISO}$	$4 \cdot 10^{12}; 8 \cdot 10^{12}; 8 \cdot 10^{12}$	s^{-1}
Filter bandwidth	Δf	2	THz
Section length	$L_{SOA}; L_{SA}; L_{ISO}$	850; 60; 30	µm
Top band frequency	Ω_T	$90 \cdot 10^{12}$	rad $\cdot s^{-1}$
SA Bandgap offset	Ω_g	5	THz
Active region internal losses rate	β	$2.56 \cdot 10^{11}$	s^{-1}
Injection current	I	45	mA
Silicon waveguide mode area	A_{Si}	$0.29 \cdot 10^{-12}$	m^2
Second-order dispersion	β_2	1.3	ps^2/m
Third-order dispersion	β_3	0.0042	ps^3/m
Silicon Kerr nonlinearity	n_2	$5{\cdot}10^{-18}$	m^2W^{-1}
Silicon waveguide losses	α	0.7	dB/cm
Two-photon absorption silicon	β_{TPA}	0.6	cm/GW
Free-carrier dispersion silicon	k_c	$1.35{\cdot}10^{-27}$	m^3
Free-carrier lifetime silicon	τ_{FCA}	1	ns
Free-carrier absorption silicon	σ	$1.45{\cdot}10^{-21}$	m^2
Facet reflectivity	$r_1; r_2$	0.5; 0.99	-

Table 3.1: Parameters used for the hybrid model. SOA is Semiconductor Optical Amplifier, SA is Saturable Absorber, ISO is Isolation region in between the SOA and SA.

An injection current of 45 mA was found to correspond with fundamental mode-locking. At this operating point, the pulse train converges after approximately 40 ns (100 roundtrips), as can be seen in Fig. 3.3 (a). The black arrow in Fig. 3.3 (a) indicates the time instant used to acquire the carrier density profiles, shown in Fig. 3.3 (b), and the individual pulse profile, shown in Fig. 3.3 (c). The output pulse has an energy of 2.11 pJ and a full-width at half maximum (FWHM) of 3.68 ps. These values are in in line with experimental results where pulses with energies on the order of 1 pJ are observed and autocorrelation measurements indicate pulsewidths around 3 ps [56, 68]. The carrier densities were normalized with respect to the transparency carrier density and were monitored in the middle of the amplifier, saturable absorber and isolation sections. The carrier density in the saturable absorber quickly saturates with the incoming pulse but recovers fast compared to the SOA. Furthermore, as the SOA is close to the output facet, the pulse propagates twice through the SOA with a short delay in between, resulting in two subsequent dips in the SOA carrier density, as can be seen in Fig. 3.3 (b). The comb spectrum, shown in Fig. 3.3 (d), exhibits a dip around 1571 nm caused by the cavity third-order nonlinearity. In addition, part of the comb spectrum is slightly red-shifted resulting from the Raman effect. The line spacing between the

comb teeth is 2.6 GHz, corresponding with the pulse repetition rate of the laser.

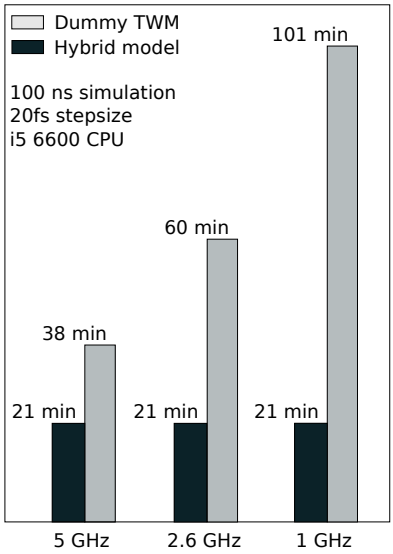

Figure 3.4: Comparison of a dummy TWM and a hybrid model for a 5 GHz, 2.6 GHz and 1 GHz repetition rate. The hybrid model computation time is approximately invariant to the extended passive waveguide cavity size as it is not modeled by a slow TWM.

Figure 3.4 shows a comparison of the hybrid model and a dummy TWM (without split-step Fourier propagation and of identical complexity) for different MLL repetition rates. In the dummy TWM case, the field propagation through the passive waveguide cavity is calculated in a traveling-wave fashion to emulate the naive incorporation of dispersive and nonlinear effects. However, actual dispersive and nonlinear effects are omitted in the dummy TWM as it solely serves as a reference for the simulation time. Note that if one does not desire to include dispersion and nonlinearity in practice, one can use a traveling-wave model with a simple boundary condition for the passive waveguide cavity, leading to a simulation time comparable to that of the hybrid model. The MLL was simulated for 100 ns with a timestep of 20 fs on a standard desktop with an i5-6600 Central Processing Unit (CPU). The MATLAB script of the hybrid model takes around 20 minutes to complete, almost independently of the passive cavity size. Note that the considered hybrid model is solely prototyped in MATLAB and does not rely on any custom memory allocation or parallelization. Switching to a low-level programming language could therefore provide for a massive speed-up, as was also exploited by earlier work [21, 22]. As the TWM dominates the total simulation time of the hybrid model, the split-step Fourier algorithm for the passive cavity only marginally increases the computation time with decreasing repetition rate. The classical TWM on the other hand, in which also the passive laser cavity is

modeled with a traveling-wave method, requires significantly more time, as is indicated in Fig. 3.4. Moreover, the simulation time of the classical TWM rapidly increases with decreasing repetition rate because the TWM complexity directly scales with the laser cavity size. This drawback highlights the benefits of a hybrid modeling strategy: it allows to include complex dispersive and nonlinear effects of the extended passive laser cavity with minimal computational penalty. This is particularly valuable for integrated MLLs with a low repetition rate [8, 11, 17], as the impact of nonlinear and dispersive effects of the cavity becomes apparent in these devices and the simulation time with existing TWMs can become impractically long.

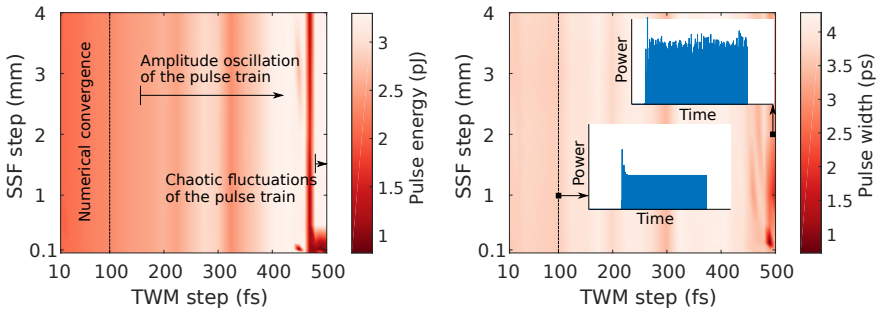

Figure 3.5: Stability analysis of the hybrid mode-locked laser model for an injection current of 45 mA. Map of the pulse energy (left) and of the pulsewidth (right) as a function of the discretization step of the TWM and the stepsize of the split-step Fourier propagation.

Figure 3.5 depicts a map of the output pulse energy (left) and the output pulse width (right) as a function of the traveling-wave discretization step and the split-step Fourier step. One finds that the stability of the TWM model degrades gradually without an abrupt transition to a numerically unstable regime. For a TWM step below approximately 100 fs, the model yields no discernible differences and convergence is achieved. However, when the TWM stepsize is further increased, the amplitude of the pulse train acquires an oscillatory fluctuation. Furthermore, for very large stepsizes, approaching 500 fs, the amplitude fluctuations appear to be chaotic and the pulse train becomes unstable, as can be seen from the inset on the right of Figure 3.5. Moreover, due to the coarse TWM grid, the pulse envelope is poorly sampled, leading to strongly distorted pulse shapes with sharp edges. Finally, it is observed that the model is robust with regard to the split-step Fourier (SSF) step size. Although the pulse energy and pulse width remain nearly identical for increasing SSF steps, the comb spectrum starts to deviate when the step size exceeds several millimeters. For all simulations in the manuscript, a step of approximately $100\,\mu\mathrm{m}$ was employed for the split-step Fourier method.

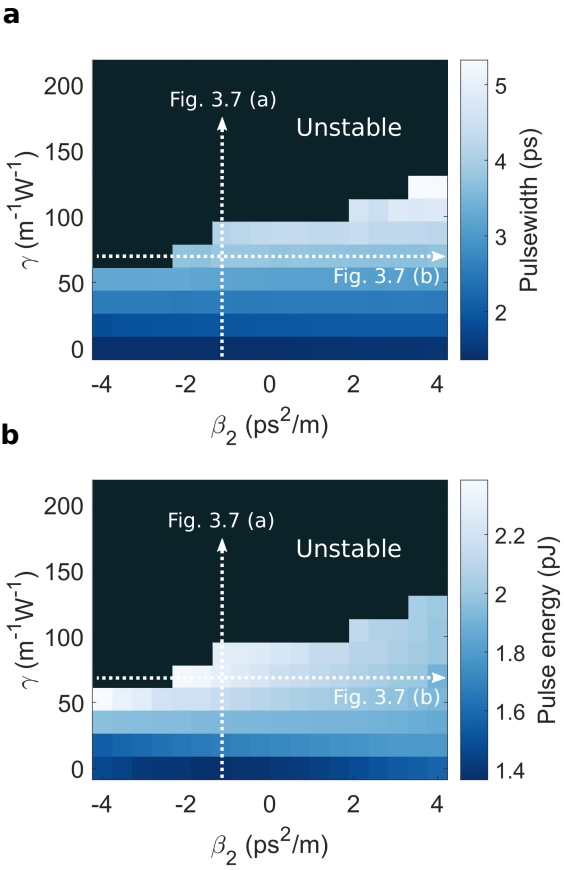

Figure 3.6: Impact of nonlinearity and dispersion of the extended passive laser cavity on the MLL performance and stability. Map of the pulse width (a) and pulse energy (b) as a function of GVD and Kerr nonlinearity. Stable fundamental mode-locking is predominantly observed for sufficiently small nonlinearities and normal dispersion.

3.4.3 Impact of dispersion and nonlinearity

It is well known that the complex interplay of dispersion and nonlinearity can greatly affect the pulse generation of MLLs. Even more so, careful management of these properties has lead to various types of soliton lasers, where the balance between quadratic [69, 70] or higher-order dispersion [71] with nonlinearity have allowed for stable ultrashort pulse generation. Although solitons have traditionally been produced with fiber MLLs, they can also arise in chip-scale devices [71]. Furthermore, even for existing integrated MLLs which do not target solitary operation, dispersive and nonlinear effects of the passive waveguides can significantly affect the properties of the pulse train, in particular for long waveguide cavities.

A map of the pulse energy and the FWHM pulse duration as a function of Kerr nonlinearity and group-velocity dispersion of the passive cavity is shown in figures 3.6(a) and 3.6(b) respectively. The injection current of the III-V-on-Silicon MLL model was fixed at 45 mA. Stable fundamental mode-locking can primarily be observed at low nonlinearities, while fundamental mode-locking ceases for anomalous dispersive and/or highly nonlinear operating points.

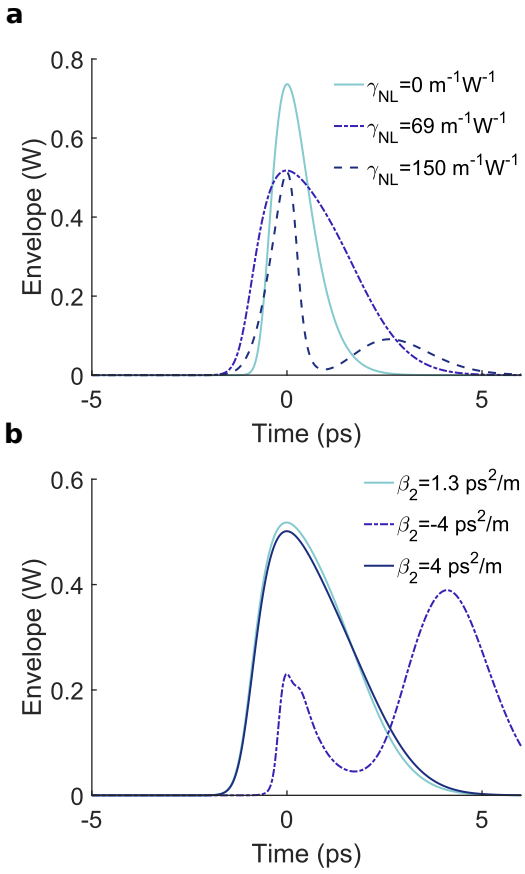

Figure 3.7: Output pulse for different nonlinearities and $\beta_2 = 1.3\ ps^2/m$ (a), and for different cavity dispersions with $\gamma_{NL} = 69\ m^{-1}W^{-1}$ (b). The corresponding operating regions on the maps 3.6 (a),(b) are indicated.

The output pulses under normal dispersion $\beta_2 = 1.3\ ps^2/m$ and Kerr nonlinearities $\gamma_{NL} = 0\ m^{-1}W^{-1}$, $\gamma_{NL} = 69\ m^{-1}W^{-1}$ and $\gamma_{NL} = 150\ m^{-1}W^{-1}$ are depicted in Fig. 3.7(a). By introducing a positive nonlinear coefficient n_2, the Self-Phase Modulation (SPM)-induced chirp leads to a spectral red-shift for the leading edge of the pulse and a blue-shift for the trailing edge. Under normal dis-

persion, this leads to enhanced pulse broadening, as can be observed in Fig. 3.7(a) and in the map Fig. 3.6(a). Furthermore, the SPM-induced chirp in combination with normal dispersion in the silicon waveguide shapes the pulse as such that it becomes rectangularly shaped with sharper leading and trailing edges, a phenomenon known as optical wave breaking [72]. This cavity pulse shaping is however not apparent from the output pulse plot as the pulse shape is also strongly affected by the amplifier and absorber sections, smoothing the sharpened pulse edges. In contrast, under anomalous dispersion the pulse duration reduces with increasing SPM. For sufficiently strong SPM, the pulseshape is distorted and experiences a temporal oscillation around the pulse peak, eventually leading to an unstable pulse train as is the case for $\gamma_{NL} = 150\ m^{-1}W^{-1}$ in Fig. 3.7(a). The output pulses for different Group-Velocity Dipsersion (GVD) values and for a nonlinearity $\gamma_{NL} = 69\ m^{-1}W^{-1}$ are shown in Fig. 3.7(b). The cases $\beta_2 = 1.3\ ps^2/m$ and $\beta_2 = 4\ ps^2/m$ lead to stable mode-locking and yield a nearly identical pulse train. On the other hand, changing the $\beta_2 = -4\ ps^2/m$ results in a chaotic pulse train with varying pulse amplitudes and the emergence of satellite peaks.

Figures 3.8(a) and (b) depict the pulse width and pulse energy for the case (1) where all aforementioned cavity effects are considered, in case (2) two-photon- and free-carrier absorption are neglected and for case (3) only dispersion is considered without nonlinearity, Raman effect or nonlinear absorption. Stable fundamental mode-locking is achieved for injection currents between 42 mA and 60 mA. For lower injection currents, the MLL operates in a noisy or Q-switched state, whereas at high injection currents, satellite peaks arise in the trailing edge of the pulse, leading to chaotic or seemingly harmonicly mode-locked operation. Omitting the nonlinearity leads to a slight enhanced stability range, ranging from 42 mA to 62 mA. For the considered operating point, the Kerr nonlinearity hence slightly deteriorates the stability of the MLL and advances the transition to an unstable pulse train regime. As a simulation time of 100 ns was used, it is feasible that some stable fundamental operating points lay outside the depicted region but require long convergence times. Furthermore a number of stable attractors are potentially not accessible by self-starting the mode-locked laser and may require some form of excitation such as a pulse injection.

For case (1) and (2) the pulsewidth increases up to an injection current around 47 mA, after which the pulse width monotonically decreases. As the pulse peak power is observed to be approximately invariant with the injection current, the pulse energy follows a similar trend as the pulsewidth, reaching the maximal pulse energy at an injection current around 47 mA. Surprisingly, here, the incorporation of two-photon- and free-carrier absorption leads to a slightly larger pulse energy. Although the pulse peak power is reduced (for injection currents below 55 mA), the pulse duration increases, leading to a slightly increased output pulse energy. As for the example considered here the effective mode area A_{eff} is relatively large

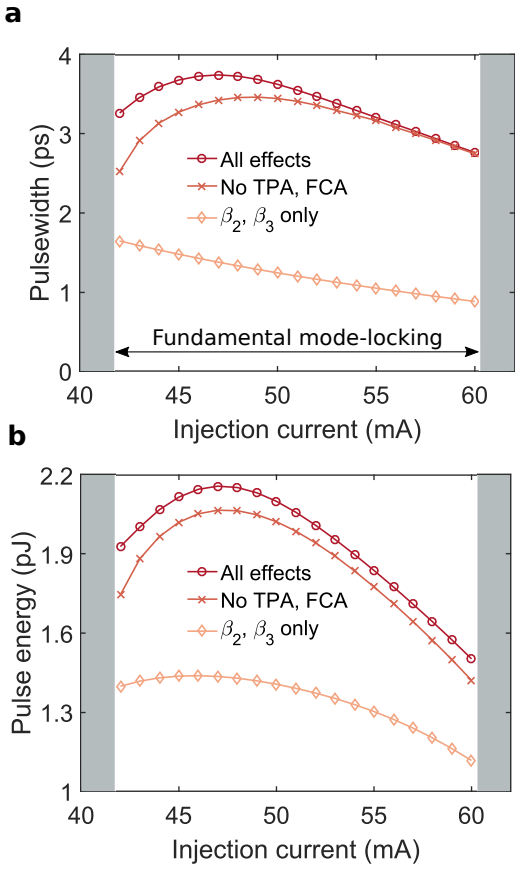

Figure 3.8: Output pulse width (a) an pulse energy (b) as a function of injection current for $\gamma_{NL} = 69\ m^{-1}W^{-1}$ and $\beta_2 = 1.3\ ps^2/m$.

and the pulse energies are rather low (<2.2 pJ intracavity energy), the significance of FCA and TPA is limited. However, in general it is expected that nonlinear losses can play a salient role in chip-scale mode-locked lasers with a silicon waveguide cavity, and pose a limiting factor to the attainable output pulse energy [46]. As outlined in the previous chapter, switching to a silicon-nitride platform could be a valuable alternative to eliminate the potentially detrimental effects of nonlinear absorption [7, 46].

In case (3), the pulse width and peak power respectively decrease and increase with injection current. Moreover, although the pulse is significantly shorter compared to cases (1) and (2), the pulse energy is greatly reduced as well, leading to a lower average output power compared to the cases where the third-order nonlinearity is included.

The temporal and spectral evolution of the pulse in the laser cavity is depicted in Fig. 3.9. The pulse and the corresponding spectrum are shown at 6 locations along the laser cavity to visualize the impact of the SA, SOA and extended silicon waveguide cavity. The spectrum after split-step Fourier propagation is strongly broadened and red-shifted and reveals a subtle oscillatory structure at the peak, as can be expected based on the SPM-induced nonlinear phase shift [73]. Furthermore, the spectral filter turns out to significantly affect the pulse spectrum and hence plays an essential role for stabilization.

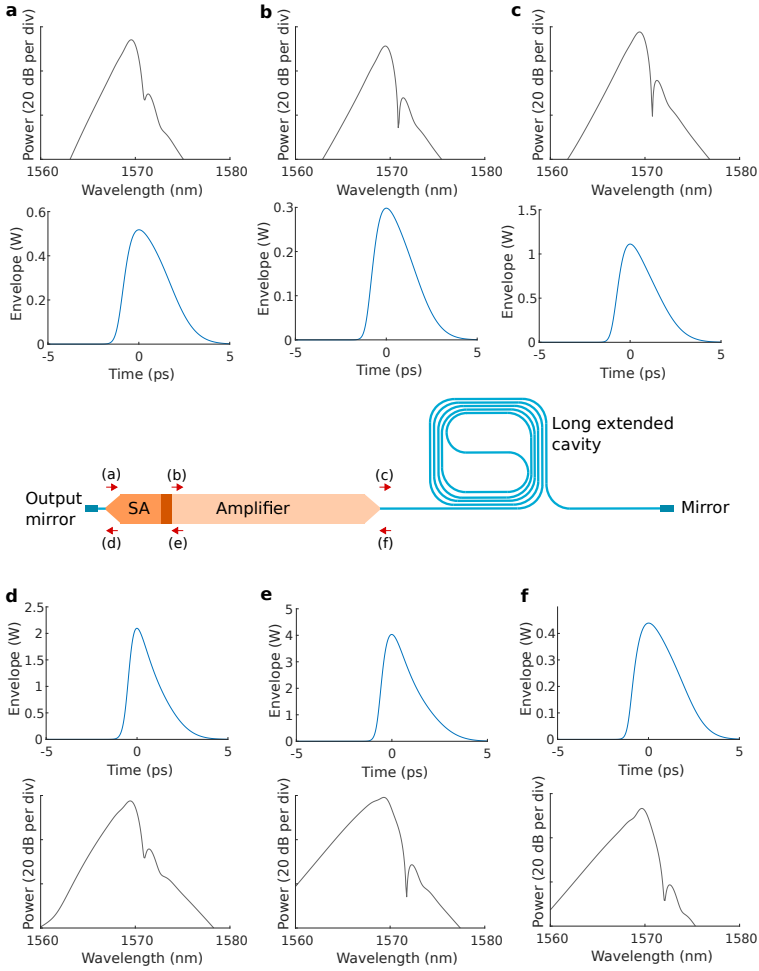

Figure 3.9: Temporal and spectral pulse evolution in the laser cavity. Pulse before the SA, after the spectral filter (a); after propagating through the SA and isolation section (b); before split-step Fourier propagation (c); after the SA, before the spectral filter and mirror (d); after amplification (e) and after propagation through the extended silicon cavity (f).

3.5 Generalized hybrid modeling approach

Although the hybrid model is suited to model conventional passively mode-locked laser diodes, the optical pulses are assumed to reside in a vanishing background to obey the periodic boundary conditions of the FFT. However, it is possible to generalize the hybrid modeling concept to extend its applicability, enabling modeling of pulsed regimes with nonvanishing backgrounds. This can be accomplished by matching the size of the temporal split-step Fourier window to the pulse repetition rate so that the periodicity condition of the FFT is always satisfied in steady-state.

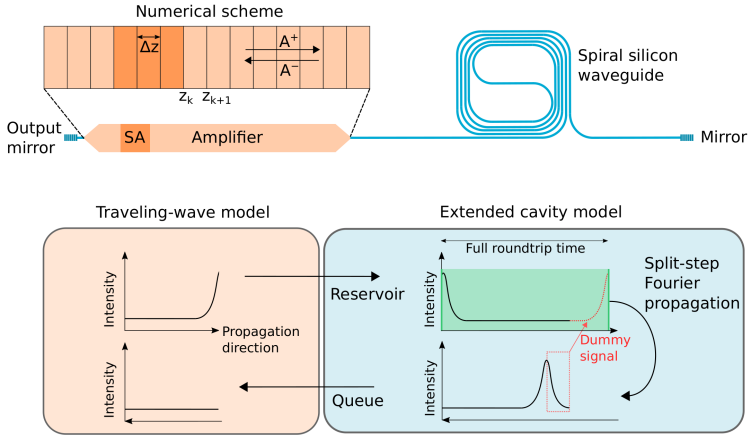

Figure 3.10: Simulation flow of the generalized hybrid mode-locked laser model.

3.5.1 Implementation

A schematic of the updated simulation flow is depicted in Fig. 3.10. For the passive waveguide, a 'reservoir' array with a size R corresponding with the total roundtrip time of the laser $\frac{\Delta T_R}{\Delta t}$, and a 'queue' array with a size Q corresponding to twice the propagation delay of the spiral waveguide cavity (i.e. $\frac{2L_{spiral}}{v_g \Delta t}$) are defined. With every time step Δt, the leading signal sample of the forward propagating wave of the TWM is added to the reservoir. At the same time, a signal sample from the queue is added to the backward propagating wave of the TWM. The forward propagating field A^+ hence feeds the reservoir, whereas the backward propagating field A^- is fed by the queue. This step-wise process continues until the queue has no remaining signal samples available for the backward propagating wave of the TWM. At this point, the reservoir – with a time span matching the total roundtrip time of the laser – is propagated using a split-step Fourier method to impose the losses, dispersive and nonlinear effects of the extended passive waveguide cavity.

The Q last signal samples of the propagated reservoir samples are subsequently substituted in the queue so that the simulation can continue. The R-Q leading samples of the propagated reservoir (highlighted in red in Fig. 1) are discarded as they solely served as dummy samples to match the split-step Fourier window to the total roundtrip time. These dummy samples are simply the trailing R-Q reservoir samples from the previous split-step Fourier step. The incorporation of dummy samples to match the split-step Fourier window size to the pulse repetition rate ensures amplitude periodicity to comply with the periodic boundary conditions of the FFT. For phase periodicity, which is generally not automatically satisfied, an artificial phase correction vector can be introduced. Here, a linearly increasing or decreasing phase correction vector $e^{j\phi}$ is multiplied with the reservoir samples prior to split-step propagation to avoid a phase jump between the first and last sample of the reservoir. After split-step propagation, the propagated reservoir samples are multiplied with the conjugate of the phase correction vector. This methodology allows one to consistently use the split-step method in contrast to our earlier work, enabling e.g. the modeling of pulsed regimes in nonvanishing backgrounds.

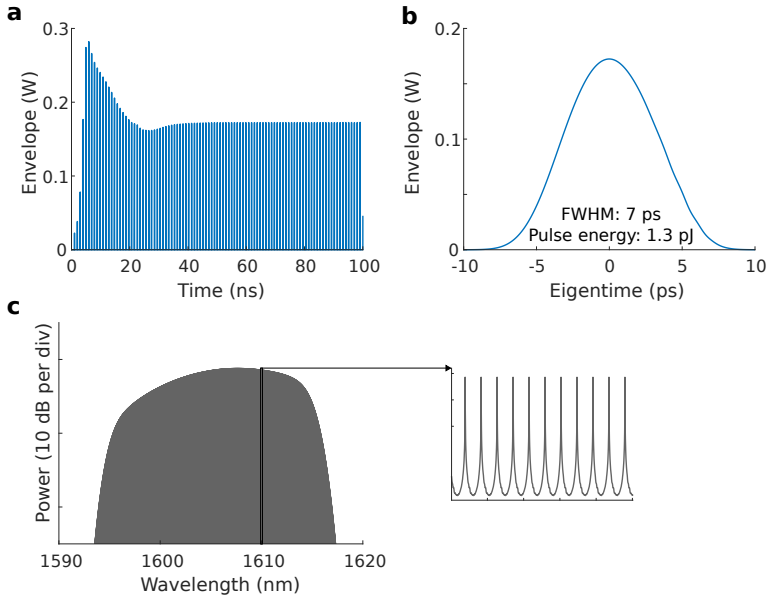

Figure 3.11: Mode-locked laser simulation example. (a) Signal build-up at the output facet. (b) Pulse profile. (c) Optical spectrum.

3.5.2 Simulation example

To exemplify the generalized hybrid model, it is applied to the 1 GHz III-V-Si mode-locked laser reported in [8]. A slightly modified traveling-wave model was employed, which includes distributed gain dispersion rather than a localized spectral filter, as outlined in section 3.3 and in [2]. The simulation results are depicted in Figure 3.11. A single broad input pulse was injected to circumvent the problem of self-starting. Some qualitative agreement can be observed with the reported experimental results, although further optimization of the model's parameters is needed. The generalized model was implemented in Python, and the code and the used parameters can be found on GitHub [74].

3.6 Conclusion

In this chapter, a hybrid modeling strategy for mode-locked laser diodes was demonstrated. The hybrid model combines the traveling-wave modeling technique for the active semiconductor laser sections with a nonlinear Schrödinger equation, implemented using a split-step Fourier method, for the extended passive waveguide cavity. This novel approach paves the way to include a wide range of physical phenomena, such as the semiconductors physics of the SOA and SA as well as the dispersive and nonlinear properties of the extended passive laser cavity while simultaneously limiting the model's computational workload. The model was exemplified using a heterogeneous III-V-on-silicon MLL example. The impact of dispersion and third-order nonlinearity on the pulse train and stability of the MLL were shown, hereby demonstrating the relevance to include these effects. We believe such a hybrid modeling strategy can be valuable to study low-repetition-rate MLLs, as for these devices dispersive and nonlinear effects of the long extended cavity can become important.

Compared to mode-locked laser models based on delay differential equations (DDEs) [27–29], the traveling-wave approach does not presume a ring-cavity geometry with unidirectional propagation. Unidirectional ring-cavity mode-locked lasers do not exist in practice and are hence merely an idealization. Furthermore, in some cases it might be desirable to account for reflections at various interfaces in the semiconductor sections of the mode-locked laser. In addition, the split-step Fourier method easily incorporates other potentially relevant effects of the extended passive waveguide such as the Raman effect. Mode-locked laser models based on DDEs have yet to demonstrate this ability. While DDE-based models can offer a powerful alternative and offer insight into the underlying dynamics, they hence exhibit a reduced physical accuracy [75, 76]. We believe a hybrid model with a TWM therefore offers a valuable complementary modeling technique to DDE-based approaches.

Recently, Ir. Maxim Torreele has incorporated the PHIsim TWM in the hybrid model in the context of his Master thesis "A Hybrid Modeling Technique for On-Chip Extended Cavity Semiconductor Mode-Locked Lasers". PHIsim is an open-source model, developed by Erwin Bente et al. at Eindhoven University of Technology [62], and includes many more physical effects (such as the Kerr-effect, TPA, etc.) compared to the simple traveling-wave model which was used in this chapter. In addition, the work of Ir. Maxim Torreele et al. further improves upon the original PHIsim code by including distributed gain dispersion. For more details, we refer to the Master Thesis of Maxim Torreele [77]. The associated Python code is available on Github [78].

Given the limited computational complexity, the hybrid modeling approach allows one to conduct extensive parametric studies and explore novel operating regimes such as chip-scale soliton mode-locking. Such studies could advance our current understanding of mode-locked laser diodes, potentially leading to a new generation of improved on-chip mode-locked lasers. However, further development is still needed to serve this vision. Firstly, the large number of parameters that needs to be set for the traveling-wave model poses a tedious optimization challenge. Although some parameters can straightforwardly be extracted from measurements (for example the gain of the SOA), typically not all parameters are easily retrieved experimentally or known in advance. Moreover, the device parameters can rely critically on the manufacturing process, ultimately limiting the attainable accuracy of the model. Building a material library or Process Design Kit (PDK) with experimentally validated amplifiers and saturable absorbers could be an approach to make the model more readily accessible and allow one to quickly obtain some approximate results. Secondly, for the generalized hybrid model, it has been noticed that for long simulation times a small periodic fluctuation can be observed. These fluctuations occur when the optical pulse shifts through the border of the SSF window. In this case, the resulting output pulse is in fact a concatenation of two pulses originates from subsequent split-step Fourier simulation cycles. This nonphysical perturbuation might be induced by the linear phase gradient that is applied over the pulse to ensure phase periodicity of the SSF window (as discussed in section 3.5.1). However, the precise origin of this bug remains unknown and should be investigated further in future work. Fortunately, for the results reported here, this fluctuation is relatively small and does not display a destabilising effect on reaching or maintaining the equilibrium mode-locked operating point. Thirdly, several physical effects have currently been ignored. For example, the incorporation of thermal effects is likely relevant, in particular when considering heterogeneous micro-transfer printed lasers which are often prone to heat accumulation. Fourthly, although PHIsim is written in the C++ language, the split-step Fourier method as well as the interface between the traveling-wave model and the split-step Fourier method are written in Python. Therefore, considerable headroom

remains to drastically bring down the overall computation time. Finally, extensive experimental validation of the model is essential to eliminate any undiscovered bugs and proof the model's physical accuracy. With the aforementioned developments that are still needed to transform the current hybrid model to an established open-source simulation package, one could consider existing commercial tools instead. Commercial models, such as those offered by Photon Design, have already been thoroughly optimized and validated, and are therefore well-suited to simulate heterogeneous mode-locked laser diodes [40].

References

[1] S. Cuyvers, S. Poelman, K. Van Gasse, and B. Kuyken. *Hybrid modeling approach for mode-locked laser diodes with cavity dispersion and nonlinearity*. Scientific Reports, 11(1):10027, May 2021.

[2] S. Cuyvers, G. Morthier, F. Leo, and B. Kuyken. *Generalized hybrid model for extended cavity mode-locked laser diodes*. In Annual Symposium of the IEEE Photonics Society Benelux Chapter, pages 1–4, 2021.

[3] A. L. Gaeta, M. Lipson, and T. J. Kippenberg. *Photonic-chip-based frequency combs*. Nature Photonics, 13(3):158–169, Mar 2019.

[4] S. A. Diddams, T. Udem, J. C. Bergquist, E. A. Curtis, R. E. Drullinger, L. Hollberg, W. M. Itano, W. D. Lee, C. W. Oates, K. R. Vogel, and D. J. Wineland. *An Optical Clock Based on a Single Trapped 199Hg+ Ion*. Science, 293(5531):825–828, 2001.

[5] S. T. Cundiff and A. M. Weiner. *Optical arbitrary waveform generation*. Nature Photonics, 4(11):760–766, Nov 2010.

[6] S. T. Cundiff and J. Ye. *Colloquium: Femtosecond optical frequency combs*. Rev. Mod. Phys., 75:325–342, Mar 2003.

[7] S. Cuyvers, B. Haq, C. Op de Beeck, S. Poelman, A. Hermans, Z. Wang, A. Gocalinska, E. Pelucchi, B. Corbett, G. Roelkens, K. Van Gasse, and B. Kuyken. *Low Noise Heterogeneous III-V-on-Silicon-Nitride Mode-Locked Comb Laser*. Laser & Photonics Reviews, 15(8):2000485, 2021.

[8] Z. Wang, K. Van Gasse, V. Moskalenko, S. Latkowski, E. Bente, B. Kuyken, and G. Roelkens. *A III-V-on-Si ultra-dense comb laser*. Light: Science & Applications, 6(5):e16260–e16260, May 2017.

[9] Z. Lu, J. Liu, S. Raymond, P. Poole, P. Barrios, and D. Poitras. *312-fs pulse generation from a passive C-band InAs/InP quantum dot mode-locked laser*. Opt. Express, 16(14):10835–10840, Jul 2008.

[10] V. Moskalenko, S. Latkowski, S. Tahvili, T. de Vries, M. Smit, and E. Bente. *Record bandwidth and sub-picosecond pulses from a monolithically integrated mode-locked quantum well ring laser*. Opt. Express, 22(23):28865–28874, Nov 2014.

[11] S. Latkowski, V. Moskalenko, S. Tahvili, L. Augustin, M. Smit, K. Williams, and E. Bente. *Monolithically integrated 2.5 GHz extended cavity mode-locked ring laser with intracavity phase modulators*. Opt. Lett., 40(1):77–80, Jan 2015.

[12] V. Corral, R. Guzmán, C. Gordón, X. J. M. Leijtens, and G. Carpintero. *Optical frequency comb generator based on a monolithically integrated passive mode-locked ring laser with a Mach–Zehnder interferometer*. Opt. Lett., 41(9):1937–1940, May 2016.

[13] J. H. Marsh and L. Hou. *Mode-Locked Laser Diodes and Their Monolithic Integration*. IEEE J. Sel. Top. Quantum Electron., 23(6):1–11, 2017.

[14] S. Liu, X. Wu, D. Jung, J. C. Norman, M. J. Kennedy, H. K. Tsang, A. C. Gossard, and J. E. Bowers. *High-channel-count 20 GHz passively mode-locked quantum dot laser directly grown on Si with 4.1 Tbit/s transmission capacity*. Optica, 6(2):128–134, Feb 2019.

[15] M.-C. Lo, R. Guzmán, and G. Carpintero. *InP femtosecond mode-locked laser in a compound feedback cavity with a switchable repetition rate*. Opt. Lett., 43(3):507–510, Feb 2018.

[16] M. L. Davenport, S. Liu, and J. E. Bowers. *Integrated heterogeneous silicon/III-V mode-locked lasers*. Photon. Res., 6(5):468–478, May 2018.

[17] K. Van Gasse, S. Uvin, V. Moskalenko, S. Latkowski, G. Roelkens, E. Bente, and B. kuyken. *Recent Advances in the Photonic Integration of Mode-Locked Laser Diodes*. IEEE Photonics Technology Letters, 31(23):1870–1873, 2019.

[18] A. M. Perego, B. Garbin, F. Gustave, S. Barland, F. Prati, and G. J. de Valcárcel. *Coherent master equation for laser modelocking*. Nature Communications, 11(1):311, Jan 2020.

[19] J. Javaloyes and S. Balle. *Mode-Locking in Semiconductor Fabry-Pérot Lasers*. IEEE Journal of Quantum Electronics, 46(7):1023–1030, 2010.

[20] J. Javaloyes and S. Balle. *Anticolliding design for monolithic passively mode-locked semiconductor lasers*. Opt. Lett., 36(22):4407–4409, Nov 2011.

[21] J. Javaloyes and S. Balle. *Freetwm: A Simulation Tool for Multisection Semiconductor Lasers.*, 2012.

[22] M. Dong, N. M. Mangan, J. N. Kutz, S. T. Cundiff, and H. G. Winful. *Traveling Wave Model for Frequency Comb Generation in Single-Section Quantum Well Diode Lasers*. IEEE Journal of Quantum Electronics, 53(6):1–11, 2017.

[23] F. Li, J. Yuan, Z. Kang, Q. Li, and P. K. A. Wai. *Modeling Frequency Comb Sources*. Nanophotonics, 5(2):292 – 315, 2016.

[24] H. A. Haus, J. G. Fujimoto, and E. P. Ippen. *Structures for additive pulse mode locking*. J. Opt. Soc. Am. B, 8(10):2068–2076, Oct 1991.

[25] H. Haus. *Mode-locking of lasers*. IEEE Journal of Selected Topics in Quantum Electronics, 6(6):1173–1185, 2000.

[26] H. Haus, J. Fujimoto, and E. Ippen. *Analytic theory of additive pulse and Kerr lens mode locking*. IEEE Journal of Quantum Electronics, 28(10):2086–2096, 1992.

[27] A. G. Vladimirov and D. V. Turaev. *A new model for a mode-locked semiconductor laser*. Radiophysics and Quantum Electronics, 47(10):769–776, Oct 2004.

[28] A. G. Vladimirov and D. Turaev. *Model for passive mode locking in semiconductor lasers*. Phys. Rev. A, 72:033808, Sep 2005.

[29] S. Slepneva, B. Kelleher, B. O'Shaughnessy, S. Hegarty, A. Vladimirov, and G. Huyet. *Dynamics of Fourier domain mode-locked lasers*. Opt. Express, 21(16):19240–19251, Aug 2013.

[30] Kane Yee. *Numerical solution of initial boundary value problems involving maxwell's equations in isotropic media*. IEEE Transactions on Antennas and Propagation, 14(3):302–307, 1966.

[31] A. Gordon, C. Y. Wang, L. Diehl, F. X. Kärtner, A. Belyanin, D. Bour, S. Corzine, G. Höfler, H. C. Liu, H. Schneider, T. Maier, M. Troccoli, J. Faist, and F. Capasso. *Multimode regimes in quantum cascade lasers: From coherent instabilities to spatial hole burning*. Phys. Rev. A, 77:053804, May 2008.

[32] Y. Wang and A. Belyanin. *Active mode-locking of mid-infrared quantum cascade lasers with short gain recovery time*. Opt. Express, 23(4):4173–4185, Feb 2015.

[33] J. Hader, J. V. Moloney, and S. W. Koch. *Microscopic theory of gain, absorption, and refractive index in semiconductor laser materials-influence of conduction-band nonparabolicity and Coulomb-induced intersubband coupling*. IEEE Journal of Quantum Electronics, 35(12):1878–1886, 1999.

[34] A. G. Vladimirov, A. S. Pimenov, and D. Rachinskii. *Numerical Study of Dynamical Regimes in a Monolithic Passively Mode-Locked Semiconductor Laser*. IEEE Journal of Quantum Electronics, 45(5):462–468, 2009.

[35] M. Homar, J. V. Moloney, and M. San Miguel. *Travelling wave model of a multimode Fabry-Perot laser in free running and external cavity configurations*. IEEE Journal of Quantum Electronics, 32(3):553–566, 1996.

[36] M. Rossetti, P. Bardella, and I. Montrosset. *Time-Domain Travelling-Wave Model for Quantum Dot Passively Mode-Locked Lasers*. IEEE Journal of Quantum Electronics, 47(2):139–150, 2011.

[37] S. Cuyvers, B. Haq, C. O. de Beeck, S. Poelman, A. Hermans, Z. Wang, G. Roelkens, K. Van Gasse, and B. Kuyken. *Ultra-Dense III-V-on-Silicon Nitride Frequency Comb Laser*. In 2020 European Conference on Optical Communications (ECOC), pages 1–3, 2020.

[38] PhotonDesign. *PICWave*. `https://www.photondesign.com/products/picwave`, 2023.

[39] PhotonDesign. *Harold*. `http://www.photond.com/products/harold`, 2023.

[40] PhotonDesign. *Mode-locked laser diode*. `https://www.photond.com/products/picwave/picwave_applications_03`, 2023.

[41] K. J. Blow and D. Wood. *Theoretical description of transient stimulated Raman scattering in optical fibers*. IEEE Journal of Quantum Electronics, 25(12):2665–2673, 1989.

[42] R. A. Fisher and W. K. Bischel. *Numerical studies of the interplay between self-phase modulation and dispersion for intense plane-wave laser pulses*. Journal of Applied Physics, 46(11):4921–4934, 1975.

[43] G. Agrawal. *Chapter 2 - Pulse Propagation in Fibers*. In G. Agrawal, editor, Nonlinear Fiber Optics (Fifth Edition), Optics and Photonics, pages 27 – 56. Academic Press, Boston, fifth edition edition, 2013.

[44] I. Cristiani, R. Tediosi, L. Tartara, and V. Degiorgio. *Dispersive wave generation by solitons in microstructured optical fibers*. Opt. Express, 12(1):124–135, Jan 2004.

[45] Q. Lin, O. J. Painter, and G. P. Agrawal. *Nonlinear optical phenomena in silicon waveguides: Modeling and applications*. Opt. Express, 15(25):16604–16644, Dec 2007.

[46] A. Hermans, K. Van Gasse, J. O. Kjellman, C. Caër, T. Nakamura, Y. Inada, K. Hisada, T. Hirasawa, S. Cuyvers, S. Kumari, A. Marinins, R. Jansen, G. Roelkens, P. Soussan, X. Rottenberg, and B. Kuyken. *High-pulse-energy III-V-on-silicon-nitride mode-locked laser*. APL Photonics, 6(9):096102, 2021.

[47] S. Roy, S. K. Bhadra, and G. P. Agrawal. *Femtosecond pulse propagation in silicon waveguides: Variational approach and its advantages*. Optics Communications, 281(23):5889 – 5893, 2008.

[48] H. Zhou, S.-W. Huang, X. Li, J. F. McMillan, C. Zhang, K. K.-Y. Wong, M. Yu, G.-Q. Lo, D.-L. Kwong, K. Qiu, and C. W. Wong. *Real-time dynamics and cross-correlation gating spectroscopy of free-carrier Drude slow-light solitons*. Light: Science & Applications, 6(6):e17008–e17008, Jun 2017.

[49] J. M. Dudley, G. Genty, and S. Coen. *Supercontinuum generation in photonic crystal fiber*. Rev. Mod. Phys., 78:1135–1184, Oct 2006.

[50] A. M. Heidt. *Efficient Adaptive Step Size Method for the Simulation of Supercontinuum Generation in Optical Fibers*. Journal of Lightwave Technology, 27(18):3984–3991, 2009.

[51] J. Wei, C. Ciret, M. Billet, F. m. c. Leo, B. Kuyken, and S.-P. Gorza. *Supercontinuum Generation Assisted by Wave Trapping in Dispersion-Managed Integrated Silicon Waveguides*. Phys. Rev. Applied, 14:054045, Nov 2020.

[52] T. R. Taha and M. I. Ablowitz. *Analytical and numerical aspects of certain nonlinear evolution equations. II. Numerical, nonlinear Schrödinger equation*. Journal of Computational Physics, 55(2):203 – 230, 1984.

[53] U. Bandelow, M. Radziunas, A. Vladimirov, B. Hüttl, and R. Kaiser. *40 GHz Mode-Locked Semiconductor Lasers: Theory, Simulations and Experiment*. Optical and Quantum Electronics, 38(4):495–512, Mar 2006.

[54] E. A. J. M. Bente, Y. Barbarin, M. J. R. Heck, and M. K. Smit. *Modeling of integrated extended cavity InP/InGaAsP semiconductor modelocked ring lasers*. Optical and Quantum Electronics, 40(2):131–148, Mar 2008.

[55] A. G. Vladimirov, D. Turaev, and G. Kozyreff. *Delay differential equations for mode-locked semiconductor lasers*. Opt. Lett., 29(11):1221–1223, Jun 2004.

[56] S. Keyvaninia, S. Uvin, M. Tassaert, X. Fu, S. Latkowski, J. Mariën, L. Thomassen, F. Lelarge, G. Duan, P. Verheyen, G. Lepage, J. V. Campenhout, E. Bente, and G. Roelkens. *Narrow-linewidth short-pulse III-V-on-silicon mode-locked lasers based on a linear and ring cavity geometry*. Opt. Express, 23(3):3221–3229, Feb 2015.

[57] G. P. Agrawal and N. A. Olsson. *Self-phase modulation and spectral broadening of optical pulses in semiconductor laser amplifiers*. IEEE Journal of Quantum Electronics, 25(11):2297–2306, 1989.

[58] S. Balle. *Simple analytical approximations for the gain and refractive index spectra in quantum-well lasers*. Phys. Rev. A, 57:1304–1312, Feb 1998.

[59] U. Bendelow, M. Radziunas, J. Sieber, and M. Wolfrum. *Impact of gain dispersion on the spatio-temporal dynamics of multisection lasers*. IEEE Journal of Quantum Electronics, 37(2):183–188, 2001.

[60] R. G. Baets, K. David, and G. Morthier. *On the distinctive features of gain coupled DFB lasers and DFB lasers with second-order grating*. IEEE Journal of Quantum Electronics, 29(6):1792–1798, 1993.

[61] H. E. Lassen, H. Olesen, and B. Tromborg. *Gain compression and asymmetric gain due to the Bragg grating induced by the standing waves in Fabry-Perot lasers*. IEEE Photonics Technology Letters, 1(9):261–263, 1989.

[62] E. A. J. M. Bente, Y. Barbarin, M. J. R. Heck, and M. K. Smit. *Modeling of integrated extended cavity InP/InGaAsP semiconductor modelocked ring lasers*. Optical and Quantum Electronics, 40(2):131–148, Mar 2008.

[63] S. Cuyvers. *HybridMLLmodel-ScientificReportsPaper*. `https://github.com/stijncuyvers/HybridMLLmodel-ScientificReportsPaper`, 2021.

[64] S. Wang, A. Docherty, B. S. Marks, and C. R. Menyuk. *Comparison of numerical methods for modeling laser mode locking with saturable gain*. J. Opt. Soc. Am. B, 30(11):3064–3074, Nov 2013.

[65] C. Gordón, M. Cumbajín, G. Carpintero, E. Bente, and J. Javaloyes. *Absorber Length Optimization of On-Chip Colliding Pulse Mode-Locked Semiconductor Laser*. IEEE Journal of Selected Topics in Quantum Electronics, 24(1):1–8, 2018.

[66] A. D. Bristow, N. Rotenberg, and H. M. van Driel. *Two-photon absorption and Kerr coefficients of silicon for 850–2200nm*. Applied Physics Letters, 90(19):191104, 2007.

[67] *Lumerical MODE*. `https://www.lumerical.com/products/mode/`. Accessed: 2020-05-08.

[68] S. Keyvaninia, S. Uvin, M. Tassaert, Z. Wang, X. Fu, S. Latkowski, J. Marien, L. Thomassen, F. Lelarge, G. Duan, G. Lepage, P. Verheyen, J. V. Campenhout, E. Bente, and G. Roelkens. *III-V-on-silicon anti-colliding pulse-type mode-locked laser*. Opt. Lett., 40(13):3057–3060, Jul 2015.

[69] F. X. Kartner, I. D. Jung, and U. Keller. *Soliton mode-locking with saturable absorbers*. IEEE Journal of Selected Topics in Quantum Electronics, 2(3):540–556, 1996.

[70] M. Marconi, J. Javaloyes, S. Barland, S. Balle, and M. Giudici. *Vectorial dissipative solitons in vertical-cavity surface-emitting lasers with delays*. Nature Photonics, 9(7):450–455, Jul 2015.

[71] A. F. J. Runge, D. D. Hudson, K. K. K. Tam, C. M. de Sterke, and A. Blanco-Redondo. *The pure-quartic soliton laser*. Nature Photonics, 14(8):492–497, Aug 2020.

[72] W. J. Tomlinson, R. H. Stolen, and A. M. Johnson. *Optical wave breaking of pulses in nonlinear optical fibers*. Opt. Lett., 10(9):457–459, Sep 1985.

[73] G. Agrawal. *Chapter 4 - Self-Phase Modulation*. In G. Agrawal, editor, Nonlinear Fiber Optics (Fifth Edition), Optics and Photonics, pages 87 – 128. Academic Press, Boston, fifth edition edition, 2013.

[74] S. Cuyvers. *GenHybridMLLmodel*. `https://github.com/stijncuyvers/GenHybridMLLmodel`, 2021.

[75] A. Pimenov, S. Slepneva, G. Huyet, and A. G. Vladimirov. *Dispersive Time-Delay Dynamical Systems*. Phys. Rev. Lett., 118:193901, May 2017.

[76] Pimenov, Alexander, Amiranashvili, Shalva, and Vladimirov, Andrei G. *Temporal cavity solitons in a delayed model of a dispersive cavity ring laser*. Math. Model. Nat. Phenom., 15:47, 2020.

[77] M. Torreele. *Hybrid Modeling Technique for On-Chip Extended Cavity Mode-Locked Semiconductor Lasers*. Master's thesis, Ghent University, 2022.

[78] M. Torreele. *MLL-hybrid-model*. `https://github.com/mtorreel/MLL-hybrid-model`, 2022.

4

Micro-transfer printing silicon thin films

In this chapter, micro-transfer printing of crystalline silicon is demonstrated to enable the integration of semiconductor optical amplifiers on generic low-refractive-index integrated photonic platforms such as silicon nitride or thin-film lithium niobate. In contrast to the custom silicon-nitride-on-silicon-on-insulator platform used in chapter 2, this chapter aims to provide a more general integration methodology which is compatible with standard commercially available low-index integrated photonic platforms, for example those currently offered by Ligentec or HyperLight. The content presented in this chapter has been published in part in [1–5].

4.1 Introduction

Silicon nitride has been widely recognized as a promising material to complement conventional silicon-on-insulator platforms [6, 7]. The importance of silicon nitride relies on its exceptional passive performance, including low propagation losses, a wide transparency window, and high power-handling capabilities. These properties have sparked academic and commercial interest in silicon nitride for diverse applications, including telecommunications [8], optical frequency comb generation [9, 10], chip-scale nonlinear photonics [11], sensing [12], and quantum photonics [13].

At the same time, thin-film lithium niobate has recently attracted considerable

attention, in particular for applications where a large electro-optic coefficient or strong second-order optical nonlinearity are desired [14]. As silicon and silicon nitride exhibit centrosymmetric crystallinity, their second-order nonlinear response vanishes [15]. Lithium niobate is therefore considered as a valuable optical material to extend the scope of integrated photonic platforms. Although lithium niobate is already widely used commercially in bulk modulators for fiber-optic communication links, the high power usage and large size of bulk lithium niobate components prohibit further scaling [14]. Significant research efforts have therefore been devoted towards the development of integrated formats, for example the thin-film lithium niobate on insulator (LNOI) platform [16] or thin-film lithium niobate on sapphire (TFLN-on-sapphire) platforms [17]. As a result, devices such as optical transceivers, among others, can enjoy the benefits of lithium niobate without sacrificing the small package sizes silicon photonics and other photonic integration approaches make possible [14]. In recent years, several devices have been demonstrated using TFLN, such as high-speed modulators with bandwidths exceeding 100 GHz [16] and frequency agile electro-optic comb generators on LNOI [18]. Moreover, the TFLN platform has recently become commercially available. For example, the Harvard spin-off company HyperLight currently offers custom solutions and foundry services based on their proprietary TFLN platform.

Still, both the silicon nitride platform and the TFLN platform by themselves are purely passive platforms (apart from thermo-optic tuning capabilities). The integration of other materials, such as III-V semiconductors, is therefore essential to enable important device functionalities, including photodetection and optical amplification [19]. However, the large refractive index difference between silicon nitride or TFLN, and III-V semiconductors (e.g. $\Delta n \sim 1.3 - 1.5$ for InP-based materials) makes it challenging to make use of direct evanescent coupling, which has been used to realize heterogeneous III-V lasers on the silicon-on-insulator platform [20]. Early demonstrations therefore relied on an edge-coupling (hybrid integration) approach instead. III-V-silicon-nitride hybrid single-mode lasers with high spectral purity [21–23] (lorentzian linewidths below 1 kHz), tunable lasers [24], and mode-locked lasers [25] have been demonstrated in recent years. Furthermore, an integrated pockels laser, where a reflective semiconductor optical amplifier (RSOA) chip was edge coupled to a LNOI PIC, was recently reported [26]. Yet, to enable dense integration of active devices, flip-chip integration or heterogeneous integration are often favored [20]. Hybrid integration through flip-chip attachment of an InP SOA on a low-loss silicon nitride platform was recently demonstrated [27]. Furthermore, flip-chip integration of a DFB InP laser on a LNOI PIC with an optical output power up to 60 mW was recently reported [28]. Such a flip-chip integration approach simultaneously enables a compact device footprint and good thermal management as the III-V chip is bonded directly on the (silicon) substrate of the target PIC [27]. Despite these advantages, hetero-

geneous integration is typically preferred when higher-volume manufacturing is envisioned, owing to the significantly lower cost.

4.2 Approaches for heterogeneous III-V integration on low-index integrated photonic platforms

Several approaches have been pursued to build heterogeneous lasers on silicon nitride. Firstly, silicon-on-insulator (SOI) wafers can be bonded on the silicon nitride wafer. After removal of the silicon substrate and the burried oxide layer, the silicon layer is patterned to form an intermediate coupling layer, enabling efficient evanescent coupling between the silicon nitride layer and the III-V waveguide [29–31]. Alternatively, the silicon nitride layer can be deposited directly, through LPCVD or PECVD, on a patterned and planarized SOI wafer [32, 33]. This approach was used in chapter 2 to build III-V-on-silicon-nitride mode-locked lasers [10]. In this case, light couples evanescently from the silicon nitride waveguide to the silicon waveguide underneath it, and subsequently from the silicon waveguide to the III-V waveguide above it. However, such an approach requires a custom platform which is expensive and currently not readily available from most commercial foundries.

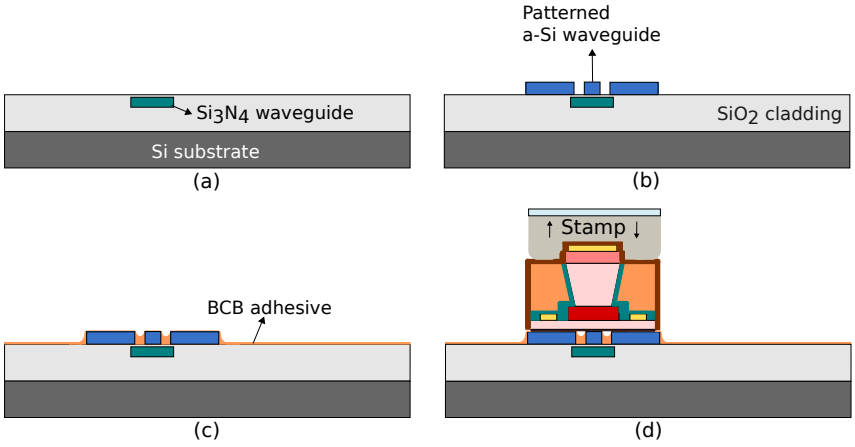

Figure 4.1: Schematic process flow for the heterogeneous integration of III-V devices on silicon nitride using an intermediate a-Si:H layer and micro-transfer printing. A similar process flow could be utilized for the thin-film lithium niobate platform. (a) Patterned and planarized silicon nitride PIC. (b) Deposition of a thin etch stop layer and an a-Si:H coupling layer. The a-Si:H is patterned using lithography and dry etching techniques. (c) Deposition of a thin BCB adhesive layer. (d) Integration of a III-V device using micro-transfer printing.

An alternative approach was proposed by C. Op de Beeck et al., where a hydrogenated amorphous silicon (a-Si:H) coupling layer is used instead of a crystalline

silicon layer [20]. This layer can be deposited with PECVD and the need for a wafer bonding step is hence omitted. To avoid the need for planarization steps, the a-Si:H and silicon nitride layer can be patterned in a top-down fashion after the a-Si:H deposition. A thin SiO_2 layer is introduced in between the silicon nitride and a-Si:H layer to avoid damaging the silicon nitride surface during the patterning of the a-Si:H layer [20]. Alternatively, in case the silicon nitride PIC has been patterned and planarized already, one can deposit a thin etch stop layer prior to the a-Si:H deposition, and pattern the a-Si:H layer. This fabrication process is illustrated in Fig. 4.1. After patterning, a thin adhesive layer of DVS-BCB can be deposited and the III-V device can be conveniently integrated on the PIC using micro-transfer printing.

Similar approaches can be employed to heterogeneously integrate active devices on TFLN. Recently, wafer-bonded III-V-on-LNOI lasers and photodetectors have been demonstrated without an intermediate coupling layer [34]. A multi-section spotsize converter with an ultra-narrow III-V taper tip of 150 nm was defined with electron beam lithography to achieve acceptable coupling efficiencies. However, requiring such narrow III-V taper tips complicates fabrication. Moreover, a high alignment accuracy between the LNOI taper and the III-V taper is essential, making such an approach unsuitable for micro-transfer printing technology. Finally, researchers recently aimed to combine the ultra-low losses of silicon nitride waveguides with the unique electro-optic and nonlinear properties of TFLN by bonding an LNOI wafer to a silicon nitride wafer. Such an approach has for example been demonstrated in [35], where a DFB laser was edge-coupled to a TFLN-on-silicon-nitride PIC to build low-noise frequency agile lasers. In principle, the laser source could also be heterogeneously integrated on either the silicon nitride or TFLN by using one of the aforementioned methods.

4.3 Heterogeneous III-V integration using two micro-transfer printing steps

Although the aforesaid heterogeneous integration techniques have proven successful to develop integrated laser sources, these approaches are currently largely incompatible with some leading commercial foundry platforms, for example the silicon nitride platform offered by Ligentec. As these silicon nitride PICs have a thick SiO_2 top cladding to enable ultra-low losses, heterogeneous integration needs to be performed in a recess. This poses a significant challenge for existing integration methods. In contrast to the obvious incompatibility of conventional wafer bonding approaches, an a-Si:H layer could in principle be deposited in a recess. However, it was found that the resulting planarity of such an a-Si:H film in a recess can be poor, making subsequent patterning irrealizable. Furthermore, the properties of

the deposited a-Si:H layer can vary significantly, as they strongly depend on the deposition parameters, complicating reproducibility. Moreover, a-Si:H typically exhibits higher waveguide losses compared to crystalline silicon, and tends to suffer from material degradation for high power pulses [36], ultimately limiting the application scope of such devices.

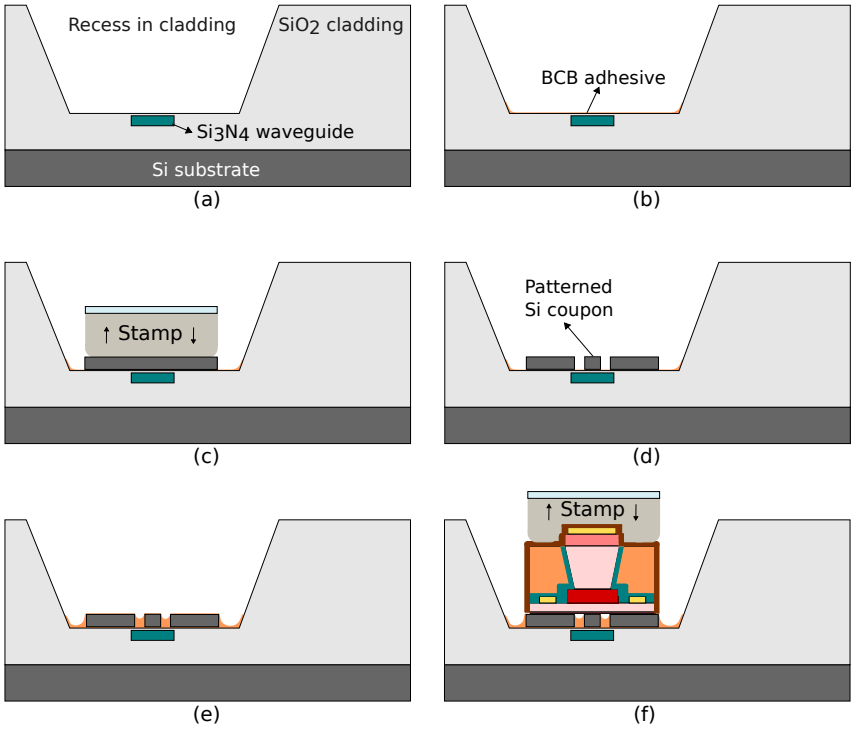

Figure 4.2: Process flow for the heterogeneous integration of III-V devices on silicon nitride (or TFLN) using two micro-transfer printing steps. (a) Patterned and planarized silicon nitride PIC. (b) Deposition of a thin etch stop layer (in case the Si coupon are patterned after the integration) and, optionally, a thin adhesive BCB layer. (c) Micro-transfer printing of the silicon coupon. (d) Patterning of the Si coupon. If desired, the Si coupon can be patterned on the SOI source wafer, prior to micro-transfer printing. (e) Deposition of a thin adhesive BCB layer. (f) Micro-transfer printing of the III-V device.

In this chapter we propose an alternative heterogeneous integration strategy based on two micro-transfer printing steps. A typical process flow is illustrated in Fig. 4.2. In a first step, a crystalline silicon coupon, which constitutes the intermediate coupling layer, is transfer printed on the target PIC. The silicon coupon can be pre-patterned prior to micro-transfer printing or it can be patterned after the integration (as is the case in Fig. 4.2). In a second step the III-V device is transfer printed on top of the patterned silicon coupon. Given the limited number

of required processing steps and the possibility to micro-transfer print in a recess, this novel approach enables rapid prototyping and allows for low-loss III-V integration on generic commercially available low-index passive photonic platforms. Moreover, as crystalline silicon is employed, material degradation at high optical powers is avoided and lower losses can, in principle, be attained compared to an a-Si:H layer [19].

In the remainder of this chapter, a detailed description of the two-step micro-transfer printing process is provided, and the design and fabrication of the Si coupons are discussed. Two different approaches are investigated: Si coupons without encapsulation, where release etching is performed using vapor-phase hydrofluoric acid (vapor-phase HF) etching, and Si coupons encapsulated with photoresist, where liquid HF release etching is used. Furthermore, some transmission measurements are discussed to evaluate the current performance of the micro-transfer printed coupling layer. Finally, some device demonstrations on silicon nitride and TFLN, led by colleagues at Ghent University - imec, are presented to exemplify the potential of the presented integration methodology. The author together with Ir. Stijn Poelman took the lead in the design, fabrication and characterization of the two-step micro-transfer printing process. Ir. Stijn Poelman carried out the electron-beam (e-beam) lithography steps and measurements on the Ligentec PIC. Ir. Jasper De Witte and and Ir. Tom Reep optimized the taper design for evanescent coupling. Ir. Tom Vandekerckhove performed the atomic force microscopy (AFM) measurements. The device demonstrations were led by the author, Ir. Stijn Poelman, Dr. Camiel Op de Beeck, and Ir. Isaac Luntadila Lufungula.

4.4 Design and fabrication of Si coupons without encapsulation

While traditional micro-transfer printing approaches typically rely on photoresist or silicon nitride encapsulation of the coupon (anchoring the coupon to the source substrate), an approach without an encapsulating material can reduce the number of required processing steps and can hence, potentially, lower the overall fabrication cost. Still, a cost trade-off exists: eliminating the encapsulation reduces the number of required processing steps at the expense of a lower achievable coupon density on the source wafer. Furthermore, the absence of an encapsulation material could eliminate possible incompatibilities with some of the widely used release etchants, such as HF, needed to suspend the coupons on the source wafer.

The Si coupons are defined on the native SOI source wafer. For the devices demonstrated in this chapter, the SOI wafer comprises a 400 nm Si device layer and a 2 μm buried SiO_2 layer. The SOI wafers are manufactured by SOITEC using

their proprietary smart cut process based on wafer bonding and ion implantation [37]. Silicon coupons can be pre-patterned on the source SOI wafer, prior to micro-transfer printing, or they can be patterned after integration. Both approaches are discussed in the following sections.

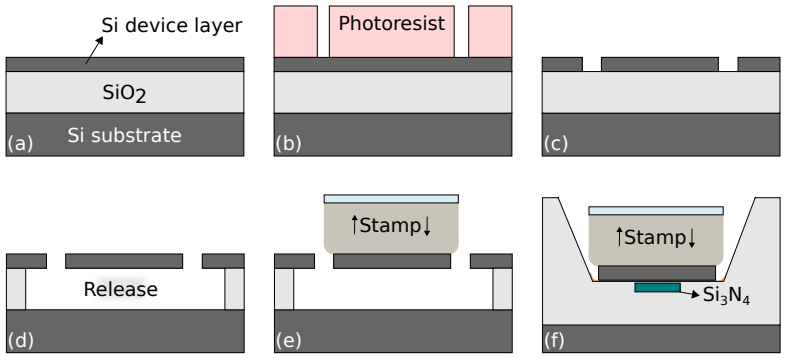

Figure 4.3: Process flow to define suspended silicon coupons for micro-transfer printing. (a) Standard silicon-on-insulator wafer. (b) Photoresist patterning. (c) RIE dry etching of the Si coupon and resist removal. (d) Release etching of the SiO_2 layer using vapor-phase HF. (e) Pickup of a suspended Si coupon. (f) Printing of the Si coupon on a Si_3N_4 PIC.

4.4.1 Unpatterned Si coupons

A schematic overview of the process flow to define Si coupons without an encapsulating material, is shown in Fig. 4.3. The sample is first thoroughly cleaned using acetone, isopropylalcohol (IPA) and an oxygen plasma treatment. If necessary, one could use a more extensive cleaning procedure based on the RCA standard clean procedure [38]. For example, wet chemical removal of particles on a silicon wafer can be done using the Standard Clean 1 solution (SC-1), which is a mixture of NH_4OH, H_2O_2 and H_2O, while metal contamination can be removed using the Standard Clean 2 solution (SC-2), based on a mixture of HCl, H_2O_2 and H_2O. Next, a TI Prime adhesion promotor (spincoated at 4000 rpm for 40s and subsequently baked at 120 °C for 3 minutes) and AZ 5214E photoresist (spincoated at 4000 rpm for 40s and subsequently baked at 100 °C for 3 minutes) are deposited. A high resolution photoresist is used to enable accurate definition of the supporting Si tethers. The photoresist is exposed for 22 s using an MA-6 contact aligner (300-320 nm lithography) and developed for approximately 35 s in AZ400K:H_2O (1:3), as illustrated in Fig. 4.3(b). Next, the Si coupons are anisotropically etched using reactive ion etching with a mixture of CF_4, SF_6, and H_2. The etch is monitored in-situ using an etch depth monitor from Intellemetrics. However, some overetching can be tolerated as the SiO_2 layer will be removed at a later stage anyway. After etching, the photoresist is stripped using acetone/IPA and an oxygen

plasma (Fig. 4.3(c)). A microscope picture of two etched Si coupons is depicted in Fig. 4.4(a). Fig. 4.4(b) shows a close-up of a corresponding tether which secures the Si coupon to the surrounding Si material. It was experimentally found that a tether breaking region width around 1 μm, combined with a tether spacing between 100 μm and 150 μm works well for micro-transfer printing 400 nm thick silicon films. However, the latter specification did not seem critical in contrast to the width of the breaking region. A breaking region which is too narrow can lead to premature tether breaking and a collapse of the Si coupon. On the other hand, when the breaking region is too wide, either the coupon cannot be picked up or part of the surrounding Si support structure is peeled of along with the coupon itself.

Finally, the SiO_2 layer underneath the coupon is etched using an Idonus HF vapor-phase etcher to suspend the Si coupons on the source wafer, without suffering from capillary forces which can lead to a collapse of the suspended Si coupon (Fig. 4.3(d)). To speed up the release etch, one can first submerge the SOI wafer in liquid HF (e.g. 40% HF) and switch to vapor-phase HF for the final part of the release process. Furthermore, depending on the dimensions of the coupon and the envisioned design, holes could be introduced in the coupon through which the HF can penetrate, reducing the required etching time.

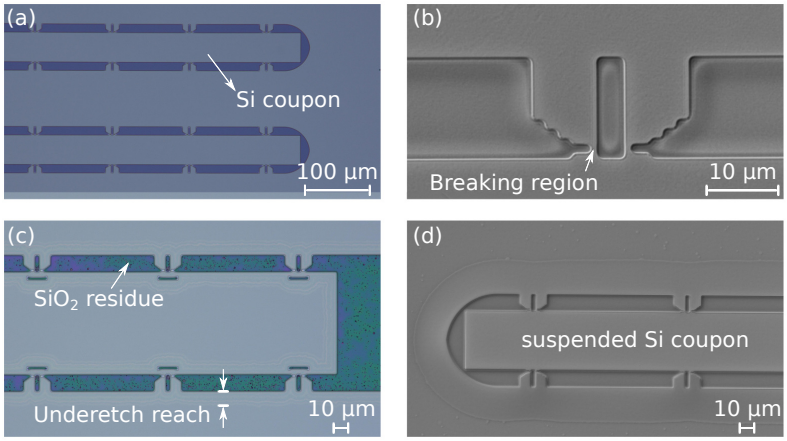

Figure 4.4: (a) Si coupons on the source SOI wafer after reactive ion etching. (b) Close-up of a tether from the Si coupon highlighted in (a). (c) Incomplete release etch, indicating a direction-dependent etch rate. (d) Suspended Si coupon after the release etch.

The vapor-phase HF etch rate of thermally grown SiO_2 is on the order of 15 μm/hour at $40\,^{\circ}$C. However, this etch rate should be considered as a ballpark number because of several reasons. Firstly, a significant start-up time seems to exist (on the order of 15 minutes), as it takes some time for the vapor-phase HF etchant to stabilize and reach the SiO_2 layer. Hence, if the sample is loaded in

the vapor-phase HF tool for 15 minutes or less, barely any SiO_2 is etched. Furthermore, it is observed that the etch rate of thermally grown SiO_2 is typically strongly anisotropic: for a given etch time, the SiO_2 seems to etch much faster in the horizontal plane compared to the vertical direction. This can be seen from Fig. 4.4(c), where a sample with Si coupons was first submerged for 90 s in 40% liquid HF and subsequently etched for 45 min in vapor-phase HF. Although the 2 μm thick SiO_2 is not completely removed where it was initially exposed (some SiO_2 residue is still visible), an underetch distance of 11 μm is observed in the horizontal direction. From this, one can conclude that the etching rates in the horizontal and vertical directions differ by roughly an order of magnitude. Amorphous SiO_2 layers such as PECVD SiO_2 do not display this anisotropic etching behavior [39]. Thirdly, some etch rate variation is found between different SOI wafers, presumably owing to different SOI manufacturing methods (smart cut versus alternative methods) or slightly different SiO_2 growth parameters. Finally, the used vapor-phase etching tool displays some etch rate variability, most likely resulting from temperature fluctuations as well as from aging and contamination of the HF in the reservoir. A more advanced vapor-phase etching tool could resolve this issue. Given the aforementioned reasons, it is recommended to check the SOI wafer at regular intervals (e.g. every 45 min) during the release etch. Such an approach also lowers the risk of unnoticed HF condensation on the wafer surface, which frequently has detrimental consequences. A microscope picture of a suspended Si coupon with a size of 1670 μm$\times$46 μm is shown in Fig. 4.4(d).

Once the Si coupons are suspended on the source SOI wafer, micro-transfer printing can commence, as illustrated in Fig. 4.3(e),(f). Some suggested micro-transer printing parameters are listed in Table 4.1. Similar to micro-transfer-printing of III-V devices, a thin adhesive DVS-BCB layer (for example CYCLOTENE 3022-35:mesitylene 1:6) can be used to ensure a high printing yield. Nevertheless, micro-transfer printing without an intermediate adhesive was also investigated and is discussed in subsequent sections.

Source Parameters	**Target Parameters**	**Clean Parameters**
Pick acceleration: 1 g	Print speed: 0.002 mm/s	Clean speed: 0.05 mm/s
Overdrive distance: 0.11 mm	Overdrive distance: 0.13 mm	Overdrive distance:: 0.13 mm
Overdrive speed: 0.02 mm/s	Overdrive speed: 0.03 mm/s	Overdrive speed: 0.03 mm/s
Pick speed: 100 mm/s	X shear distance: 0.02 mm	
	Y shear distance: 0.01 mm	
	Shear speed: 0.1 mm/s	
	Shear duration: 5 s	

Table 4.1: Micro-transfer printing parameters for Si thin films as set in the X-Celeprint µTP-100 tool. The default working distance of 100 μm is assumed.

After micro-transfer printing, the BCB is cured at 280°C in vacuum. Next, the

Si coupon is patterned on the target PIC using electron-beam lithography and the same reactive ion etching recipe as was used to pattern the coupons on the source wafer. As the BCB adhesive is etched approximately half as fast as the Si during dry etching, and as the BCB layer is much thinner than the Si (<100 nm versus 400 nm), no BCB remains around the Si coupon. A separate etch stop layer, here 35 nm of Al_2O_3 (etched at approximately 5 nm/min), is therefore needed to protect the silicon nitride or TFLN below. If desired, this Al_2O_3 layer can be removed after etching using a strongly diluted KOH solution or a KOH-based photoresist developer. An etch rate of 10 nm/min was measured for evaporated Al_2O_3 in AZ400K:H_2O 1:3.

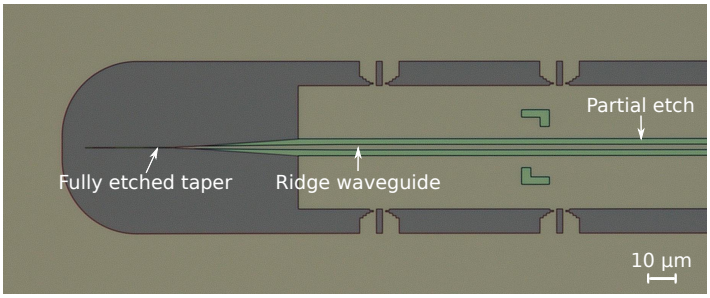

Figure 4.5: Microscope picture of a pre-patterned Si coupon on the source SOI wafer. A first full etch defines the coupon periphery and tapers. A second partial etch step defines the ridge waveguide and markers for alignment during micro-transfer printing.

4.4.2 Pre-patterned Si coupons

To facilitate rapid prototyping, it is possible to pre-pattern the Si coupons on the source SOI wafer. In this case, an additional lithography and etching step are required during the source processing, but no patterning is required on the target PIC. Similar to the unpatterned Si coupons, the first dry etching step etches completely through the 400 nm Si layer. However, in contrast to the unpatterned Si coupons, e-beam lithography is employed rather than contact lithography because the narrow Si tapers (for evanescent coupling) are now defined simultaneously with the coupon periphery. The second patterning step is used to define a ridge waveguide in the center of the Si coupon. Again, e-beam lithography is employed to ensure a high resolution. To define the ridge waveguide, 180 nm is etched, leaving 220 nm of Si at the sides. A microscope picture of a pre-patterned Si coupon on the source SOI wafer is shown in Fig. 4.5. A transition region is included to adiabatically transition from a fully etched waveguide to a partially edged ridge waveguide. Furthermore, some overlap between the partial etch and full etch masks is introduced to tolerate some alignment error during e-beam lithography.

Although utilizing pre-patterned coupons minimizes the number of processing steps required on the target PIC, a number of challenges are associated with this approach. Firstly, the Si coupon needs to be accurately positioned on the target PIC to ensure efficient evanescent coupling. Although the taper design can be optimized for alignment tolerance, this typically requires longer (and hence more fragile) tapers [40, 41]. In contrast, the previous approach with unpatterned Si coupons benefits from lithographic alignment precision because the Si is patterned only after micro-transfer printing. Secondly, depending on the PIC platform used and the thickness of the silicon nitride or TFLN layer, the tapers possibly need to be long and narrow to acquire adequate coupling. Such long and narrow tapers are inherently fragile, leading to curling or rupturing during the release etch or during micro-transfer printing. As an example, Fig. 4.6(a) shows a printed coupon with a curled taper, after micro-transfer printing. To mechanically protect the tapers, two approaches were investigated. A first approach is to leave a thin sheet of Si (e.g. 30 nm) around the taper to mechanically support the taper at all times, as depicted in Fig. 4.6(b). However, such an approach requires an additional lithography and etching step. Moreover, a thin sheet is easily deformed and dents are observed in the sheet after the vapor-phase release etch. Although the sheet serves its purpose and tapers can remain intact during micro-transfer printing (provided that shear forces during micro-transfer printing are kept to a minimum), some excess losses can likely be expected from the dented sheet around the taper.

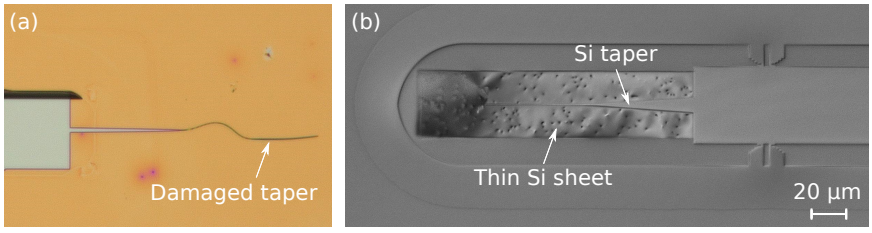

Figure 4.6: (a) Damaged Si taper after micro-transfer printing. (b) Suspended Si coupon on the source SOI wafer with a 30 nm thin sheet to mechanically support the taper.

A second approach consists of encapsulating the coupon and tapers with photoresist. For example, TI 35E photoresist can be used as it is specifically tailored to withstand HF etching. After micro-transfer printing, the resist encapsulation can be removed with an oxygen plasma. It was found that this approach is successful in protecting the tapers, although again, very little shear (particularly in the direction perpendicular to the taper) can be tolerated to avoid taper damage.

In summary, pre-patterned coupons can be of use to enable rapid prototyping, but they require careful alignment on the target PIC and, depending on the required taper dimensions, restrict the achievable yield of the micro-transfer printing process, as little shear forces can be applied during printing. For this reason,

unpatterned Si coupons are used in the remainder of this chapter.

Figure 4.7: Micro-transfer printed Si coupons on a Si dummy wafer. Most coupons suffer from cracks induced by stress at the supporting tethers of the coupon.

4.4.3 Crack barriers for enhanced yield

During micro-transfer printing, stress induced at the tethers can result in crack formation and propagation through the entire structure, leading to severe and intolerable damage to the integrated coupon. A microscope picture of micro-transfer printed Si coupons on a Si dummy wafer, shown in Fig. 4.7, illustrates this phenomenon. The crack occurrence probability depends on the dimensions of the tether's breaking region: a sufficiently weak breaking region in principle leads to seamless breakage and only sporadically leads to crack propagation through the coupon. However, the breaking region cannot be too thin either as this will lead to premature tether breaking and coupon collapse. This delicate balance therefore leaves little margin for fabrication tolerances and limits the overall micro-transfer printing yield. For this reason, so-called crack barriers are introduced as a way to mitigate crack propagation, originating from stress induced at the supporting tethers of a suspended material membrane, during micro-transfer printing.

Fig. 4.8 depicts a possible design of a Si coupon with crack barriers. A crack barrier is placed for every tether of the coupon as cracks can originate from any tether with approximately the same likelihood. The crack barrier consists of:

1. A trench, here 2 µm wide and 16 µm long, where the material is locally removed (i.e. partially or completely etched through). This trench can be fabricated using lithographic patterning and dry- or wet etching techniques.

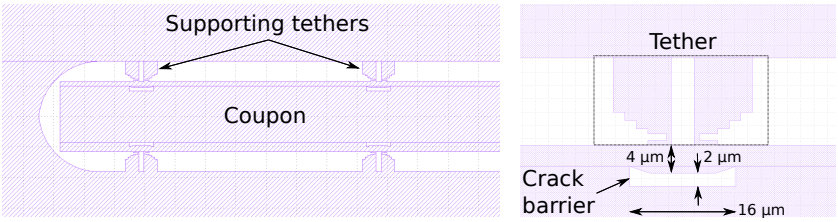

Figure 4.8: Designed Si coupon with crack barriers (image from GDS design file).

For the Si coupons presented here, the crack barriers are patterned in the same step as the coupon periphery and tethers. This avoids the need for additional processing steps.

2. It is important that the span of the trench exceeds the span of the tether's breaking region(s). This ensures that a crack originating from the tether reaches the crack barrier and avoids further crack propagation through the coupon.

3. The width of the barrier should be sufficiently small to limit the required area of the barrier while being sufficiently large to allow reliable patterning and etching with the available nanofabrication tools.

4. The specific shape of the crack barrier is not critical for its purpose. Here, a half bowtie shape is employed. The slightly larger width at the sides of the crack barrier provides a way to surround the tether, mitigating the impact of cracks that propagate under a larger angle (along the horizontal direction of the coupon).

5. The distance between the tether and the crack barrier, here 4 µm as depicted in Fig. 4.8, should be small enough to minimize the unusable space of the coupon while ensuring sufficient mechanical strength to certify that the weakest point remains at the intended tether breaking region.

A microscope picture of suspended Si coupons with crack barriers is shown in Fig. 4.9(a) and (b). Fig. 4.9(c) depicts a micro-transfer printed Si coupon on a silicon nitride PIC from Ligentec. The effectiveness of the crack barrier is illustrated in Fig. 4.9(d), where a propagating crack is blocked by the crack barrier, safeguarding the functional integrity of the coupon. Provided that the source SOI wafer is properly underetched, a near perfect picking and printing yield can be achieved for these 400 nm thick Si coupons, and several tens of coupons have been successfully integrated on various target PICs.

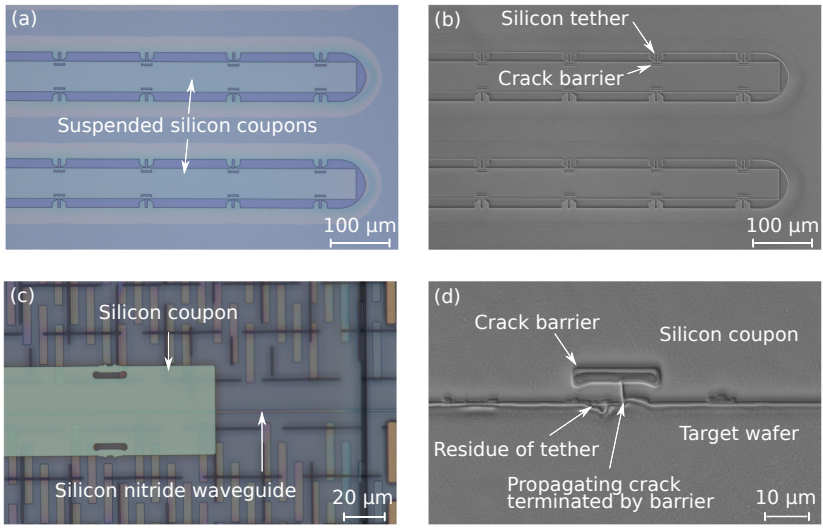

Figure 4.9: Experimental results of micro-transfer printed 400 nm thick Si coupons with crack barriers. Suspended Si coupons on the source SOI wafer: (a) microscope image and (b) shadow-effect-mode image. (c) Micro-transfer printed Si coupon on a silicon nitride PIC from Ligentec. (d) Example of crack propagation induced at the tether and terminated by the crack barrier.

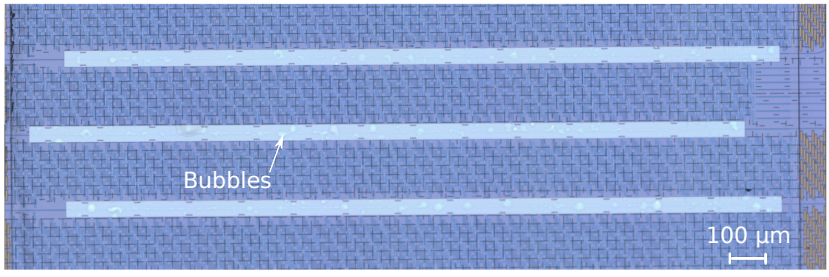

Figure 4.10: Micro-transfer printed Si coupons on a Ligentec silicon nitride PIC. Several bubbles are visible underneath the printed coupons, originating from particles on the PIC surface, contamination of the BCB adhesive, or residue from vapor-phase etching sticking to the coupon backside.

In some cases, bubbles are observed underneath the printed Si coupons. An extreme example is shown in Fig. 4.10. This problem can often be attributed to the presence of particles on the target PIC and contamination of the BCB mixture. A clean target surface can be achieved using a combination of acetone/IPA, Piranha (a mixture of H_2SO_4, H_2O_2, H_2O), standard cleaning solutions (see [38, 42]), or an oxygen plasma treatment. Furthermore, contaminants in the adhesive BCB

solution can (partially) be filtered using e.g. a Whatman PTFE membrane filter with 0.2 µm pore size. However, in some cases, the observed bubbles originate from surface roughness or residual oxide particles remaining after vapor-phase etching. This is most easily observed when coupons are micro-transfer printed without a BCB adhesive, as elaborated in the following section.

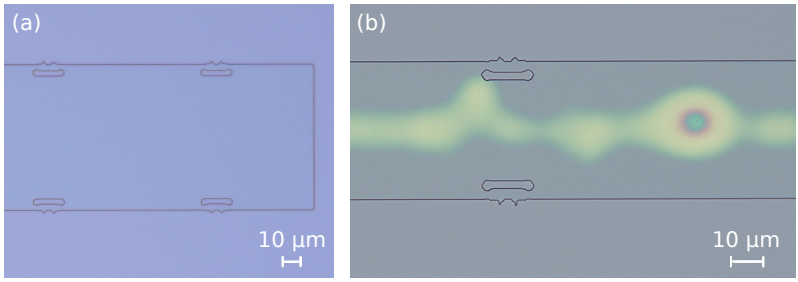

Figure 4.11: Silicon coupons on a dummy substrate, micro-transfer printed without an adhesive layer. (a) Low surface roughness and no apparent surface contamination. (b) Significant roughness on the coupon backside, apparent from the color difference at the center of the coupon, leads to poor adhesion of the coupon to the target surface.

4.4.4 Printing tests without a BCB adhesive

In some cases it is desirable to micro-transfer print without a BCB adhesive. For example, to minimize optical losses, to reduce the thermal resistance between the active device and the substrate, or when the temperature required to cure the BCB cannot be tolerated by the target PIC. It has been shown that when both the target and coupon surfaces have low roughness, below the nanometer level, micro-transfer printing can be reliably carried out without the use of an adhesive layer [43–45].

Fig. 4.11(a) depicts an 80 µm wide Si coupon on a dummy substrate, micro-transfer printed without an adhesive layer. The target surface was heated to 80°C and the target overdrive speed was reduced to 0.006 mm/s to facilitate the micro-transfer printing process. The printed coupon displays few bubbles or fringes, indicating a low surface roughness and few residual particles on the involved surfaces. The surface roughness of the coupon backside was measured with atomic force microscopy (AFM), and a RMS surface roughness of 0.12 nm was obtained, as illustrated in Fig. 4.12(a). In contrast, Fig. 4.11(b) depicts a printed Si coupon where a clear color difference can be observed at the center of the coupon. The fact that the color difference extends over the entire coupon length and is not limited to a few randomly located points, hints at a high surface roughness. Indeed, as illustrated in Fig. 4.12(b), the RMS surface roughness is 3.3 nm, and hence much higher compared to the printed coupon of Fig. 4.11(a). As the SOI souce

samples of Figs. 4.11(a), (b) originate from the same SOI wafer, this discrepancy can be attributed to the vapor-phase release etch. Although the exact mechanism is currently not well understood, it is probable that temperature fluctuations during vapor-phase etching (which in turn lead to etch rate fluctuations) play a role in the resulting surface roughness.

Besides variations in surface roughness, the current vapor-phase etching process often leaves some residual (oxide) particles on the source sample, as depicted in Fig. 4.13. During micro-transfer printing, some of these particles can stick to the coupon backside, leading to bubbles on the target PIC and, possibly, excessive waveguide losses. It was observed that additional vapor-phase etching does not dissolve the residual particles, in contrast to liquid HF which easily dissolves any residues. A more advanced vapor-phase etcher, with accurate temperature control and an active, continuous gas flow, can possibly resolve these issues.

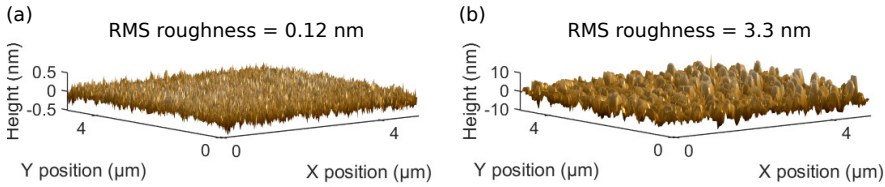

Figure 4.12: Surface roughness, measured with AFM, of the backside of a Si coupon with low roughness (a) and a coupon with high roughness (b).

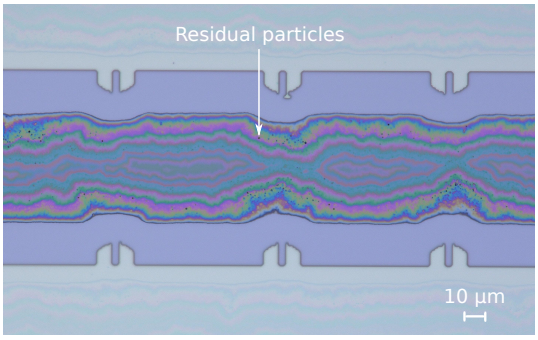

Figure 4.13: Residual particles (black dots) remaining on the SOI source sample after vapor-phase etching and coupon pick-up. Due to the anisotropic etching rate of thermal SiO_2, a pile of SiO_2 remains at the center, as is apparent from the colored fringes.

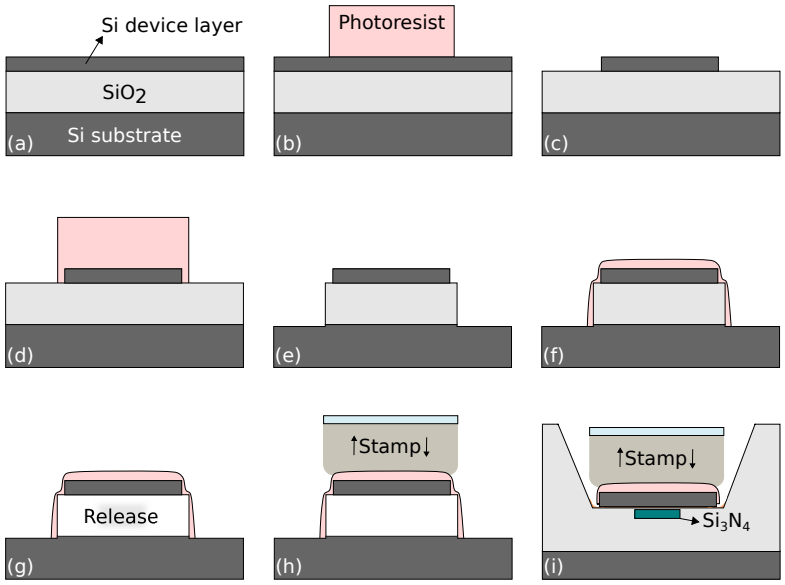

Figure 4.14: Process flow to define suspended photoresist-encapsulated silicon coupons for micro-transfer printing. (a) Standard silicon-on-insulator wafer. (b) Photoresist patterning. (c) RIE dry etching of the Si coupon and resist removal. (d) Photoresist patterning to define a mask for patterning the release layer. (e) RIE dry etching of the SiO_2 release layer and 100 nm of the Si substrate underneath. The resist is removed after etching. (f) Acid dip to remove the native oxide on the silicon substrate, and photoresist encapsulation of the coupons. (g) Release etching of the SiO_2 layer using liquid HF. (h) Pickup of a suspended Si coupon. (i) Printing of the Si coupon on a Si_3N_4 PIC.

4.5 Design and fabrication of Si coupons with photoresist encapsulation

To overcome the current challenges with vapor-phase etching, an alternative process flow was developed to enable liquid HF release etching. In this case, the coupons are encapsulated using photoresist and anchored to the silicon substrate. Although such a process flow requires more processing steps, coupons can be more densely integrated on the source wafer, hence making more efficient use of the source material. In addition, as the coupon is secured to the substrate, a long release etch can be tolerated, making careful timing of the release etch redundant. Alternatively, one could possibly stick to the previous process flow and employ critical point-drying to avoid coupon collapse during liquid release etching.

The process flow is schematically illustrated in Fig. 4.14. After thorough cleaning of the SOI sample, AZ5214E photoresist is patterned to serve as a mask for the coupon definition using RIE dry etching, analogous to the previously dis-

cussed process flow. However, in this case only the coupon itself is patterned and no surrounding silicon remains. A microscope picture of the patterned 80 μm wide coupons is depicted in Fig. 4.15(a). After resist stripping and cleaning, a second lithography step is performed to enable patterning of the SiO_2 release layer. A thicker TI35E photoresist is used for this purpose to ensure sufficient resist thickness to withstand the subsequent RIE dry etching step. The recipe used to dry etch the SiO_2 is based on a mixture of CF_4, SF_6, H_2 and exhibits an etching selectivity close to 1:1 with the photoresist. To ensure optimal adhesion of the photoresist encapsulation to the silicon substrate, etching is continued 100 nm into the substrate. A microscope picture of the resulting coupons is shown in Fig. 4.15(b).

Next, the coupons are encapsulated in photoresist. Just prior to the lithography step, an acid dip is performed, consisting of 7 s submersion in BHF:H_2O 1:10 and 7 s in H_2SO_4:H_2O_2:H_2O to remove the native oxide on the silicon substrate. The sample is subsequently rinsed in IPA and thoroughly dried with a nitrogen gun. The photoresist encapsulation is spincoated and patterned immediately afterwards. Two photoresists were tested for encapsulation: TI35E (4.1 μm thick) and AZ10XT (6.5 μm thick). The superior thickness of the latter is expected to provide more mechanical strength, and hence keep the coupons more easily suspended during the release etch. A microscope picture of the encapsulated coupons with AZ10XT photoresist is shown in Fig. 4.15(c). The sample with TI35E encapsulation was baked for 3 min at 125°C and flood exposed for 180 s, to increase its resilience to HF. However, it was later found that this is not strictly necessary, and both photoresists seem to survive the release etch without any additional measures. Finally, the SiO_2 release layer is selectively removed using 40% liquid HF for ∼15 min. The samples are subsequently rinsed using three cups of DI water, and left to dry in air. Blow drying is not recommended to avoid coupon collapse. A microscope picture of AZ10XT-encapsulated suspended coupons is shown in Fig. 4.15(d). For the sample with AZ10XT encapsulation, all coupons remained suspended. This is apparent from the colored fringes, as visible in Fig. 4.15(d). In contrast, a collapsed coupon displays no fringes and exhibits a dark color over the coupon surface. For the sample with TI35E encapsulation, roughly 1 out of 4 coupons collapsed, while all coupons remained suspended on another sample with the same TI35E encapsulation. From these observations, one can roughly conclude that the TI35E photoresist suffices for coupon widths $<$80 μm, while a thicker photoresist, such as AZ10XT, seems more appropriate for wide coupons ($\geq$80 μm).

To confirm the successful completion of the release etch, multiple 2000 μm × 80 μm Si coupons were micro-transfer printed on a dummy substrate, without using an adhesive layer. To facilitate the micro-transfer printing process, the target surface was heated to 80°C, analogous to previously discussed printing tests.

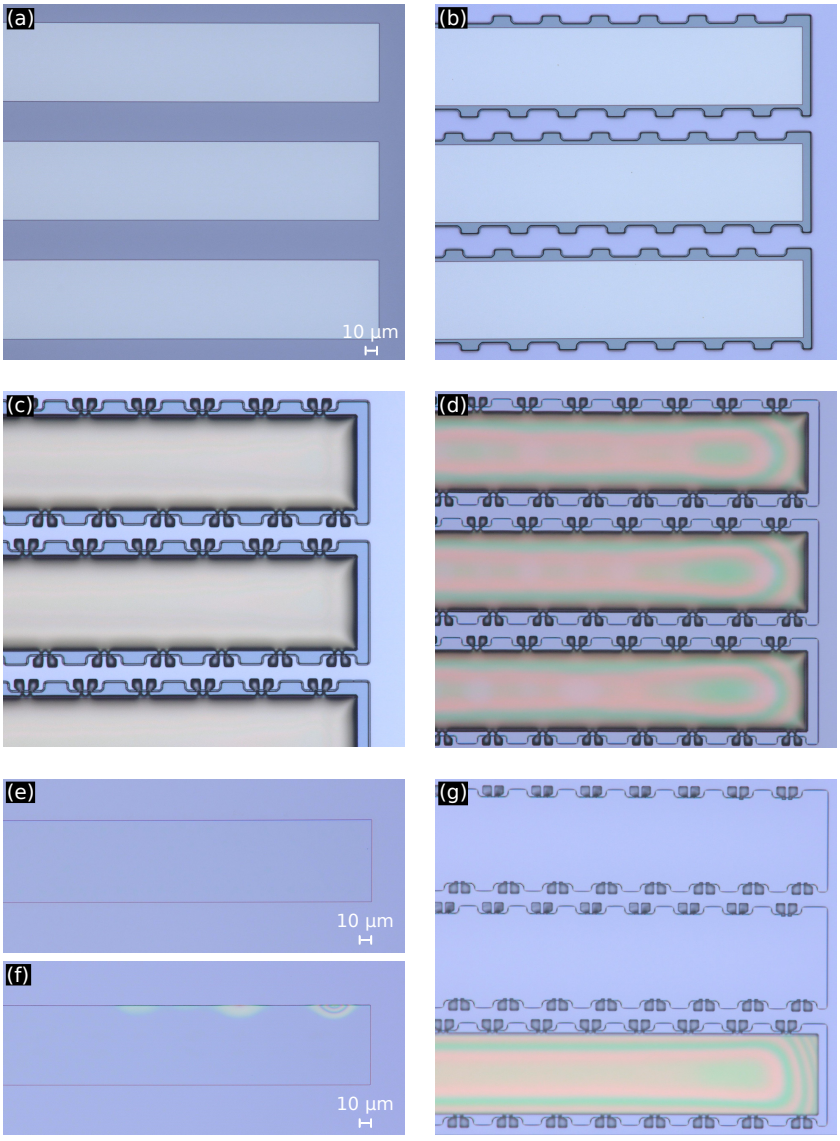

Figure 4.15: Microscope pictures of the Si coupons at various stages of the process flow. (a) Coupons after dry etching and resist removal. (b) Coupons after release layer patterning. (c) Coupons after photoresist encapsulation. (d) Suspended coupons after release etching with liquid HF. (e) Printed coupon after removal of the AZ10XT photoresist. (f) Printed coupon (from a different source sample than (e)) after removal of the TI35E photoresist. Some fringes are visible at the sides of the coupon, originating from photoresist particles underneath the coupon edge. (g) Source sample after picking up two coupons. The pick-up site is clean and no SiO_2 or residual particles are visible.

Figures 4.15(e) and (f) depict a micro-transfer printed Si coupon, respectively based on AZ10XT- and TI35E-photoresist encapsulation, after removal of the encapsulation with an oxygen plasma. In both cases, the coupon looks clean and no bubbles or particles are apparent, except for the top side of the coupon in Fig. 4.15(f). Here, some resist from the encapsulation got underneath the coupon during the pick-up process. This issue can typically be resolved by optimizing the tether dimensions and by increasing the size of the remaining SiO_2 layer prior to photoresist encapsulation, hereby ensuring that the tethers break in the horizontal plane. Furthermore, the seamless printing process, in spite of the absence of an adhesive layer, indicates a clean backside surface with a low surface roughness. This assumption is supported by the clean pick-up site on the source SOI sample, as depicted in Fig. 4.15(g). In contrast to the samples released with vapor-phase etching, no residual particles remain.

At the time of writing, over 60 photoresist-encapsulated Si coupons have been micro-transfer printed without an adhesive layer, with perfect yield, confirming the reliability and reproducibility of the process. Given the high yield, low surface roughness and superior cleanliness of the Si coupon backside, the approach based on photoresist-encapsulation and liquid HF release etching is currently preferred over the approach based on vapor-phase etching. Appendix C summarizes both process flows in detail to serve as a future reference.

4.6 Transmission measurements

A key property of the intermediate silicon coupling layer is its transmission loss, as this ultimately limits the total cavity loss of the heterogeneous III-V/Si/Si_3N_4 (or III-V/Si/TFLN) laser. To evaluate this property, Si coupons were micro-transfer printed on patterned Si_3N_4 PICs. After patterning the Si coupons with e-beam lithography and dry etching, the transmission losses were characterized with a Santec TSL510 tunable laser and a HP 8153A optical power meter. Three PICs were fabricated for characterization.

A first PIC, manufactured by Ligentec, incorporates 800 nm thick, 2 μm wide Si_3N_4 waveguides. Silicon coupons, fabricated through vapor-phase HF release etching, were micro-transfer printed on the Si_3N_4 waveguides (with a 35 nm Al_2O_3 etch stop layer and a 50 nm BCB adhesive layer in between the Si_3N_4 and the Si). Horizontal transmission measurements were carried out for two reference waveguides (without a silicon coupon on top) and two waveguides with a 2 mm long patterned silicon coupon. The Si tapers, used to adiabatically couple the fundamental TE mode from the Si_3N_4 waveguide to the Si waveguide and vice versa, are 170 μm long. The results are depicted in Fig. 4.16. The waveguides with a Si coupon were measured twice, each time with a different polarization. Furthermore, as the fiber drifted significantly during the measurements,

the reference transmission regularly drops below the transmission of the waveguides with a Si coupon. For this reason, coarse estimates on the excess loss, induced by the patterned Si coupon, are calculated based on the difference between the maximal reference transmission and the average transmission of the Si_3N_4/Si waveguides, as indicated in Fig. 4.16. Based on this approach, the first waveguide with a Si coupon exhibits an excess loss on the order of 3 dB while the second coupon-loaded waveguide exhibits an excess loss on the order of 6 dB. This discrepancy can likely be attributed to absorption by a residual particle underneath the Si coupon and/or higher coupling losses with the lensed fibers. Furthermore, strong resonance dips are observed in the transmission spectra of the first Si_3N_4/Si waveguide. The origin of these resonances is currently not well understood, but it is possibly caused by a damaged taper. The same reference waveguide on another PIC with the same Si structures did not display such resonances.

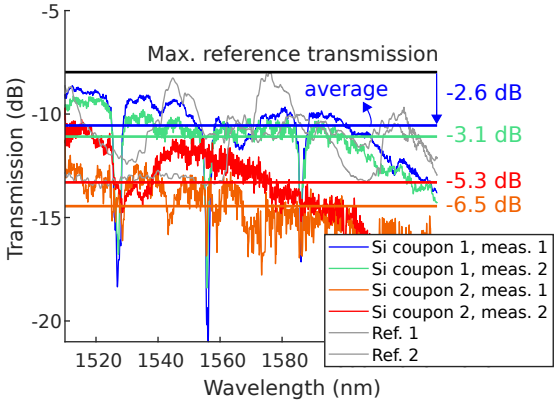

Figure 4.16: Horizontal transmission measurements of a silicon nitride PIC from Ligentec. Two silicon nitride waveguides with 2 mm long Si waveguides on top, and two reference waveguides without a Si coupon were measured. Estimates on the excess loss induced by the patterned Si coupon are calculated based on the difference between the maximal reference transmission and the average transmission of the Si_3N_4/Si waveguides.

As the present Ligentec design contains few test waveguides for characterization, a second, dedicated silicon nitride PIC was fabricated based on a 300 nm LPCVD Si_3N_4 wafer from LioniX. The design incorporates 24, 3 μm wide, silicon nitride waveguides with micro-transfer printed Si coupons, and 6 reference waveguides without a Si coupon. In contrast to the Ligentec PIC, the silicon coupons were here fabricated through photoresist encapsulation and liquid HF release etching, and coupons were printed without an adhesive BCB layer. The photoresist encapsulation was simply removed with acetone. From the 24 printed coupons, one detached during this cleaning step. Furthermore, grating couplers are used for

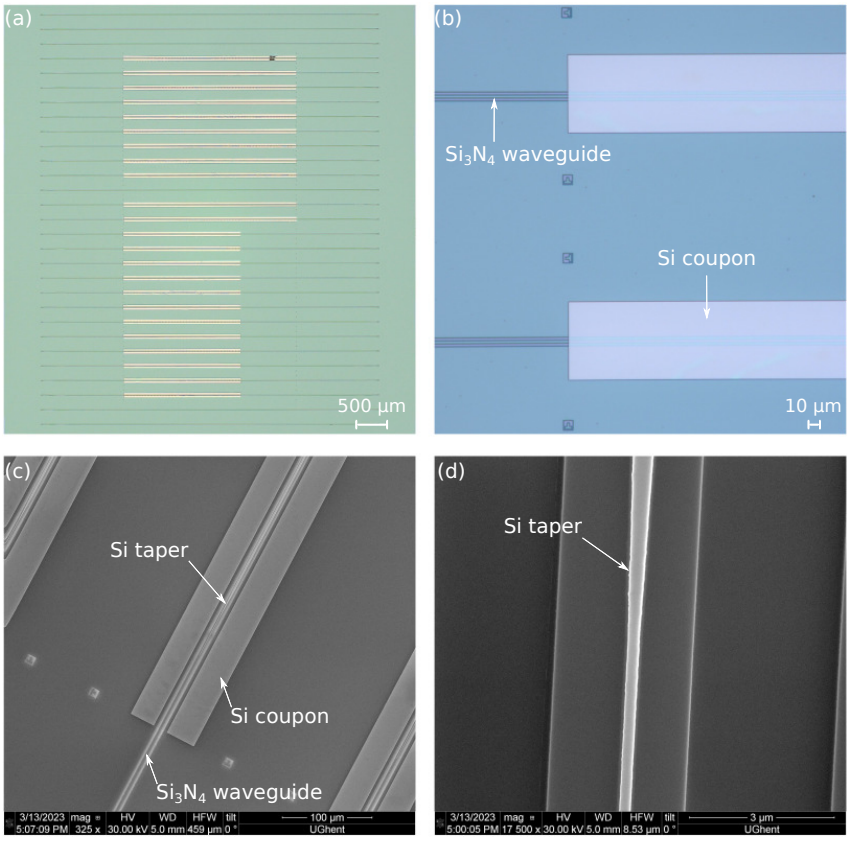

Figure 4.17: Images of a silicon nitride PIC with micro-transfer printed Si coupons. (a) Microscope picture of the sample with 23 printed coupons. (b) Close-up of two printed coupons. (c) SEM image of the sample after patterning of the Si waveguides. (d) Close-up SEM image, displaying significant sidewall roughness of the Si taper.

optical coupling. A microscope picture of the PIC with micro-transfer printed Si coupons is shown in Fig. 4.17(a) and a close-up of two printed coupons is shown in Fig. 4.17(b). A SEM image of a Si_3N_4 waveguide with a patterned Si coupon is shown in Fig. 4.17(c). The Si taper has a length of 84 µm. To differentiate grating coupler losses, Si taper losses, and Si_3N_4/Si waveguide losses (for a fixed Si waveguide width of 2 µm), the number of tapers along a single coupon is varied from 2 to 8, and also the waveguide lengths are varied. The measurement results were analyzed through multiple linear regression to estimate the individual loss contributions, depicted in Figs. 4.18(a), (b) and (c). From the 29 measurements, 8 were omitted for the analysis, as these waveguides suffered from one or more damaged tapers or a particle on the waveguide.

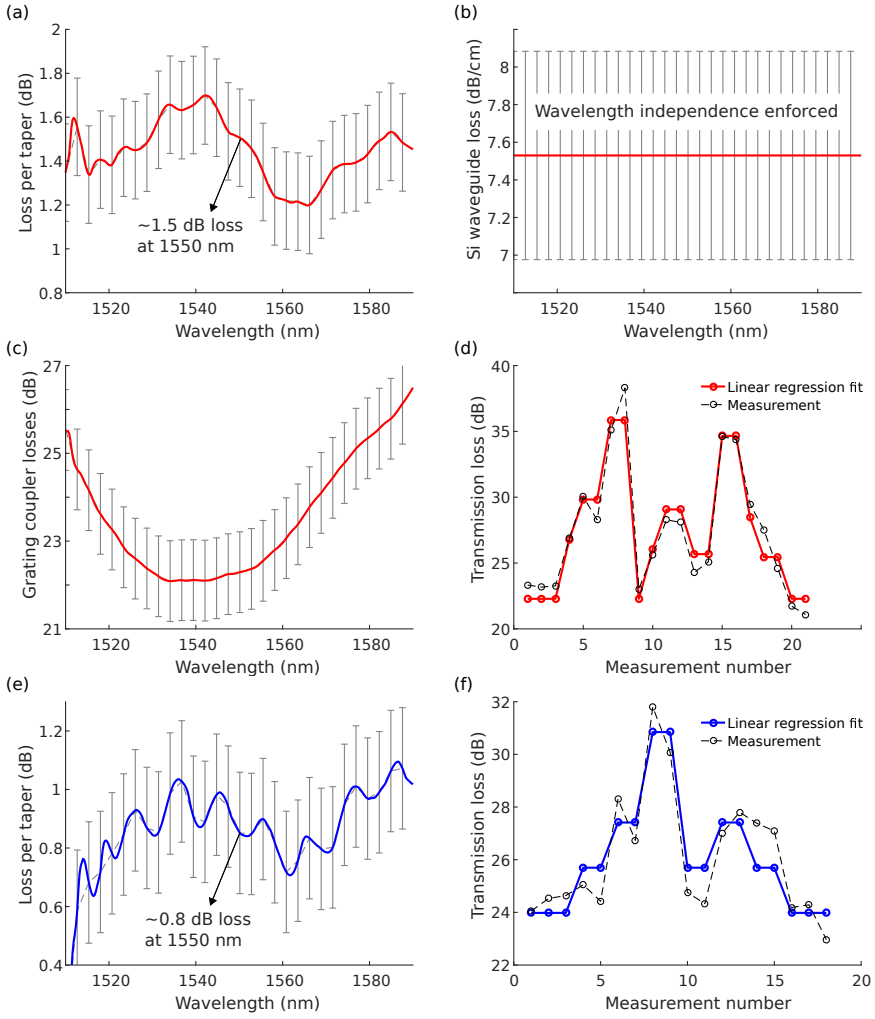

Figure 4.18: Estimation of the losses from the Si taper (a), Si waveguide (b), and silicon nitride grating couplers (c) based on multiple linear regression of 21 measurements. The Si coupons were micro-transfer printed on a patterned silicon nitride PIC from LioniX. The Si waveguide loss was enforced to be wavelength independent to improve the quality of the fit. The 95% confidence intervals of the parameter estimates are indicated with grey error bars. (d) Comparison of the total measured transmission losses and the corresponding predictions of the fit at 1550 nm. (e), (f) Measurement results of another PIC with the same design, where the Si taper dimensions were pre-compensated to account for the observed waveguide narrowing during the fabrication process. Assuming the same waveguide losses as in (b), the estimated taper losses are reduced from 1.5 dB/taper to 0.8 dB/taper at 1550 nm.

The waveguide loss was assumed to be wavelength independent to improve the fitting quality. Furthermore, the 95% confidence intervals of the parameter

estimates are indicated to quantify the uncertainty of the fit. Fig. 4.18(d) compares the total measured transmission loss with the prediction of the fit for each of the 21 considered measurements, indicating reasonable agreement. At a wavelength of 1550 nm, the loss per taper is approximately 1.5 dB, whereas the excess loss of the 2 μm wide Si waveguide on Si_3N_4 is around 7.5 dB/cm. Given that typical waveguide losses of fully etched SOI waveguides - based on the same e-beam lithography and etching processes - are on the order of 8-9 dB/cm, the latter indicates that losses of micro-transfer printed Si waveguides are comparable to conventional SOI waveguides.

It was observed with SEM that the Si tapers are approximately 55 nm narrower than initially designed. Simulations indicate that at 1550 nm, such a deviation results in a 1.2 dB transmission loss per taper (due to evanescent coupling to higher order modes), suggesting that the taper losses are currently dominated by the divergent taper dimensions. This issue can easily be resolved by pre-compensating the design before e-beam exposure.

A third PIC, with the same structures as the aforementioned LioniX PIC, was fabricated with pre-compensated Si taper dimensions. All 24 printed coupons remained attached to the target PIC during the encapsulation removal with acetone. The measurements were again analysed using multiple linear regression, and the results are depicted in Figs. 4.18(e) and (f). Assuming that the Si waveguide losses remain unchanged, the estimated taper loss at 1550 nm is reduced to 0.8 dB/taper. Due to some lateral misalignment of the Si taper during e-beam lithography, part of the optical power in the fundamental TE mode is coupled to a higher order TE mode ($\Delta n_g \approx 0.6$ [1]). This manifests itself as a ripple in the transmission spectrum. Provided that this misalignment can be largely mitigated in the future, a taper loss <0.4 dB/taper is expected to be possible. This estimate is based on considering the envelopes of the current transmission spectra for the regression analysis. Further improvement of the losses can be achieved by optimizing the e-beam and etching processes, as significant roughness is currently observed (as apparent from the SEM image in Fig. 4.17(d)). In addition, a Si ridge waveguide could be employed instead of a fully etched waveguide to reduce the impact of the waveguide's sidewall roughness.

4.7 Overview of device demonstrations

To exemplify the relevance and applicability of the two-step micro-transfer printing process, some recent demonstrations - mainly led by colleagues from Ghent

[1] The periodicity of the ripple in the transmission spectrum can be calculated based on the difference in group index between the fundamental and higher order mode (Δn_g), the length of the patterned Si coupon (L), and the central wavelength (λ_0): $\Delta\lambda_{ripple} = \frac{\lambda_0^2}{\Delta n_g L}$

University-imec - are discussed below. The Si coupons used in these demonstrations were fabricated with vapor-phase HF etching without a photoresist encapsulation.

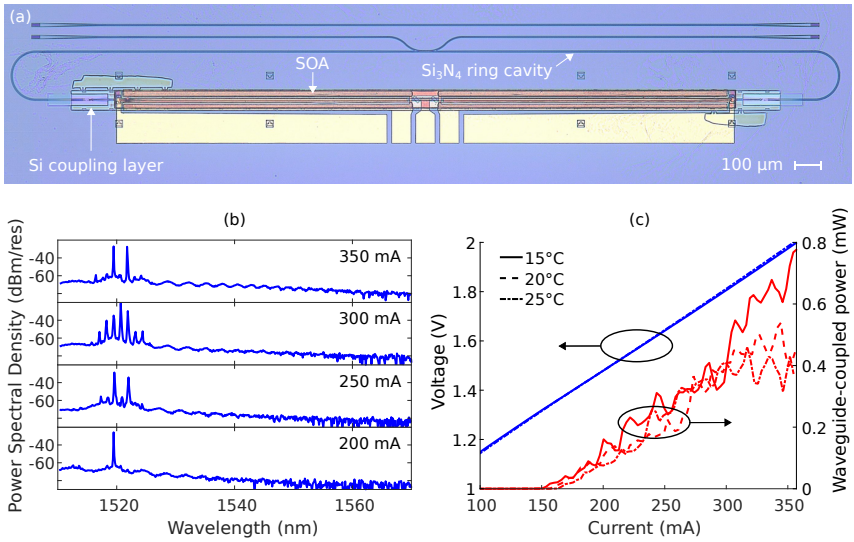

Figure 4.19: (a) Microscope image of the heterogeneous Si_3N_4/Si/III-V ring laser. (b) Optical spectra of the laser above threshold at 19°C, recorded with a resolution of 30 pm. (c) LIV curves of the laser at different temperatures. The estimated slope efficiency at 20°C is approximately 2.8 µW/mA.

4.7.1 Heterogeneous lasers on silicon nitride

A first, simple demonstration comprises a Si_3N_4 ring laser with a micro-transfer printed Si coupling layer and 2.5 mm long InP/InAlGaAs-based SOA with 6 quantum wells. A microscope picture of the device is shown in Fig. 4.19(a). The used silicon coupons, which were fabricated through vapor-phase HF release etching, have slightly oversized tether dimensions, causing part of the supporting Si structure to remain attached to the Si coupon (left and right side of the SOA in Fig. 4.19(a)). The laser consists of a 4.5 mm Si_3N_4 cavity and includes a directional coupler to extract around 8% of power from the cavity. Some lasing spectra for different injection currents, measured at 19°C, are depicted in Fig. 4.19(b). At low injection currents, single-mode lasing is achieved with output powers $>$0.1 mW and side-mode suppression ratios $>$36 dB. However, for high injection currents, multiple longitudinal modes start to lase. To achieve stable single-mode lasing, a spectral filter can be incorporated in the cavity, for example using a microring resonator or a DBR mirror. The voltage-current (V-I) and light-current (L-I) curves

of the laser, measured at 15°C, 20°C and 25°C, are depicted in Fig. 4.19(c). Output powers close to 1 mW are demonstrated, indicating that the intracavity power exceeds 10 mW. The slope efficiency is approximately 2.8 µW/mA at 20°C. The relatively high threshold current of 150 mA results from the high cavity losses, which are dominated by the losses of the Si tapers. The piecewise linear taper employed in this design contained a design flaw and did not prove sufficiently robust to tolerate the change in taper dimensions and the lateral misalignment error. Simulations in Lumerical's eigenmode expansion solver indicate a loss of 3 dB per taper. As such, significant headroom remains to greatly advance current performance.

Recently, more advanced heterogeneous Si_3N_4/Si/III-V lasers have been developed on the Ligentec platform using a similar process flow (a project led by Ir. Stijn Poelman). Particularly, a heterogeneous passively mode-locked laser was demonstrated with a 10-dB optical comb span exceeding 6.6 nm, containing more than 1000 densely spaced coherent comb lines [46].

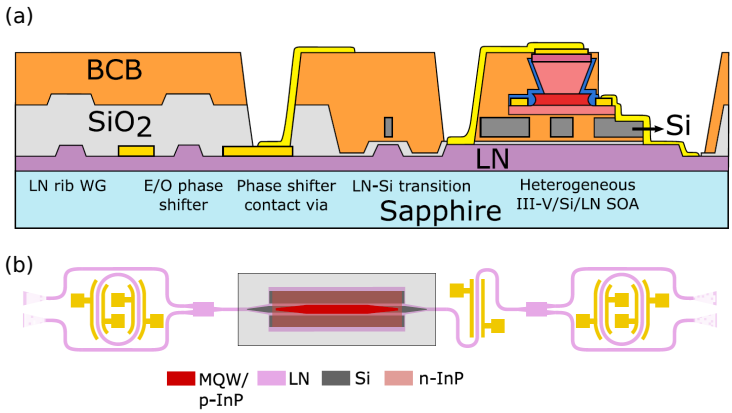

Figure 4.20: (a) Schematic cross sections of the TFLN-on-sapphire platform. (b) Design of the heterogeneous single-mode laser with electro-optic tunability. Reproduced from [4].

4.7.2 Tunable laser on thin-film lithium niobate

Besides heterogeneous Si_3N_4/Si/III-V lasers, the two-step micro-tranfser printing process can also be utilized to build heterogeneous lasers on the thin-film lithium niobate platform. By micro-transfer printing 1.6 mm long Si coupons and 1.3 mm long InP/InAlGaAs-based SOA's on a 500 nm x-cut lithium-niobate-on-sapphire sample, Dr. Camiel Op de Beeck and coworkers recently demonstrated heterogeneous amplifiers, multimode ring lasers, and single-mode tunable lasers [4]. A cross-section of the platform and a schematic of the tunable single-mode laser are respectively shown in Figs. 4.20(a) and (b). The 1.6 mm Si coupon exhibited a

total excess loss of 1.5 dB. By integrating an SOA on top, gain up to 11.8 dB at 1537 nm was achieved. Furthermore, single-mode lasing with output powers up to 0.77 mW, linewidths below 1.5 MHz, and 21 nm of electro-optic tunability were demonstrated.

4.7.3 Electro-optic comb generator on thin-film lithium niobate

The availability of a strong second-order susceptibility in TFLN not only enables fast electro-optic wavelength tuning, but also facilitates the development of a plethora of nonlinear optical devices on-chip. One noteworthy example is the generation of an electro-optic frequency comb with a single photonic chip, as recently demonstrated by Ir. Isaac Luntadila Lufungula and coworkers [5]. In contrast to the unpatterned Si coupons of the aforementioned demonstrations, here, a distributed Bragg grating is pre-patterned in the silicon layer before micro-transfer printing. This way, a DFB laser can be readily integrated on a patterned TFLN circuit to pump a high-Q racetrack resonator on the same PIC. A schematic of the on-chip electro-optic comb device is depicted in Fig. 4.21(a). The resonator, driven by the electrically-pumped heterogeneously integrated laser, produces more than 25 comb lines at 19 GHz spacing, as shown in Fig. 4.21(b). It is expected that significantly broader combs can be generated by improving the Q-factor of the LN racetrack resonator, by improving the laser power, or by increasing the RF power of the electro-optic modulator.

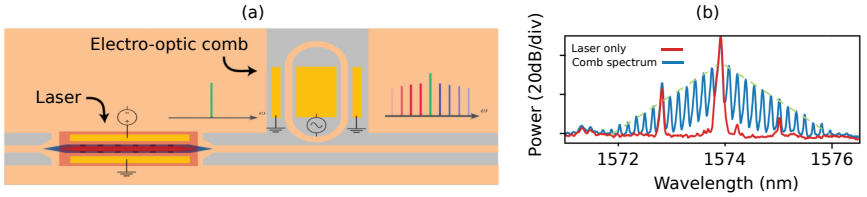

Figure 4.21: (a) Schematic of the on-chip electro-optic comb generator. (b) The optical spectrum generated by the DFB laser and the electro-optic comb. Reproduced from [5].

4.8 Conclusion

In this chapter, micro-transfer printing of crystalline silicon was presented to enable heterogeneous laser integration on generic and commercially available low-refractive-index integrated photonic platforms such as silicon nitride or thin film lithium niobate. Two distinct approaches have been investigated to create micro-transfer printable Si coupons, namely coupons without an encapsulation, where release etching is performed using vapor-phase HF etching, and Si coupons encapsulated with photoresist, in which case liquid HF release etching can be used.

While both approaches have proven successful, the latter method is currently preferred owing to the absence of residual particles and the consistently low surface roughness of the Si coupon backside. Still, the approach based on vapor-phase etching could be valuable for other materials, for example when the adhesion between the encapsulating material and the thin film is poor, or when no post-printing treatment, required to remove the encapsulation, can be tolerated.

A number of transmission measurements were carried out on patterned Si coupons to demonstrate low attainable propagation losses. Importantly, it was confirmed that the micro-tranfser printed silicon waveguides exhibit losses comparable to standard SOI waveguides. It is expected that a further reduction of the losses is possible by optimizing the e-beam lithography and etching processes. Furthermore, a number of devices were presented to demonstrate the potential and the relevance of the integration methodology, including heterogeneous lasers on silicon nitride, as well as electro-optic tunable lasers and an electro-optic comb generator on thin-film lithium niobate.

Besides heterogeneous laser integration, the ability to micro-transfer print crystalline silicon can also serve other purposes. One example is the generation of entangled photon pairs through spontaneous parametric down conversion in quantum photonics applications. In this case, a pump photon (often at visible wavelengths) generates a wavelength-doubled signal and idler photon. As silicon absorbs at wavelengths below 1100 nm, a patterned Si coupon could prove simple yet effective to eliminate the strong pump while imposing minimal losses on the generated signal and idler photons. Another example is the integration of Si photodiodes on silicon nitride, a topic discussed in the following chapter. Finally, the presented integration methodology is largely transferable to other materials. For example, similar techniques are being employed to micro-transfer print lithium niobate on silicon nitride [1, 47, 48]. This enables one to profit from the unique properties of lithium niobate while retaining the CMOS-compatibility of the silicon nitride platform.

References

[1] S. Cuyvers, T. Vanackere, T. Vandekerckhove, S. Poelman, C. Op de Beeck, J. De Witte, A. Hermans, K. Van Gasse, N. Picqué, D. Van Thourhout, G. Roelkens, S. Clemmen, and B. Kuyken. *High-Yield Heterogeneous Integration of Silicon and Lithium Niobate Thin Films*. In 2022 Conference on Lasers and Electro-Optics (CLEO), pages 1–2, 2022.

[2] S. Poelman, S. Cuyvers, J. De Witte, A. Hermans, K. Van Gasse, N. Picqué, G. Roelkens, D. Van Thourhout, and B. Kuyken. *Generic Heterogeneous Integration Process Flow for Commercial Foundry Low-Index Photonic Platforms*. In Frontiers in Optics, pages FM1B–6. Optica Publishing Group, 2021.

[3] S. Cuyvers, , G. Roelkens, K. Van Gasse, and B. Kuyken. *A source wafer and methods related thereto for micro-transfer printing*, Patent Cooperative Treaty international application, publication number: WO2023094232, published in 2023.

[4] C. Op de Beeck, F. M. Mayor, S. Cuyvers, S. Poelman, J. F. Herrmann, O. Atalar, T. P. McKenna, B. Haq, W. Jiang, J. D. Witmer, G. Roelkens, A. H. Safavi-Naeini, R. V. Laer, and B. Kuyken. *III/V-on-lithium niobate amplifiers and lasers*. Optica, 8(10):1288–1289, Oct 2021.

[5] I. L. Lufungula, A. Shams-Ansari, D. Renaud, C. Op de Beeck, S. Cuyvers, S. Poelman, G. Roelkens, M. Loncar, and B. Kuyken. *On-chip electro-optic frequency comb generation using a heterogeneously integrated laser*. In Conference on Lasers and Electro-Optics, page JTh6B.7. Optica Publishing Group, 2022.

[6] A. Rahim, E. Ryckeboer, A. Z. Subramanian, S. Clemmen, B. Kuyken, A. Dhakal, A. Raza, A. Hermans, M. Muneeb, S. Dhoore, Y. Li, U. Dave, P. Bienstman, N. Le Thomas, G. Roelkens, D. Van Thourhout, P. Helin, S. Severi, X. Rottenberg, and R. Baets. *Expanding the Silicon Photonics Portfolio With Silicon Nitride Photonic Integrated Circuits*. Journal of Lightwave Technology, 35(4):639–649, 2017.

[7] D. J. Blumenthal, R. Heideman, D. Geuzebroek, A. Leinse, and C. Roeloffzen. *Silicon Nitride in Silicon Photonics*. Proceedings of the IEEE, 106(12):2209–2231, 2018.

[8] P. Marin-Palomo, J. N. Kemal, M. Karpov, A. Kordts, J. Pfeifle, M. H. P. Pfeiffer, P. Trocha, S. Wolf, V. Brasch, M. H. Anderson, R. Rosenberger, K. Vijayan, W. Freude, T. J. Kippenberg, and C. Koos. *Microresonator-based*

solitons for massively parallel coherent optical communications. Nature, 546(7657):274–279, Jun 2017.

[9] B. Shen, L. Chang, J. Liu, H. Wang, Q.-F. Yang, C. Xiang, R. N. Wang, J. He, T. Liu, W. Xie, J. Guo, D. Kinghorn, L. Wu, Q.-X. Ji, T. J. Kippenberg, K. Vahala, and J. E. Bowers. *Integrated turnkey soliton microcombs*. Nature, 582(7812):365–369, Jun 2020.

[10] S. Cuyvers, B. Haq, C. Op de Beeck, S. Poelman, A. Hermans, Z. Wang, A. Gocalinska, E. Pelucchi, B. Corbett, G. Roelkens, K. Van Gasse, and B. Kuyken. *Low Noise Heterogeneous III-V-on-Silicon-Nitride Mode-Locked Comb Laser*. Laser & Photonics Reviews, 15(8):2000485, 2021.

[11] D. J. Moss, R. Morandotti, A. L. Gaeta, and M. Lipson. *New CMOS-compatible platforms based on silicon nitride and Hydex for nonlinear optics*. Nature Photonics, 7(8):597–607, Aug 2013.

[12] G. Antonacci, J. Goyvaerts, H. Zhao, B. Baumgartner, B. Lendl, and R. Baets. *Ultra-sensitive refractive index gas sensor with functionalized silicon nitride photonic circuits*. APL Photonics, 5(8):081301, 2020.

[13] J. M. Arrazola, V. Bergholm, K. Brádler, T. R. Bromley, M. J. Collins, I. Dhand, A. Fumagalli, T. Gerrits, A. Goussev, L. G. Helt, J. Hundal, T. Isacsson, R. B. Israel, J. Izaac, S. Jahangiri, R. Janik, N. Killoran, S. P. Kumar, J. Lavoie, A. E. Lita, D. H. Mahler, M. Menotti, B. Morrison, S. W. Nam, L. Neuhaus, H. Y. Qi, N. Quesada, A. Repingon, K. K. Sabapathy, M. Schuld, D. Su, J. Swinarton, A. Száva, K. Tan, P. Tan, V. D. Vaidya, Z. Vernon, Z. Zabaneh, and Y. Zhang. *Quantum circuits with many photons on a programmable nanophotonic chip*. Nature, 591(7848):54–60, Mar 2021.

[14] G. Chen, N. Li, J. D. Ng, H.-L. Lin, Y. Zhou, Y. H. Fu, L. Y. T. Lee, Y. Yu, A.-Q. Liu, and A. J. Danner. *Advances in lithium niobate photonics: development status and perspectives*. Advanced Photonics, 4(3):1 – 43, 2022.

[15] R. W. Boyd. *Nonlinear Optics, Third Edition*. Academic Press, Inc., USA, 3rd edition, 2008.

[16] C. Wang, M. Zhang, X. Chen, M. Bertrand, A. Shams-Ansari, S. Chandrasekhar, P. Winzer, and M. Lončar. *Integrated lithium niobate electro-optic modulators operating at CMOS-compatible voltages*. Nature, 562(7725):101–104, Oct 2018.

[17] J. Mishra, T. P. McKenna, E. Ng, H. S. Stokowski, M. Jankowski, C. Langrock, D. Heydari, H. Mabuchi, M. M. Fejer, and A. H. Safavi-Naeini. *Mid-infrared nonlinear optics in thin-film lithium niobate on sapphire*. Optica, 8(6):921–924, Jun 2021.

[18] M. Zhang, B. Buscaino, C. Wang, A. Shams-Ansari, C. Reimer, R. Zhu, J. M. Kahn, and M. Lončar. *Broadband electro-optic frequency comb generation in a lithium niobate microring resonator*. Nature, 568(7752):373–377, Apr 2019.

[19] C. Xiang, W. Jin, and J. E. Bowers. *Silicon nitride passive and active photonic integrated circuits: trends and prospects*. Photon. Res., 10(6):A82–A96, Jun 2022.

[20] C. Op de Beeck, B. Haq, L. Elsinger, A. Gocalinska, E. Pelucchi, B. Corbett, G. Roelkens, and B. Kuyken. *Heterogeneous III-V on silicon nitride amplifiers and lasers via microtransfer printing*. Optica, 7(5):386–393, May 2020.

[21] B. Stern, X. Ji, A. Dutt, and M. Lipson. *Compact narrow-linewidth integrated laser based on a low-loss silicon nitride ring resonator*. Opt. Lett., 42(21):4541–4544, Nov 2017.

[22] K.-J. Boller, A. van Rees, Y. Fan, J. Mak, R. E. M. Lammerink, C. A. A. Franken, P. J. M. van der Slot, D. A. I. Marpaung, C. Fallnich, J. P. Epping, R. M. Oldenbeuving, D. Geskus, R. Dekker, I. Visscher, R. Grootjans, C. G. H. Roeloffzen, M. Hoekman, E. J. Klein, A. Leinse, and R. G. Heideman. *Hybrid Integrated Semiconductor Lasers with Silicon Nitride Feedback Circuits*. Photonics, 7(1), 2020.

[23] C. Xiang, P. A. Morton, and J. E. Bowers. *Ultra-narrow linewidth laser based on a semiconductor gain chip and extended Si3N4 Bragg grating*. Opt. Lett., 44(15):3825–3828, Aug 2019.

[24] Y. Lin, C. Browning, R. B. Timens, D. H. Geuzebroek, C. G. H. Roeloffzen, M. Hoekman, D. Geskus, R. M. Oldenbeuving, R. G. Heideman, Y. Fan, K. J. Boller, and L. P. Barry. *Characterization of Hybrid InP-TriPleX Photonic Integrated Tunable Lasers Based on Silicon Nitride (Si 3N4/SiO2) Microring Resonators for Optical Coherent System*. IEEE Photonics Journal, 10(3):1–8, 2018.

[25] E. Vissers, S. Poelman, C. Op de Beeck, K. V. Gasse, and B. Kuyken. *Hybrid integrated mode-locked laser diodes with a silicon nitride extended cavity*. Opt. Express, 29(10):15013–15022, May 2021.

[26] M. Li, L. Chang, L. Wu, J. Staffa, J. Ling, U. A. Javid, Y. He, R. Lopez-rios, S. Xue, T. J. Morin, B. Shen, H. Wang, S. Zeng, L. Zhu, K. J. Vahala, J. E. Bowers, and Q. Lin. *Integrated Pockels Laser*, 2022.

[27] M. Theurer, M. Moehrle, A. Sigmund, K.-O. Velthaus, R. M. Oldenbeuving, L. Wevers, F. M. Postma, R. Mateman, F. Schreuder, D. Geskus, K. Wörhoff, R. Dekker, R. G. Heideman, and M. Schell. *Flip-Chip Integration of InP and SiN*. IEEE Photonics Technology Letters, 31(3):273–276, 2019.

[28] A. Shams-Ansari, D. Renaud, R. Cheng, L. Shao, L. He, D. Zhu, M. Yu, H. R. Grant, L. Johansson, M. Zhang, and M. Lončar. *Electrically pumped laser transmitter integrated on thin-film lithium niobate*. Optica, 9(4):408–411, Apr 2022.

[29] C. Xiang, W. Jin, J. Guo, J. D. Peters, M. J. Kennedy, J. Selvidge, P. A. Morton, and J. E. Bowers. *Narrow-linewidth III-V/Si/Si3N4 laser using multilayer heterogeneous integration*. Optica, 7(1):20–21, Jan 2020.

[30] M. Piels, J. F. Bauters, M. L. Davenport, M. J. R. Heck, and J. E. Bowers. *Low-Loss Silicon Nitride AWG Demultiplexer Heterogeneously Integrated With Hybrid III–V/Silicon Photodetectors*. J. Lightwave Technol., 32(4):817–823, Feb 2014.

[31] C. Xiang, J. Liu, J. Guo, L. Chang, R. N. Wang, W. Weng, J. Peters, W. Xie, Z. Zhang, J. Riemensberger, J. Selvidge, T. J. Kippenberg, and J. E. Bowers. *Laser soliton microcombs heterogeneously integrated on silicon*. Science, 373(6550):99–103, 2021.

[32] W. D. Sacher, Y. Huang, G. Lo, and J. K. S. Poon. *Multilayer Silicon Nitride-on-Silicon Integrated Photonic Platforms and Devices*. J. Light. Technol., 33(4):901–910, 2015.

[33] Q. Wilmart, H. El Dirani, N. Tyler, D. Fowler, S. Malhouitre, S. Garcia, M. Casale, S. Kerdiles, K. Hassan, C. Monat, X. Letartre, A. Kamel, M. Pu, K. Yvind, L. K. Oxenløwe, W. Rabaud, C. Sciancalepore, B. Szelag, and S. Olivier. *A Versatile Silicon-Silicon Nitride Photonics Platform for Enhanced Functionalities and Applications*. Applied Sciences, 9(2), 2019.

[34] X. Zhang, X. Liu, R. Ma, Z. Chen, Z. Yang, Y. Han, B. Wang, S. Yu, R. Wang, and X. Cai. *Heterogeneously integrated III–V-on-lithium niobate broadband light sources and photodetectors*. Opt. Lett., 47(17):4564–4567, Sep 2022.

[35] V. Snigirev, A. Riedhauser, G. Lihachev, J. Riemensberger, R. N. Wang, C. Moehl, M. Churaev, A. Siddharth, G. Huang, Y. Popoff, U. Drechsler, D. Caimi, S. Hoenl, J. Liu, P. Seidler, and T. J. Kippenberg. *Ultrafast tunable lasers using lithium niobate integrated photonics*, 2022.

[36] B. Kuyken, H. Ji, S. Clemmen, S. K. Selvaraja, H. Hu, M. Pu, M. Galili, P. Jeppesen, G. Morthier, S. Massar, L. Oxenløwe, G. Roelkens, and R.

Baets. *Nonlinear properties of and nonlinear processing in hydrogenated amorphous silicon waveguides*. Opt. Express, 19(26):B146–B153, Dec 2011.

[37] M. Bruel and B. A. Auberton-Hervé. *Smart-Cut: A New Silicon On Insulator Material Technology Based on Hydrogen Implantation and Wafer Bonding*. Japanese Journal of Applied Physics, 36(3S):1636, mar 1997.

[38] W. Kern. *The Evolution of Silicon Wafer Cleaning Technology*. Journal of The Electrochemical Society, 137(6):1887, jun 1990.

[39] R. Kirchner, V. Neumann, F. Winkler, C. Strobel, S. Völkel, A. Hiess, D. Kazazis, U. Künzelmann, and J. W. Bartha. *Anisotropic Etching of Pyramidal Silica Reliefs with Metal Masks and Hydrofluoric Acid*. Small, 16(43):2002290, 2020.

[40] J. De Witte, S. Cuyvers, S. Poelman, B. Kuyken, and D. Van Thourhout. *Realization of fabrication-tolerant Si3N4-Si mode transformers*. In 2021 IEEE Photonics Conference (IPC), pages 1–2. IEEE, 2021.

[41] B. Haq and G. Roelkens. *Alignment-tolerant taper design for transfer printed III-V-on-Si devices*. In 21st European Conference on Integratred Optics (ECIO 2019), 2019.

[42] G. Roelkens. *Heterogeneous III-V/Silicon Photonics: Bonding Technology and Integrated Devices*. PhD thesis, Ghent University, 2007.

[43] B. Guilhabert, S. P. Bommer, N. K. Wessling, D. Jevtics, J. A. Smith, Z. Xia, S. Ghosh, M. Kappers, I. M. Watson, R. A. Oliver, M. D. Dawson, and M. J. Strain. *Advanced Transfer Printing With In-Situ Optical Monitoring for the Integration of Micron-Scale Devices*. IEEE Journal of Selected Topics in Quantum Electronics, 29(3: Photon. Elec. Co-Inte. and Adv. Trans. Print.):1–11, 2023.

[44] J. McPhillimy, C. Klitis, P. Hill, S. May, B. Guilhabert, M. D. Dawson, M. Sorel, and M. J. Strain. *Towards 3D optical integration by micro-transfer printing of ultra-thin membrane devices*. In 2018 IEEE British and Irish Conference on Optics and Photonics (BICOP), pages 1–4, 2018.

[45] J. McPhillimy, D. Jevtics, B. J. E. Guilhabert, C. Klitis, A. Hurtado, M. Sorel, M. D. Dawson, and M. J. Strain. *Automated Nanoscale Absolute Accuracy Alignment System for Transfer Printing*. ACS Applied Nano Materials, 3(10):10326–10332, Oct 2020.

[46] S. Poelman, S. Cuyvers, E. Vissers, J. D. Witte, B. Haq, A. Hermans, N. Picque, G. Roelkens, and B. Kuyken. *Low Repetition Rate Mode-Locked*

Laser on a Commercial Foundry Low-Index Photonic Platform. In Conference on Lasers and Electro-Optics (CLEO), San Jose, USA, 5 2023. CLEO.

[47] T. Vanackere, T. Vandekerckhove, L. Bogaert, M. Billet, S. Poelman, S. Cuyvers, J. V. Kerrebrouck, A. Moerman, O. Caytan, S. Lemey, G. Torfs, G. Roelkens, S. Clemmen, and B. Kuyken. *High-Speed Lithium Niobate Modulator on Silicon Nitride using Micro-Transfer Printing*. In Conference on Lasers and Electro-Optics (CLEO), San Jose, USA, 5 2023. CLEO.

[48] T. Vandekerckhove, T. Vanackere, J. D. Witte, S. Cuyvers, L. Reis, M. Billet, G. Roelkens, S. Clemmen, and B. Kuyken. *Pillar-Based High-Yield Heterogeneous Integration of Lithium Niobate and Gallium Phosphide Thin Films*. In Conference on Lasers and Electro-Optics (CLEO), San Jose, USA, 5 2023. CLEO.

5

Silicon photodiodes on silicon nitride for near-visible light detection

In the previous chapters, demonstrated devices on silicon nitride have operated at telecommunication wavelengths. Yet, to unlock the full potential of silicon nitride, lasers and detectors for wavelengths below 850 nm are essential to serve applications such as biosensing, imaging and quantum photonics amongst others. In this chapter, we present the design, fabrication and characterization of micro-transfer printed Si p-i-n photodiodes on a commercially available silicon nitride platform to target wavelengths in the near-visible spectral range (<850 nm). The content presented in this chapter has been published in part in [1].

5.1 Introduction

Silicon nitride (Si_3N_4) has been widely recognized as a promising integrated photonic platform to complement silicon-on-insulator technology owing to its low propagation losses, high power-handling capabilities, and wide transparency window [2, 3]. In addition, the low index contrast with silicon oxide results in enhanced resilience to fabrication errors and a reduced mode confinement. This has made Si_3N_4 the material of choice for life-science and bio-sensing applications at visible wavelengths [4–6]. However, developments with regard to heterogeneous integration of active devices on Si_3N_4 have mostly focused on infrared wavelengths in the telecom range. Demonstrations of light sources and detectors

on Si_3N_4 beyond the classic telecom wavelengths remain scarce, hampering the adoption of Si_3N_4 photonic integrated circuits (PICs) for several applications.

State-of-the-art photodetectors (PDs) on Si_3N_4 have been developed on a variety of material platforms such as germanium [7], silicon (Si) [8–10] and III-V semiconductors [11, 12]. Yet, few demonstrations are geared towards detection below 850 nm. An edge-coupled monolithic Si rib avalanche photodetector (APD) on Si_3N_4 for 685 nm was demonstrated in [9], whereas micro-transfer printed grating-assisted GaAs p-i-n photodiodes, targeting wavelengths around 800 nm, were reported in [12]. Although a low dark current and a high responsivity were reported in the latter, a silicon platform is generally preferred for avalanche gain multiplication [13].

In this chapter, we present, to the best of our knowledge, the first micro-transfer printed Si p-i-n photodiodes on Si_3N_4 for wavelengths below 850 nm. The photodetector is based on a doped silicon rib waveguide and is printed on top of imec's BioPIX plasma-enhanced chemical vapor deposition (PECVD) Si_3N_4 platform. The low deposition temperature of PECVD Si_3N_4 ensures full compatibility with complementary metal-oxide semiconductor (CMOS) technology [14]. Furthermore, a vapor-HF-based fabrication process is used to suspend the Si p-i-n devices on the silicon-on-insulator (SOI) source wafer with a high yield, enabling seamless heterogeneous integration on commercial Si_3N_4 platforms. Such a process flow is similar to what was demonstrated in Chapter 4. Moreover, the devices are fabricated using wafer-scale technology, allowing for low-cost and scalable manufacturing.

In the remainder of this chapter, the layout, simulations, fabrication and characterization of the heterogeneously integrated Si p-i-n photodiodes on Si_3N_4 are discussed [1]. The Si_3N_4 target PIC was designed by Dr. Jeroen Goyvaerts, while the process flow was developed by Dr. Artur Hermans and the author. The heterogeneous integration, post-processing and characterization was performed by the author. Max Kiewiet assisted with the high-speed measurements.

5.2 Device design and fabrication

The Si p-i-n photodetectors are realized on imec's iSiPP25G integrated silicon photonics platform through a multi-project wafer (MPW) run. Rib waveguides are defined in a 220 nm Si layer on top of a 2 μm thermally grown silicon oxide (SiO_2) layer. The rib has a width of 500 nm and a shallow etch depth of 70 nm. The intrinsic region spans over 1.3 μm, as depicted in Fig. 5.1. At the sides, 850 nm wide P- and N-doped regions with a doping concentration of $1.5{\cdot}10^{18}$ cm^{-3}, and 4.3 μm wide P^+/N^+ doped regions with a doping concentration of 10^{20} cm^{-3} are created.

The photonic target wafer comprises a Si_3N_4 PIC based on imec's BioPIX plat-

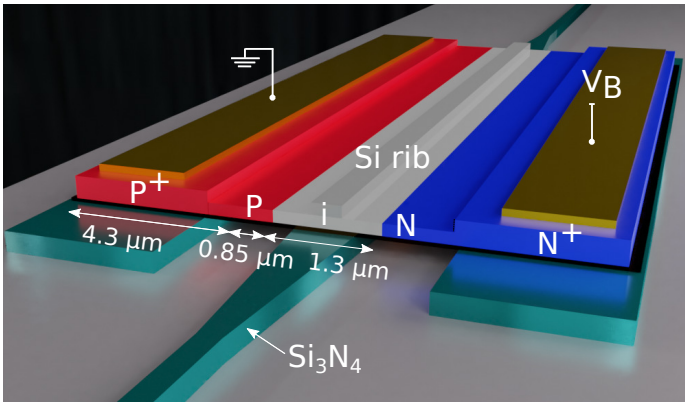

Figure 5.1: Rendering of the Si p-i-n photodiode on top of a Si_3N_4 waveguide. The device is reverse biased by applying a voltage V_B via the metal contacts on top of the doped P^+/N^+ regions.

form. BioPIX is imec's technology platform for fabricating PECVD Si_3N_4 based PICs, based on imec's 200mm CMOS pilot line. The 300 nm thick Si_3N_4 layer is deposited using PECVD on top of a 3.3 µm SiO_2-on-Si wafer. Furthermore, a 2 µm deep recess is locally etched in the SiO_2 top cladding using dry etching techniques to expose part of the Si_3N_4 waveguides, enabling evanescent coupling to the Si rib waveguide above it. The BioPIX chip used for this work was originally designed for a different application, and optimal index matching is hence not achieved for the current demonstration. Nevertheless, the work presented in this chapter offers a valuable proof-of-concept to demonstrate the potential of Si photodetectors on silicon nitride for near-infrared and visible light detection, and for the manufacturing methodology in general. It is expected that a significant performance enhancement is within reach by using an optimized silicon nitride design.

For the heterogeneous integration of the photodiodes, the micro-transfer printing technique is used [12, 15]. Here, an important advantage of micro-transfer printing is the ability to integrate devices in a recess, an attribute that is essential for compatibility with top-cladded passive photonic platforms.

Before the micro-transfer printing process can commence, the photodetectors need to be encapsulated and suspended on the source SOI wafer. As a first step, the sample is submerged in buffered hydrofluoric acid (HF) to remove the SiO_2 cladding on top of the Si device layer (Fig. 5.2(a)-(b)). Next, a TI-35E photoresist is spincoated and patterned to define the encapsulation tethers (Fig. 5.2(c)). Although a photoresist encapsulation is not strictly required - the tethers can also solely be defined in the silicon device layer, as was outlined in Chapter 4 - the silicon device layer is here only 220 nm thick, making it mechanically more fragile.

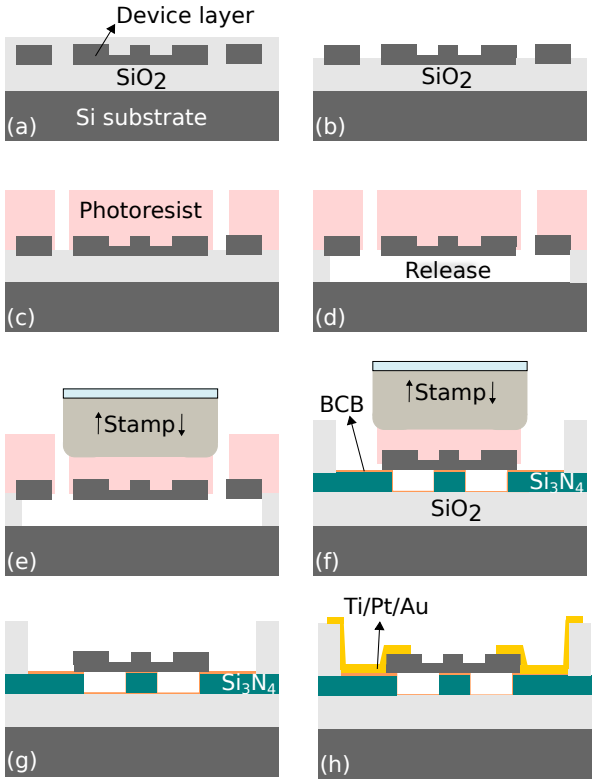

Figure 5.2: Device process flow. (a) Si device layer on imec's iSiPP25G platform, (b) top oxide removal using buffered HF, (c) photoresist encapsulation and patterning, (d) vapor-phase HF release etch, (e) pick-up from source wafer, (f) print on Si_3N_4 target wafer, (g) encapsulation removal, (h) final metallization.

A photoresist encapsulation is therefore utilized to safeguard the device integrity. After patterning the photoresist, an RIE dry etch (using CF_4, H_2, SF_6) is used to pattern the Si device layer. To make the photoresist more resilient to the HF release etchant, a hard bake at 145°C is performed. The sample is subsequently cooled down at a slow pace of ∼10°C/min to avoid cracks in the photoresist. However, it was later found that this is not strictly necessary, and the photoresist seems to survive the release etch without any additional measures. Finally, the sacrificial SiO_2 layer underneath the Si coupons is underetched for 3 hours using HF vapor (Fig. 5.2(d)). The vapor-HF chamber temperature was fixed at 40°C. Vapor-phase HF provides a near 100% picking yield as it does not suffer from capillary forces which can lead to a collapse of the suspended Si device layer, as was discussed in Chapter 4. After the release etch, the coupons are solely supported by the tethers and are ready for micro-transfer printing. Figure 5.3(a) depicts the 200 µm

Source Parameters	Target Parameters	Clean Parameters
Pick acceleration: 1 g Overdrive distance: 0.11 mm Overdrive speed: 0.02 mm/s Pick speed: 100 mm/s	Print speed: 0.002 mm/s Overdrive distance: 0.14 mm Overdrive speed: 0.03 mm/s X shear distance: 0.02 mm Y shear distance: 0.01 mm Shear speed: 0.1 mm/s Shear duration: 5 s	Clean speed: 0.05 mm/s Overdrive distance:: 0.145 mm Overdrive speed: 0.03 mm/s

Table 5.1: Micro-transfer printing recipe parameters.

long suspended Si photodiode on the source silicon-on-insulator wafer, along with the photoresist encapsulation, as well as the tethers that support the suspended structure. The photoresist encapsulation exhibits some wrinkles which are a result of the vapor-HF release etch. The standard TI-35E photoresist used in this work can nevertheless withstand the HF release etchant without observable mechanical degradation. Furthermore, note that the top and bottom parts of the Si coupon in Fig. 3(a) do not contribute to the actual photodiode (as depicted in Fig. 5.1) and are merely dummy Si material used to match the size of the coupon to the size of the PDMS stamp used for micro-transfer printing. If desired, one could hence significantly reduce the size of the Si coupon in the lateral dimension.

To ensure a high printing yield, an 80 nm adhesive DVS-BCB:mesitylene 1:5 layer is spincoated on the target Si_3N_4 wafer at 3000 rpm for 40 s. The adhesive layer is subsequently baked at 150°C for 10 minutes. The source and target wafer are then loaded in the X-Celeprint μTP-100 micro-transfer printing tool. A PDMS stamp with a size of 200 $\mu m \times 50\ \mu m$ was used to pick up and print the photodiode. The micro-transfer printing step is illustrated in Figs. 5.2(e), (f). The Si_3N_4 target PIC was kept at a fixed temperature of 80°C to ease the micro-transfer printing process. The micro-transfer printing parameters used are listed in Table 5.1. Although pattern recognition markers enable automated alignment of the photodiodes on the target wafer, manual alignment was performed for the devices demonstrated in this chapter. Furthermore, if wafer-scale fabrication is envisioned, array stamps can be utilized to enable multiple coupons to be picked up and printed simultaneously. After transfer printing, the photoresist encapsulation is removed using an oxygen plasma reactive ion etch (RIE) (Fig. 5.2(g)). Thereafter the sample is baked at 280°C in vacuum to cure the BCB layer. Finally, a lift-off process is employed to pattern the Ti/Pt/Au metal contact pads (Fig. 5.2(h)). Just prior to the metal deposition, the sample is submerged for 5 seconds in diluted buffered HF and subsequently for 5 seconds in H_2SO_4:H_2O_2:H_2O (1:1:40), to remove the native oxide, reducing the metal-semiconductor contact resistance. A microscope picture of the post-processed Si p-i-n photodetector on the silicon nitride waveguide is shown in Fig. 5.3(b).

Figure 5.4 depicts a damaged Si p-i-n photodetector on Si_3N_4. Here, the vapor-HF etch time was insufficient to fully release the Si device, leaving a small chunk of the Si PD on the source wafer and a noticeable defect on the target wafer. As it is generally difficult to observe the release layer underneath the coupon, one should take some margin for the vapor-HF release etch time to make sure the device is completely released and suspended.

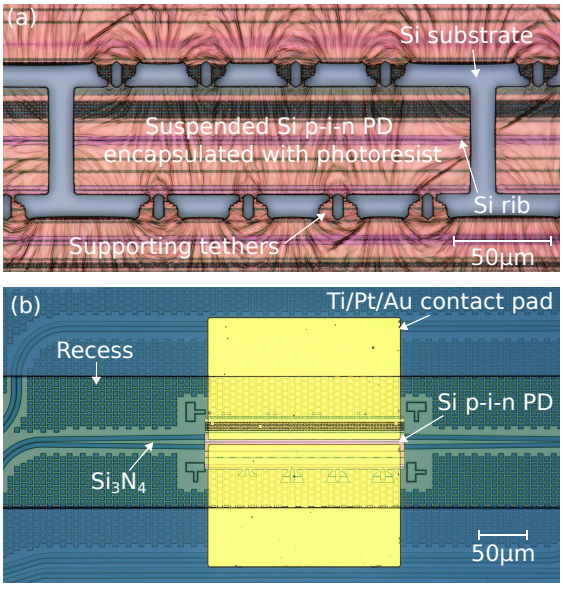

Figure 5.3: Microscope pictures of the suspended photodiode on the source wafer (a) and the micro-transfer printed and post-processed photodiode on the silicon nitride target (b).

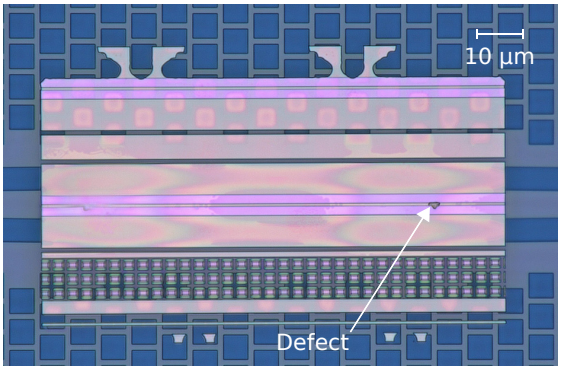

Figure 5.4: Microscope picture of a micro-transfer printed Si p-i-n photodiode on silicon nitride with a defect, originating from an incomplete vapor-HF release etch.

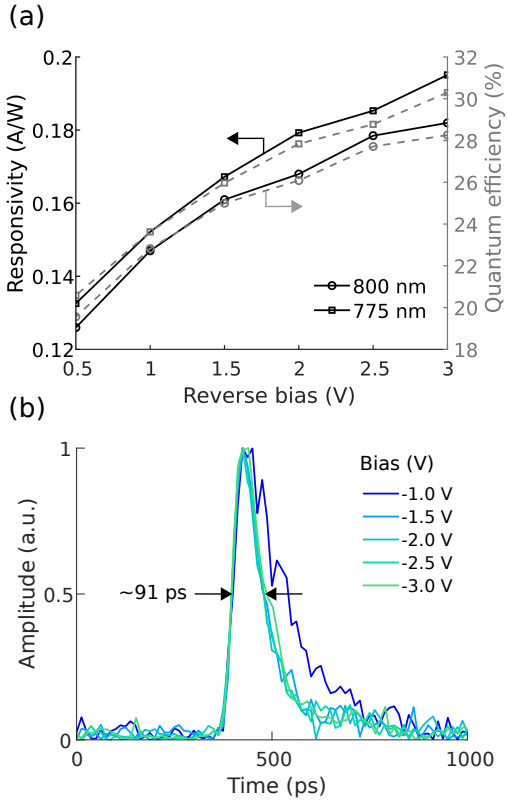

Figure 5.5: Measured photodiode responsivity and external quantum efficiency (a) and measured impulse response (b) as a function of reverse bias voltage.

5.3 Characterization

5.3.1 Dark current and responsivity

The photodetector was characterized at room temperature using electrical contact probes and a Keithley 2400A voltage-current source. The optical input was provided using a silicon nitride grating coupler and a cleaved fiber. A polarization controller was used to couple in TE-polarized light. From the V-I measurements it was found that the differential resistance converges to a value of 40 Ω. Furthermore, a dark current of 107 pA was measured at a reverse bias voltage of 3 V. This dark current is low compared to most state-of-the-art integrated photodetectors [8, 11, 16, 17] and comparable to the results in [9]. The waveguide-referred responsivity was measured at 800 nm and 775 nm. The waveguide-referred responsivity was defined with respect to the optical power inside the silicon nitride waveguide, hence taking into account the Si_3N_4-Si coupling but not the

losses of the grating couplers. This figure-of-merit is used as it most appropriately represents the performance of the photodetector as a building block in a photonic integrated circuit. The relation between the waveguide-referred responsivity and the external quantum efficiency is here defined as

$$R_{WG} = \frac{e}{\hbar\omega} \cdot EQE, \tag{5.1}$$

where R_{WG} is the waveguide-referred responsivity and EQE is the external quantum efficiency. A Ti:sapphire continuous wave laser (M2 SolsTis) was used for characterization at 800 nm, whereas a Onefive Katana picosecond laser was used for measurements at 775 nm. The photodetector was not characterized below 775 nm as no laser sources were available for this wavelength range. The responsivity and corresponding external quantum efficiency as a function of reverse bias voltage are depicted in Fig. 5.5(a).

Similar responsivities around 0.19 A/W and external quantum efficiencies around 30% at -3 V bias voltage are obtained for both wavelengths. The responsivity was also simulated using Lumerical's FDTD and CHARGE simulators by calibrating the recombination parameters to match simulated and measured dark currents. The resulting simulated responsivity is approximately 14% higher than the experimental results. This discrepancy can likely be attributed to an overestimation of the optical input power and some uncertainty in the model's recombination parameters. Furthermore, simulations show a $\sim$2% reduction in responsivity for a lateral misalignment of 1 μm, demonstrating robustness against alignment offsets of the micro-transfer printing process.

5.3.2 High-speed measurements

To estimate the photodetector bandwidth, its impulse response was captured using a Teledyne Lecroy 65 GHz real-time oscilloscope (RTO) and a Onefive Katana picosecond laser. The latter generates optical pulses with a duration around 35 ps. The Keithley current-voltage source and RTO were connected to the high-speed radio frequency (RF) probe using a bias tee, as depicted in Fig. 5.6.

A full width at half maximum around 91 ps is obtained for reverse bias voltages in excess of -1.5 V, as depicted in Fig. 5.5(b). From this, the 3-dB bandwidth can be estimated by Fourier transforming the measured impulse response and dividing it by the Fourier transform of the time-domain optical picosecond pulse trace, which is provided in the Onefive Katana laser output specification sheet. This derivation yields a 3-dB bandwidth of 6 GHz. To identify whether the RC time delay or the transit time dominate the bandwidth, the S_{11} parameter of the photodiode at 3 V reverse bias is measured using a TITAN MPI T40A GS 100 contact probe and a Keysight N5247B Network Analyzer. Fitting a simple RC circuit to the measurement data between 0 and 6 GHz yields a resistance of 183 Ω

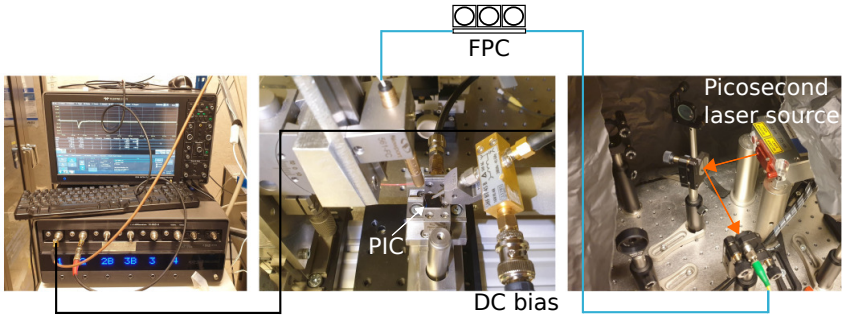

Figure 5.6: Measurement setup used to characterize the bandwidth of the Si p-i-n photodiode. The output of the 775 nm picosecond laser is first coupled to a single mode fiber using a tunable mirror and collimator, and subsequently through a fiber polarization controller (FPC) to the photonic chip. The photodiode is probed with a ground-signal-ground RF probe and connected to a Keithley DC bias source and a Lecroy real-time oscilloscope using a bias tee.

and a capacitance of 133 fF. The resulting RC time constant is found to be $f_{RC} \approx$ 6.5 GHz. Using the following relation for the overall 3-dB bandwidth of the photodetector [18]:

$$\frac{1}{f_{3dB}^2} = \frac{1}{f_{RC}^2} + \frac{1}{f_T^2}, \tag{5.2}$$

one finds that the transit-time-limited bandwidth f_T is approximately 15 GHz. The RC constant is hence dominant for the present device. The relatively large value of the resistance can be attributed to the high contact resistance of the metal-semiconductor contact. Although an acid dip was used prior to metalization to remove the native oxide, a metal deposition tool with RF pre-sputtering or a build-in Argon ion gun [19, 20], or a rapid-thermal annealing treatment [21] can be utilized to further reduce the contact resistance.

5.3.3 Avalanche operation

For applications where high receiver sensitivities are indispensable, on-chip avalanche photodiodes (APDs) with an internal multiplication gain offer an attractive solution [17]. In this case, strong reverse biasing provides a high field strength across the depletion region, leading to a phenomenon called impact ionization. Accelerating electrons can acquire enough energy to ionize atoms in the material when colliding with them. This way, a single electron-hole pair can generate many secondary electrons and holes, all of which contribute to the photocurrent. Due to this internal gain mechanism, the responsivity can be much larger compared to a conventional p-i-n photodetector. As silicon exhibits a low impact ionization

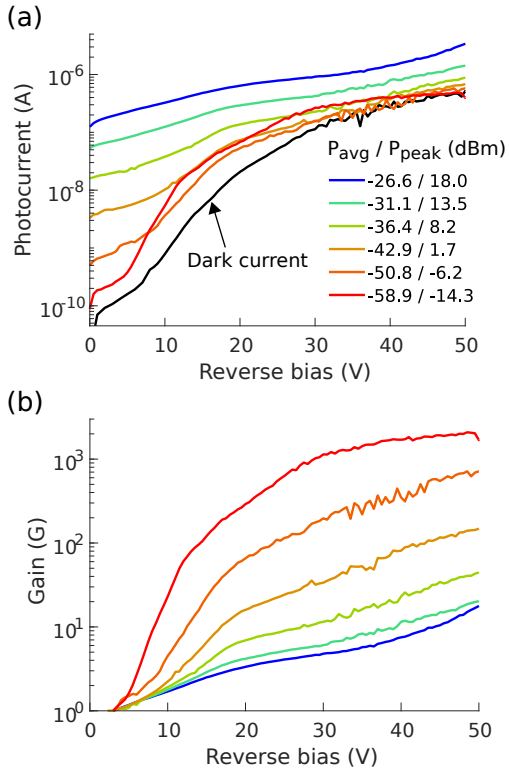

Figure 5.7: Current-voltage measurements at different optical input powers (a) and the corresponding avalanche gain (b). A picosecond laser at 775 nm was used as an optical source. The dark current measured without illumination is shown as well in (a), reaching 107 pA at 3 V. The reverse bias voltage was swept until 50 V, sufficiently below the observed breakdown voltage $V_{br} \approx 80$ V.

ratio (the ratio between the impact ionization coefficients of electrons and holes) and consequently limited excess noise, Si-based APDs are particularly suited for avalanche detection [13]. To investigate the avalanche capabilities of the micro-transfer printed Si p-i-n photodiode, the current-voltage relation was measured for reverse bias voltages up to 50 V, below the breakdown voltage $V_{br} \approx 80$ V. The I-V measurements were carried out with different optical input powers at 775 nm, as shown in Fig. 5.7(a). The specified power values take into account the grating coupler losses and hence represent the optical power in the Si_3N_4 waveguide. The avalanche gain $G(V_B)$, shown in Fig. 5.7(b), can be calculated as the ratio of the photocurrent at a given reverse bias voltage V_B divided by the photocurrent at the unity gain point. The latter is here defined as the point where the second derivative of the photocurrent with respect to bias crosses zero (here at $V_B \approx 3$ V), in correspondance with [9]. Figure 5.8 depicts the measured gain-bandwidth product

(GBP) as a function of the gain. The highest observed gain-bandwidth product is 68 GHz at 45 V reverse bias for an optical input power of $P_{opt} \approx$ -26 dBm. From 5.7(b), it is obvious that the observed avalanche gain is higher for lower optical input powers. This can be expected as more charge carriers are generated at higher optical input powers, leading to an enhanced space charge effect and consequently saturation of the photocurrent [9]. Moreover, as a picosecond laser source was used as an input, this saturation effect is more pronounced. Although the photodiode reverse bias voltage was here swept until 50 V, typical CMOS platforms only supply voltages up to 12 V [13]. At this bias point, avalanche gains up to $\sim$60 are observed for low optical input powers. Photodiodes with a narrower intrinsic region or an interdigitated structure could be used to reduce the breakdown voltage and boost the avalanche gain at lower bias voltages, although this typically comes at the expense of an increased dark current [9].

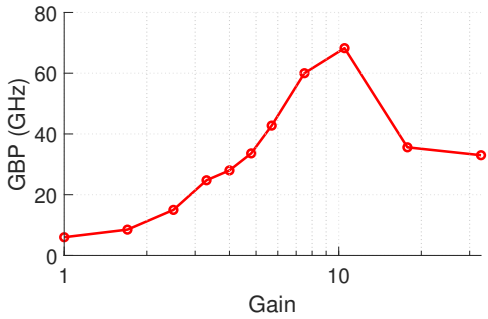

Figure 5.8: Plot of the gain-bandwidth product (GBP) as a function of the gain for an input optical power of $P_{opt} \approx$ -26 dBm. The highest observed GBP is 68 GHz at a reverse bias voltage of 45 V.

5.4 Comparison with state-of-the-art

In Table 5.2, the performance of the presented photodiode is compared with other recent demonstrations of visible and near-infrared PDs and APDs on Si_3N_4. Note that this list is not exhaustive. Edge-coupled monolithic Si rib avalanche photodetectors on Si_3N_4 for 685 nm are reported in [9, 25]. These devices offer a high responsivity up to 0.8 A/W as well as a high 3-dB bandwidth up to 19.1 GHz and a GBP of 234 GHz. This high performance can largely be attributed to the smaller device size: a length of 16 µm was used compared to 200 µm for the device presented in this chapter. This is an important advantage of an edge-coupled device as longer coupling lengths are required to achieve efficient evanescent coupling, in particular at short wavelengths. A larger device size decreases the bandwidth due

Table 5.2: Comparison of state-of-the-art visible and near-infrared PDs and APDs on Si_3N_4. R: responsivity, I_{dark}: dark current, BW: 3-dB bandwidth, GBP: gain-bandwidth product. The reverse bias voltage is specified between brackets. The work presented in this chapter as well as the work reported in [12, 22–24] rely on micro-transfer printing. Other listed devices are fabricated monolithically.
* These results were not explicitly reported but inferred from relevant data.

Ref.; year	Type	Wavelength (nm)	R (A/W)	I_{dark} (nA)	BW (GHz)	GBP (GHz)
[25]; 2022	End-fire Si_3N_4/SOI, PIN	685	0.8 (5.5 V)	0.05 (5.5 V)	11 (18 V)	98 (18 V)
[25]; 2022	End-fire Si_3N_4/SOI, PIN	685	0.8 (7.25 V)	0.1 (7.25 V)	8.8 (18 V)	142 (18 V)
[9]; 2021	End-fire Si_3N_4/SOI, PN	685	0.83 (2 V)	$\sim$ 0.001 (2 V)	19.1 (20 V)	234 (20 V)
[26]; 2022	Si_3N_4-on-Si, PIN;PN	405	*0.15 (13.3 V)	0.144 (5 V)	8.6 (20 V)	173 (13.3 V)
[27]; 2022	a-Si:H-on-Si_3N_4, MSM	660	0.03 (8 V)	0.025 (4 V)	-	-
[28]; 2006	poly-Si/Si_3N_4, MSM	654	0.35 (10 V)	0.2 (5 V)	-	-
[22]; 2018	GaAs-on-Si_3N_4, MSM	850	0.1 (2 V)	22 (2 V)	20 (2 V)	-
[29]; 2019	Si_3N_4-on-SOI, PIN	850	0.29 (20 V)	75 (20 V)	14 (20 V)	*20.3 (20 V)
[12]; 2020	GaAs-on-Si_3N_4, PIN	850	0.3 (2 V)	0.02 (2 V)	-	-
[30]; 2022	Si_3N_4-on-SOI, PN	850	0.11 (1 V)	-	-	-
[23]; 2022	InGaAsP-on-Si_3N_4/Si, UTC	1310	0.42 (3 V)	30 (3 V)	54 (3 V)	-
[24]; 2023	InP-on-Si_3N_4, UTC	1550	0.3 (0 V)	10 (1 V)	155 (1 V)	-
This work; 2022	Si-on-Si_3N_4, PIN	775	0.19	0.107 (3 V)	6 (3 V)	68 (45 V)

to the RC limitation, and increases dark noise due to a larger active volume [9]. Still, such an edge-coupling approach is more challenging to fabricate or requires a custom silicon nitride-on-SOI platform. Furthermore, it is shown in [25] that the doping profile plays a significant role for APD performance. Hence, it is expected that careful optimization of the doping profile along with an enhanced device geometry, could greatly improve the GBP of our presented device. In addition, this could possibly enable stable, low-noise Geiger-mode operation for single-photon detection in integrated quantum photonics applications [25].

State-of-the-art evanescently coupled Si_3N_4-on-Si PN and PIN APDs for operation around 405 nm are demonstrated in [26]. Using a well optimized coupling structure, a record-high EQE of 60%, an 8.6 GHz 3-dB bandwidth and a 173 GHz GBP were demonstrated using a 50 μm long device. Moreover, wafer-level performance is reported with performance variations limited to 30%. It is expected that for the device presented in this chapter, optimization of the Si_3N_4-Si coupling could deliver similar performance while offering full compatibility with generic Si_3N_4 platforms. However, wafer-level variability still needs to be investigated for such micro-transfer printed devices. Careful control of the alignment accuracy and BCB thickness (or omitting the adhesive layer altogether) amongst others, is likely paramount to minimize performance variations.

Metal-semiconductor-metal (MSM) PDs integrated on Si_3N_4, respectively using a-Si:H, poly-Si, and GaAs, are reported in [27], [28] and [22]. MSM PDs operate as photoconductive detectors where incident photons are absorbed in the semiconductor layer and current flows between the two Schottky contacts [31]. Using interdigitated contacts, the capacitance and transit time can be minimized, enabling MSM PDs to achieve high bandwidths. However, this typically comes at the expense of poor responsivity and high dark current. For example, the GaAs MSM PD for photonic interposers reported in [22] provides a bandwidth up to 20 GHz, but suffers from a low responsivity of 0.1 A/W and a higher dark current of 22 nA. Furthermore, the a-Si:H PD reported in [27] benefits from a simple fabrication process, but a low responsivity of 0.03 A/W and a low bandwidth (MHz range) are achieved. Still, given the low complexity, such devices can be appropriate for in-line power monitoring for reconfiguration and stabilization operations [27].

Finally, the devices reported in [23] and [24] are included in Table 5.2 to illustrate the potential of micro-transfer printing for bringing high-speed photodiodes to the Si_3N_4 platform. In this case, uni-traveling-carrier (UTC) photodiodes are utilized. The fundamental bandwidth limitation of conventional state-of-the-art p-i-n photodetectors is the transit time required by the electrons and holes to reach the electrodes. Although this time can be reduced by using a thinner intrinsic layer, this comes at the expense of a reduced responsivity and dynamic range. An alternative is to rely exclusively on high-mobility carriers by including an absorbing

(blocking) layer. By solely relying on electrons as active carriers and blocking the transit of holes, which have a significantly lower mobility compared to the electrons, a considerable improvement in bandwidth can be achieved. Record bandwidths up to 155 GHz have been reported using micro-transfer printed UTC PDs on Si_3N_4 [24].

5.5 Conclusion

In this chapter, we have successfully demonstrated the first micro-transfer printed Si photodiodes, based on imec's iSiPP25G integrated silicon photonics platform, on a generic commercially available Si_3N_4 platform for wavelengths below 850 nm. This heterogeneous integration approach offers full CMOS compatibility and enables wafer-scale manufacturing. Furthermore, a vapor-HF-based process flow for micro-transfer printing was utilized, similar to the process flow presented in chapter 4. A vapor-phase release etch provides a near 100% picking yield as it does not suffer from capillary forces which can lead to a collapse of the suspended Si layer. Our device features competitive performance with a low dark current of 107 pA at 3 V reverse bias, external quantum efficiencies around 30% at 775 nm and 800 nm, and a 3-dB bandwidth of 6 GHz. In addition, avalanche gain was demonstrated to serve applications where higher receiver sensitivities are needed. These results showcase that our heterogeneously integrated photodiodes can conveniently extend the scope of commercial Si_3N_4 platforms to serve applications beyond the telecom domain, such as biosensing, imaging, and quantum photonics.

References

[1] S. Cuyvers, A. Hermans, M. Kiewiet, J. Goyvaerts, G. Roelkens, K. V. Gasse, D. V. Thourhout, and B. Kuyken. *Heterogeneous integration of Si photodiodes on silicon nitride for near-visible light detection*. Opt. Lett., 47(4):937–940, Feb 2022.

[2] A. Rahim, E. Ryckeboer, A. Z. Subramanian, S. Clemmen, B. Kuyken, A. Dhakal, A. Raza, A. Hermans, M. Muneeb, S. Dhoore, Y. Li, U. Dave, P. Bienstman, N. Le Thomas, G. Roelkens, D. Van Thourhout, P. Helin, S. Severi, X. Rottenberg, and R. Baets. *Expanding the Silicon Photonics Portfolio With Silicon Nitride Photonic Integrated Circuits*. Journal of Lightwave Technology, 35(4):639–649, 2017.

[3] D. J. Blumenthal, R. Heideman, D. Geuzebroek, A. Leinse, and C. Roeloffzen. *Silicon Nitride in Silicon Photonics*. Proceedings of the IEEE, 106(12):2209–2231, 2018.

[4] C. Bruschini, H. Homulle, I. M. Antolovic, S. Burri, and E. Charbon. *Single-photon avalanche diode imagers in biophotonics: review and outlook*. Light: Science & Applications, 8(1):87, Sep 2019.

[5] M. A. Porcel, A. Hinojosa, H. Jans, A. Stassen, J. Goyvaerts, D. Geuzebroek, M. Geiselmann, C. Dominguez, and I. Artundo. *[INVITED] Silicon nitride photonic integration for visible light applications*. Optics & Laser Technology, 112:299–306, 2019.

[6] H. Zhao, S. Clemmen, A. Raza, and R. Baets. *Stimulated Raman spectroscopy of analytes evanescently probed by a silicon nitride photonic integrated waveguide*. Opt. Lett., 43(6):1403–1406, Mar 2018.

[7] X. Hu, D. Wu, H. Zhang, W. Li, D. Chen, L. Wang, X. Xiao, and S. Yu. *High-speed and high-power germanium photodetector with a lateral silicon nitride waveguide*. Photon. Res., 9(5):749–756, May 2021.

[8] A. Chatterjee, Saumitra, S. K. Sikdar, and S. K. Selvaraja. *High-speed waveguide integrated silicon photodetector on a SiN-SOI platform for short reach datacom*. Opt. Lett., 44(7):1682–1685, Apr 2019.

[9] S. Yanikgonul, V. Leong, J. R. Ong, T. Hu, S. Y. Siew, C. E. Png, and L. Krivitsky. *Integrated avalanche photodetectors for visible light*. Nature Communications, 12(1):1834, Mar 2021.

[10] M. Bernard, F. Acerbi, G. Paternoster, G. Piccoli, L. Gemma, D. Brunelli, A. Gola, G. Pucker, L. Pancheri, and M. Ghulinyan. *Top-down convergence of*

near-infrared photonics with silicon substrate-integrated electronics. Optica, 8(11):1363–1364, Nov 2021.

[11] Q. Yu, J. Gao, N. Ye, B. Chen, K. Sun, L. Xie, K. Srinivasan, M. Zervas, G. Navickaite, M. Geiselmann, and A. Beling. *Heterogeneous photodiodes on silicon nitride waveguides*. Opt. Express, 28(10):14824–14830, May 2020.

[12] J. Goyvaerts, S. Kumari, S. Uvin, J. Zhang, R. Baets, A. Gocalinska, E. Pelucchi, B. Corbett, and G. Roelkens. *Transfer-print integration of GaAs p-i-n photodiodes onto silicon nitride waveguides for near-infrared applications*. Opt. Express, 28(14):21275–21285, Jul 2020.

[13] Z. Huang, C. Li, D. Liang, K. Yu, C. Santori, M. Fiorentino, W. Sorin, S. Palermo, and R. G. Beausoleil. *25 Gb/s low-voltage waveguide Si-Ge avalanche photodiode*. Optica, 3(8):793–798, Aug 2016.

[14] L. Hoffman, A. Subramanian, P. Helin, B. Du Bois, R. Baets, P. Van Dorpe, G. Gielen, R. Puers, and D. Braeken. *Low Loss CMOS-Compatible PECVD Silicon Nitride Waveguides and Grating Couplers for Blue Light Optogenetic Applications*. IEEE Photonics Journal, 8(5):1–11, 2016.

[15] S. Cuyvers, B. Haq, C. Op de Beeck, S. Poelman, A. Hermans, Z. Wang, A. Gocalinska, E. Pelucchi, B. Corbett, G. Roelkens, K. Van Gasse, and B. Kuyken. *Low Noise Heterogeneous III-V-on-Silicon-Nitride Mode-Locked Comb Laser*. Laser & Photonics Reviews, 15(8):2000485, 2021.

[16] B. Wang, Z. Huang, Y. Yuan, D. Liang, X. Zeng, M. Fiorentino, and R. G. Beausoleil. *64 Gb/s low-voltage waveguide SiGe avalanche photodiodes with distributed Bragg reflectors*. Photon. Res., 8(7):1118–1123, Jul 2020.

[17] L. Virot, P. Crozat, J.-M. Fédéli, J.-M. Hartmann, D. Marris-Morini, E. Cassan, F. Boeuf, and L. Vivien. *Germanium avalanche receiver for low power interconnects*. Nature Communications, 5(1):4957, Sep 2014.

[18] L. Zheng, X. Zhang, Y. Zeng, S. Tatavarti, S. Watkins, C. Bolognesi, S. Demiguel, and J. Campbell. *Demonstration of high-speed staggered lineup GaAsSb-InP unitraveling carrier photodiodes*. IEEE Photonics Technology Letters, 17(3):651–653, 2005.

[19] S. Kapoor, R. Laishram, H. Saini, S. Mahajan, R. K. Chaubey, D. S. Rawal, and S. Vinayak. *Effect of Argon Plasma Treatment on Ohmic Contact Formation in AlGaN/GaN HEMTs*. In R. K. Sharma and D. Rawal, editors, The Physics of Semiconductor Devices, pages 191–198, Cham, 2019. Springer International Publishing.

[20] J.-M. Lee, K.-K. Kim, S.-J. Park, and W.-K. Choi. *Low-resistance and non-alloyed ohmic contacts to plasma treated ZnO*. Applied Physics Letters, 78(24):3842–3844, 2001.

[21] Y. Wang, Y. Wang, L. Li, Y. Zhao, G. Feng, and X. Wang. *Research on rapid thermal annealing of ohmic contact to GaAs*. In 2012 International Conference on Optoelectronics and Microelectronics, pages 61–63, 2012.

[22] G. Chen, J. Goyvaerts, S. Kumari, J. V. Kerrebrouck, M. Muneeb, S. Uvin, Y. Yu, and G. Roelkens. *Integration of high-speed GaAs metal-semiconductor-metal photodetectors by means of transfer printing for 850 nm wavelength photonic interposers*. Opt. Express, 26(5):6351–6359, Mar 2018.

[23] F. Yu, T.-C. Tzu, J. Gao, T. Fatema, K. Sun, P. Singaraju, S. M. Bowers, C. Reyes, and A. Beling. *High-Power High-Speed MUTC Waveguide Photodiodes Integrated on Si3N4/Si Platform Using Micro-Transfer Printing*. IEEE Journal of Selected Topics in Quantum Electronics, 29(3: Photon. Elec. Co-Inte. and Adv. Trans. Print.):1–6, 2023.

[24] D. Maes, S. Lemey, G. Roelkens, M. Zaknoune, V. Avramovic, E. Okada, P. Szriftgiser, E. Peytavit, G. Ducournau, and B. Kuyken. *High-speed uni-traveling-carrier photodiodes on silicon nitride*. APL Photonics, 8(1):016104, 2023.

[25] P. Gundlapalli, V. Leong, J. R. Ong, T. Y. Ang, S. Yanikgonul, S. Y. Siew, C. E. Png, and L. Krivitsky. *Visible-Light Integrated PIN Avalanche Photodetectors With High Responsivity and Bandwidth*. Journal of Lightwave Technology, pages 1–8, 2022.

[26] Y. Lin, Z. Yong, X. Luo, S. S. Azadeh, J. C. Mikkelsen, A. Sharma, H. Chen, J. C. C. Mak, P. G.-Q. Lo, W. D. Sacher, and J. K. S. Poon. *Monolithically integrated, broadband, high-efficiency silicon nitride-on-silicon waveguide photodetectors in a visible-light integrated photonics platform*. Nature Communications, 13(1):6362, Oct 2022.

[27] C. D. Vita, F. Toso, N. G. Pruiti, C. Klitis, G. Ferrari, M. Sorel, A. Melloni, and F. Morichetti. *Amorphous-silicon visible-light detector integrated on silicon nitride waveguides*. Opt. Lett., 47(10):2598–2601, May 2022.

[28] G. Yuan, R. Pownall, P. Nikkel, C. Thangaraj, T. Chen, and K. Lear. *Characterization of CMOS compatible waveguide-coupled leaky-mode photodetectors*. IEEE Photonics Technology Letters, 18(15):1657–1659, 2006.

[29] A. Chatterjee, Saumitra, S. K. Sikdar, and S. K. Selvaraja. *High-speed waveguide integrated silicon photodetector on a SiN-SOI platform for short reach datacom*. Opt. Lett., 44(7):1682–1685, Apr 2019.

[30] M. Bernard, L. Gemma, D. Brunelli, G. Paternoster, and M. Ghulinyan. *Coupling of Photonic Waveguides to Integrated Detectors Using 3D Inverse Tapering*. J. Lightwave Technol., 40(18):6201–6206, Sep 2022.

[31] P. Berger. *MSM photodiodes*. IEEE Potentials, 15(2):25–29, 1996.

6

Micro-transfer printed Gallium Arsenide semiconductor optical amplifiers

In the previous chapter, detectors on silicon nitride for the (near-)visible spectral region were presented. In this chapter, the toolbox for integrated photonics in the (near-)visible spectrum is further extended with micro-transfer printable GaAs semiconductor optical amplifiers. This development constitutes a first step towards heterogeneous lasers on silicon nitride that emit around 780 nm. The material presented in this chapter has in part been published in [1].

6.1 Introduction

In recent years, considerable effort has been devoted to extend the application scope of integrated photonics to the shorter wavelength spectrum below the silicon bandgap. At (near-)visible wavelengths, numerous applications can benefit from on-chip solutions, including optical coherence tomography (OCT) [2], augmented reality/virtual reality (AR/VR) applications [3], imaging, biosensing and quantum communications [4]. In addition, more fundamental applications can be envisioned, such as probing matter in atomic physics [5] or building ultra precise optical atomic clocks based on the two-photon transition in Rubidium [6]. Moreover, a shorter wavelength platform enables superior high temperature perfor-

mance for coherent light sources, which could be leveraged to improve the overall energy efficiency in datacenters or for deployment in hot environments [4] .

As the silicon nitride platform, which is favored for applications in the (near-)visible spectral range, is a purely passive platform, optical amplification and detection rely critically on the co-integration of other materials. In the previous chapter, silicon photodiodes on silicon nitride were presented to enable light detection below 850 nm. For optical amplification in the (near-)visible spectral region, III-V semiconductors such as GaAs or GaN remain indispensable.

Several demonstrations of integrated laser sources for the visible spectrum have recently been reported in the literature. A hybrid-integrated diode laser operating around 684 nm is demonstrated in [7]. By butt-coupling an optical amplifier to a silicon nitride feedback chip with a Vernier mirror, 10.8 nm of tunability and an intrinsic linewidth of 2.3 kHz are achieved. Such a butt-coupling approach was also employed in [8], where commercial Fabry-Pérot laser diodes are coupled to a silicon nitride chip containing a ring resonator with a feedback loop to enable self-injection locking. Such an approach is well suited to stabilize an integrated laser without requiring additional hardware such as electronic control circuitry [9]. When the laser frequency is closely aligned to a resonance of the ring, the reflected optical field provides continuous feedback to align the laser to the ring resonance, greatly reducing the laser linewidth [9]. By using multiple laser diodes, wavelengths between 404 nm up to 780 nm are readily available, covering the entire visible spectrum. Furthermore, a coarse tunability up to 12.5 nm, fine-tuning speeds up to 267 GHz μs^{-1}, intrinsic linewidths down to a few kilohertz, and output powers up to 10 mW are reported [8]. However, efficient butt-coupling requires maximal spatial overlap between the optical modes of the two chips being coupled. This complicates packaging and impedes low-cost and high-volume wafer-scale manufacturing. Heterogeneous GaAs lasers on silicon nitride, as demonstrated in [10] and [4], are therefore an attractive alternative. In [10], lasers operating around 990 nm are realized using a proprietary edge-coupling technique to limit the coupling loss to approximately 0.5 dB. In [4], microresonator combs and lasers operating around 980 nm with 20 nm tunability, a fundamental linewidth of 2.8 kHz and $>$10 mW output power are reported. For this, an intermediary dielectric waveguide is introduced to couple in two steps. On one side, the geometry of the intermediary waveguide is optimized for butt-coupling to the GaAs semiconductor optical amplifier (SOA) and on the other end, it is optimized for evanescent coupling to the silicon nitride waveguide. Coupling efficiencies up to 70% are demonstrated, and improvements up to 90% are supposedly possible.

In [11], GaAs epitaxial coupons are micro-transfer printed on a silicon substrate and subsequently processed into Fabry-Pérot ridge waveguide lasers. However, the potential of micro-transfer printing is not fully exploited because the GaAs processing is performed on the target wafer. Moreover, no external silicon

nitride cavity is included, prohibiting functionalities such as wide tunability and high coherence. Although wavelength tunability is not strictly required for a number of applications, some tunability nevertheless remains desirable to relax fabrication tolerances while enabling precise control over the emission wavelength, e.g. to target atomic transitions [4]. Another recent demonstration of micro-transfer printed lasers for the (near-)visible spectral region is found in [12], where mass-manufacturable GaAs vertical-cavity surface-emitting lasers (VCSELs) on silicon nitride are reported. The VCSELs emit at 850 nm to target sensing and communication applications, and exhibit 5 nm tunability, a sub-mA threshold current and 0.1 mW of output power.

In this chapter, etched-facet GaAs SOA's are presented as a first step towards narrow-linewidth-, tunable- and mode-locked lasers on silicon nitride using micro-tranfser printing. The SOA's operate around 780 nm and constitute a key building block to develop a versatile silicon nitride platform for applications in the (near-)visible spectrum. In the remainder of this chapter, the design, fabrication and characterization of the SOA's is discussed. The GaAs process flow was initially conceived by Dr. Artur Hermans and Dr. Jeroen Goyvaerts and later optimized by the author and Max Kiewiet. Furthermore, the author took the lead in the fabrication and characterization of the first processing runs, while Max Kiewiet led later processing runs based on an optimized epitaxy. At the time of writing, this project is still under development and has become the main research subject of Max Kiewiet.

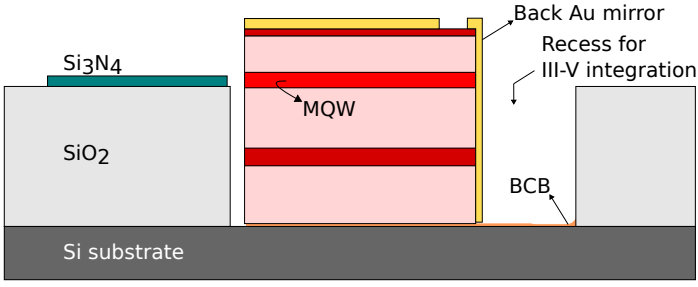

Figure 6.1: Proposed integration strategy. The GaAs SOA is micro-transfer printed directly on the silicon substrate for improved thermal performance. The output of the SOA can be directly coupled into a Si_3N_4 spot size converter.

6.2 Design and fabrication

The GaAs SOA discussed in this chapter is optimized for edge-coupling. This is in contrast to the heterogeneous lasers discussed in chapters 2 and 4 where evanescent coupling was employed. A similar integration strategy is demonstrated

Type	Number of layers	Material	Thickness (nm)	Doping type	Doping level (cm^{-3})	Al content
Contact	1	GaAs	50 (**200**)	p	1e19 (**2.5e19**)	-
Transition	1	AlGaAs	50	p	2e18	0.4-0.05
Cladding	1	AlGaAs	1100	p	1e18	0.4
Cladding	1	AlGaAs	100	p	2-5e17	0.4
Transition	1	AlGaAs	35	-	-	0.3-0.4
Barrier	4	AlGaAs	8	-	-	0.3
QW	4	AlGaAs	5.5	-	-	0.05
Barrier	1	AlGaAs	8	-	-	0.3
Transition	1	AlGaAs	35	-	-	0.4-0.3
Cladding	1	AlGaAs	1465	n	1e18	0.4
Contact	1	AlGaAs (**GaAs**)	500	n	2e18 (**3e18**)	0.2
Cladding	1	AlGaAs	1465	n	1-2e18	0.4
Transition	1	AlGaAs	50	n	2e18	0.05-0.4
Buffer	1	GaAs	20	n	2e18	-
Sacrificial	1	GaInP	500	n	2e18	-
Buffer	1	GaAs	100	n	2e18	-

Table 6.1: Epitaxial layer stack for the GaAs SOA's. Zn was used for p-doping whereas Si was used for the n-doped layers. Modifications made to the epitaxial layers for improved metal-semiconductor contacts are highlighted in brackets.

in [13], where InP Fabry-Pérot lasers are micro-transfer printed and edge-coupled to a silicon waveguide. A schematical representation of an envisioned GaAs SOA edge-coupled to a silicon nitride waveguide is shown in Fig. 6.1. The front facet at the Si_3N_4 side is angled (7°) to reduce reflections. To minimize optical losses at the backside facet, a Au back mirror is incorporated. Although the coupling efficiency can be a concern for edge-coupled devices, such SOA's can be integrated directly on the silicon substrate. This dramatically reduces the thermal impedance of the device and minimizes performance degradation at elevated temperatures or for high electrical injection currents. A more rigorous thermal comparison is presented in Appendix A. In addition, an edge-coupling approach does not require intermediate layers such as silicon [14] or amorphous silicon [15], enabling utilization of the full transparency range of the silicon nitride platform without being limited by the bandgap of the intermediate layer [10]. This is particularly advantageous at short wavelengths, as few transparent materials are appropriate to bridge the large refractive index contrast between the III-V gain material and silicon nitride.

The (Al)GaAs epitaxial layer stack, grown using metalorganic vapor-phase epitaxy (MOVPE), is outlined in Table 6.1. The wafers were initially ordered from Tyndall and later from III-V Lab. Four AlGaAs quantum wells are included with a photoluminescence wavelength of 780 nm. Furthermore, a 500 nm thick InGaP sacrificial layer is included which can be selectively etched with respect to GaAs using HCl [16]. This allows one to suspend the SOA's on the GaAs source

substrate and enable micro-transfer printing. An InGaP sacrificial layer has the advantage that no oxide residues are formed upon exposure to air, in contrast to Al-containing layers. $Al_xGa_{1-x}As$ is also attacked by HCl, but the etching rate is only significant when the Al content exceeds 0.6 [17, 18]. The SOA coupons are oriented under a 45° angle on the source wafer, similar to what was proposed for GaAs VCSELs [19]. However, as InGaP etching in HCl is quasi-isotropic, it is expected that this is not strictly necessary. The epitaxy was modified at a later stage to improve the metal-semiconductor contact resistivities. The modifications are highlighted in brackets in Table 6.1 and are discussed in more detail in subsection 6.2.3. For the results discussed in the remainder of this chapter, the original epitaxy was used unless mentioned otherwise.

6.2.1 GaAs semiconductor optical amplifier fabrication

The GaAs SOA process flow is schematically illustrated in Fig. 6.2. A simplified representation of the GaAs epitaxy is shown in Fig. 6.2(a). The following paragraphs describe the process flow in greater detail.

Ridge waveguide definition

As a first step, a 300 nm PECVD Si_3N_4 layer is deposited which serves as a hard mask for the subsequent ridge waveguide definition. As the ridge is only 2 μm wide, an AZ 5214E photoresist is used in positive mode to ensure sufficient adhesion of the long and narrow resist feature on the surface. The Si_3N_4 hard mask is subsequently patterned using RIE dry etching (using CF_4, SF_6 and H_2), followed by resist removal and ICP dry etching of the (Al)GaAs layers. As the photoresist polymerizes during the plasma etching step, a short oxygen plasma is used to clean the sample after rinsing with acetone, IPA and deionized (DI) water. For the ICP dry etch, a BCl_3/N_2 chemistry is used to etch trenches until approximately 300 nm is left above the top transition layer. The etching selectivity of (Al)GaAs with respect to PECVD Si_3N_4 was measured to be slightly larger than 10:1. Typically, some dark residual features can be observed after ICP etching, which is possibly caused by $AlCl_3$ byproduct formation on the sample surface [20]. Fortunately, this byproduct can easily be removed using standard cleaning with a solvent such as acetone and IPA.

Next, a 300 nm Si_3N_4 passivation layer is deposited with PECVD. An acid dip (5 s HCl:H_2O 1:1) is performed before the sample is loaded in the PECVD at room temperature to avoid oxidation of the Al-containing epitaxial layers (which would result in extra losses). Hydrochloric acid (HCl) by itself, without H_2O_2, does not attack GaAs. However, it can remove natural oxides from the GaAs surface [21]. After Si_3N_4 passivation, the sample is planarized with BCB (Cyclotene 3022-57), which is spincoated for 40 s at 2000 rpm and cured at 280°C to yield a film thick-

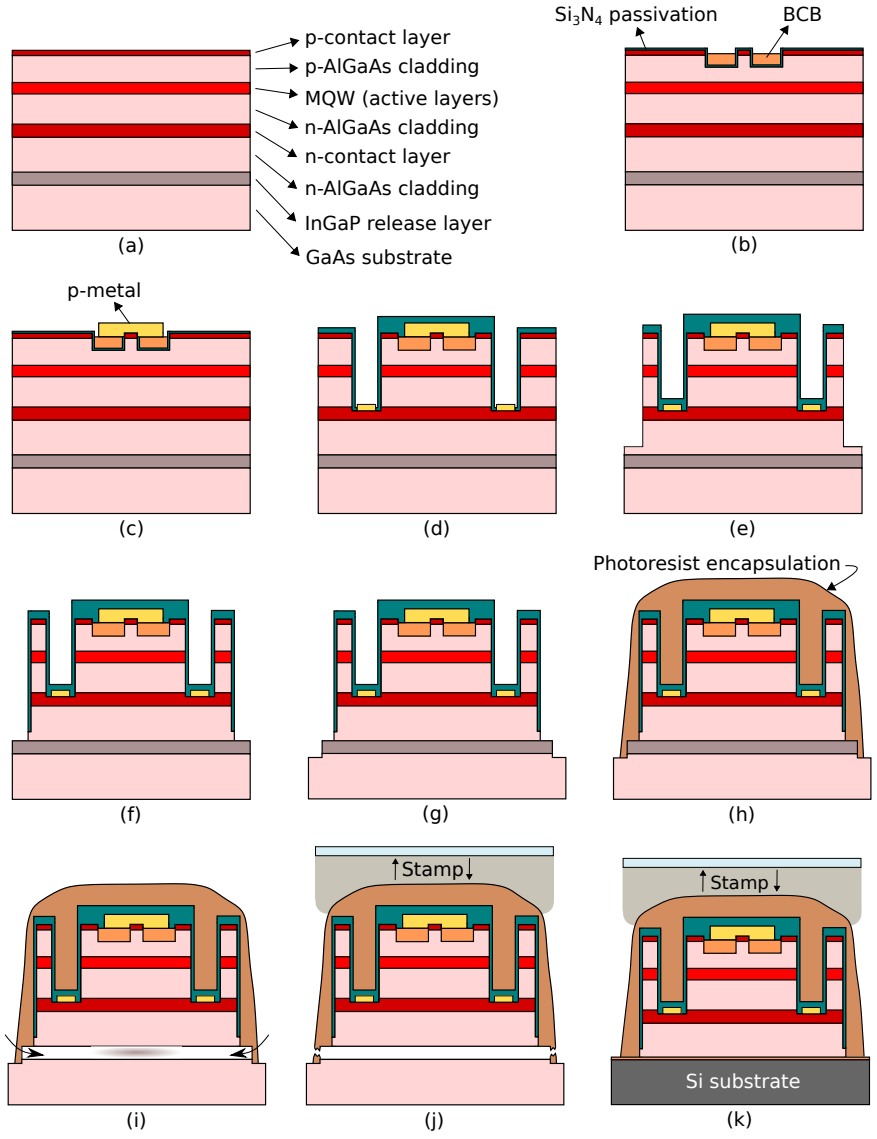

Figure 6.2: Illustration of the SOA process flow. (a) III-V layer stack, (b) ridge waveguide definition, PECVD Si_3N_4 passivation, and planarization with BCB, (c) Ti/Au p-metal definition, (d) n-via definition and n-metal deposition, (e) dry etch to define the coupon facets, (f) after the mirror deposition (not shown), a second facet etch (wet) is used until the sacrificial layer is reached, (g) release layer patterning, (h) photoresist encapsulation and tether definition, (i) release etch, (j) coupon pick-up, (k) coupon printing on a target substrate.

ness of approximately 8 µm. The BCB is subsequently etched back using RIE dry etching (based on O_2 and SF_6) to solely leave the previously etched trenches of the ridge waveguide filled with BCB (Fig. 6.2(b)).

In case a GaAs-based mode-locked laser is envisioned, a saturable absorber can be defined hereafter by electrically isolating a part of the SOA. For this, an additional contact lithography and ICP dry etching step are used to locally remove the GaAs p-contact layer and part of the AlGaAs p-cladding under a 45° angle to reduce back reflections.

P-type contact metallization

In a next step, the p-contacts are defined with contact lithography using a TI 35E photoresist with image reversal. The remaining Si_3N_4 on top of the GaAs p-contact is removed using RIE dry etching and a 5 s acid dip in HCl:H_2O 1:1 is performed to remove the native oxide on GaAs prior to depositing 40 nm Ti and 250 nm Au with electron beam evaporation. The resulting device after lift-off is schematically shown in Fig. 6.2(c).

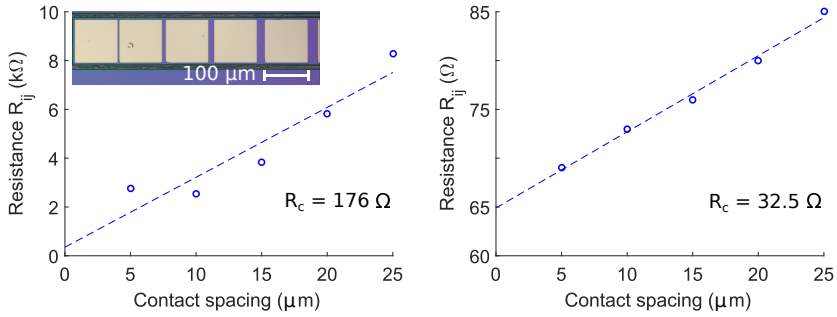

Figure 6.3: Measured resistances between the TLM contact pads as a function of the spacing between the pads. The measurement data before and after RTA are respectively shown on the left and right. A microscope picture of the TLM test structure is shown on the top left. The dotted line represents a linear fit to the measurement data to estimate the contact resistance R_c and transfer length L_T.

Figure 6.3 depicts the measured resistances between the 100 µm×100 µm contact pads of the Transfer Length Method (TLM) test structure. Details on this measurement method can be found in [22]. A high contact resistance of $R_c \approx 176\ \Omega$ is extracted. Rapid thermal annealing (RTA) at 380°C reduces the contact resistance by roughly an order of magnitude to $R_c \approx 32.5\ \Omega$. Furthermore, the transfer length L_T post-RTA is estimated to be 41 µm, resulting in a contact resistivity of $\rho_c = R_c \cdot W \cdot L_T \approx 1.3 \cdot 10^{-3}\ \Omega\,\text{cm}^2$, where W=100 µm is the width of the contact pad. Despite RTA, this value is significantly larger than typical values reported in the literature [23–25]. This issue is discussed in greater detail in section 6.2.3.

Si_3N_4 passivation and N-via etch

After p-metallization, 300 nm of PECVD Si_3N_4 is deposited to serve as a hard mask for the subsequent n-via opening. Contact lithography with TI 35E photoresist is used to pattern the Si_3N_4 hard mask. Next, the photoresist is removed and trenches are etched to reach the 500 nm thick n-contact layer using the aforementioned ICP etching recipe. The n-contact layer is deliberately overetched by approximately 100 nm to make sure that no AlGaAs cladding remains on top. The sample is subsequently passivated once again with 300 nm of PECVD Si_3N_4 to cover the sidewalls of the n-via and avoid potential shorts with the p-doped layers and p-metal.

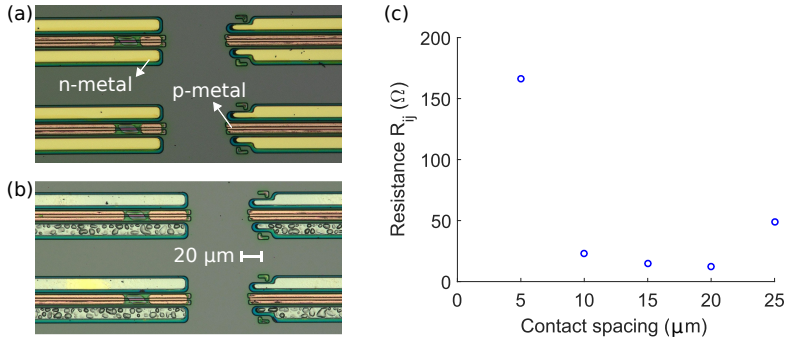

Figure 6.4: Microscope pictures of of the GaAs SOA coupons after the n-metal lift-off before annealing (a) and after annealing (b). (c) Measured resistances (after annealing) between the n-TLM contact pads as a function of the spacing between the pads.

N-type contact metallization

Analogous to the p-contacts, the n-contacts are defined with contact lithography using a TI 35E photoresist with image reversal. The remaining Si_3N_4 on top of the n-contact layer is removed using RIE dry etching. The sample is then dipped for 5 s in HCl:H_2O 1:1 to remove the native oxide on the n-contact layer prior to the deposition of Ni/Ge/Au/Ti/Au (30/20/50/40/100 nm). Ge/Au and Ni/Ge/Au films are widely used for fabricating ohmic contacts to n-type (Al)GaAs [23, 26–28]. Annealing leads to diffusion of Ge into the n-type (Al)GaAs layer, lowering the contact resistance [29]. Moreover, adding small amounts of Ni to the Ge/Au stack can further reduce the contact resistance while improving adhesion and maintaining a smooth surface morphology [19, 26]. Still, good ohmic contacts have also been achieved without Ni, for example by using a Ge/Au(alloy)/Pd/Au metal stack [30]. The GaAs SOA coupon after n-metal lift-off is schematically shown in Fig. 6.2(d) and a microscope picture is shown in Fig. 6.4(a).

As the contacts of the n-TLM test structure exhibit a current-voltage behavior similar to a Schottky junction, a RTA annealing step is conducted at $380°C$. During annealing, the Au and Ge diffuse, resulting in a change of color and some bubble formation, as shown in Fig. 6.4(b). Typically, these effects are not clearly visible because a thick metal layer is present on top. However, because the top Au layer is here only 100 nm thick, these changes can easily be observed.

Fig. 6.4(c) shows the measured resistances between adjacent contact pads of the n-TLM test structure. As the measurements points deviate strongly from a linear fit, it is difficult to reliably estimate the contact resistance R_c and transfer length L_T. However, as the resistance does not monotonically increase with increasing contact spacing, the metal-semiconductor contact resistance R_c likely dominates the total measured resistance $R_{total} = 2R_c + 2R_m + R_s$, where R_m is the resistance of the contact metal (which can usually be neglected), and R_s is the resistance in the semiconductor. If one assumes that $R_{total} \approx 2R_c$ and ignores the outlier measured at a 5 μm contact spacing, one obtains that $R_c \approx 12\ \Omega$. Subsection 6.2.3 elaborates on the origin of this high contact resistance.

Dry etching of the coupon facets

In a next step, the sample is once again passivated with 300 nm PECVD Si_3N_4, followed by a contact lithography step (using TI 35E photoresist in positive mode) to define the facets of the coupon. Based on [19], the mask is defined with rounded edges to mitigate pinhole formation in the corners and avoid penetration of the HCl etchant through the Si_3N_4 passivation during release etching.

The Si_3N_4 is patterned using RIE dry etching and the photoresist is removed thereafter. Next, an ICP dry etch is used to etch through the (Al)GaAs layers until approximately 300 nm of (Al)GaAs is left above the sacrificial layer. This step is schematically shown in Fig. 6.2(e).

Mirror definition

Next, the sample is dipped in HCl:H_2O 1:1 for 5 s and loaded in the PECVD at room temperature to deposit a 500 nm thick Si_3N_4 passivation layer at $270°C$. Afterwards, a contact lithography step is used to define the backside mirror of the SOA. For the first two processing runs, a TI 35E photoresist (spincoated at 3000 rpm) with image reversal was used. The patterned photoresist is shown in Fig. 6.5(a). A short oxygen plasma step (1 min) is used to make sure that no resist remains in the trench. Afterwards, a short 'flash' of Ti (for adhesion promotion) and 400 nm of Au are deposited and lift-off is performed. The Ti layer is kept as thin as possible to minimize light absorption. Fig. 6.5(b) shows a scanning electron microscope (SEM) image of the backside mirror of a GaAs coupon that was printed on top of a Si dummy sample. The close-up shown in Fig. 6.5(c) reveals that the metal coverage on the facet is poor. This can be solved by tilting

the sample during the metal deposition, in combination with a bilayer lift-off process. Tilting the sample ensures proper metal coverage of the coupon facet, while the bilayer lift-off process is useful to acquire a sufficiently strong resist undercut. The latter avoids that the deposited metal completely covers the resist edge, which typically leads to lift-off problems (e.g. the gold mirror can stick out several microns above the coupon after lift-off). Details on the bilayer lift-off process can be found in Appendix C.

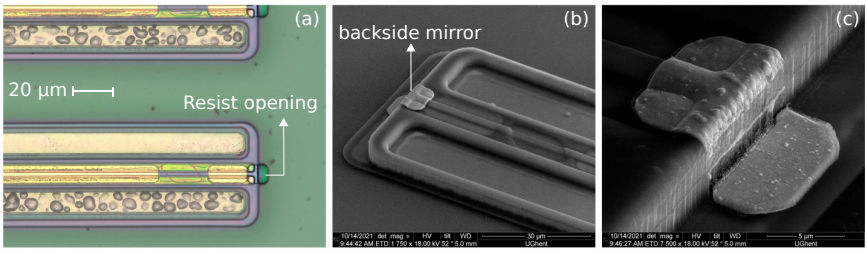

Figure 6.5: Backside mirror of the GaAs coupon. (a) Microscope picture of the patterned photoresist before metal deposition. (b) SEM image of the backside mirror after lift-off. (c) SEM image of the backside mirror, showing the poor coverage on the coupon facet.

Wet etching of the coupon facets

The remaining ∼300 nm of (Al)GaAs above the sacrificial layer is patterned to complete the facet definition of the coupons. For this, a contact lithography step with TI 35E photoresist is used to define the periphery of the coupon, and RIE dry etching is used to etch the surrounding Si_3N_4 passivation layer. Afterwards, the (Al)GaAs is wet etched using H_3PO_4(85%):H_2O_2(30%):H_2O (3:1:25). This solution selectively etches GaAs and AlGaAs at a rate around 100 nm/min and stops on the InGaP layer (see also [31]). The resulting coupon is schematically represented in Fig. 6.2(f) and a microscope picture is shown on the left in Fig. 6.6.

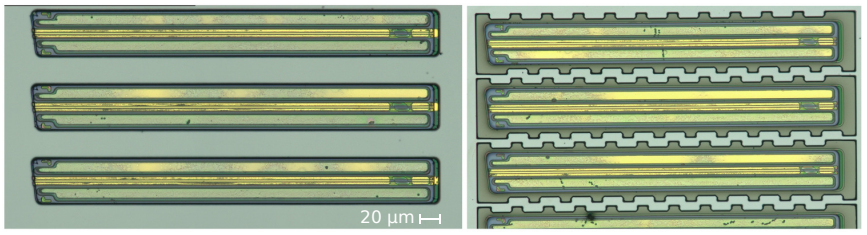

Figure 6.6: Microscope picture of GaAs coupons after the second facet etching step (left), and after the photoresist definition to pattern the release layer (right).

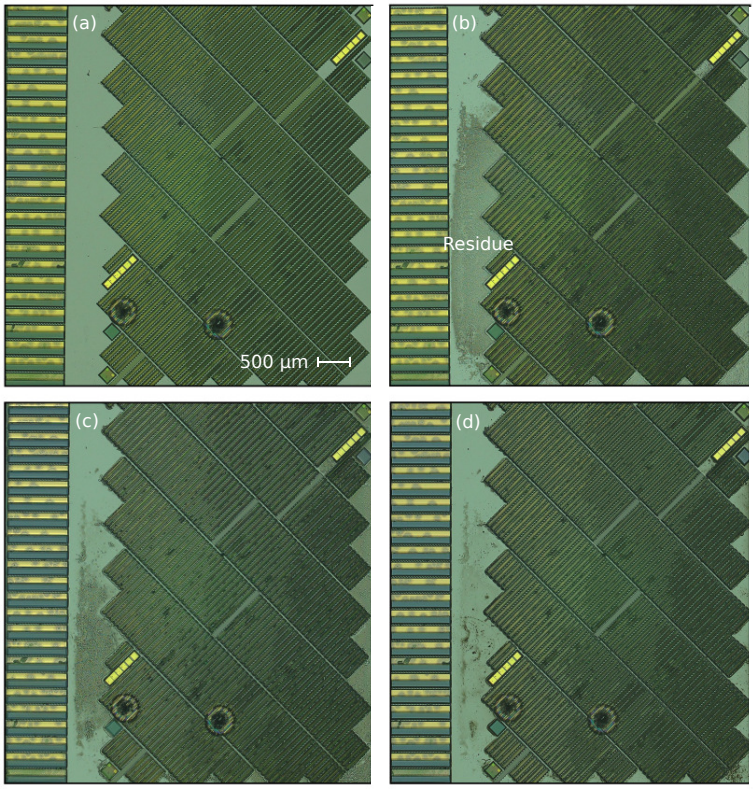

Figure 6.7: Microscope pictures of the GaAs sample prior to InGaP release layer patterning (a), and after 1 min (b), 2 min (c), and 5 min (d) of HCl wet etching. Some redeposited residue is observed after 1 min of HCl etching, and evolves as the InGaP is further etched. When the InGaP etching is complete, some residue remains stuck to the GaAs surface and no further changes are observed when HCl etching is continued. A digital etching process with H_2O_2 and HCl can be used to clean the contaminated surface. The two bubbles at the bottom of the sample originate from the earlier BCB planarization step.

Release layer patterning

After removing the photoresist from the previous step, contact lithography is used to define the release layer pattern with TI 35E photoresist (used in positive mode). A microscope picture of the coupons with patterned photoresist is shown on the right side of Fig. 6.6. The InGaP release layer is subsequently etched using HCl (32%, undiluted) at a rate of approximately 200 nm/min. Typically, some bubble formation can be observed during the etching process [31]. Completion of the etching step was confirmed using a profilometer. Although HCl etches the InGaP highly selective, the absence of an oxidizing agent such as H_2O_2 leaves the InGaP surface relatively rough [16]. More importantly, it was observed that some residue,

which is presumably a byproduct of the etching process, can redeposit on the GaAs substrate. From Fig. 6.7(a)-(d) one can see how some residue is visible after 1 min of HCl etching, and subsequently evolves as the InGaP is further etched. When the InGaP etching is complete, the undissolved residue remains stuck to the GaAs surface and no further changes are observed when HCl etching is continued. A close-up image at the borders of the coupon is shown in Fig. 6.8. To keep the surface clean, a digital etching process can be used. For this, HCl etching is alternated with H_2O_2 etching. The sample should be thoroughly rinsed in between the two etching steps to avoid mixing of the H_2O_2 and HCl solution, which can lead to significant etching of GaAs (etch rates of $>$400 nm/min have been measured for 1:1 HCl:H_2O_2 [16]). Such a digital etching process can also be used to slowly etch GaAs with great etch depth control around 1.2 nm/cycle [19]. A stable native oxide forms at the GaAs surface upon submersion in H_2O_2, and is subsequently etched away by HCl while leaving the GaAs underneath unaffected [32].

After the wet etch, $\sim$200 nm of the GaAs substrate is etched with the same photoresist mask using ICP dry etching. This ensures that no residual material remains between the GaAs substrate and the supporting tethers that will be defined in the next step. The photoresist is stripped after etching using standard cleaning with acetone, IPA, deionized water, and an oxygen plasma. The resulting SOA is schematically depicted in Fig. 6.2(g).

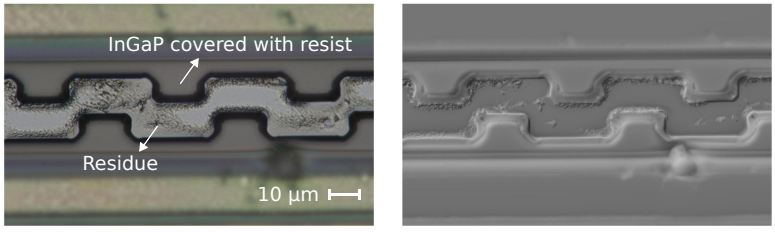

Figure 6.8: Microscope picture (left) and shadow-effect-mode image (right) of the coupon periphery after 5 min of HCl etching to pattern the release layer.

Coupon encapsulation

As a final step before the release etch, the coupons are encapsulated with photoresist. The sample is first dipped for 5 s in HCl:H_2O 1:1 to remove the native oxide that would otherwise be attacked during the release etch and lead to delamination of the supporting tethers. The sample is then briefly rinsed in deionized water and IPA and thoroughly dried with a nitrogen gun. A TI prime adhesion promotor and a TI35 E photoresist are spincoated immediately afterwards. No baking step is included before the first spincoating step to suppress native oxide growth. The encapsulated coupon is schematically shown in Fig. 6.2(h) and a microscope pic-

ture of the sample is shown in Fig. 6.9. The breaking regions of the tethers are designed to be approximately 2.5 µm wide.

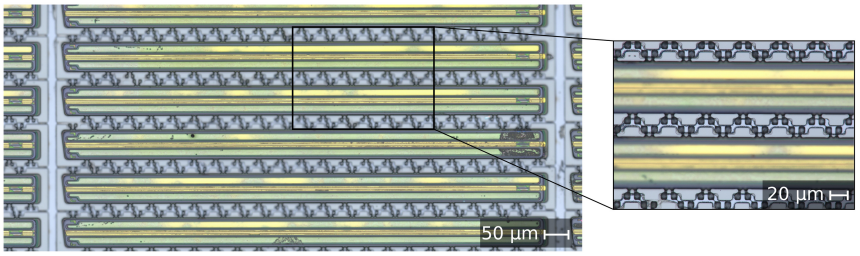

Figure 6.9: Microscope picture of the encapsulated GaAs coupons before release etching.

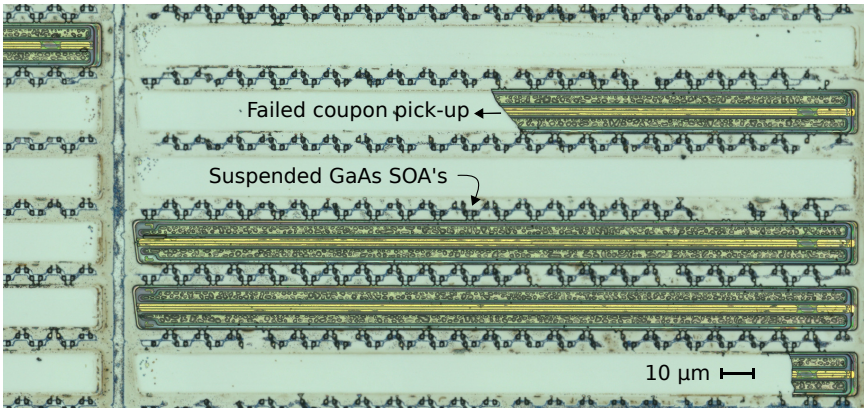

Figure 6.10: Microscope picture of suspended GaAs SOA's after the release etch. Residue from the outer InGaP remains and appears as a light brown film accompanied by some particles at the periphery of the coupons. To verify whether release etching was successful, some coupons were picked up with scotch tape. However, because the tethers were still too strong, some coupons broke in half and part of the coupon remained on the source. Still, the pick-up site turns out clean and smooth which confirms the successful completion of the release etch.

Release etch

Finally, the coupons are released in HCl (undiluted, 32%), for a duration of 90 minutes. The sample is then carefully rinsed using three beakers with deionized water to remove the HCl, and left to dry in the wet bench (blow drying with nitrogen could lead to a collapse of the suspended coupons). Residues from the outer InGaP remain, as can be seen from Fig. 6.10. Such residues were also reported for GaAs VCSELs [19]. Again, a digital etch process can be used to remove the

residue and clean the substrate (e.g. 30 s H_2O_2 and 10 s HCl:H_2O (1:2) [19]), although this is not always strictly necessary for successful micro-transfer printing. Completion of the release etch is tested by attempting to pick up coupons using scotch tape. However, as the strength of the supporting tethers prevented any coupons from being picked up, the tethers were thinned down with a 3-minute oxygen plasma treatment at a rate of 100 nm/min. While some coupons could be picked up with scotch tape after the treatment, others broke in half during the process (as can be seen from Fig. 6.10), suggesting that the tethers are still too wide and need further thinning. Despite these problems, the pick-up site as well as the coupon backside are found to be clean and smooth, indicating a successful completion of the release etch. Based on some preliminary micro-transfer printing tests, the tethers appear sufficiently thin after 6 min of oxygen plasma. The devices are now ready for pick-up and printing, as illustrated in 6.2(i)-(k).

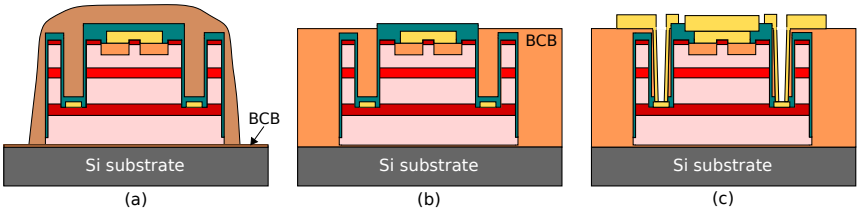

Figure 6.11: Post-processing on the Si target. (a) micro-transfer printed GaAs SOA, (b) encapsulation removal and BCB planarization, (c) via opening and final metallization.

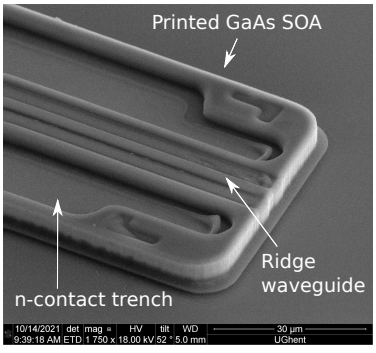

Figure 6.12: SEM image of a micro-transfer printed GaAs SOA.

6.2.2 Micro-transfer printing and post-processing

To enable characterization of the GaAs SOA's, some coupons are printed and post-processed on a Si dummy substrate. The processing steps are schematically illus-

trated in Fig. 6.11.

Markers are first etched in the Si using a photoresist mask to enable proper alignment during micro-transfer printing. After cleaning of the target sample, a thin adhesive layer of DVS-BCB (Cyclotene 3022-35), diluted with mesitylene to a 1:5 volumetric ratio, is spincoated at 3000 rpm for 40 s and baked at 150°C for 10 min. Although a BCB layer degrades the thermal contact with the Si substrate, it is generally required to tolerate some roughness at the GaAs coupon backside. For future developments, the BCB thickness could be optimized to minimize the thermal penalty while ensuring a reliable bond. A stamp with a size of 1050 μm$\times$70 μm is used to pick-up and print three GaAs coupons with a size of 1020 μm$\times$65 μm. A SEM image of a micro-transfer printed coupon is depicted in Fig. 6.12. After micro-transfer printing and encapsulation removal, the adhesive BCB layer is cured in vacuum at 280°C. Next, a thick BCB cladding (Cyclotene 3022-57) is spincoated for 40 s at 2000 rpm and cured at 280°C, yielding a film thickness of approximately 8 μm. The BCB is then etched back using RIE dry etching (using O_2 and SF_6) at a rate of approximately 340 nm/min until no BCB remains on top of the p-contact layer. Fig. 6.13 depicts the measured profile across the SOA before BCB spincoating, as well as during and after BCB etching. Prior to the BCB deposition, the n-via's and ridge waveguide can clearly be observed. In a next step, contact lithography with TI 35E photoresist and image reversal is used to open the p-contact layer. RIE dry etching is employed to etch the remaining Si_3N_4 (using CF_4, SF_6 and H_2). After removing the photoresist, a second contact lithography and etching step are performed to open the n-via's. For this, an AZ10XT photoresist is selected which, after development, is reflowed for 1 min at 120°C to acquire sloped sidewalls. This helps to achieve proper metal coverage across the large step height of the via's. Finally, 1 μm Au with a 40 nm Ti adhesion layer is patterned using lift-off for electrical contacting. A microscope picture of the resulting SOA is depicted in Fig. 6.14. The sample is afterwards diced near the facets of the GaAs SOA's so that the optical output can be coupled to a lensed fiber. The measurement results are discussed in section 6.3.

6.2.3 Improving the metal-semiconductor contacts

As discussed in section 6.2.1 (Figures 6.3 and 6.4(c)), the measured metal-semiconductor contact resistances, both for the p- and n-layer, remain significantly higher than typical values reported in the literature [23]. Based on feedback from III-Lab (France) and the Ferdinand-Braun-Institut (Germany), the poor performance of the contacts is primarily attributed to the following reasons.

Firstly, the p-contact layer thickness is relatively thin [33]. Depending on the treatment used to remove the native oxide and prepare the surface for metallization, some etching of the contact layer might occur. A contact layer thickness $>$150 nm

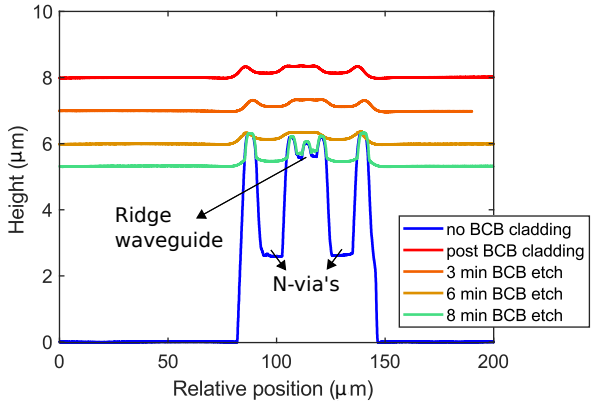

Figure 6.13: Profile measurement of a micro-transfer printed GaAs coupon on a Si substrate before BCB planarization and after the BCB blanket etch.

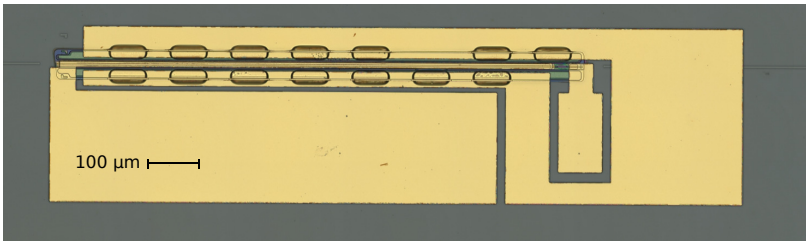

Figure 6.14: Microscope picture of a post-processed GaAs coupon before dicing of the target sample.

is typically recommended. For the n-contact layer, a sufficiently thick layer is especially important to reproducibly reach the n-contact layer without entering adjacent layers. Fortunately, for edge-coupled SOA's, the n-contact layer can be chosen relatively thick, e.g. currently 500 nm.

Secondly, the p-doping level of 1e19 cm^{-3} is rather low compared to typical values reported in the literature [23, 33]. By increasing the doping level, the depletion region at the metal-semiconductor interface becomes narrower, allowing electrons to flow in both directions easily at any bias by tunneling through the barrier [34].

Thirdly, as the n-contact layer currently contains Al, the slightest trace of oxide linked to the Al will tend to push the contact towards Schottky rather than ohmic behavior. For this reason, it is often preferred to use a GaAs n-contact instead. Still, good ohmic contacts are also manufacturable using n-type AlGaAs layers, for example by introducing a thin buffer GaAs contact layer. The buffer layer prevents oxidation of Al and also helps to improve adhesion [26].

Furthermore, if available, one can use RF pre-sputtering or an Argon ion gun to sputter of any native oxide just prior to the metal deposition. Contacts prepared with low-energy Argon bombardment typically exhibit improved conductivity as compared to contacts that were solely pre-cleaned chemically [35]. Still, the use of ion bombardment is a compromise solution as it introduces some radiation damage in the disordered subsurface layer. As a result, vacancies, interstitials and defects can be created which deteriorate the electrical performance [35]. Finally, one can slightly increase the temperature of the RTA step, e.g. 430°C instead of 380°C, to further bring down the contact resistivity.

Based on these findings, the epitaxy is modified as follows:

1. GaAs p-contact layer thickness: 50 nm $\rightarrow$ 200 nm
2. GaAs p-contact doping level: 1e19 cm^{-3} $\rightarrow$ 2.5e19 cm^{-3}
3. AlGaAs n-contact layer $\rightarrow$ GaAs n-contact layer
4. n-contact layer doping level: 2e18 cm^{-3} $\rightarrow$ 3e18 cm^{-3}

These changes are also highlighted in Table 6.1. Using this optimized epitaxy, a contact resistance $R_c = 2.8\ \Omega$ and contact resistivity $\rho_c = 9.5 \cdot 10^{-6}\ \Omega\ cm^2$ are achieved for the p-contact after RTA at 430°C (before annealing, $R_c = 31.8\ \Omega$ and $\rho_c = 2.8 \cdot 10^{-3}\ \Omega\ cm^2$). For the n-contact, $R_c = 2.1\ \Omega$ and $\rho_c = 6 \cdot 10^{-5}\ \Omega\ cm^2$ are achieved after RTA at 430°C (before annealing the n-contacts exhibited strong Schottky behavior). These results confirm the significance of the epitaxial changes to greatly improve the metal-semiconductor contact quality. It is expected that the contact resistance can further be improved by including RF pre-sputtering or Ar bombardment with an ion-gun prior to metallization. The optimized epitaxy has been used for more recent GaAs processing efforts, including the recent demonstration of pre-processed etched-facet GaAs Fabry-Pérot lasers on silicon led by Max Kiewiet [1].

6.3 Preliminary measurements

Figure 6.15 shows a picture of the diced sample (left) and the measurement setup used to capture the optical output with a lensed fiber (right). DC contact probes and a Keithley 2400 current source are used to bias the device, and some red light can clearly be observed with the naked eye when the biasing current exceeds $\sim$20 mA. The measured voltage-current curve and differential resistance after RTA are depicted in Fig. 6.16. The differential resistance reaches 14.3 Ω at 60 mA bias current (corresponding with a current density of $\sim$3 kA/cm^2), which, as expected, is relatively large compared to typical values reported in the literature [36]. The measured amplified spontaneous emission (ASE) spectrum is visualized with an

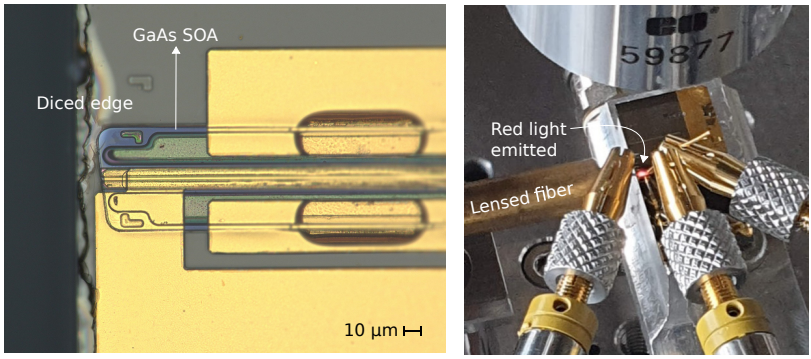

Figure 6.15: Microscope picture of the diced target sample with a post-processed GaAs SOA (left) and the emitted ASE observed with the naked eye (right).

Anritsu MS9740A OSA, and is centered around 770 nm at a bias current of 45 mA, as shown in Fig. 6.17 (left). Furthermore, the measured optical power in the fiber as a function of bias current is depicted in Fig. 6.17 (right). The origin of the limited output power is twofold. First of all, the high device resistance limits the optical output power that can be attained. Secondly, the rough edge resulting from dicing the sample likely blocks part of the emitted light that can be captured with the lensed fiber. Both issues have been addressed in a following processing run, led by Max Kiewiet, by using the new optimized epitaxial stack as well as by introducing a deeply etched trench at the facet of the SOA before dicing the sample. The epitaxial changes led to a differential resistance $2\times$ smaller than what is demonstrated here. Moreover, Fabry-Pérot lasing has recently been achieved [1] by using an SOA with a straight facet and improved metal coverage of the backside mirror. Although an angled facet is essential for coupling to an extended Si_3N_4 cavity, it obviously prevents Fabry-Pérot lasing of the standalone SOA.

6.4 Conclusion

In this chapter, we have demonstrated pre-processed and etched-facet micro-transfer printed GaAs semiconductor optical amplifiers which serve as a key component to build heterogeneous Si_3N_4 lasers for operation around 780 nm. The process flow was covered in detail, and some changes to the epitaxial stack have been discussed to improve the metal-semiconductor contact resistance, and correspondingly, the device differential resistance. It is expected that continuous development of the process flow will reveal some additional possible improvements to the epitaxy. For example, it was recently observed that a slightly thicker buffer layer above the sacrificial layer might be desirable to avoid penetration of HCl into the AlGaAs layers above it during release etching.

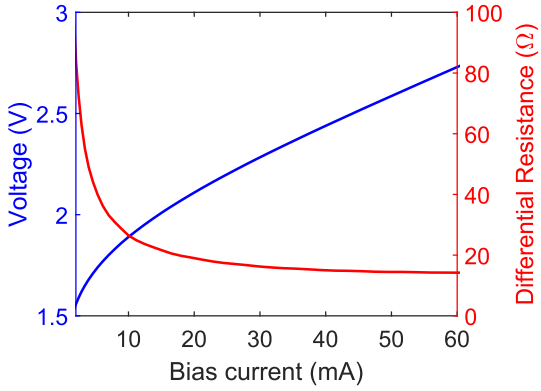

Figure 6.16: V-I curve and differential resistance of the GaAs SOA.

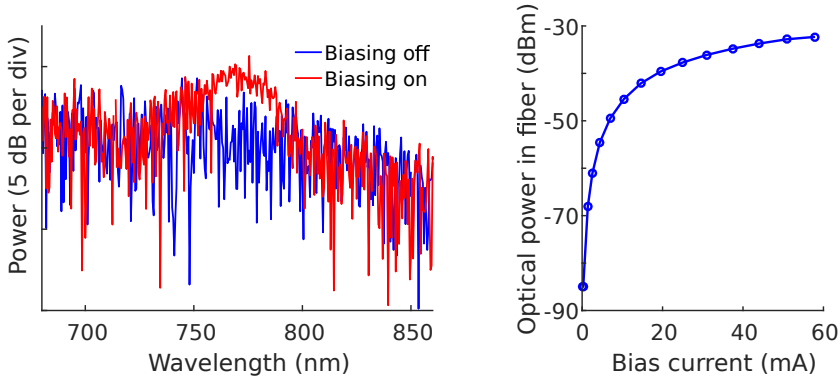

Figure 6.17: Amplified spontaneous emission spectrum at 45 mA bias current (left) and measured optical power in the fiber as a function of bias current.

A dummy sample was fabricated to test the SOA's, and ASE around 770 nm was observed. Building further on these results, GaAs Fabry-Pérot lasers on silicon with 3 mW fiber-coupled output powers have recently been demonstrated by Max Kiewiet based on the optimized (Al)GaAs epitaxy and the processing refinements discussed in this chapter. A next step comprises a more extensive characterization of the SOA's (to estimate the amplifier gain, gain bandwidth, etc.) as well as the design and fabrication of a Si_3N_4 cavity and a spot-size converter to build tunable-, narrow-linewidth-, and mode-locked lasers on Si_3N_4 that operate around 780 nm. Some preliminary work about efficient coupling of light between a Si_3N_4 waveguide and a GaAs SOA is presented in [37]. It is expected that such lasers will play a vital role to expand the current scope of heterogeneous Si_3N_4 photonics and serve numerous applications in the (near-)visible spectrum.

References

[1] M. Kiewiet, S. Cuyvers, A. Hermans, M. Billet, J. Zhang, G. Roelkens, K. V. Gasse, and B. Kuyken. *Scalable Heterogeneous Integration of a Pre-Processed Facet-Emitting Visible-Wavelength GaAs Laser*. In Conference on Lasers and Electro-Optics (CLEO), San Jose, USA, 5 2023. CLEO.

[2] X. Shu, L. J. Beckmann, and H. F. Zhang. *Visible-light optical coherence tomography: a review*. Journal of Biomedical Optics, 22(12):121707, 2017.

[3] T. Masood and J. Egger. *Augmented Reality: Focusing on Photonics in Industry 4.0*. IEEE Journal of Selected Topics in Quantum Electronics, 27(6):1–11, 2021.

[4] M. A. Tran, C. Zhang, T. J. Morin, L. Chang, S. Barik, Z. Yuan, W. Lee, G. Kim, A. Malik, Z. Zhang, J. Guo, H. Wang, B. Shen, L. Wu, K. Vahala, J. E. Bowers, H. Park, and T. Komljenovic. *Extending the spectrum of fully integrated photonics to submicrometre wavelengths*. Nature, 610(7930):54–60, Oct 2022.

[5] N. Chauhan, A. Isichenko, K. Liu, J. Wang, Q. Zhao, R. O. Behunin, P. T. Rakich, A. M. Jayich, C. Fertig, C. W. Hoyt, and D. J. Blumenthal. *Visible light photonic integrated Brillouin laser*. Nature Communications, 12(1):4685, Aug 2021.

[6] K. W. Martin, G. Phelps, N. D. Lemke, M. S. Bigelow, B. Stuhl, M. Wojcik, M. Holt, I. Coddington, M. W. Bishop, and J. H. Burke. *Compact Optical Atomic Clock Based on a Two-Photon Transition in Rubidium*. Phys. Rev. Appl., 9:014019, Jan 2018.

[7] C. A. A. Franken, A. van Rees, L. V. Winkler, Y. Fan, D. Geskus, R. Dekker, D. H. Geuzebroek, C. Fallnich, P. J. M. van der Slot, and K.-J. Boller. *Hybrid-integrated diode laser in the visible spectral range*. Opt. Lett., 46(19):4904–4907, Oct 2021.

[8] M. Corato-Zanarella, A. Gil-Molina, X. Ji, M. C. Shin, A. Mohanty, and M. Lipson. *Widely tunable and narrow-linewidth chip-scale lasers from near-ultraviolet to near-infrared wavelengths*. Nature Photonics, Dec 2022.

[9] B. Li, W. Jin, L. Wu, L. Chang, H. Wang, B. Shen, Z. Yuan, A. Feshali, M. Paniccia, K. J. Vahala, and J. E. Bowers. *Reaching fiber-laser coherence in integrated photonics*. Opt. Lett., 46(20):5201–5204, Oct 2021.

[10] H. Park, C. Zhang, M. A. Tran, and T. Komljenovic. *Heterogeneous silicon nitride photonics*. Optica, 7(4):336–337, Apr 2020.

[11] J. Justice, C. Bower, M. Meitl, M. B. Mooney, M. A. Gubbins, and B. Corbett. *Wafer-scale integration of group III–V lasers on silicon using transfer printing of epitaxial layers*. Nature Photonics, 6(9):610–614, Sep 2012.

[12] J. Goyvaerts, A. Grabowski, J. Gustavsson, S. Kumari, A. Stassen, R. Baets, A. Larsson, and G. Roelkens. *Enabling VCSEL-on-silicon nitride photonic integrated circuits with micro-transfer-printing*. Optica, 8(12):1573–1580, Dec 2021.

[13] J. Juvert, T. Cassese, S. Uvin, A. de Groote, B. Snyder, L. Bogaerts, G. Jamieson, J. V. Campenhout, G. Roelkens, and D. V. Thourhout. *Integration of etched facet, electrically pumped, C-band Fabry-Pérot lasers on a silicon photonic integrated circuit by transfer printing*. Opt. Express, 26(17):21443–21454, Aug 2018.

[14] S. Poelman, S. Cuyvers, J. D. Witte, A. Hermans, K. V. Gasse, N. Picqué, G. Roelkens, D. V. Thourhout, and B. Kuyken. *Generic Heterogeneous Integration Process Flow for Commercial Foundry Low-Index Photonic Platforms*. In Frontiers in Optics + Laser Science 2021, page FM1B.6. Optica Publishing Group, 2021.

[15] C. Op de Beeck, B. Haq, L. Elsinger, A. Gocalinska, E. Pelucchi, B. Corbett, G. Roelkens, and B. Kuyken. *Heterogeneous III-V on silicon nitride amplifiers and lasers via microtransfer printing*. Optica, 7(5):386–393, May 2020.

[16] J. R. Flemish and K. A. Jones. *Selective Wet Etching of GaInP , GaAs , and InP in Solutions of HCl , CH3COOH , and H2O2*. Journal of The Electrochemical Society, 140(3):844, mar 1993.

[17] S. Kumari. *GaAs VCSEL Integration on SiN Waveguide Circuits: Design, Technology and Devices*. PhD thesis, Ghent University, 2017.

[18] C. Zhang, D. Lubyshev, T. N. Jackson, D. L. Miller, and T. S. Mayer. *The Effect of Al0.7Ga0.3As Etch Stop Removal on the Preparation of Wafer-Bonded Compliant Substrates*. Journal of The Electrochemical Society, 146(4):1597, apr 1999.

[19] J. Goyvaerts. *Near-Infrared GaAs-on-SiN Photonic Integration Platform Based on Micro-Transfer-Printing*. PhD thesis, Ghent University, 2021.

[20] J. L. Shohet. *Boron Tricholoride Dry Etching*. In Encyclopedia of Plasma Technology-Two Volume Set. CRC press, 2016.

[21] J. Skriniarova, J. Kovac, J. Breza, and D. Gregusova. *Wet Etching of InGaP and GaAs in HCl: H3PO4: H2O2*. Sensors and materials, 10:213–218, 1998.

[22] D. K. Schroder. *Semiconductor material and device characterization*. John Wiley & Sons, 2015.

[23] A. Baca, F. Ren, J. Zolper, R. Briggs, and S. Pearton. *A survey of ohmic contacts to III-V compound semiconductors*. Thin Solid Films, 308-309:599–606, 1997.

[24] T. Lin, J. nan Xie, S. huan Ning, Q. min Li, and B. Li. *Study on the p-type ohmic contact in GaAs-based laser diode*. Materials Science in Semiconductor Processing, 124:105622, 2021.

[25] H. Okada, S. ichi Shikata, and H. Hayashi. *Electrical Characteristics and Reliability of Pt/Ti/Pt/Au Ohmic Contacts to p-Type GaAs*. Japanese Journal of Applied Physics, 30(4A):L558, apr 1991.

[26] S. S. Gill, M. A. Crouch, and J. R. Dawsey. *Ni-Ge-Au ohmic contacts for GaAs and GaAlAs*, US patent application US07/834.561.

[27] T. Ehara, N. Shibata, H. Ohta, T. Nukui, and T. K. T. Kazuno. *Contact Resistivity and Adhesion of Ni/AuGe/Ag/Au Ohmic Contact Directly to n-Type AlGaAs*. Japanese Journal of Applied Physics, 34(6R):3051, jun 1995.

[28] N. E. Lumpkin, G. R. Lumpkin, and K. S. A. Butcher. *Investigation of low- and high-resistance Ni–Ge–Au ohmic contacts to n+ GaAs using electron microbeam and surface analytical techniques*. Journal of Materials Research, 11(5):1244–1254, May 1996.

[29] E. J. Koop, M. J. Iqbal, F. Limbach, M. Boute, B. J. van Wees, D. Reuter, A. D. Wieck, B. J. Kooi, and C. H. van der Wal. *On the annealing mechanism of AuGe/Ni/Au ohmic contacts to a two-dimensional electron gas in GaAs/AlxGa1-xAs heterostructures*. Semiconductor Science and Technology, 28(2):025006, jan 2013.

[30] J. Zhang, I. Krestnikov, R. Loi, P. Ossieur, G. Lepage, P. Verheyen, and J. Van. *Micro-Transfer-Printed O-band GaAs QD Ill-V-on-Si DFB Laser*. In European Conference on Integratred Optics (ECIO 2022), 2022.

[31] U. D. Dave. *X(2) nonlinear optics on a III-V/silicon platform*. PhD thesis, Ghent University, 2017.

[32] S. Uvin. *Heterogeneous Integration of InAs/GaAs Quantum Dot Lasers on Silicon Photonics*. PhD thesis, Ghent University, 2020.

[33] W. T. Tsang. *In situ Ohmic-contact formation to n- and p-GaAs by molecular beam epitaxy*. Applied Physics Letters, 33(12):1022–1025, 1978.

[34] S. Sze and K. K. Ng. *Metal-Semiconductor Contacts*, pages 134–196. John Wiley & Sons, Ltd, 2006.

[35] G. Stareev. *Formation of extremely low resistance Ti/Pt/Au ohmic contacts to p-GaAs*. Applied Physics Letters, 62(22):2801–2803, 1993.

[36] X. Li, Z. Liu, D. Zhao, D. Jiang, P. Chen, J. Zhu, J. Yang, L. Le, W. Liu, X. He, X. Li, F. Liang, L. Zhang, J. Liu, H. Yang, Y. Zhang, and G. Du. *Comparative study of the differential resistance of GaAs- and GaN-based laser diodes*. Journal of Vacuum Science & Technology B, 34(4):041211, 2016.

[37] M. Kiewiet, S. Cuyvers, G. Roelkens, K. Van Gasse, and B. Kuyken. *Facet-coupled heterogeneous integration of GaAs SOAs on silicon nitride through micro-transfer printing for near-visible applications*. In Annual Symposium of the IEEE Photonics Society Benelux Chapter, 2022.

7

Conclusions and perspectives

Silicon nitride has emerged as an indispensable material to complement conventional silicon photonic integrated circuits. Its relevance is underpinned not only by the attainable ultra-low waveguide losses, but also by its high power-handling capabilities and its wide transparency window, extending into the visible spectral range. This combination of properties has made silicon nitride a promising material for a wide range of applications, including but not limited to LiDAR, imaging and (spectroscopic) sensing, and quantum photonics. Still, the silicon nitride platform by itself is a purely passive platform (apart from thermo-optic tuning capabilities) and therefore relies critically on hybrid- or heterogeneous integration methods to build active devices and unlock its full technological potential.

The primary objective of this PhD project was to extend the application scope and corresponding functionalities of silicon nitride (Si_3N_4) photonic integrated platforms by heterogeneously integrating active devices and materials using micro-transfer printing. Specifically, our objectives have been to

- Build advanced heterogeneous devices on silicon nitride at telecom wavelengths, namely mode-locked comb lasers to support emerging applications such as portable dual-comb spectroscopic sensors.

- Develop a novel process flow, based on micro-transfer printing, to enable heterogeneous laser integration on generic, commercial silicon nitride platforms.

- Develop micro-transfer printable photodetectors and semiconductor optical amplifiers to expand the toolbox of silicon nitride for applications in the (near-)visible spectral range.

These objectives have been addressed throughout this dissertation as follows.

7.1 On-chip mode-locked lasers and their prospects

In chapter 2, the first heterogeneous III-V-on-silicon-nitride passively mode-locked laser was presented. Based on a custom Si_3N_4-on-silicon-on-insulator platform with a low-loss Si_3N_4 ring cavity and a micro-transfer printed InP amplifier with saturable absorber, excellent noise performance was achieved with an optical linewidth below 200 kHz and a fundamental amplified spontaneous emission limited radiofrequency linewidth of 1 Hz. Moreover, the low pulse repetition rate of 755 MHz is well suited to serve applications such as high-resolution dual-comb spectroscopy.

For future work, the limited output power (currently 125 μW) and optical comb span (currently 3.3 nm) can likely be improved by optimizing the mode confinement in the III-V quantum wells, by spectral shaping of the gain, and by optimizing the overall cavity dispersion, ideally using thick anomalously dispersive Si_3N_4 waveguides. The latter approach was recently pursued in [1], and a significantly wider comb spectrum ($>$ 6.6 nm) was achieved. In addition, replacing the quantum-well gain material with quantum dot material could further improve the optical gain bandwidth and the mode-locked laser performance in general. To the best of our knowledge, no quantum dot mode-locked lasers with an on-chip external cavity have been demonstrated. Another promising direction for future work is to combine other material platforms, such as GaSb, with an external cavity to target the spectral region beyond 2 μm, uncovering the full capabilities of on-chip spectroscopic sensing. Furthermore, the mode-locked laser design could be extended with a ring resonator- or MZI-based filter to effectively multiply the comb line spacing without sacrificing the low-noise performance [2, 3]. The ability to increase the repetition rate to $\sim$20 GHz and beyond while keeping the excellent noise properties would greatly expand the application scope of on-chip mode-locked lasers, for example to serve as a multi-wavelength source for high-speed optical links [4], to build hyperspectral dual-comb imaging or holography systems [5], or to implement the critical clockwork in future miniature optical atomic clocks [6]. Alternatively, mode-locked lasers could be utilized to pump a nonlinear microresonator. Pulsed pumping enables the generation of bright soliton Kerr combs with a high conversion efficiency, avoiding the complexity and typical limited spectral bandwidth dark soliton combs bring with them [7, 8]. Such an approach has

already been pursued using electro-optic pump combs, reaching a conversion efficiency as high as 54% [7]. Still, several challenges remain to implement such an approach with mode-locked lasers, particularly to match the pulse repetition rate of the mode-locked laser to the free spectral range of the microresonator.

Chapter 3 complemented chapter 2 by introducing a novel hybrid modeling concept to simulate mode-locked laser diodes with an extended cavity. As the performance of such devices is currently largely unpredictable due to a lack of appropriate modeling tools and a limited understanding of the mode-locking dynamics, such a hybrid modeling approach could prove valuable to serve as a design tool and enable parametric studies. The hybrid model combines the traveling-wave modeling technique for the active semiconductor laser sections with a nonlinear Schrödinger equation, implemented using a split-step Fourier method, for the extended passive waveguide cavity. This approach paves the way to include a wide range of physical phenomena, such as the semiconductors physics of the semiconductor optical amplifier and saturable absorber, as well as the dispersive and nonlinear properties of the extended passive laser cavity, while simultaneously limiting the model's computational workload. The hybrid modeling concept was recently generalized to extend its application scope, and combined with the PHIsim open-source simulation package, developed at Eindhoven University of Technology [9, 10]. Still, further development is needed to enhance the model's accessibility by building a material or component library, and to include other relevant physical phenomena, for example thermal effects. In addition, extensive experimental validation of the model remains essential to eliminate any remaining bugs and proof the model's physical accuracy.

7.2 Building lasers on generic commercial platforms

In chapter 4, a novel integration methodology was presented to enable heterogeneous laser integration on generic, commercial Si_3N_4 platforms, or other low-index integrated photonic platforms such as thin-film lithium niobate, with a high yield. Although a multi-layer Si_3N_4-on-silicon-on-insulator platform, as used in chapter 2, can provide excellent performance, such a custom platform is currently expensive and not (yet) readily available from most commercial foundries. It is therefore invaluable to have an alternative process methodology available that is compatible with current offerings of commercial silicon nitride (or thin-film lithium niobate) foundries. Furthermore, the presented approach overcomes some of the drawbacks of a hydrogenated amorphous silicon intermediate coupling layer. The novel integration methodology consists of two micro-transfer printing steps. In a first step, a thin film of crystalline silicon is micro-transfer printed on

the silicon nitride or thin-film lithium niobate waveguide to serve as an intermediate coupling layer. The coupling layer is essential to efficiently bridge the large refractive index difference between the Si_3N_4 or thin-film lithium niobate waveguide and the III-V gain waveguide. The crystalline Si coupon can be patterned before or after micro-transfer printing. Once the Si layer is patterned, the III-V amplifier is integrated with a second micro-transfer printing step. Two different approaches were presented to create crystalline silicon coupons for micro-transfer printing, either through vapor-phase release etching or through a liquid release etch with a photoresist encapsulation. Although the latter requires more processing steps, the coupons benefit from a consistently low surface roughness and do not suffer from residual particles, in contrast to vapor-phase etching experiments. A number of transmission measurements were carried out on patterned Si coupons to demonstrate low attainable propagation losses, currently 0.8 dB/taper and excess waveguide losses of 7.5 dB/cm (for a 2 μm wide, 400 nm thick fully etched Si waveguide). Importantly, these measurements confirm that the micro-transfer printed silicon waveguides exhibit losses comparable to standard SOI waveguides. Furthermore, the potential of this integration methodology was exemplified with an overview of demonstrated devices, including heterogeneous lasers on Si_3N_4 and thin-film lithium niobate, as well as an on-chip electro-optic comb generator with a heterogeneously integrated pump laser. It is expected that several other heterogeneous devices will soon extend this list.

For future work, the simultaneous transfer of multiple silicon coupons using array stamps still needs to be demonstrated. Such a demonstration would proof the compatibility with high-volume manufacturing. In addition, it is desirable to further optimize the losses of the silicon coupling layer (to minimize the total cavity losses of the lasers) by optimizing the e-beam lithography and etching processes. Furthermore, besides heterogeneous laser integration, other applications are envisioned to benefit from micro-transfer printable crystalline silicon as well. One example is a patterned Si waveguide on Si_3N_4 to absorb the pump background for entangled photon pair generation through spontaneous parametric down conversion.

7.3 Moving towards the visible spectrum

In chapters 5 and 6, the focus was shifted from telecom wavelengths to wavelengths below 850 nm. As several applications operate with light in the visible or near-visible spectral range, it is essential to develop the necessary active components for this wavelength range and conveniently integrate them on the silicon nitride platform, for example using micro-transfer printing.

In chapter 5, micro-transfer printed silicon photodiodes on silicon nitride were demonstrated. These devices feature competitive performance with a low dark

current of 107 pA at 3 V reverse bias, external quantum efficiencies close to 30% at 775 nm and 800 nm, and a 3-dB bandwidth of 6 GHz. Moreover, avalanche gain multiplication was demonstrated with a gain-bandwidth product of 68 GHz, serving applications which require high receiver sensitivities. It is expected that the performance can further be improved by optimizing the optical coupling between the silicon nitride waveguide and the silicon photodiode. Furthermore, it was shown in [11] that the doping profile plays a significant role for avalanche operation. Hence, it is expected that careful optimization of the doping profile along with an optimized device geometry, could greatly enhance the gain-bandwidth product of the presented device. Eventually, this could possibly enable stable, low-noise Geiger-mode operation for single-photon detection in integrated quantum photonics applications [11].

In chapter 6, micro-transfer printable GaAs semiconductor optical amplifiers (SOA's) were presented as a first step towards heterogeneous lasers on silicon nitride for operation around 780 nm. In contrast to the heterogeneous lasers from chapters 2 and 4 where evanescent coupling was used, the GaAs SOA's are optimized for edge-coupling, hereby benefitting from a reduced thermal impedance and omitting the need for an intermediate coupling layer. A preliminary dummy sample was fabricated with micro-transfer printed GaAs SOA's and amplified spontaneous emission around 770 nm was observed. Building further on these results, GaAs Fabry-Pérot lasers on silicon with 3 mW fiber-coupled output powers were recently demonstrated by Max Kiewiet and coworkers, based on the optimized (Al)GaAs epitaxy and the processing refinements discussed in chapter 6 [12]. A next step comprises the design and fabrication of a silicon nitride external cavity and a spot-size converter to build tunable-, narrow-linewidth-, and mode-locked lasers on silicon nitride that operate around 780 nm. Some preliminary work on efficient coupling of light between a silicon nitride waveguide and a GaAs SOA has been presented in [13].

Recent research efforts have also focused on developing micro-transfer printable GaN-based light sources. This development enables the generation of light at wavelengths ranging from 450 nm to 650 nm, complementing the wavelength range covered by GaAs-based light sources. [14].

Given current developments, it is expected that optical detection and analysis systems in the (near-)visible spectrum will soon benefit from a myriad of active components on silicon nitride. As life science institutions have embraced the opportunities to miniaturize their optical instruments and sensors, it will only be a matter of time for diagnostic and therapeutic procedures to become vastly more efficient and cost-effective [15]. Optical coherence tomography systems for example, could be implemented on a photonic chip to achieve a tremendous reduction in size and cost, expanding the technological potential in medical diagnostics and industrial monitoring. Furthermore, fully integrated microfluidic lab-on-a-chip de-

vices could be build to target, for example, flow cytometry, facilitating cell therapy cancer treatments and biopharmaceutical developments [15, 16]. At the same time, more fundamental applications are envisioned to benefit from silicon nitride's extending portfolio. Precise control of atoms with visible-wavelength lasers could help advance quantum computing research, while probing the two-photon transition in Rubidium aids the development of compact optical atomic clocks, serving the vision to revolutionize timekeeping and global navigation.

7.4 The future of micro-transfer printing

Overall, micro-transfer printing has proven to be a powerful integration technique to extend the functionalities of silicon nitride photonic integrated circuits, and integrated photonic platforms in general. Importantly, micro-transfer printing benefits from unparalleled versatility: devices or materials can be integrated at an early stage in the fabrication process to benefit from wafer-scale manufacturing, similar to (die-to-) wafer bonding, or pre-processed devices can be integrated at the back-end-of-line, similar to flip-chip integration. For the case of silicon and silicon nitride wafers that are manufactured in CMOS fabs, the latter approach is essential to integrate CMOS-incompatible materials such as lithium niobate or III-V semiconductors because it minimizes the number of post-processing steps and hence the required number of dedicated processing tools. Another important advantage is the ability to integrate different materials and devices on the same PIC to implement diverse functionalities, resembling the original vision of integrated optics [17].

A variety of materials and components have already been integrated using micro-transfer printing, including semiconductor optical amplifiers, photodetectors, electro-optic modulators [18] and nonlinear materials [19]. Various other important components are currently under development to extend this list, including Ce:YIG magneto-optic materials for optical isolators, periodically poled lithium niobate for nonlinear optics, and BiCMOS electronic chiplets [20]. Furthermore, solid-state gain materials could be heterogeneously integrated using micro-transfer printing to build on-chip lasers that outperform their III-V-semiconductor-based counterparts. In contrast to semiconductor lasers, solid-state lasers exhibit a near-zero linewidth enhancement factor and can therefore offer ultra-narrow-linewidth lasing. Recently, a GaN-diode-pumped Ti:Sapphire laser was demonstrated on a silicon nitride PIC [21]. The Ti:Sapphire crystal was integrated using bonding, although a similar result can likely be achieved with micro-transfer printing. With Ti:Sapphhire's extremely wide emission spectra ranging from 650 nm to 1100 nm, narrow-linewidth tunable lasers with tuning ranges up to $\sim$400 nm could be developed on-chip. Furthermore, the broad gain spectrum enables the generation of

ultrashort femtosecond mode-locked pulses, possibly revolutionizing the field of on-chip optical comb generation.

While micro-transfer printing has matured considerably in recent years, some challenges remain before widespread commercial adoption can commence. Scaling up the technology to 200 mm and 300 mm wafers is still under development [20]. In addition, further improvement of device performance, particularly in terms of laser wall plug efficiency and thermal management, is desirable. Finally, extensive studies are needed to evaluate the yield and reliability of micro-transfer printed devices [20]. Provided that these challenges are appropriately addressed, micro-transfer printing holds great promise to become a key technology for next generation silicon and silicon nitride photonic integrated circuits.

References

[1] S. Poelman, S. Cuyvers, E. Vissers, J. D. Witte, B. Haq, A. Hermans, N. Picque, G. Roelkens, and B. Kuyken. *Low Repetition Rate Mode-Locked Laser on a Commercial Foundry Low-Index Photonic Platform*. In Conference on Lasers and Electro-Optics (CLEO), San Jose, USA, 5 2023. CLEO.

[2] K. Bagnell, A. Klee, P. J. Delfyett, J. J. Plant, and P. W. Juodawlkis. *Demonstration of a highly stable 10 GHz optical frequency comb with low timing jitter from a SCOWA-based harmonically mode-locked nested cavity laser*. Opt. Lett., 43(10):2396–2399, May 2018.

[3] L. Nielsen and M. J. R. Heck. *Fully integrated 45-GHz harmonically mode-locked ring laser with an intra-cavity Mach–Zehnder filter*. Opt. Lett., 46(4):880–883, Feb 2021.

[4] X. Guan, W. Shi, and L. A. Rusch. *Ultra-Dense Wavelength-Division Multiplexing With Microring Modulator*. Journal of Lightwave Technology, 39(13):4300–4306, 2021.

[5] E. Vicentini, Z. Wang, K. Van Gasse, T. W. Hänsch, and N. Picqué. *Dual-comb hyperspectral digital holography*. Nature Photonics, 15(12):890–894, Dec 2021.

[6] Z. L. Newman, V. Maurice, T. Drake, J. R. Stone, T. C. Briles, D. T. Spencer, C. Fredrick, Q. Li, D. Westly, B. R. Ilic, B. Shen, M.-G. Suh, K. Y. Yang, C. Johnson, D. M. S. Johnson, L. Hollberg, K. J. Vahala, K. Srinivasan, S. A. Diddams, J. Kitching, S. B. Papp, and M. T. Hummon. *Architecture for the photonic integration of an optical atomic clock*. Optica, 6(5):680–685, May 2019.

[7] J. Li, C. Bao, Q.-X. Ji, H. Wang, L. Wu, S. Leifer, C. Beichman, and K. Vahala. *Efficiency of pulse pumped soliton microcombs*. Optica, 9(2):231–239, Feb 2022.

[8] J. M. C. Boggio, D. Bodenmüller, S. Ahmed, S. Wabnitz, D. Modotto, and T. Hansson. *Efficient Kerr soliton comb generation in micro-resonator with interferometric back-coupling*. Nature Communications, 13(1):1292, Mar 2022.

[9] E. A. J. M. Bente, Y. Barbarin, M. J. R. Heck, and M. K. Smit. *Modeling of integrated extended cavity InP/InGaAsP semiconductor modelocked ring lasers*. Optical and Quantum Electronics, 40(2):131–148, Mar 2008.

[10] M. Torreele. *Hybrid Modeling Technique for On-Chip Extended Cavity Mode-Locked Semiconductor Lasers*. Master's thesis, Ghent University, 2022.

[11] P. Gundlapalli, V. Leong, J. R. Ong, T. Y. Ang, S. Yanikgonul, S. Y. Siew, C. E. Png, and L. Krivitsky. *Visible-Light Integrated PIN Avalanche Photodetectors With High Responsivity and Bandwidth*. Journal of Lightwave Technology, pages 1–8, 2022.

[12] M. Kiewiet, S. Cuyvers, A. Hermans, M. Billet, J. Zhang, G. Roelkens, K. V. Gasse, and B. Kuyken. *Scalable Heterogeneous Integration of a Pre-Processed Facet-Emitting Visible-Wavelength GaAs Laser*. In Conference on Lasers and Electro-Optics (CLEO), San Jose, USA, 5 2023. CLEO.

[13] M. Kiewiet, S. Cuyvers, G. Roelkens, K. Van Gasse, and B. Kuyken. *Facet-coupled heterogeneous integration of GaAs SOAs on silicon nitride through micro-transfer printing for near-visible applications*. In Annual Symposium of the IEEE Photonics Society Benelux Chapter, 2022.

[14] S. Poelman, M. Billet, A. Hermans, N. Fiuczek, H. Turski, and B. Kuyken. *Transfer Printing of InGaN/GaN Quantum-Well based Light Emitting Diodes*. In Conference on Lasers and Electro-Optics (accepted, to be published), 2023.

[15] I. Artundo. *Photonic Integration: New Applications Are Visible: Optical chips allow to miniaturize not only communication components, but also a new generation of life sciences devices*. Optik & Photonik, 12(3):22–25, 2017.

[16] U. Blache, R. Weiss, A. Boldt, M. Kapinsky, A.-R. Blaudszun, A. Quaiser, A. Pohl, T. Miloud, M. Burgaud, V. Vucinic, et al. *Advanced flow cytometry assays for immune monitoring of CAR-T cell applications*. Frontiers in Immunology, 12:658314, 2021.

[17] P. Tien. *Integrated optics and new wave phenomena in optical waveguides*. Reviews of Modern Physics, 49(2):361, 1977.

[18] T. Vanackere, M. Billet, C. Op de Beeck, S. Poelman, G. Roelkens, S. Clemmen, and B. Kuyken. *Micro-Transfer Printing of Lithium Niobate on Silicon Nitride*. In 2020 European Conference on Optical Communications (ECOC), pages 1–4, 2020.

[19] M. Billet, L. Reis, Y. Léger, C. Cornet, F. Raineri, I. Sagnes, K. Pantzas, G. Beaudoin, G. Roelkens, F. Leo, et al. *Gallium phosphide-on-insulator integrated photonic structures fabricated using micro-transfer printing*. Optical Materials Express, 12(9):3731–3737, 2022.

[20] G. Roelkens, J. Zhang, L. Bogaert, M. Billet, D. Wang, B. Pan, C. J. Kruckel, E. Soltanian, D. Maes, T. Vanackere, et al. *Micro-transfer printing for heterogeneous Si photonic integrated circuits*. IEEE Journal of Selected Topics in Quantum Electronics, 29(3: Photon. Elec. Co-Inte. and Adv. Trans. Print.):1–14, 2022.

[21] Y. Wang, J. A. Holguín-Lerma, M. Vezzoli, Y. Guo, and H. X. Tang. *Photonic-circuit-integrated titanium:sapphire laser*. Nature Photonics, Jan 2023.

A

Thermal performance of micro-transfer printed lasers

In this appendix, the thermal performance of micro-transfer printed semiconductor optical amplifiers is studied with simulations using Lumerical's HEAT package. The III-V-Si-Si_3N_4 photonic platform is compared to the III-V-on-SOI platform, and approaches are presented to reduce the thermal impedance. Finally, some guidelines are provided for future experimental investigations.

A.1 Introduction

Heterogeneous integration using micro-transfer printing on silicon (nitride) photonic platforms is a promising route for manufacturing high-performance integrated laser sources in high volumes at a low cost. However, such devices typically suffer from poor thermal performance owing to the low thermal conductivity of the buried oxide layer. This oxide layer is required to ensure sufficient vertical confinement and avoid optical leakage to the silicon substrate. This suboptimal thermal management results in a lower laser efficiency, reduced output power, and poor laser performance, particularly at elevated temperatures or for high electrical injection currents. In order to study the thermal behavior of these devices and to evaluate possible approaches to improve thermal performance, a two-dimensional finite element solver is used (Lumerical HEAT [1]) to simulate a standalone SOA.

A.2 Simulations

To calculate the steady-state temperature profile of the device, the Fourier equation is solved in a cross-section of the SOA [2]:

$$\mathbf{q} = -k\nabla T, \tag{A.1}$$

where $\mathbf{q}$ is the local heat flux density (W/m^2), k is the thermal conductivity of the material (W/m·K) and ∇T is the temparuture gradient (K/m). Furthermore, $\mathbf{q}$ satisfies $\nabla \cdot \mathbf{q} = 0$ outside the heat source and $\nabla \cdot \mathbf{q} = Q$ inside the heat source, with Q the generated heat per unit volume (W/m^3). Alongside the aforementioned equations, appropriate boundary conditions are included: a Dirichlet condition of constant temperature at the bottom of the silicon substrate (here fixed to 295 K), and a Neumann condition at the edges of the simulation region ($\frac{\partial T}{\partial n} = 0$, with n the surface normal direction). Furthermore, thermal conduction and convection are considered while radiative heat transfer is neglected. To simplify the simulation, it is assumed that the total electrical power is dissipated in the MQW layers. In reality, heat generation is more distributed as it originates from both Joule heating associated to the resistance of the device and by non-radiative processes such as Auger recombination and free carrier absorption which generate heat mainly in the active region and in the adjacent p-cladding layer [3, 4]. Nevertheless, the current approximation can offer valuable insight and has therefore been used extensively in other reports [5–7].

Material	Thermal conductivity (W/m·K)	Reference
Silicon	148	Lumerical
Si_3N_4	18.5	Lumerical
SiO_2	1.38	Lumerical
DVS-BCB	0.29	[8]
InP	68	Lumerical
InGaAs	1.4	Lumerical
$In_{0.53}(Al_{0.9}Ga_{0.1})_{0.47}As$, transition layer	14.39	[7, 9]
$In_{0.53}(Al_{0.7}Ga_{0.3})_{0.47}As$, SCH layer	11	[7, 9]
$In_{0.7}(Al_{0.25}Ga_{0.75})_{0.3}As$, QW layer	7.71	[7, 9]
$In_{0.49}(Al_{0.45}Ga_{0.55})_{0.51}As$, barrier layer	8.17	[7, 9]
MQW average	8	
Au	316	Lumerical
Ti	22	[10]

Table A.1: Thermal conductivities of the materials used in the simulations.

Table A.1 lists the thermal conductivities of the various materials used in the simulations. The thermal conductivities of the quaternary III-V materials were calculated using interpolation formulas based on the binary III-V compounds [7, 9]. Furthermore, the quantum well and barrier layers were combined in a single MQW layer with a thermal conductivity based on a weighed average. It is apparent

that silicon benefits from a much higher thermal conductivity compared to the other non-metallic solids because phonons can move efficiently through the silicon crystal lattice. Besides phonon-mediated heat transport, also displacements of free electrons can contribute to the overall thermal conductivity of the solid [2].

In order to avoid the influence of the boundary conditions and to be able to include the final metal layer of the SOA (used to bias the device), a wide simulation region of 400 µm is chosen. The thickness of the silicon substrate is set to 3 µm, and a metal heatsink with a fixed temperature (295 K) is placed below the silicon substrate. Due to the high thermal conductivity of silicon, the substrate thickness is not critical and it was confirmed that increasing it does not yield a discernible difference.

The SOA under consideration has a length of approximateley 1.4 mm and a 60 nm DVS-BCB adhesive layer is assumed for micro-transfer printing. The cross-sectional dimensions and details of the epitaxial stack are provided in [11]. The dissipated electrical power in the MQW layer is set to 300 mW, similar to the power levels reported in [11]. Furthermore, to validate the accuracy of the presented simulations, the current model was compared to the results reported in [7] where COMSOL was used. For the same dissipated power levels, a similar temperature profile (difference $< 1.3\ K$) was obtained.

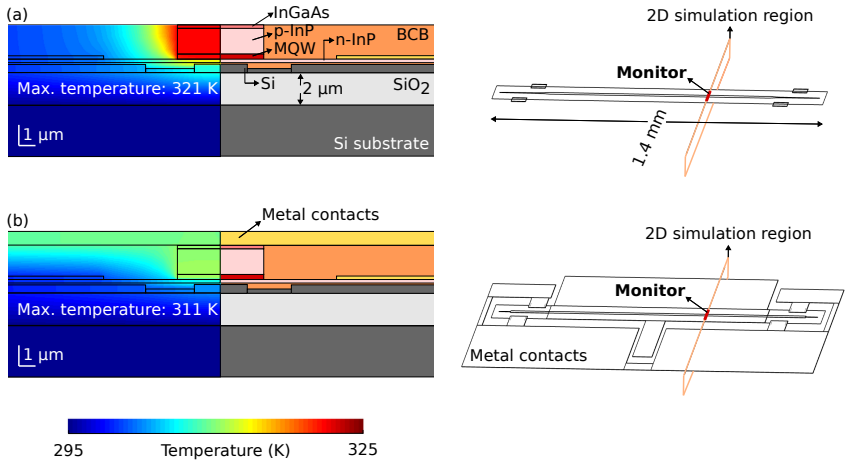

Figure A.1: Thermal simulations of an InP SOA micro-transfer printed on top of a standard 400 nm SOI stack. For the simulations, 300 mW of power is dissipated in the MQW region. Left: temperature profile with the device cross-section. Right: position of the 2D simulation region and thermal monitor. (a), (b) Thermal simulation respectively without and with a 1 µm thick Au layer, in correspondence with practical devices.

A.2.1 Thermal performance of the III-V-SOI platform

Figure A.1(a) depicts the temperature profile together with an overlay of the material stack for the InP SOA on a patterned SOI wafer (assuming a 400 nm thick Si device layer). The considered simulation region as well as the monitor position are highlighted on the right of Fig. A.1(a). From the maximum temperature elevation of ΔT=26 K, one can calculate the thermal impedance of the device as:

$$Z_T = \frac{T_{max} - T_0}{P}, \tag{A.2}$$

where $T_{max} - T_0$ is the maximal temperature elevation with respect to the substrate temperature, and P represents the dissipated power in the MQW layer. It is assumed that the optical output power is negligible compared to the injected electrical power. For lasers with a high wall-plug efficiency, the dissipated power P should be calculated as the difference of the electrical power and the optical output power. For the case of Fig. A.1(a), one obtains $Z_T = 86.7\ K/W$.

Fig. A.1(b) shows the temperature profile when a 1 μm thick Au metal layer, used for biasing the device, is included. The layout of the metal contact layer, shown on the right of Fig. A.1(b), corresponds with the layout used in practical devices. Typically, a thin (40 nm) Ti layer is used for enhanced adhesion of the Au layer. However, it was observed that such a thin Ti layer has a negligible effect on the thermal behavior of the device, and for simplicity it was therefore omitted in the simulations. When the metal contact layer is included, the maximum elevated temperature is greatly reduced due to a heat spreading effect, resulting in a ΔT=16 K and a thermal impedance of $Z_T = 53.3\ K/W$.

A.2.2 Thermal performance of the III-V-Si-Si_3N_4 platform

The thermal performance of micro-transfer printed SOA's on a Si_3N_4 PIC are shown in Fig. A.2. Fig. A.2(a) depicts the temperature profile and device stack when the metal contact layer is omitted. The maximum temperature elevation is ΔT=34 K, a 31% increase compared to the SOI platform (Fig. A.1(a)), resulting in a high thermal impedance of $Z_T = 113.3\ K/W$. This increased thermal impedance is mainly attributed to the thicker BOX layer compared to the SOI platform. Again, including the metal contact layer greatly reduces the maximum temperature, resulting in ΔT=21 K and a thermal impedance of $Z_T = 70\ K/W$.

For practical measurements in a lab environment, DC probes are used to bias the SOA. As these probes are made of metal and hence exhibit a high thermal conductivity, the thermal impedance of the biased device is expected to decrease. To quantify this effect, a thermal simulation was conducted with two probes, which were simplified as two bars of Au with an arbitrary 30 μm$\times$30 μm square profile. The bars are assumed to be 0.2 mm long and are connected to a large metal chuck

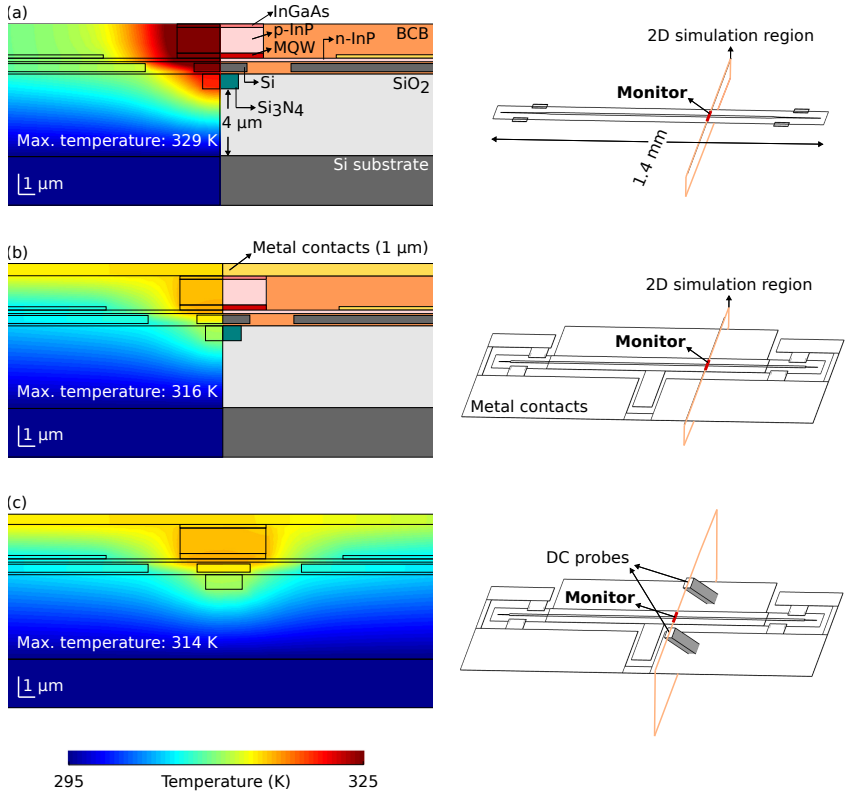

Figure A.2: Thermal simulations of an InP SOA micro-transfer printed on top of a Si_3N_4 PIC which includes a 4 µm BOX layer, an 800 nm thick Si_3N_4 waveguide, and a 400 nm intermediate crystalline silicon layer. For the simulations, 300 mW of power is dissipated in the MQW region. Left: temperature profile with the device cross-section. Right: position of the 2D simulation region and thermal monitor. (a), (b) Thermal simulation respectively without and with a 1 µm thick Au layer, in correspondence with practical devices. (c) Thermal simulation (b) with the addition of contact probes.

which serves as a simple heatsink. From Fig. A.2(c), it can be seen that the maximal temperature is reduced by 2 K, resulting in a thermal impedance $Z_T = 63.3\ K/W$ compared to $Z_T = 70\ K/W$ for the case without the presence of the probes. Hence, although the effect is noticeable, the simulations indicate it does not play a significant role. This is attributed to the large distance between the probes and the SOA: in the simulation the p-contact probe, which is the dominant heat sinking probe, is 43 µm away from the center of the SOA. When the probes are positioned at the edges of the coupon, only 20 µm away from the center of the SOA, the temperature elevation further decreases by 1.4 K, leading to a thermal impedance of $Z_T = 58.7\ K/W$. In reality, heat transport through the contact

probes is also influenced by e.g. the Peltier effect, which relates the heating or cooling effect that occurs at the junction of two different types of materials when an electric current passes through. In principle, this effect amongst others can be included using a more rigorous thermoelectric simulation.

The thermal impedance of the SOA (corresponding with the device depicted in Fig. A.2(b)) as a function of the thickness of the metal contact layer is depicted in Fig. A.3(a). It can be seen that the thermal impedance initially decreases rapidly with increasing metal thickness, and than flattens beyond $\sim$1 μm. In case a thick metal layer is desired, one could use electroplating to achieve metal thicknesses beyond what is typically attainable using sputtering- or evaporation-based deposition techniques. Besides the metal thickness, the cooling capabilities are also affected by the area of the metal through convection to air. However, for applications where many SOA's are densely integrated on a PIC, the available area to realize heatspreaders might be limited. The sensitivity of the thermal impedance to the BOX layer thickness is shown in Fig. A.3(b). As expected, the thermal impedance increases monotonically as the BOX layer becomes thicker. Unfortunately, the BOX layer thickness is rarely an available design parameter. Moreover, it cannot be reduced substantially as sufficient optical confinement needs to be assured.

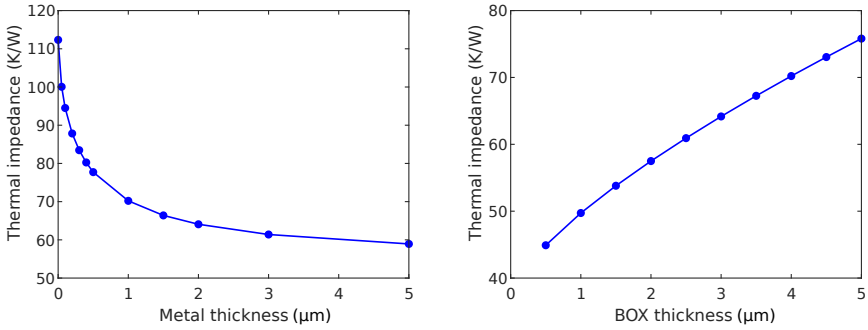

Figure A.3: Thermal impedance as a function of the metal contact layer thickness (left) and the BOX thickness (right) for an InP SOA micro-transfer printed on top of a Si_3N_4 PIC.

A.2.3 Approaches to reduce the thermal impedance

To overcome the poor thermal contact with the silicon substrate, thermal vias (or shunts) can be introduced. In this case, typically either a metal layer is connected to the silicon substrate by etching a via through the BOX layer, or the etched thermal vias are backfilled with a high thermal conductivity material [12]. Previous reports have successfully demonstrated poly-Si thermal shunts [12] and metal shunts [13] to mitigate the thermal barrier imposed by the buried oxide layer, reducing the

thermal impedance respectively by ∼25% and ∼60%. In the case of metallic thermal vias, a thin oxide layer can be required to prevent a parasitic parallel current path [14].

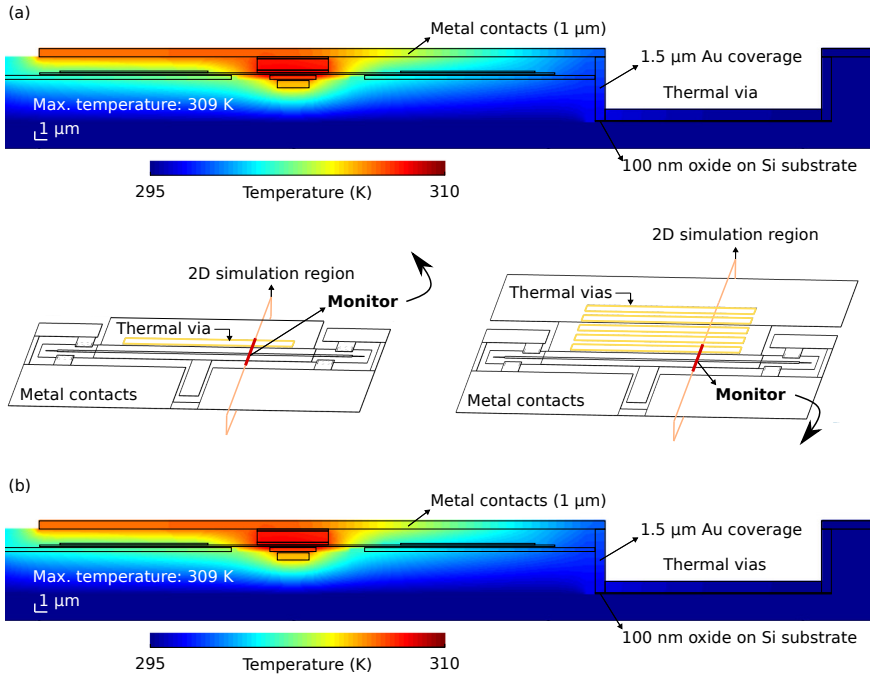

Figure A.4: Thermal simulations of an InP SOA micro-transfer printed on top of a Si_3N_4 PIC which includes a 4 µm BOX layer, an 800 nm thick Si_3N_4 waveguide, and a 400 nm intermediate crystalline silicon layer. For the simulations, 300 mW of power is dissipated in the MQW region. (a) Thermal simulation with a single thermal via. The sides and bottom of the via are covered with 1.5 µm Au and connected to the p-metal contact layer. To avoid a parasitic leakage currents, 100 nm of SiO_2 is left above the silicon substrate. (b) Thermal simulation with 5 thermal vias.

Figure A.4(a) depicts the layout and temperature profile of the InP SOA on the III-V-Si-Si_3N_4 platform (corresponding with Fig. A.2(b)) when a single thermal via is introduced. The thermal via is 20 µm wide and located 23 µm away from the center of the SOA (which has a width of 45 µm). It is assumed that the via is coated with 1.5 µm Au and connected to the p-contact metal layer used for biasing. To avoid any parasitic leakage current, 100 nm of oxide is left in between the Si substrate and the bottom of the via. However, in [13] such an insulating layer was omitted. It can be seen that the thermal shunt reduces the maximum temperature elevation significantly: ΔT=14 K compared to ΔT=21 K for the case without the thermal via. The resulting thermal impedance is $Z_T = 46.7\ K/W$, a reduction

of 33%. When additional thermal vias are introduced, which are all connected to the p-metal layer, the thermal impedance remains approximately unchanged. This can be expected from the temperature profile: the thermal via closest to the SOA dominates the thermal impedance and any additional thermal shunt further away barely contributes to the heatsinking capabilities. Still, for practical devices it might be worthwhile to include multiple thermal vias to ensure some redundancy.

To further reduce the thermal impedance, one could also introduce a thermal shunt connected to the n-contact layer, as demonstrated in [13]. However, simulations indicate that for the SOA under consideration, Z_T remains unchanged as the thermal n-via is further away (45 µm) from the SOA. This is necessary to avoid possible shorting of the p- and n-contacts during the final metallization step. Moreover, heat is more effectively transported through the p-InP layers due to the limited thickness (200 nm) of the n-InP layer that is required for evanescently coupled SOA's. For the presented device, the p-doped side hence dominates the overall thermal performance.

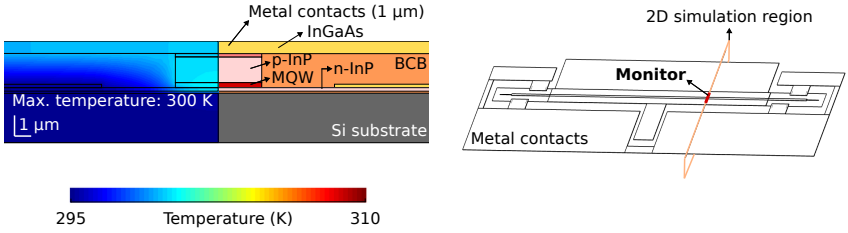

Figure A.5: Thermal simulations of the same InP SOA from Figures A.1,A.2,A.4, micro-transfer printed directly on the Si substrate with a 60 nm DVS-BCB layer in between. Left: temperature profile with the device cross-section. Right: position of the 2D simulation region and thermal monitor.

Besides thermal shunts, another possibility to improve the thermal performance is to either integrate the SOA upside down on a metal submount in contact with the Si substrate, achieving optical coupling through a grating [15, 16], or by integrating the SOA directly on the Si substrate and than edge coupling to the waveguide [17]. The latter approach was also discussed in Chapter 6 for micro-transfer printed GaAs SOA's. In this case, no BOX layer remains in between the SOA and the Si substrate, yielding a greatly enhanced thermal impedance. Such an approach is shown in Fig. A.5 where the same SOA from previous simulations (figures A.1, A.2, A.4) has been positioned directly on the Si substrate with a 60 nm DVS-BCB adhesive in between. The maximal temperature elevation is in this case only ΔT=5 K, resulting in a low thermal impedance of $Z_T = 16.7\ K/W$, more than 2x smaller than what was achieved using thermal shunts. Note that in practice, the SOA stack for edge-coupled SOA's differs from evanescently coupled

SOA's: the n-cladding layer is typically much thicker to ensure that the optical mode is well confined in the SOA and positioned at the correct height to enable efficient edge coupling to the neighboring waveguide. Still, compared to thermal shunts, direct thermal contact with the Si substrate seems preferred to achieve the best thermal performance of micro-transfer printed SOA's, possibly at the expense of a slightly higher coupling loss.

It is important to realize that the overall thermal performance of the device greatly depends on the packaging conditions. Furthermore, for practical devices the bottom surface of the Si substrate can not always be considered as an ideal isothermal heatsink, especially when the PIC is not mounted on a temperature-controlled chuck. It is important to keep these limitations in mind when comparing the aforementioned simulation results.

Finally, thermal management could also be implemented on the package level, for example by mounting a heat spreader to the laser diode, either connected to a thermoelectric cooler element [18] or directly connected to a forced air convection heat sink [19]. In [20], it was found that for flip-chip InP-Si DFB lasers, the best thermal performance could be obtained by directly mounting a heat sink on top of the laser surface. A more detailed analysis can be found in [20].

A.3 Measurement guidelines

The thermal performance of micro-transfer printed lasers can also be investigated experimentally. For example, one could quantify self-heating by measuring the peak optical output power of a laser diode as a function of the duty cycle of a square wave current pulse applied to the diode, as elaborated in [14]. Alternatively, one can measure the thermal impedance directly using a combination of two measurements [21]. In a first measurement, the shift in lasing wavelength as a function of the temperature of the stage (on which the device is mounted), $\partial\lambda/\partial T$, is measured. This experiment is best performed pulsed to ensure there is minimal device heating so that the temperature of the active region is close to the chosen temperature of the stage. In a second measurement which is performed in CW, the wavelength shift is measured as a function of the applied electrical power to obtain $\partial\lambda/\partial P$. The thermal impedance is than given by [20, 21]:

$$Z_T = \left[\frac{\partial\lambda}{\partial T}\right]^{-1}\left[\frac{\partial\lambda}{\partial P}\right] \tag{A.3}$$

This approach was first carried out for standalone micro-transfer printed SOA's on a SOI platform in order to compare the thermal performance with and without thermal vias. In this case, the shift of the amplified spontaneous emission (ASE) spectrum is measured. Unfortunately, as the ASE spectrum not only shifts but also changes shape due to self heating and carrier injection, accurate quantification of

$\partial\lambda/\partial T$ and $\partial\lambda/\partial P$ is infeasible. Hence, a simple Fabry-Pérot multimode laser with a sufficiently large mode spacing (to make sure the modes are distinguishable) [21], a DFB laser [20], or a ring laser [13] are more appropriate to properly quantify the thermal impedance. An extensive experimental thermal study for flip-chip InP-Si DFB lasers was presented in [20]. In a similar fashion, a simple micro-transfer printed laser on silicon nitride could be used in future work to experimentally validate the simulation results discussed in this appendix.

References

[1] *Lumerical HEAT: 3D Heat Transport Simulator*. `https://www.ansys.com/products/photonics/heat`. Accessed: 2023-01-19.

[2] M. Kaviany. *Essentials of Heat Transfer: Principles, Materials, and Applications*, page 152–323. Cambridge University Press, 2011.

[3] J. Piprek, P. Abraham, and J. E. Bowers. *Carrier nonuniformity effects on the internal efficiency of multiquantum-well lasers*. Applied Physics Letters, 74(4):489–491, 1999.

[4] J. Piprek, J. White, and A. SpringThorpe. *What limits the maximum output power of long-wavelength AlGaInAs/InP laser diodes?* IEEE Journal of Quantum Electronics, 38(9):1253–1259, 2002.

[5] R. Loi, J. O'Callaghan, B. Roycroft, Z. Quan, K. Thomas, A. Gocalinska, E. Pelucchi, A. J. Trindade, C. A. Bower, and B. Corbett. *Thermal Analysis of InP Lasers Transfer Printed to Silicon Photonics Substrates*. Journal of Lightwave Technology, 36(24):5935–5941, 2018.

[6] I. Lucci, C. Cornet, M. Bahri, and Y. Léger. *Thermal Management of Monolithic Versus Heterogeneous Lasers Integrated on Silicon*. IEEE Journal of Selected Topics in Quantum Electronics, 22(6):35–42, 2016.

[7] C. Op de Beeck. *Heterogeneous Integration of III-V Semiconductor Light Sources on Low-Refractive-Index Platforms*. PhD thesis, Ghent University, 2022.

[8] A. Modafe, N. Ghalichechian, M. Powers, M. Khbeis, and R. Ghodssi. *Embedded benzocyclobutene in silicon: An integrated fabrication process for electrical and thermal isolation in MEMS*. Microelectronic Engineering, 82(2):154–167, 2005.

[9] S. Adachi. *III-V Ternary and Quaternary Compounds*, pages 735–752. Springer US, Boston, MA, 2007.

[10] K. A. Aissa, N. Semmar, A. Achour, Q. Simon, A. Petit, J. Camus, C. Boulmer-Leborgne, and M. A. Djouadi. *Achieving high thermal conductivity from AlN films deposited by high-power impulse magnetron sputtering*. Journal of Physics D: Applied Physics, 47(35):355303, aug 2014.

[11] B. Haq, S. Kumari, K. Van Gasse, J. Zhang, A. Gocalinska, E. Pelucchi, B. Corbett, and G. Roelkens. *Micro-Transfer-Printed III-V-on-Silicon C-Band Semiconductor Optical Amplifiers*. Laser Photonics Rev., 14(7):1900364, 2020.

[12] M. N. Sysak, D. Liang, R. Jones, G. Kurczveil, M. Piels, M. Fiorentino, R. G. Beausoleil, and J. E. Bowers. *Hybrid Silicon Laser Technology: A Thermal Perspective*. IEEE Journal of Selected Topics in Quantum Electronics, 17(6):1490–1498, 2011.

[13] C. Zhang, D. Liang, G. Kurczveil, J. E. Bowers, and R. G. Beausoleil. *Thermal Management of Hybrid Silicon Ring Lasers for High Temperature Operation*. IEEE Journal of Selected Topics in Quantum Electronics, 21(6):385–391, 2015.

[14] G. Roelkens. *Heterogeneous III-V/Silicon Photonics: Bonding Technology and Integrated Devices*. PhD thesis, Ghent University, 2007.

[15] B. Song, C. Stagarescu, S. Ristic, A. Behfar, and J. Klamkin. *3D integrated hybrid silicon laser*. Opt. Express, 24(10):10435–10444, May 2016.

[16] B. Song, L. Megalini, S. Dwivedi, S. Ristic, and J. Klamkin. *High-Thermal Performance 3D Hybrid Silicon Lasers*. IEEE Photonics Technology Letters, 29(14):1143–1146, 2017.

[17] J. Juvert, T. Cassese, S. Uvin, A. de Groote, B. Snyder, L. Bogaerts, G. Jamieson, J. V. Campenhout, G. Roelkens, and D. V. Thourhout. *Integration of etched facet, electrically pumped, C-band Fabry-Pérot lasers on a silicon photonic integrated circuit by transfer printing*. Opt. Express, 26(17):21443–21454, Aug 2018.

[18] J. O'Connor and J. Punch. *The thermal behavior of a flip-chip laser array within a Photonics Integrated Circuit (PIC)*. In 13th InterSociety Conference on Thermal and Thermomechanical Phenomena in Electronic Systems, pages 325–332, 2012.

[19] J. E. Johnson, K. Bacher, R. Schaevitz, and V. Raghunathan. *Performance and Reliability of Advanced CW Lasers for Silicon Photonics Applications*. In 2022 Optical Fiber Communications Conference and Exhibition (OFC), pages 1–27, 2022.

[20] D. Coenen, H. Sar, H. Oprins, A. Marinins, Y. De Koninck, S. Smyth, Y. Ban, J. Van Campenhout, and I. De Wolf. *Thermal Characterisation of Hybrid, Flip-Chip InP-Si DFB Lasers*. Micromachines, 14(2), 2023.

[21] M. N. Sysak, H. Park, A. W. Fang, J. E. Bowers, R. Jones, O. Cohen, O. Raday, and M. Paniccia. *Experimental and theoretical thermal analysis of a Hybrid Silicon Evanescent Laser*. Opt. Express, 15(23):15041–15046, Nov 2007.

B

Optical pulse propagation in dispersive nonlinear waveguides

This appendix provides a mathematical description of optical pulses traveling through a dispersive and nonlinear waveguide. First the nonlinear wave equation is derived from Maxwell's equations and the concept of nonlinear polarization is introduced. Afterwards, the nonlinear Schrödinger equation is derived which serves as a basic equation to describe propagation of optical pulses in single-mode waveguides.

B.1 Nonlinear Wave Equation

For a linear material, the induced electric polarization is related to the electric field **E** by the following relation

$$\mathbf{P}_L(\mathbf{r},t) = \epsilon_0 \int_{-\infty}^{t} \chi^{(1)}(t-t') \cdot \mathbf{E}(\mathbf{r},t')dt', \tag{B.1}$$

where ϵ_0 is the vacuum permittivity and $\chi^{(1)}$ represents the linear susceptibility in the time domain. In the frequency domain one can write

$$\mathbf{P}_L(\mathbf{r},\omega) = \epsilon_0 \chi^{(1)}(\omega)\mathbf{E}(\mathbf{r},\omega) \tag{B.2}$$

However, in practice the polarization is not perfectly linear with the electric field, and the polarization can be written as the sum of a linear and a nonlinear term (neglecting any static field-independend polarization term)

$$\mathbf{P}(\mathbf{r},t) = \mathbf{P}_L(\mathbf{r},t) + \mathbf{P}_{NL}(\mathbf{r},t) \tag{B.3}$$

where the nonlinear polarization is much smaller than the linear polarization term, and can hence be treated perturbatively with regard to $\mathbf{P}_L$. The nonlinear part $\mathbf{P}_{NL}$ in principle entails all polarization terms $\mathbf{P}_{NL}^{(i)}$ proportional to $\mathbf{E}^i$ with $i > 1$. In the most general case, the nonlinear polarization $\mathbf{P}_{NL}^{(i)}$ can be expressed as

$$\mathbf{P}_{NL}^{(i)}(\mathbf{r},t) = \epsilon_0 \int_{-\infty}^{\infty} dt_1 ... \int_{-\infty}^{\infty} dt_i \int_{-\infty}^{\infty} d\mathbf{r}_1 ... \int_{-\infty}^{\infty} d\mathbf{r}_i \\ \mathbf{T}^{(i)}(\mathbf{r},t,\mathbf{r}_1,t_1 ...,\mathbf{r}_i,t_i)|\mathbf{E}(\mathbf{r}_1,t_1)...\mathbf{E}(\mathbf{r}_i,t_i), \tag{B.4}$$

where $\mathbf{T}^{(i)}$ is a measure for the contribution of the electrical fields to the i-th order polarization, and the $|$ operator comprises the summation of all the weighted contributions of the electric field components, as elaborated in [1]. Fortunately, several approximations can be made to simplify the expression for the nonlinear polarization terms. For example, one can typically assume that the response to the electric field is local, an approximation which is denoted as the electric dipole approximation. A rigorous mathematical treatment can be found in [1].

With the expression B.3 for the electric polariation, one can derive the nonlinear wave equation which can be used to describe the propagation of optical fields through nonlinear optical media. Starting from Maxwell's equations, assuming a nonmagnetic material

$$\nabla \times \mathbf{E} = -\frac{\partial \mathbf{B}}{\partial t} \tag{B.5}$$

$$\nabla \times \mathbf{H} = \mathbf{J} + \frac{\partial \mathbf{D}}{\partial t} \tag{B.6}$$

$$\nabla \cdot \mathbf{D} = \rho \tag{B.7}$$

$$\nabla \cdot \mathbf{B} = 0 \tag{B.8}$$

and the constitutive relations

$$\mathbf{B} = \mu_0 \mathbf{H} \tag{B.9}$$

$$\mathbf{D} = \epsilon_0 \mathbf{E} + \mathbf{P} \tag{B.10}$$

where $\mathbf{E}$ and $\mathbf{H}$ are the electric and the magnetic field vectors, $\mathbf{D}$ and $\mathbf{B}$ are the corresponding electric and magnetic flux densities, $\mathbf{J}$ is the current density, ρ is the charge density, and μ_0 is the vacuum permeability. Taking the curl of equation B.5, one gets

$$\nabla \times \nabla \times \mathbf{E} = -\nabla \times \frac{\partial \mathbf{B}}{\partial t} \tag{B.11}$$

One can rewrite equation B.11 as

$$\nabla(\nabla \cdot \mathbf{E}) - \nabla^2 \mathbf{E} = -\mu_0 \nabla \times \frac{\partial \mathbf{H}}{\partial t} \tag{B.12}$$

By assuming there are no free charges, hence $\rho = 0$ and $\mathbf{J} = 0$, one obtains

$$\nabla(\nabla \cdot \mathbf{E}) - \nabla^2 \mathbf{E} = -\frac{1}{c^2}\frac{\partial^2 \mathbf{E}}{\partial t^2} - \mu_0 \frac{\partial^2 \mathbf{P}}{\partial t^2} \tag{B.13}$$

Furthermore, assuming an isotropic medium with a spatially independent permittivity ϵ one obtains

$$\nabla^2 \mathbf{E} = \frac{1}{c^2}\frac{\partial^2 \mathbf{E}}{\partial t^2} + \mu_0 \frac{\partial^2 \mathbf{P}}{\partial t^2}, \tag{B.14}$$

where the relation $\nabla \cdot \mathbf{D} = \nabla \cdot \epsilon \mathbf{E} = \epsilon \nabla \cdot \mathbf{E} = 0$ was used. Fourier transformation of this equation yields

$$\nabla^2 \mathbf{E}(\mathbf{r}, \omega) = \frac{-\omega^2}{c^2}\mathbf{E}(\mathbf{r}, \omega) - \mu_0 \omega^2 \mathbf{P}(\mathbf{r}, \omega), \tag{B.15}$$

Using $n^2 = 1 + \chi^{(1)}$ for the linear refractive index, one finally obtains

$$\nabla^2 \mathbf{E}(\mathbf{r}, \omega) = \frac{-n^2\omega^2}{c^2}\mathbf{E}(\mathbf{r}, \omega) - \mu_0 \omega^2 \mathbf{P}_{NL}(\mathbf{r}, \omega), \tag{B.16}$$

B.2 Extended Nonlinear Schrödinger Equation

When short optical pulses (typically assuming a pulse duration between 10 fs and 10 ns [2]) travel in a waveguide, both the dispersion and nonlinearity can greatly influence the pulse shape and spectrum. For this reason, it's useful to acquire a basic equation that governs the evolution of the propagating pulse. To enable a straightforward analytical treatment, several simplifying assumptions are made. Firstly, it is assumed that the propagating field maintains its polarization, an approximation that works quite well in practice [2]. Secondly, the pulse spectral width $\Delta\omega_0$ is assumed to be much smaller than the center frequency ω_0 so that the field can be considered as quasi-monochromatic. This assumption is justified for pulse widths down to approximately 100 fs [2]. Furthermore, to adopt the slowly varying envelope approximation, it is convenient to split the electric field into its slowly varying amplitude and its rapidly varying phase term. Similar expressions can be written for the (non)linear part of the polarization

$$\mathbf{E}(\mathbf{r}, t) = \frac{1}{2}\hat{\mathrm{x}}\,[E(\mathbf{r},\mathrm{t})\exp(j\omega_0 t) + \text{ c.c.}] \tag{B.17}$$

Here, $\hat{\mathrm{x}}$ is the unit vector along the direction of polarization and $E(\mathbf{r},\mathrm{t})$ is the slowly varying amplitude. "c.c." refers to "complex conjugate". Furthermore, the

waveguide medium is assumed to have a centrosymmetric crystal structure (which is valid for most common integrated photonic waveguide platforms such as silicon (nitride)-on-insulator), meaning that the second order nonlinar polarization term is zero. This can easily be understood from the fact that due to the symmetry, if an opposite electric field is applied, the nonlinear polarization also needs to be opposite. However, due to the square dependence on the electric field, it is clear that $\mathbf{P}_{NL}^{(2)}(t) = -\mathbf{P}_{NL}^{(2)}(t)$ and the second order nonlinearity hence vanishes. Neglecting higher-order nonlinear terms one can therefore restrict the considered nonlinearity to the third-order contribution $\mathbf{P}_{NL}^{(3)}$. Assuming the nonlinear response is instantaneous and local, one can write [2]

$$\mathbf{P}_{NL}^{(3)}(\mathbf{r},t) = \epsilon_0 \chi^{(3)} |\mathbf{E}(\mathbf{r},t)\mathbf{E}(\mathbf{r},t)\mathbf{E}(\mathbf{r},t) \tag{B.18}$$

Assuming an instantaneous response means contributions of molecular vibrations to the third-order nonlinearity are neglected (i.e. the Raman response). This is a reasonable approximation for pulsewidths exceeding 1 ps [2]. To enable treatment of shorter optical pulses, the Raman contribution is incorporated separately at a later stage. Combining equations B.17 and B.18, one finds

$$P_{NL,\omega_0}^{(3)}(\mathbf{r},t) = \epsilon_0 \frac{3}{4} \chi^{(3)} |E(\mathbf{r},t)|^2 E(\mathbf{r},t) \tag{B.19}$$

To ease further mathematical treatment, it's convenient to transition to the frequency domain. However, given the intensity dependent nature of the third-order nonlinearity, this is generally not feasible. Fortunately, under the slowly varying envelope approximation and given that the nonlinearity is treated perturbatively, one can approximate $\epsilon_{NL} = \frac{3}{4}\chi^{(3)}|E(\mathbf{r},t)|^2$ as a constant. The Fourier transform of the amplitude of the electric field, centered around ω_0, than satisfies the wave equation

$$\nabla^2 \tilde{\mathrm{E}} + \epsilon(\omega) k_0^2 \tilde{\mathrm{E}} = 0 \tag{B.20}$$

where $k_0 = \omega/c$ and

$$\tilde{\mathrm{E}}(\mathbf{r}, \omega - \omega_0) = \int_{-\infty}^{+\infty} E(\mathbf{r},\mathrm{t}) \exp\left[-j(\omega - \omega_0)t\right] dt \tag{B.21}$$

$$\epsilon(\omega) = 1 + \chi^{(1)}(\omega) + \epsilon_{NL} \tag{B.22}$$

By using the method of separation of variables, one can write the electric field component $\tilde{\mathrm{E}}$ as the product of a slowly varying peak amplitude, a modal distribution and a phase factor. The modal distribution $F(x,y)$ is normalized such that $\int\int_{-\infty}^{+\infty} |F(x,y)|^2 dxdy = 1$.

$$\tilde{\mathrm{E}}(\mathbf{r}, \omega - \omega_0) = F(x,y)\tilde{\mathrm{A}}(z,\ \omega - \omega_0) \exp(-j\beta_0 z) \tag{B.23}$$

where $\tilde{\mathrm{A}}(z,\ \omega-\omega_0)$ is a slowly varying function of the propagation distance z, and β_0 is the wave number. One can now substitute equation B.23 into the wave equation B.20

$$\nabla^2_{x,y}F(x,y)\tilde{\mathrm{A}}(z,\ \omega-\omega_0)\exp(-j\beta_0 z)+\frac{\partial^2}{\partial z^2}\left[F(x,y)\tilde{\mathrm{A}}(z,\ \omega-\omega_0)\exp(-j\beta_0 z)\right] + \epsilon(\omega)k_0^2F(x,y)\tilde{\mathrm{A}}(z,\ \omega-\omega_0)\exp(-j\beta_0 z)=0 \quad \text{(B.24)}$$

Which can be rewritten as

$$\frac{1}{F(x,y)}\left[\nabla^2_{x,y}F(x,y)+\epsilon(\omega)k_0^2F(x,y)\right] = - \frac{1}{\tilde{\mathrm{A}}(z,\ \omega-\omega_0)\exp(-j\beta_0 z)}\frac{\partial^2}{\partial z^2}\left[\tilde{\mathrm{A}}(z,\ \omega-\omega_0)\exp(-j\beta_0 z)\right] \quad \text{(B.25)}$$

Using $\tilde{\beta}^2$ as a separation constant, one obtains two equations for F(x,y) and $\tilde{\mathrm{A}}(z,\ \omega-\omega_0)$

$$\nabla^2_{x,y}F-(\tilde{\beta}^2-\epsilon k_0^2)F=0 \quad \text{(B.26)}$$

$$2j\beta_0\frac{\partial\tilde{A}}{\partial z}-(\tilde{\beta}^2-\beta_0^2)\tilde{A}=0 \quad \text{(B.27)}$$

where the $\frac{\partial^2\tilde{\mathrm{A}}}{\partial z^2}\exp(-j\beta_0 z)$ term was neglected in the second equation under the slowly varying envelope approximation. Using a perturbative expression for the propagation constant $\tilde{\beta}(\omega)=\beta(\omega)+\Delta\beta$ where $\Delta\beta$ is given by [2]

$$\Delta\beta=\frac{k_0\int\int_{-\infty}^{+\infty}\Delta\tilde{n}(x,y)|F(x,y)|^2dxdy}{\int\int_{-\infty}^{+\infty}|F(x,y)|^2dxdy} \quad \text{(B.28)}$$

and approximating $\tilde{\beta}^2-\beta_0^2\approx 2\beta_0\left(\beta(\omega)+\Delta\beta-\beta_0\right)$ one can write the slowly varying amplitude equation as

$$\frac{\partial\tilde{A}}{\partial z}=-j\left[\beta(\omega)+\Delta\beta-\beta_0\right]\tilde{A} \quad \text{(B.29)}$$

At this point, it is useful to express the propagation constant $\beta(\omega)$ as a Taylor expansion $\beta(\omega)=\beta_0+\beta_1(\omega-\omega_0)+\frac{\beta_2}{2}(\omega-\omega_0)^2+\ldots$. Higher order terms can be neglected as long as $\Delta\omega << \omega_0$ and when β_2 is not close to zero. The coefficients β_1, β_2 and β_3 are respectively the inverse of the group velocity v_g, the group velocity dispersion (GVD), and the third-order dispersion parameter. Inserting the expansion for $\beta(\omega)$ up to third-order, one obtains

$$\frac{\partial \tilde{A}}{\partial z} = -j\left[\beta_1(\omega-\omega_0) + \frac{\beta_2}{2}(\omega-\omega_0)^2 + \frac{\beta_3}{6}(\omega-\omega_0)^3 + \Delta\beta\right]\tilde{A} \quad \text{(B.30)}$$

approximating $\Delta\beta$ as constant, in the time domain this translates translates to

$$\frac{\partial A}{\partial z} = -\beta_1\frac{\partial A}{\partial t} + j\frac{\beta_2}{2}\frac{\partial^2 A}{\partial t^2} + \frac{\beta_3}{6}\frac{\partial^3 A}{\partial t^3} - j\Delta\beta A \quad \text{(B.31)}$$

Rewriting $\Delta\beta$ yields

$$\Delta\beta = \frac{k_0\int\int_{-\infty}^{+\infty}\Delta\tilde{n}|F(x,y)|^2dxdy}{\int\int_{-\infty}^{+\infty}|F(x,y)|^2dxdy} \quad \text{(B.32)}$$

$$\approx \frac{k_0\int\int_{-\infty}^{+\infty}(\bar{n}_2|E|^2 - j\frac{\alpha_0}{2k_0})|F(x,y)|^2dxdy}{\int\int_{-\infty}^{+\infty}|F(x,y)|^2dxdy} \quad \text{(B.33)}$$

$$\approx k_0\bar{n}_2|A|^2\frac{\int\int_{-\infty}^{+\infty}|F(x,y)|^4dxdy}{\int\int_{-\infty}^{+\infty}|F(x,y)|^2dxdy} - j\frac{\alpha_0}{2} \quad \text{(B.34)}$$

$$\approx k_0\bar{n}_2|A|^2\frac{1}{A_{eff}}\int\int_{-\infty}^{+\infty}|F(x,y)|^2dxdy - j\frac{\alpha_0}{2} \quad \text{(B.35)}$$

$$\approx |A|^2\bar{\gamma} - j\frac{\alpha_0}{2} \quad \text{(B.36)}$$

where the complex refractive index perturbation $\Delta n = \bar{n}_2|A|^2 - j\frac{\alpha_0}{2k_0}$, with α_0 the linear waveguide loss, and with $\bar{\gamma}$ defined as

$$\bar{\gamma} = \frac{\bar{n_2}\omega_0}{cA_{eff}} \quad \text{(B.37)}$$

with the effective mode area A_{eff}

$$A_{eff} = \frac{\left(\int\int_{-\infty}^{+\infty}|F(x,y)|^2dxdy\right)^2}{\int\int_{-\infty}^{+\infty}|F(x,y)|^4dxdy} \quad \text{(B.38)}$$

Inserting the expression for $\Delta\beta$ into equation B.31, one obtains

$$\frac{\partial A}{\partial z}(z,t) + \beta_1\frac{\partial A}{\partial t}(z,t) - j\frac{\beta_2}{2}\frac{\partial^2 A}{\partial t^2}(z,t) - \frac{\beta_3}{6}\frac{\partial^3 A}{\partial t^3}(z,t) = -\frac{\alpha}{2}A(z,t) - j\bar{\gamma}|A(z,t)|^2A(z,t) \quad \text{(B.39)}$$

Converting equation B.39 so that $|A(z,t)|^2$ represents the optical power in the pulse, one obtains

$$\frac{\partial A}{\partial z}(z,t) + \beta_1 \frac{\partial A}{\partial t}(z,t) - j\frac{\beta_2}{2}\frac{\partial^2 A}{\partial t^2}(z,t) - \frac{\beta_3}{6}\frac{\partial^3 A}{\partial t^3}(z,t) = -\frac{\alpha}{2}A(z,t) - j\gamma|A(z,t)|^2 A(z,t) \quad \text{(B.40)}$$

where the nonlinear parameter $\gamma = \frac{\bar{n_2}\omega_0}{cA_{eff}}$ and where the material nonlinear coefficient $n_2 = \frac{2}{n_0}\sqrt{\frac{\mu_0}{\epsilon_0}}\bar{n_2}$. Equation B.40 (which resembles the nonlinear Schrödinger (NLS) equation) describes the propagation of a picosecond optical pulse in single-mode waveguides, including the effects of linear waveguide loss (α_0), dispersion (β_1, β_2, β_3) and third-order nonlinearity (γ). Althouh equation B.40 provides an adequate description for many cases, some modifications are needed when ultrashort pulses (on the order of 1 ps or less) are considered. One effect that becomes non-negligible for ultrashort optical pulses is intrapulse Raman scattering, which causes a transfer of energy from the high-frequency components to the low-frequency components of the same pulse. This leads to a spectral redshift of the pulse spectrum. The assumption that the nonlinear response is instantaneous is in this case no longer valid as the vibrational Raman response has a delayed nature. To incorporate the Raman response, one can introduce a so-called nonlinear response function R(t) [2, 3] which accounts for the delayed temporal response of the nonlinear polarization to the electric field. The pulse propagation equation than becomes

$$\frac{\partial A}{\partial z}(z,t) + \beta_1 \frac{\partial A}{\partial t}(z,t) - j\frac{\beta_2}{2}\frac{\partial^2 A}{\partial t^2}(z,t) - \frac{\beta_3}{6}\frac{\partial^3 A}{\partial t^3}(z,t) = -\frac{\alpha}{2}A(z,t) - j\gamma A(z,t)\int_0^\infty R(t')|A(z,t-t')|^2 dt' \quad \text{(B.41)}$$

where the nonlinear response function $R(t) = (1 - f_R)\delta(t) + f_R h_R(t)$ with f_R the fractional contribution of the delayed Raman response to the nonlinear polarization and $h_R(t)$ the Raman response function, which can be approximated by an analytical function [3–5]

$$h_R(t) = \frac{\tau_1^2 + \tau_2^2}{\tau_1 \tau_2^2} e^{-t/\tau_2} sin(t/\tau_1) \quad \text{(B.42)}$$

where $\tau_2 = 1/\Gamma_R$, $\tau_1 = 1/(\omega_R^2 - \Gamma_R^2)^{1/2}$, and for a silicon waveguide, $\Gamma_R/\pi \approx$105 GHz and $\omega_R/2\pi$=15.6 THz respectively determine the Raman-gain bandwidth and Raman shift [5].

Furthermore, the frequency dependency of γ can be included and approximated as

$$\gamma(\omega) \approx \gamma(\omega_0) + \frac{d\gamma}{d\omega}\Big|_{\omega=\omega_0}(\omega-\omega_0) \approx \gamma(\omega_0) + \frac{\gamma(\omega_0)}{\omega_0} \tag{B.43}$$

leading to the pulse propagation equation

$$\begin{aligned}&\frac{\partial A}{\partial z}(z,t) + \beta_1\frac{\partial A}{\partial t}(z,t) - j\frac{\beta_2}{2}\frac{\partial^2 A}{\partial t^2}(z,t) - \frac{\beta_3}{6}\frac{\partial^3 A}{\partial t^3}(z,t)\\ &= -\frac{\alpha}{2}A(z,t) - j(\gamma(\omega_0) - j\frac{\gamma(\omega_0)}{\omega_0}\frac{\partial}{\partial t})A(z,t)\int_0^\infty R(t')|A(z,t-t')|^2 dt'\end{aligned} \tag{B.44}$$

By using the Taylor expansion $|A(z,t-t')|^2 \approx |A(z,t)|^2 - t'\frac{\partial}{\partial t}|A(z,t-t')|^2$, defining $T_R = \int_0^\infty tR(t)dt$, assumptions which are reasonable for pulsewidths exceeding 100 fs [2], and by introducing a reference frame moving with the pulse at the group velocity v_g by using the transformation

$$T = t - z/v_g = t - \beta_1 z \tag{B.45}$$

one obtains

$$\begin{aligned}&\frac{\partial A}{\partial z} - j\frac{\beta_2}{2}\frac{\partial^2 A}{\partial T^2} - \frac{\beta_3}{6}\frac{\partial^3 A}{\partial T^3} + \frac{\alpha}{2}A =\\ &\qquad - j\gamma(|A|^2 A - \frac{j}{\omega_0}\frac{\partial}{\partial T}(|A|^2 A) - T_R A\frac{\partial |A|^2}{\partial T})\end{aligned} \tag{B.46}$$

where the term containing T_R/ω_0 was neglected. Equation B.46 is called the extended (or generalized) nonlinear Schrödinger equation. The term $\frac{j}{\omega_0}\frac{\partial}{\partial T}(|A|^2 A)$ accounts for the self-steepening effect, resulting from the intensity dependency of the group-velocity (the velocity of the peak of the pulse is reduced, leading to an increasing slope of the trailing part of the pulse hence the name self-steepening).

Finally, as optical pulses with high intensities can suffer considerably from two (or multi)-photon absorption as well as from absorption due to optically generated free carriers [6], it is desirable to include these absorption terms in equation B.46. This leads to the following equation [7, 8]:

$$\begin{aligned}&\frac{\partial A}{\partial z} - j\frac{\beta_2}{2}\frac{\partial^2 A}{\partial T^2} - \frac{\beta_3}{6}\frac{\partial^3 A}{\partial T^3} + \frac{\alpha}{2}A - \frac{\beta_{TPA}}{2A_{eff}}|A|^2 A - \frac{\sigma N_c}{2}A\\ &\qquad = -j\gamma(|A|^2 A - \frac{j}{\omega_0}\frac{\partial}{\partial T}(|A|^2 A) - T_R A\frac{\partial |A|^2}{\partial T}) + jk_c k_0 N_c A\end{aligned} \tag{B.47}$$

where β_{TPA} is the two-photon absorption parameter, and the free-carrier absorption and dispersion are included through the free-carrier absorption coefficient

σ and the free-carrier dispersion parameter k_c. The time dependence of the free-carrier density is described through the auxiliary equation

$$\frac{dN_c}{dt} = \frac{\beta_{TPA}}{2\hbar\omega_0 A_{eff}^2}|A|^4 - \frac{N_c}{\tau_{FCA}}, \tag{B.48}$$

where τ_{FCA} is the free-carrier lifetime in the waveguide and $\hbar\omega_0$ is the photon energy.

References

[1] R. W. Boyd. *Nonlinear Optics, Third Edition*. Academic Press, Inc., USA, 3rd edition, 2008.

[2] G. Agrawal. *Chapter 2 - Pulse Propagation in Fibers*. In G. Agrawal, editor, Nonlinear Fiber Optics (Fifth Edition), Optics and Photonics, pages 27 – 56. Academic Press, Boston, fifth edition edition, 2013.

[3] K. J. Blow and D. Wood. *Theoretical description of transient stimulated Raman scattering in optical fibers*. IEEE Journal of Quantum Electronics, 25(12):2665–2673, 1989.

[4] I. Cristiani, R. Tediosi, L. Tartara, and V. Degiorgio. *Dispersive wave generation by solitons in microstructured optical fibers*. Opt. Express, 12(1):124–135, Jan 2004.

[5] Q. Lin, O. J. Painter, and G. P. Agrawal. *Nonlinear optical phenomena in silicon waveguides: Modeling and applications*. Opt. Express, 15(25):16604–16644, Dec 2007.

[6] A. Hermans, K. Van Gasse, J. O. Kjellman, C. Caër, T. Nakamura, Y. Inada, K. Hisada, T. Hirasawa, S. Cuyvers, S. Kumari, A. Marinins, R. Jansen, G. Roelkens, P. Soussan, X. Rottenberg, and B. Kuyken. *High-pulse-energy III-V-on-silicon-nitride mode-locked laser*. APL Photonics, 6(9):096102, 2021.

[7] S. Roy, S. K. Bhadra, and G. P. Agrawal. *Femtosecond pulse propagation in silicon waveguides: Variational approach and its advantages*. Optics Communications, 281(23):5889 – 5893, 2008.

[8] H. Zhou, S.-W. Huang, X. Li, J. F. McMillan, C. Zhang, K. K.-Y. Wong, M. Yu, G.-Q. Lo, D.-L. Kwong, K. Qiu, and C. W. Wong. *Real-time dynamics and cross-correlation gating spectroscopy of free-carrier Drude slow-light solitons*. Light: Science & Applications, 6(6):e17008–e17008, Jun 2017.

C

Cleanroom process details

C.1 Bilayer lift-off process

Lift-off refers to the process of exposing a pattern in photoresist, depositing a thin film (typically a metal or dielectric) over the entire sample, and then removing the photoresist with a wet chemical to leave behind the film only in the patterned areas. Typically, a single negative (or image reversed) photoresist is used to create a negative resist slope at the edges, facilitating the lift-off process. However, in some cases the undercut achieved with a single photoresist layer is insufficient to successfully complete the lift-off. For these cases, a bilayer lift-off method is particularly useful. By using two different types of resist on top of each other, one can pattern the top resist layer and undercut the bottom layer to achieve the desired resist profile.

A process flow example for the LOR B series photoresist is outlined below.

1. Spincoat LOR 20B photoresist at 4000 rpm for 40 s (5000 rpm for lift-off of submicron thick layers)

2. Bake sample at 170°C for 3 min

3. Spincoat TI 35E photoresist at 3000 rpm for 40 s (4000 rpm for lift-off of submicron thick layers)

4. Bake sample at 100°C for 3 min

5. Expose for 55 s in contact mode (exposure with Karl Suss MA-6 mask aligner, lamp intensity around 5 mW/cm^2)

6. Wait for 10 min after the exposure

7. Reversal bake at 125°C for 3 min

8. Flood exposure for 185 s

9. Development in AZ400K:H_2O 1:3 for $\sim 2 \times 1$ min (possibly combined with oxygen plasma)

The above process has been used successfully to pattern the backside mirror of edge-coupled GaAs semiconductor optical amplifiers (see chapter 6) and to pattern the final metal layer of a heterogeneous Si_3N_4/Si/III-V mode-locked laser in the recess of a commercial Si_3N_4 PIC from Ligentec (see chapter 4). The latter example is depicted in Fig. C.1.

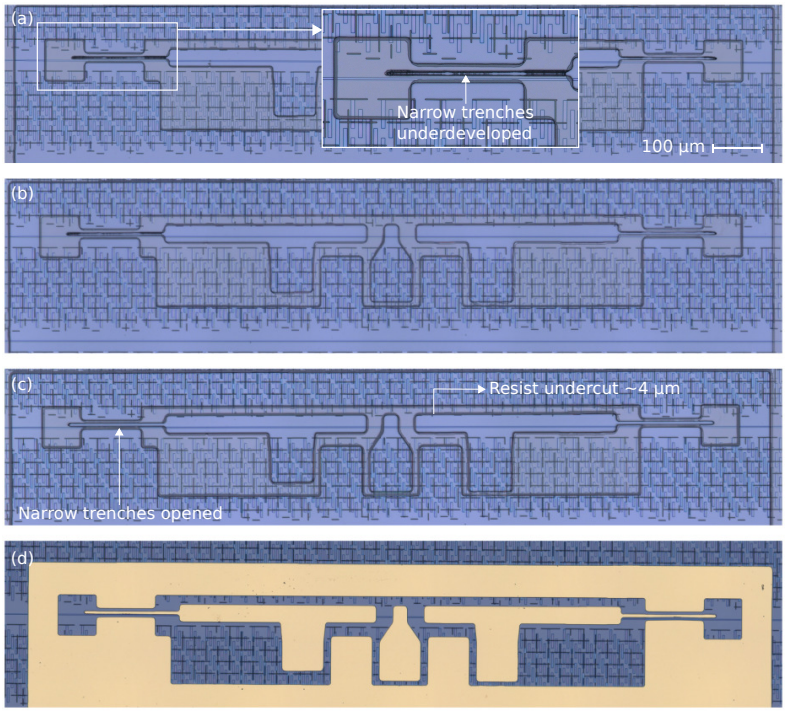

Figure C.1: Example of a bilayer lift-off process to pattern the final metal layer on a Si_3N_4 PIC. Patterned photoresist after development in AZ400K:H_2O 1:3 (a), after 5 min of additional oxygen plasma to remove the resist in the narrow trenches (b), after 10 s of extra development in AZ400K:H_2O 1:3 (c), and after lift-off with Ti/Au (d).

Fig. C.1(a) shows the patterned photoresist after development in AZ400K:H_2O 1:3. As some photoresist remains in the narrow trenches, 5 min of oxygen plasma is used to clear the trenches without suffering from an excessive undercut that would result from a longer development time (Fig. C.1(b)). Afterwards, 10 s of additional development is used to create some undercut in the trenches as well (Fig. C.1(c)). Finally, Ti/Au (40/1000 nm) are deposited and lift-off is performed on a rotator using Remover PG, which is a proprietary NMP-based solvent. The resulting metal layer is depicted in Fig. C.1(d).

It was observed that exposed BCB films are prone to delamination during immersion in Remover PG. To mitigate this, it's recommended to perform the lift-off process at room temperature and limit the exposure time to the solvent. Alternatively, protection of the BCB could be achieved by covering it with another material, for example SiO_2.

C.2 Si coupons for micro-transfer printing

Detailed process flows to define 400 nm thick Si micro-transfer printable coupons on a silicon-on-insulator wafer are outlined below, either based on vapor-phase HF release etching (without coupon encapsulation) or liquid HF release etching (with photoresist encapsulation). For the latter case, the photoresist needs to be sufficiently thick to ensure sufficient mechanical strength to avoid possible collapse of the coupons. Similar process flows can be employed for other Si thicknesses, e.g. 220 nm.

C.2.1 Process flow for vapor-phase HF release etch

1. Contact lithography for coupon and tether definition
   (a) Spincoat TI prime adhesion promotor at 4000 rpm, 40 s
   (b) Bake sample at 120°C for 3 min
   (c) Spincoat AZ5214 photoresist at 4000 rpm, 40 s
   (d) Bake sample at 100°C for 3 min
   (e) Expose for 22 s in contact mode (exposure with Karl Suss MA-6 mask aligner, lamp intensity around 5 mW/cm^2)
   (f) Development in AZ400K:H_2O 1:3 for $\sim$35 s
2. RIE dry etching
   (a) Clean chamber of the RIE
   (b) 30 s oxygen plasma (soft removal)
   (c) Si dry etch using CF_4, SF_6, H_2, etch rate approximately 80 nm/min

(d) Strip photoresist

3. Vapor HF release etch

   (a) Optional: 2 min liquid HF (40%) etch to speed up release etching

   (b) Vapor-HF etching at 40°C in cycles of <45 min (regularly check for condensation) until underetch is complete

4. Micro-transfer print to verify successful completion of the release etch

C.2.2 Process flow for liquid HF release etch

1. Contact lithography for coupon definition

   (a) Spincoat TI prime adhesion promotor at 4000 rpm, 40 s

   (b) Bake sample at 120°C for 3 min

   (c) Spincoat AZ5214 photoresist at 4000 rpm, 40 s

   (d) Bake sample at 100°C for 3 min

   (e) Expose for 22 s in contact mode (exposure with Karl Suss MA-6 mask aligner, lamp intensity around 5 mW/cm^2)

   (f) Development in AZ400K:H_2O 1:3 for ∼35 s

2. RIE Si dry etching

   (a) Clean chamber of the RIE

   (b) 30 s oxygen plasma (soft removal)

   (c) Si dry etch using CF_4, SF_6, H_2, etch rate approximately 80 nm/min

   (d) Strip photoresist

3. Contact lithography for release layer patterning

   (a) Spincoat TI prime adhesion promotor at 4000 rpm, 40 s

   (b) Bake sample at 120°C for 3 min

   (c) Spincoat TI35E photoresist at 2000 rpm, 40 s

   (d) Bake sample at 100°C for 3 min

   (e) Expose for 140 s in contact mode (exposure with Karl Suss MA-6 mask aligner, lamp intensity around 5 mW/cm^2)

   (f) Wait 10 min

   (g) Development in AZ400K:H_2O 1:3 for ∼1min45 s

4. RIE SiO_2 dry etching

(a) Clean chamber of the RIE

(b) SiO_2 dry etch using CF_4, SF_6, H_2, etch rate approximately 40 nm/min (selectivity with photoresist $\sim$1:1)

(c) Si dry etch into substrate using CF_4, SF_6, H_2 for 2 min, etch rate approximately 80 nm/min

(d) Strip photoresist

5. Contact lithography for encapsulation, using either TI35E or AZ10XT photoresist. The latter is recommended for wide coupons (e.g. $\geq$80 μm width).

(a) Native oxide removal:
Acid dip 7 s BHF:H_2O 1:10 + 7 s H_2SO_4:H_2O_2:H_2O 1:1:10

(b) Rinse in IPA, thorough drying with nitrogen gun

(c) *Spincoat TI prime adhesion promotor at 4000 rpm, 40 s (in case of AZ10XT photoresist)*

(d) *Bake sample at 120°C for 3 min (in case of AZ10XT photoresist)*

(e) Spincoat TI35E photoresist at 2000 rpm, 40 s *(or AZ10XT photoresist at 4000 rpm, 40 s)*

(f) Bake sample at 100°C for 3 min *(110°C for 2 min in case of of AZ10XT photoresist)*

(g) *Wait 30 min (in case of AZ10XT photoresist)*

(h) Expose for 140 s in contact mode *(120 s in case of AZ10XT photoresist)*

(i) Wait 10 min *(skip this step in case case of AZ10XT photoresist)*

(j) Development in AZ400K:H_2O 1:3 for $\sim$1min45 s *($\sim$4min30 s in case of AZ10XT photoresist)*

(k) Bake sample at 125°C for 3 min *(skip this step in case case of AZ10XT photoresist)*

(l) Flood exposure for 180 s *(skip this step in case case of AZ10XT photoresist)*

6. Release etch in HF

(a) Submerge for 15 min in 40% liquid HF

(b) Carefully rinse sample with 3 cups of DI water

(c) Leave the sample to dry in air, do not blow dry to avoid coupon collapse

7. Micro-transfer print to verify successful completion of the release etch